# One and Two Point Micro-Rheology of Hard Sphere Suspensions


*Andrew W. Harrison*

A thesis submitted in fulfilment of the requirements
for the degree of Doctor of Philosophy
to the
University of Edinburgh

October 13, 2010

## Book of Days

One Day, one Night, one Moment,
My Dreams could be tomorrow,
One Step, one Fall, one Falter,
East or West,
Over Earth or by Ocean,
One way to be my Journey,
This way could be my Book of Days.

Ò lá go lá, mo thuras,
An bealac fada romham,
Ò oich fo hoiche, mo thuras,
Na scéalta nac mbeifh a choích.

*From Day to Day my Journey,*
*The long Pilgrimage before me,*
*From Night to Night, my Journey,*
*The Stories that will never be again.*

No Day, no Night, no Moment,
Can hold me back from trying,
I'll Flag, I'll Fall, I'll Falter,
I'll find my Day maybe Far and Away,
Far and Away.

One Day, one Night, one Moment,
With a Dream to Believe in,
One Step, one Fall, one Falter,
And a new Earth across a Wide Ocean,
This way became my Journey,
This day ends together,
Far and Away.

This day ends together,
Far and Away,
Far and Away.

Book of Days by *Enya*

# Abstract

The material that is covered in this thesis concerns the calibration and application of a set of optical tweezers to be used for one- and two-point micro-rheology experiments on hard sphere colloidal suspensions. The colloidal suspensions that were used in this study were all quasi-monodisperse density- and refractive index-matched PMMA particles that had a radii, $a = 0.90 \pm 0.05\mu$m or $a = 0.86 \pm 0.07$ for one-point micro-rheology experiments and radii $a = 0.90 \pm 0.05\mu$m or $a = 0.133 \pm 0.010\mu$m for the two-point micro-rheology experiments.

By collecting the forward scattered light from a single optically trapped particle the particle's displacements in time were used to determine passive microviscosity, $\eta_{\mu}^{(Passive)}$, for colloidal suspension in the range of $0.10 < \phi < 0.57$ and comparison with literature data has been made and agreement found.

Actively dragging an optically trapped particle through suspensions with volume fractions of the same range has yielded the active microviscosities, $\eta_{\mu}^{(Active)}$, for both high and low shear regimes, displaying shear thinning behaviour. Comparison to literature data has been made and agreement found as well.

Collecting the forward scattered light from two optically trapped particles has been used to determine the cross-correlated motion of the two particles in bare solvent and in suspensions with volume fraction $\phi = 0.02$. The friction coefficients $\xi_{1,1}$ and $\xi_{1,2}$ were extracted from the cross-correlated motion of the particles and agreement was found with theoretical predictions for bare solvent only. The suspensions with volume fraction $\phi = 0.02$ were found to have a friction coefficient $\xi_{1,1}$ that was greater than what theory predicted with the suspension with bath particles $a = 0.90 \pm 0.05\mu$m had the greater magnitude. The magnitude $\xi_{1,2}$ was found to decrease for the suspension with bath particles of radius $a = 0.133 \pm 0.010\mu$m and to increase for the suspension with bath particles $a = 0.90 \pm 0.05\mu$m.

# Declaration

This thesis has been composed by myself and has not been submitted in any previous application for a degree. The material reported within has been executed by myself, except where explicitly stated.

*Andrew W. Harrison*
June 2010

# Acknowledgements

I would like to thank first Wilson Poon for providing me with the direction, support and motivation in carrying out this work that has been my life for the past few years. I would be negligent if I did not also thank Laurence Wilson who has had to put up with my, what would seem like, constant bothering concerning the Optical Tweezers, but for mostly being a very supportive friend through this endeavour.

For technical work and great patience for the demands that were made at short notice I have to thank Andrew Downie and Andrew Garrie.

I must thank Anne Pawsey for the time and effort she put in to proof read this thesis in its many incarnations and wish her well when it comes to write her own. I would also like to thank Tiffany Wood who also proof read this document and for the many helpful conversations in guiding and understanding the material that has been included.

Other individuals who are also worthy of note are Judith McCarron for the refreshing conversations that had nothing do with work, Susie Alison whose giggle always brightened those mornings when work had to start early, Helen Casely for telling me that I was making progress and to relax by playing cricket and watching the Ashes, Paul Tulip for putting up with me whinging so often about so many things but for also being a great office mate for the brief time we shared an office and to Fionna Conway who never understood any of my work but always listened and didn't mind.

For the many beers that kept me sane I have to thank firstly Andrew Schofield, Colin McGuinness and Danielle van 't Zand.

I would have been lost if not for the helpful discussions from Rut Besseling, Lucio Isa and Job Thijssen that helped me understand the finer points of this field.

The $E = mcc$ who have allowed me to play many games of cricket and though we have only one game in the time here; I have enjoyed every minute of batting in the rain in the attempt to help the Captain winning Buckfast Moment of the Year and thereby winning myself the Champagne Moment of the Year.

The 'Manchester Crowd' also have to be mentioned Alexander Barker, Chris Sampson, Elaine Gibbs, Helen Brooks, Alexandra Hughes, Helen Mytton-Mills, Simon

Barlow, Nicholas Shipillis and Steve Pritchard who always supported me since I met them.

And a final thank you to the numerous people that cannot be listed here that offered me the encouragement to continue with my work.

# Contents

# List of Figures

# List of Tables

# Chapter 1

# Introduction

Rheology is the study of how materials flow and deform and 'complex fluids' in particular are of interest to the field of rheology. Complex fluids tend be fluids that have either colloidal particles or small molecules, suspended through out the fluid, where the particles or molecules have a typical size ranging from tens of nanometres to a few microns. The spacing of the particles or small molecules in the fluid has a typical lengthscale ($\sim \mu$m) that is much larger than the separation of the atoms or molecules of the host fluid ($\sim$ 10nm). As such if the fluid is deformed it will take time for the particles or molecules to relax back to the lengthscale associated with the unpeturbed system. The timescale that these relaxations occur over, the Brownian relaxation time, are large enough that they are observable to us in everyday life ($\sim$ms), examples of such materials are foods and cosmetics; foods like whipped cream will flow quickly when force is applied but is highly viscous when no force is applied and cosmetics that are pastes need to be able to flow so that they can be applied but then not run off the skin that they have been applied to. The investigation and understanding of how these complex fluids flow and deform is rheology.

## 1.1 Micro-rheology

Micro-rheology, like the name suggests, is the study of how a material deforms and flows on microscopic scale, which may not be the same as the bulk rheology of the material. In order to study materials on a microscopic level several techniques have been developed that generally utilise a microscope in some manner such as, video tracking, epi-flourescence, confocal microscopy. The systems mentioned are what would be described as passive measurements as they do not impart any net force onto the material, for passive systems the sample needs to have been or be perturbed in some manner to make it flow.

## 1.2 Optical Tweezers

Optical tweezers [9] are a tool that allows the manipulation of objects on a microscopic level using the momentum of photons provided by focussed laser beam. This tool allows the rheologist to no longer be a passive observer of the system but to actually be able to actively probe the micro-rheology of the material. Apart from being able to be used as a microscopic manipulation tool optical tweezers can also be used to determine the forces exerted by, and within, the material with a higher temporal resolution than most of the passive micro-rheology systems mentioned earlier. Accordingly the use of optical tweezers in the measurement of forces with in a system is of interest in haematology [10], fungal biology [11] and condensed matter[12, 13] to name but a few specialities.

## 1.3 Optical Tweezers with Colloids

It is specifically hard sphere colloidal suspensions that are investigated in this thesis using optical tweezer measurements to determine the micro-rheology of the system. The optical tweezers can be used to hold a single particle and measure the fluctuations that it experiences and how they change as more colloidal particles are added to the suspension. The tweezers can also be used to move one of the particles through the suspension and measure the forces that the particle experiences. Additionally optical tweezers are not confined to holding only one particle [14, 15, 16, 17].

## 1.4 Thesis Outline

This thesis is comprised of three parts, the first describes the theory behind the optical tweezers and the analytical methods that were used and can be found in chapter 2. The second part outlines the characterisation of the optical tweezers that were used and the materials that were used with them, chapters 3 and 4 respectively. The final part describes one-point micro-rheology experiments, two-point micro-rheology experiments and a summary of the conclusions that can be drawn, chapters 5-7 respectively.

Chapter 2 describes the theory behind the trapping force of the optical tweezers and mathematics that can be used to model the force exerted by an optical trap. It then explains the analytical methods that were used to calibrate the optical traps and the methods that were used to analyse the experimental data obtained.

Chapter 3 describes the design of the optical tweezers and the apparatus that had been used to construct them. A complete description of how to calibrate the the optical trap stiffnesses and sensitivities. A description of how to account for the anharmonicity in the potential of the optical traps is also given along with how to correct for the

overestimation of the particle position at large displacements by the quadrant photo diode detectors used.

Chapter 4 introduces the colloidal system that was used for the experiments. It describes the characteristics that were required of the colloidal particles and the methods used to ensure that they interacted as hard spheres. It briefly describes some of the micro-rehological techniques that were used in this thesis but focusses on the ones that were used to characterise the colloidal particles and the solvents that they were suspended in.

Chapter 5 gives the experimental results for the one-point micro-rheology experiments. The passive microviscosity, $\eta_{\mu}^{(Passive)}$, of colloidal suspensions with volume fractions below the glass transition is measured and compared with established dynamic light scattering data that can be found in the literature [5]. It then describes the results for the active microviscosity, $\eta_{\mu}^{(Active)}$, of suspensions in the same range and compares the microviscosity with the (bulk) macroviscosities that can also be found in the literature [18]. A final section is included in the design and calibration of a parallel plate shear cell that was to be used in conjunction with the optical tweezers.

Chapter 6 gives the experimental results for two-point micro-rheology experiments. The cross-correlated motion of two particles suspended in a fluid is measured and compared to established theory. The cross-correlated motions of two particles in a finite colloidal suspension is then described followed by an investigation of the friction coefficients associated with the trapped particles $\xi_{1,1}$, $\xi_{1,2}$ and how they interact to produce features associated with correlated and anti-correlated motion of the two particles respectively.

Finally chapter 7 summarises the information obtained and describes future experimental work based on the work presented in this thesis.

# Chapter 2

# Optical Theory & Analytical Methods

This chapter first details the mathematical theory that describes how colloidal particles can be confined by an optical trap provided they have a different refractive index to the solvent that they are suspended in. How the potential of the optical trap and the force exerted by it can be modelled as a harmonic spring is then explained.

The second part of this chapter describes the analytical methods that were used to calibrate the optical tweezers and to analyse data from one-trap experiments. Special attention is paid to the use of the power spectrum of a particle confined by a single optical trap.

The methods that were used to balance the stiffnesses of two independent optical traps are explained, followed by the analytical method used to determine cross-correlationsfrom two-trap data.

## 2.1 Optical Forces

An optical trap is in effect a focussed laser beam. In such a situation there are two distinct forces that the laser will exert on a particle that encounters the optical trap, a scattering force and a gradient force. The scattering force is more intuitive to understand; it is the force exerted by the coherent photons travelling along the laser beam and exert their force along the propagation direction of the laser beam. The gradient force on the other hand is more complex and is due to the laser beam being focussed. This results in variations of the intensity of the laser beam across the beam's diameter in the region of focus. The direction of this force is directed towards the the focal point of the laser beam with the highest intensity that constitutes the optical trap and can be best described in figure 2.1. Mathematically the two forces are

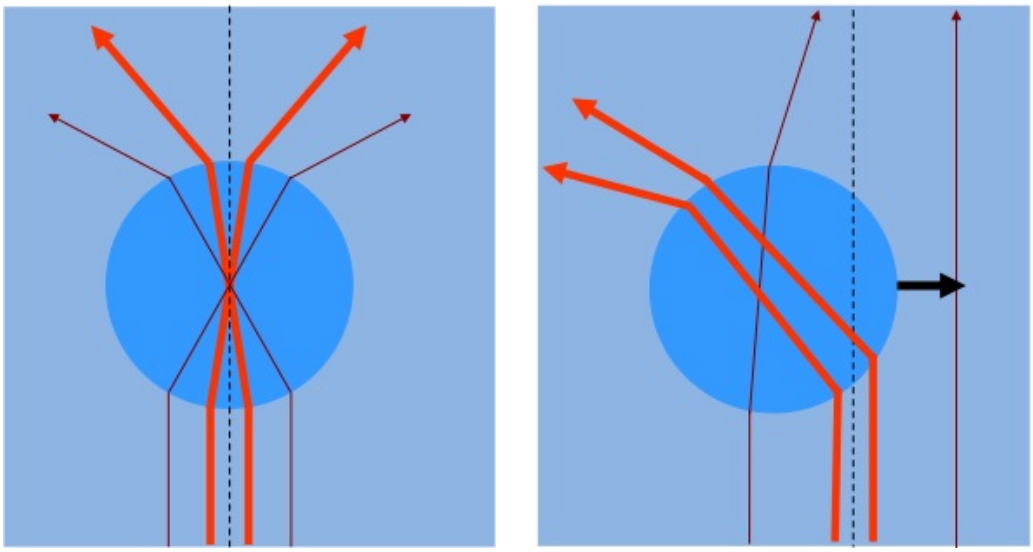

(a) (b)

Figure 2.1: Schematic of the gradient force exerted by a focussed laser on a dielectric particle for (a) a particle held in equilibrium (black dotted line) and (b) a particle out of equilibrium where a restoring force is being exerted by the region of greater laser intensity. The thicker ray paths of the laser indicate greater laser intensity.

easily distinguished. The scattering force depends on only the number photons that are propagating along the laser beam and as such will be a function of the square of the laser beam's electric field, $E^2$. The gradient force will also be dependant on the number of photons that pass through the focus of the laser beam but because there are regions of greater intensity of photons the force can therefore be described by the gradient of the square of the laser beam's electric field, $\nabla(E^2)$. The combination of these two functions can then be used to model the force exerted by the optical traps as that of a harmonic spring.

### 2.1.1 Scattering Force

The scattering force is more commonly described by light radiation pressure. A laser beam contains photons that are coherent and have momenta that are aligned along the propagation direction of the beam. If small particles encounter the laser beam the stream of photons will exert a radiation pressure on the particles and will push them along the propagation direction of the beam [19].

A single photon has momentum $\mathbf{p} = \hbar\mathbf{k}$, where $\mathbf{k}$ is the wave-vector of the photon. When a photon is reflected by $\pi$ radians it will have had a change in its momentum

and as such exert a force $\mathbf{F}$ over time $\Delta t$ on the object.

$$\begin{aligned} \mathbf{F} &= \frac{2\mathbf{p}}{\Delta t} \\ \mathbf{F} &= \frac{2\hbar\mathbf{k}}{\Delta t}. \end{aligned} \tag{2.1}$$

The force exerted by a single photon is incredibly small but an appreciable force (in terms of hundreds of pico-newtons) can be exerted by a laser. If a laser has a photon flux $N_p$ per unit time the power $P$ of the beam is,

$$P = \frac{N_p c\hbar k}{\Delta t}, \tag{2.2}$$

and the scalar force exerted by a cumulative stream of photons would be:

$$F = \frac{2N_p p}{\Delta t}. \tag{2.3}$$

Using this result and equation 2.2 yields the resultant scattering force exerted by a laser on an object in the path of the laser beam.

$$F = \frac{2P}{c}. \tag{2.4}$$

A laser with output of 25mW would produce a scattering force $\sim$ 150pN. This may not appear to be a large force compared what people experience everyday when lifting a coffee mug ($\sim 1N$) but on the microscopic level it is significant, as only 50pN is required to unwind a strand of DNA [20].

### 2.1.2 Gradient Force

The optical gradient force has two regimes depending on the radius $a$ of the object compared to the wavelength of the laser, they are $\lambda \ll a$ (ray optics regime) and $\lambda \gg a$ (Rayleigh regime). It should be noted for $\lambda \approx a$ there is no well established theory but in [21] the generalised Mie model has proved useful.

To calculate the the force exerted upon a dielectric material by an electromagnetic wave the Maxwell stress tensor, $\sigma_{ik}$, must be integrated over the surface of the dielectric involved [22].

$$F_i = \oint \sigma_{ik} \mathrm{d}S_k. \tag{2.5}$$

The elements of the stress tensor are functions of the amplitudes of electric and magnetic

fields at the surface of the dielectric concerned,

$$\sigma_{ik} = \frac{1}{4\pi}\left[\varepsilon E_i E_k + B_i B_k - \frac{1}{2}(\varepsilon E_i E_i + B_i B_i)\right]. \tag{2.6}$$

A complete description of the mathematical treatment involved can be found in [21]. Two simplifying assumptions to this treatment, suggested in [23], provide quantitative predictions of the force imparted on a dielectric by a focussed laser beam. The first assumption is that the electric field terms of the Maxwell stress tensor dominate over the magnetic field terms so that equation 2.6 reduces to,

$$\sigma_{ik} = \frac{1}{4\pi}\left[\varepsilon E_i E_k - \frac{1}{2}\varepsilon E_i E_i\right]. \tag{2.7}$$

The second assumption is that the dominant force interaction between the dielectric and laser beam comes from the gradient force. The force can then be calculated from the change in the energy of the dipole interaction with the electric field as a function of the dielectric particle's position. The energy of the dipole interaction of a dielectric particle, $U(r)$, with polarisation, $\mathbf{P}$, in an external electric field $\mathbf{E_0}$ is

$$U(r) = -\frac{1}{2}\int_V \mathbf{E_0}\cdot\mathbf{P}\mathrm{d}V, \tag{2.8}$$

where $V$ is the volume of the dielectric particle, and the polarisation is given by:

$$\mathbf{P} = \varepsilon_0\chi\mathbf{E_0}. \tag{2.9}$$

Here, $\chi$, is the dielectric susceptibility of the particle and has the form $\chi = \frac{\varepsilon_r - 1}{4\pi}$ with $\varepsilon_r$ the relative permittivity between the dielectric and the medium that it is suspended in. If $\chi$ is less than unity equation 2.8 becomes:

$$U(r) = -\frac{\chi}{2}\int_V \varepsilon_0 E_0^2 \mathrm{d}V \tag{2.10}$$

$$U(r) = -\alpha\int_V I\mathrm{d}V, \tag{2.11}$$

where $I$ is the intensity of the laser beam integrated over the volume of the particle in the beam. Equation 2.11 uses an expression for the energy as a function of intensity, $I = \frac{\varepsilon_0 E_0^2}{8\pi}$. The other term in equation 2.11, $\alpha$, is the permittivity difference of the two mediums, the particle and what surrounds it, $\alpha = \frac{\varepsilon_p}{\varepsilon_0} - 1$. If the permeability of a particle is close to 1 an approximation for the refractive index can be used, $n \approx \sqrt{\varepsilon}$. For all the particles and solvents used in this research this is indeed the case. The

$\alpha$ term demonstrates that the trapping force is directly proportional to the refractive index difference between the particle and the medium it is occupying and it is this trapping force that is calibrated in Chapter 3 and used to obtain the results described in Chapters 5 and 6.

A detailed comparison between the theory of optical trapping and experimental results for particles with $a \approx \lambda$ can be found in [24].

## 2.2 Data Analysis

The experimental data that has been acquired using the optical tweezers has been analysed using either time domain analysis methods or frequency domain analysis methods. These methods are equivalent but can be used to determine different aspects associated with the behaviour of colloidal suspensions. Frequency domain analysis is most often used in light scattering experiments and is used in rheology experiments to determine the storage $G'$ and loss modulus $G''$ of complex materials as functions of frequency. By analysing the micro-rheology results presented here in frequency domain a direct comparison to the bulk rheology can be made. Frequency domain analysis was used to calibrate the stiffness and sensitivities of the of the optical traps described in Chapter 3 and in the measurement of the passive microviscosity $\eta_{\mu}^{(Passive)}$ described in Chapter 5.

It should be noted that the host solvent can be described as a Newtonian fluid; the fluid is incompressible and has a viscosity that is constant at all frequencies (or at least the spectrum of frequencies considered in this research).

Time domain analysis is certainly more intuitive and is more directly interpretable and was used for the majority of the results that are described in Chapters 5 and 6.

### 2.2.1 Modelling the Optical Trap

The force that the optical trap exerts upon a trapped particle can be modelled as a spring where the potential of the optical trap is harmonic about the point of equilibrium and has a specific stiffness $\kappa$. The motion of the confined particle in one dimension can be described by the equation of a damped oscillator being driven by an external force. The motion of the particle in the perpendicular direction to the laser is expected to be uncorrelated but will probably have slightly different stiffness and sensitivity most likely due to slight differences in the optical alignment along these directions and imperfections in the optical components used. The potential along the propagation direction of the laser beam is not symmetrical about the centre of equilibrium as the

scattering of the laser light down-stream of the trapped particle will reduce the stiffness.

The motion of the particle from the centre of optical trap is opposed by the Stokes drag coefficient associated with the host fluid $\xi_0 = 6\pi\eta a$ and in one dimension the motion can be described by a Langevin equation,

$$m\ddot{x}(t) + \xi_0\dot{x}(t) + \kappa x(t) = F(t), \tag{2.12}$$

where $F(t)$ describes the Brownian forces that the confined particle experiences. As these forces are Brownian their average value will be zero over a long enough time period. The first term in equation 2.12, which can be described by the the inertial time $t_{inertial} = m/\xi_0$, is several orders of magnitude less that than the other timescales of the colloidal system that was used [25], allowing us to remove the inertial term from any further processing,

$$\xi_0\dot{x}(t) + \kappa x(t) = F(t). \tag{2.13}$$

This modified Langevin equation was used as the basis for all subsequent analysis.

### 2.2.2 Frequency Domain Analysis

Taking equation 2.13, applying the methods described by *Gittes et al.* [26] and solving using a Fourier transform it can be converted from time domain in to frequency domain.

$$x(t) = \mathcal{F}^{-1}[X(f)] = \int_{-\infty}^{\infty} X(f)e^{-2\pi fit}\mathrm{d}f. \tag{2.14}$$

The modified Langevin equation becomes the following in frequency domain:

$$(f_c - if)X(f) = \frac{F(f)}{2\pi\xi_0}, \tag{2.15}$$

where the term $f_c$ is equal to $\kappa/2\pi\xi_0$, the 'corner frequency' of the trap [27]. This corner frequency corresponds to the timescale where the restoring force of the optical trap is equal to the timescale of the Brownian forces. At high frequencies (short time periods) the Brownian force dominates the confined particle's motion and at low frequencies (long time periods) the optical trap confines the particle's motion to a small region around equilibrium.

As can be seen from the definition of $f_c$, the corner frequency is directly proportional to the stiffness of the trap (the power of the confining laser beam), this feature will be used Chapter 3 in the characterisation of the optical trap. We can access $f_c$ and the other frequencies more readily by squaring equation 2.15, and thereby removing any complex components created during the Fourier transform, to produce a power

spectrum:

$$4\pi^2\xi_0^2(f_c^2 + f^2) = S_F(f). \tag{2.16}$$

As the Brownian force averages to zero in the time domain, and in frequency-domain this will correspond to a constant frequency, $F(f) = 4\xi_0 k_B T$. Using this relation the solutions to equation 2.16 are:

$$S_x(f) = \frac{k_B T}{\xi_0 \pi^2 (f_c^2 + f^2)}. \tag{2.17}$$

In practise the time-series data obtained by the experiment is discrete and real valued, the Fourier transform of the data series will be complex and part of the information will be lost in the transformation (the phase). The data obtained using this method have a large noise signal. The standard deviation of a single data-point is roughly the same as the mean value for that point. To reduce the noise of each data point and to improve the accuracy of the fit to the power spectrum the data set is divided into sections of equal length. The power spectra of each section is obtained and the average for each data set calculated across all sections.

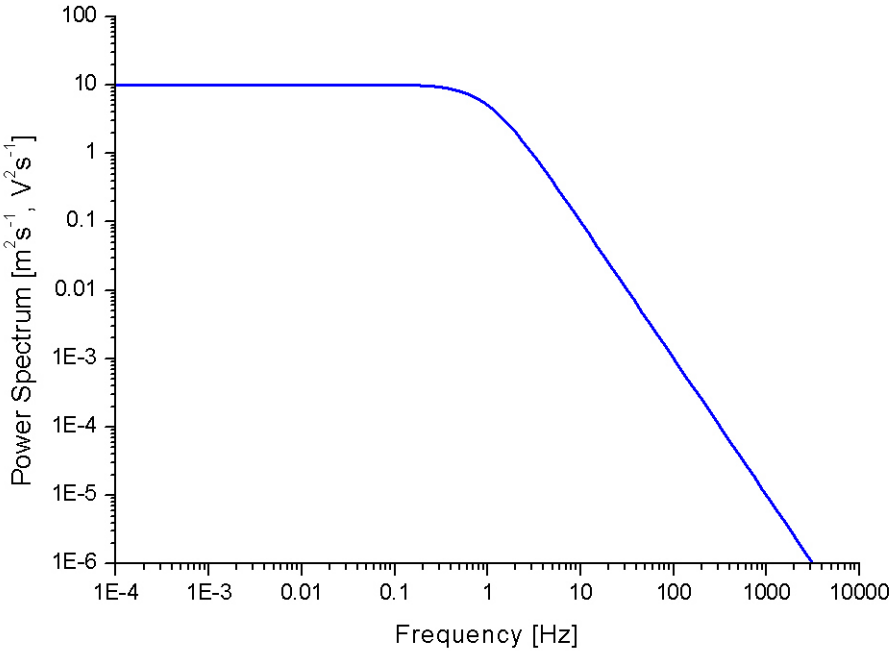


Figure 2.2: An Ideal Lorentzian with a corner frequency of 1 and $\frac{k_B T}{\xi_0} = 100$.

To analyse the power spectrum a log-log plot of the data set is obtained and a Lorentzian function is fitted (figure 2.2). The location of the corner frequency and the intercept allows for stiffness and sensitivity of the trap to be calibrated. The calibration of the stiffness is, in theory, fairly straight forward as the corner frequency is directly proportional to the stiffness and needs only a measurement of the viscosity of the host to calculate the Stokes drag parameter. The calibration of stiffness in experimental practise is more subtle, as the raw data is recorded in volts and the $y$ axis intercept has units of $V^2s^{-1}$. The $y$ axis intercept relates to the free diffusion coefficient which has units $m^2s^{-1}$, using this relation allows a calibration of volts to nano-metres to be made. A full description of this method and results will be given in Chapter 3.

### 2.2.3 Time Domain Analysis

Time domain analysis was carried out once the conversions from volts to nano-meters or pico-newtons had been made, depending on the desired variable.

Measurements of the mean squared displacements (MSDs) were used to determine diffusion co-efficients and trap stiffnesses of particles confined in the optical traps. To

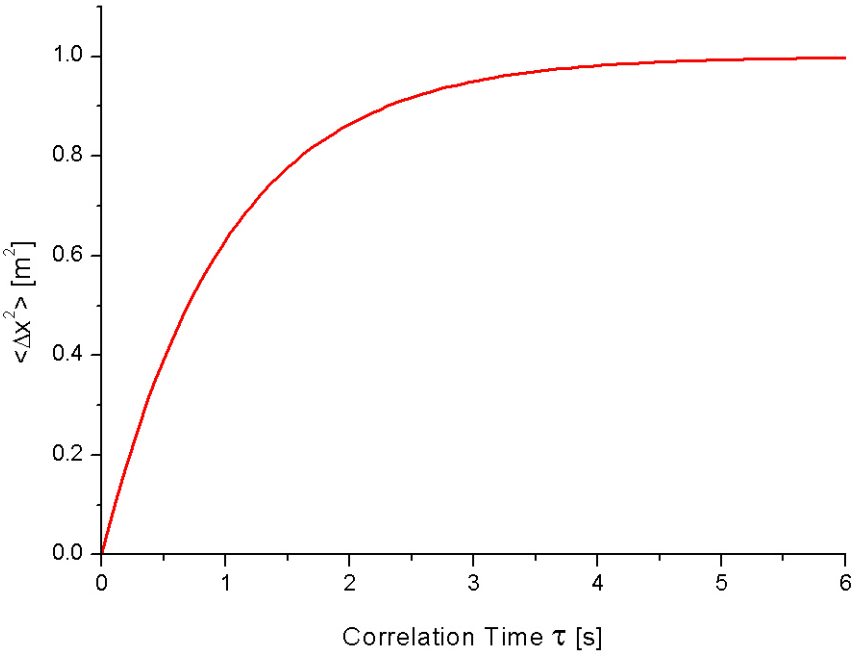


Figure 2.3: Calculated mean squared displacement graph of an optically trapped particle in a fluid.

analytically calculate the MSD the variance in position over a period of time and the auto-correlation function of the particle's position were used,

$$\langle \Delta x^2(\tau) \rangle = 2\sigma^2 - 2\langle x(t)x(t+\tau) \rangle. \tag{2.18}$$

The angled brackets indicate an average over all values of $t$, and $\sigma^2$ is the variance of the particle's position. For timescales greater than $t = 10^{-15}s$ (the inertial time regime of the particle) the MSD has the form:

$$\langle \Delta x^2(\tau) \rangle = \frac{2k_BT}{\kappa} \left[ 1 - e^{-\frac{\kappa\tau}{\xi_0}} \right]. \tag{2.19}$$

The graph in figure 2.3 shows the that at short time scales the particle is free to diffuse and at longer time scales becomes confined by the optical trap. The initial slope of the graph at short time scales can be used to find the short time free diffusion of the particle $D^{(Short)}$.

The MSD of a particle confined in each optical trap was used in the experiments described in Chapter 6 to ensure that the stiffnesses of both traps were equal. The MSD of a freely diffusing particle would be a straight line that starts at the origin and has a gradient equal to the diffusion coefficient and the MSD of bound particle will be a horizontal flat line. This can be seen in figure 2.3 at correlation times $\tau > 6s$ the MSD has reached a plateau value and at times $\tau \ll 1$ the particle is freely diffusing. The point at which these two regimes cross over can be characterised by a corner time of the MSD and is illustrated in figure 2.4.

To determine the corner time $\tau_c$ equation 2.19 has to be solved for correlation times $\tau \ll 1$, this can be done by expanding the exponential term.

$$\begin{aligned} \langle \Delta x^2(\tau) \rangle &= \frac{2k_BT}{\kappa} \left( 1 - e^{\frac{-\kappa\tau}{\xi_0}} \right) \\ &= \frac{2k_BT}{\kappa} \left( 1 - \left[ 1 + \frac{\left(\frac{-\kappa\tau}{\xi_0}\right)}{1!} + \frac{\left(\frac{-\kappa\tau}{\xi_0}\right)^2}{2!} + \ldots \right] \right). \end{aligned} \tag{2.20}$$

Solving to first order we obtain the very short time limit,

$$\begin{aligned} \lim_{\tau \to 0} \langle \Delta x^2(\tau) \rangle &= \frac{2k_BT}{\kappa} \left( 1 - \left[ 1 + \frac{-\kappa\tau}{\xi_0} \right] \right) \\ &= \frac{2k_BT\kappa\tau}{\kappa\xi_0} \\ &= \frac{2k_BT\tau}{\xi_0}. \end{aligned} \tag{2.21}$$

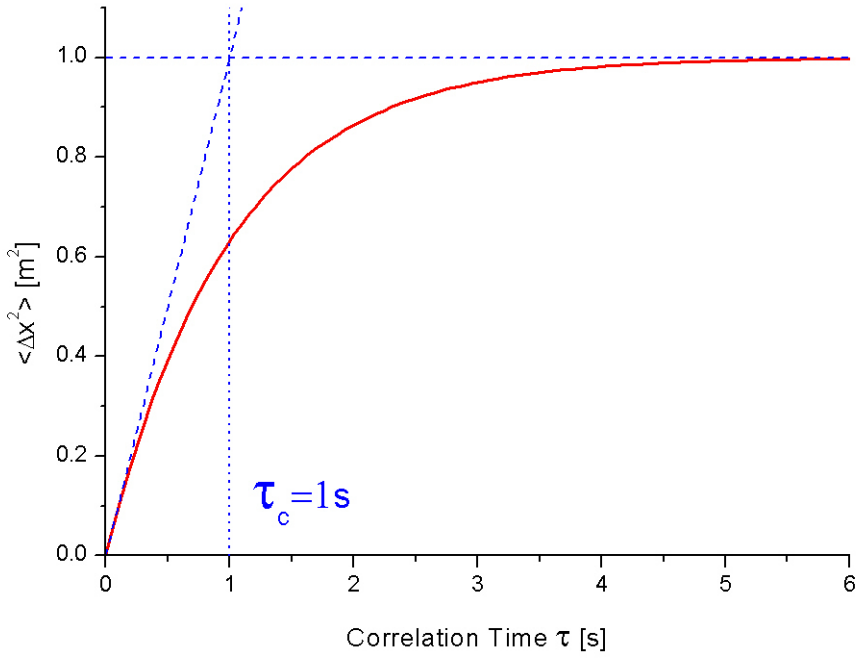


Figure 2.4: Reproduction of figure 2.3 with the cross over between free diffusion and optical confinement, with a corner time of $\tau_c = 0.5$.

Notably the stiffness drops out of the equation which is what should be expected as equation 2.19 has been solved for the time regime where the trapped particle does not experience a trapping force and is freely diffusing. Equation 2.21 gives the short time limit that is needed in part to determine the corner time $\tau_c$. The long time limit can be determined using experimental data that has been recorded and equation 2.18. In the long time regime the auto-correlation function $\langle x(t)x(t+\tau)\rangle$ will decay to zero and equation 2.18 will simplify to,

$$\lim_{\tau\to\infty}\langle\Delta x^2(\tau)\rangle = 2\sigma^2. \tag{2.22}$$

Equating equations 2.21 and 2.22 and solving for time yields the corner time $\tau_c$ of the MSD.

$$\tau_c = \frac{\xi\sigma^2}{k_B T}. \tag{2.23}$$

In Chapter 6, where two optical traps have been used, the calculating of the corner times for each trap allows the relative stiffness of each trap to be determined and when they are equal they can be described as exerting the same trapping force on their

trapped particles. This method can be used even when there is a difference between the two laser intensities that are imaged onto the detectors described in Chapter 3. A full proof showing that this is the case can be found in Appendix B.

### 2.2.4 Cross-Correlation Analysis

Cross-correlation analysis was used to determine how much one set of data is alike to another, in the data that is presented in Chapter 6 the two data sets are both positional time series and were used to determine on what time-scale the motion of one particle held in an optical trap affected the motion of another particle held in another optical trap some distance away.

Mathematically the cross-correlation function is defined as,

$$\langle x_i(t)x_j(t+\tau)\rangle = \int_{-\infty}^{\infty} x_i^*(t)x_j(t+\tau)\mathrm{d}\tau, \tag{2.24}$$

where $x_i^*(t)$ is the complex conjugate of $x_i(t)$. The data that are recorded cannot be described as being a continuous function of time, it is instead a discrete series of positions recorded at finite time intervals. The numerical equivalent for a finite data series of equation 2.24 is

$$\begin{aligned} \langle x_i(t)x_j(t+\tau)\rangle &= C_{ij}(\tau) \\ &= \frac{1}{N}\sum_{\tau=0}^{N-1} x_i^*(t)x_j(t+\tau), \end{aligned} \tag{2.25}$$

where $N$ is the total length of the data set. The equivalence of equation 2.24 and 2.25 is only true if $N$ is at least an order of magnitude greater than the time-scale that is being investigated, otherwise systematic errors occur and the cross-correlation calculated will be offset by a some value. A description of how this comes about can be found in Appendix C.

Like with the frequency domain analysis the standard deviation of a single data point will be the roughly the same as the mean value for the data point and as will have a large noise signal. The same method was also used here to reduce the noise signal by breaking the entire data set into sections of equal length and taking an average over all the data sets to determine the cross-correlation.

# Chapter 3

# Optical Setup

This chapter details the characterisation of the optical tweezers system that was used in this research[1]. A description of the difference between constant force and constant velocity tweezers is given followed by a description of the layout of the components that made up the optical tweezers. The beam paths taken by the laser that were associated with *Trap1* and *Trap2* are then described.
A complete description of the calibration of the components used to monitor the laser beam power in the experiments is given and a full characterisation for each of the two optical traps and their detectors. This is followed by a summary of the calibrated parameters.

## 3.1 Optical Tweezers

Optical tweezers have found their way into many applications for the investigation of microscopic substances and materials and can be used in conjunction with commercial microscopes [28]. Although primarily used as a micro-manipulation tool where an object in the specimen can be 'picked up' by the optical trap and moved to another location, they can also be used to probe the forces within the microscopic materials. Provided the material is optically transparent at the tweezing laser wavelength then optical tweezers can be used as a non invasive 'in situ' probe of microscopic samples such as biological cells. The wavelength of the tweezer can also be chosen so that the laser light will not damage the sample. For this reason a wavelength in the infra-red part of the spectrum is often chosen for biological samples.

Optical tweezers are not necessarily confined to operating with a single optical

[1]The apparatus was originally built by *Dr. Jochen Arlt* & *Dr. Laurence Wilson*, with further modifications being made by myself. Where appropriate the individuals responsible will be mentioned and the work that was completely by them stated.

trap, holographic systems have been developed that create arrays of traps for the manipulation of many objects at a time [14]. The use of acousto-optic-modulators (AOM) has been used to create line traps (also possible with holographic tweezers) [15] as well as arrays where the optical trap's position was scanned rapidly between locations (time-shared) [16].

There is also a simple method to create two optical traps from a single laser where the laser beam is split into two polarisations such that each polarisation can be used as a separate optical trap [17]. It is this system that is employed in this research.

If the light downstream of the trapped particle is collected, the optical tweezer can be used for measuring forces within the sample. There are however two distinct types of force measurement optical tweezers, constant force and constant velocity.

Constant force tweezers utilise a force feedback system where the probe is dragged

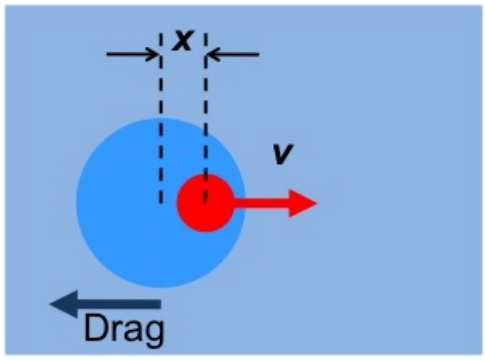


Figure 3.1: Diagram showing constant particle displacement when being dragged through a Newtonian fluid with an optical trap. The red arrow indicates the direction of the force being exerted by the optical trap and the dark blue arrow indicates the direction of the drag force. The lengths of the arrows reflect the magnitude and in the case shown both forces are equal in magnitude.

at a velocity such that it experiences a constant force. In a Newtonian liquid, where the Stokes drag velocity scales linearly with force, the probe will be dragged with a constant velocity and will experience a constant force pushing it out of the equilibrium position of the trap, figure 3.1. However if the probe encounters an object that it will have to 'push' out of the way the velocity at which the probe is being dragged will decrease (to compensate the force being exerted by the object pushing on the probe). Consequently in constant force tweezers the velocity at which the trapped particle is moved may not necessarily be constant.

Constant velocity tweezers on the other hand must drag the trapped particle with a constant velocity. In the case of the Newtonian fluid the trapped probe will be

dragged at a constant velocity and will experience a constant drag force. As such for a Newtonian fluid constant force and constant velocity tweezers can be considered as identical. The difference between the modes arise when an object is encountered. For an optical trap with a perfectly harmonic potential and with no spatial boundaries, the probe will be displaced further and further out of equilibrium by the object until it reaches a force large enough to push the object out of the way. The probe effectively bulldozes its way through the sample pushing all objects out of its way moving with a constant velocity but may experience a force greater than the Stokes drag. In a real experimental system the harmoic potential does have limits. If the probe encounters an object that exerts a sufficient force the probe will be pushed out of the optical trap and lost.

The distinction between the two systems has been described here as constant force measurements have been constructed from constant velocity results in Chapter5.

A constant velocity optical tweezer system with two optical traps was used in this research. The characterisation and calibration of this system is described below.

## 3.2 Apparatus Setup

### 3.2.1 Optical Alignment

The system used was constructed around a custom built inverted microscope. A Nd:Yag solid state pump diode laser with an operating wavelength of $\lambda = 1064nm$ was used as the trapping laser (figure 3.2). As the laser beam is polarised a $\lambda/2$ retarder was used to rotate the polarisation so that a polarising beamsplitter could be used to split the beam into two separate linear polarisations – one for each trap. The $\lambda/2$ retarder was primarily used to control the trapping strength of *Trap1*, there are three $\lambda/2$ retarders used in this system, this one will be referred to as $\lambda/2_{(1)}$ from here onwards. A beam expander was placed in the beam path between the $\lambda/2_{(1)}$ retarder and the beam splitter. The beam expander (consisting of a diverging and converging lens pair) is used to increase the diameter of the laser beam from a width of a few millimetres to a width of $\sim$ 3cm. The larger beam width is needed to ensure that the back focal plane of the objective lens is overfilled. In addition to increasing the beam width the beam expander was also set to ensure that the laser beam was collimated. The collimation of the beam was confirmed using an optical shear plate. If only one optical trap was needed for experiments *Trap1* was used and the beam of *Trap2* was blocked just after the beam splitter. When operating as single traps the maximum laser power of each trap was limited to the initial power of the laser beam once losses in the optical components had been taken into account. When both traps were operating together

the maximum power of each trap was limited to half the initial power of the laser with loses taken into account.

The details of how *Trap1* and *Trap2* were created and controlled are individually explained in the following sections.

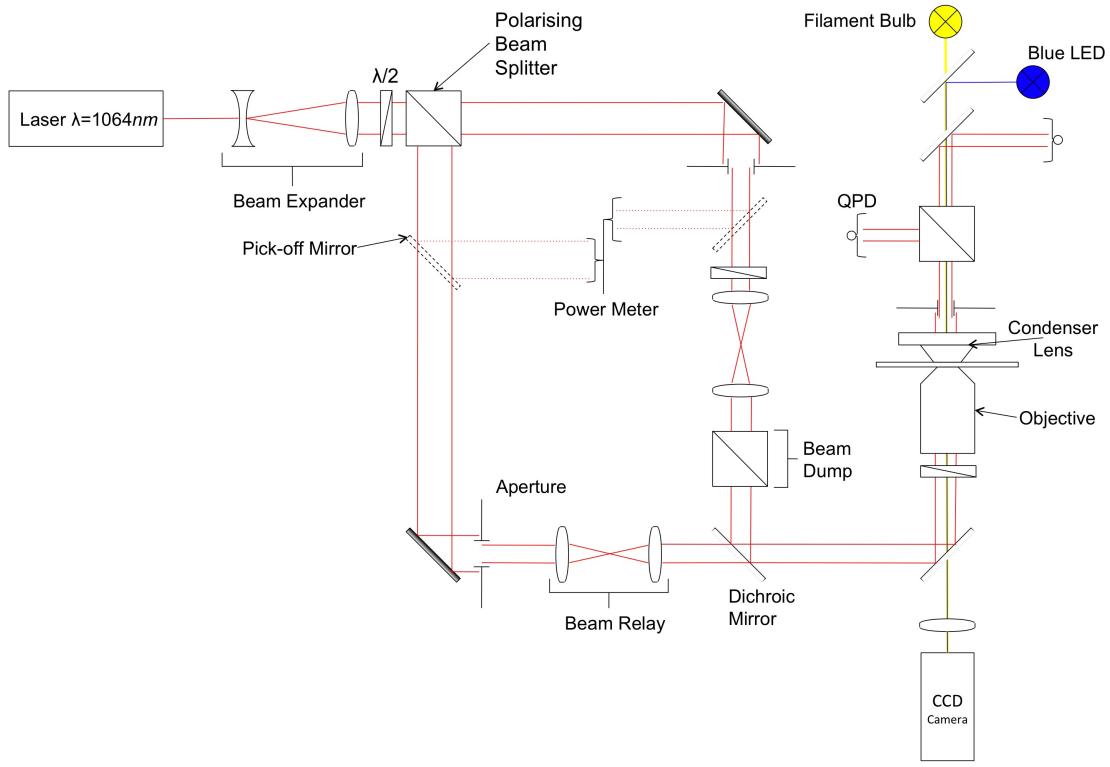


Figure 3.2: Ray optics diagram of the optical set-up that was used for the dual trap optical tweezers.

### *Trap1*

For *Trap1* one of the polarisations was reflected off of a galvo-mounted mirror through a beam relay and into the back focal plane (BFP) of the objective lens. The beam relay had a magnification of one. Since the mirror surface was conjugate to the BFP of the objective lens, any angular movement of the mirror's surface resulted in a lateral movement of the optical trap in the image plane of the objective whilst the strength of the optical trap was maintained.

An aperture was incorporated after the mirror to 'clean' the laser beam. This removed any stray reflections associated with the mirror's edge due to the beam width being greater than the diameter of the mirror. These stray reflections would be detrimental to the stiffness and sensitivity of the optical trap. The laser power that was delivered

to the optical trap was monitored by a 4% pick off mirror located between the beam splitter and the galvo-mounted mirror. The pick-off mirror consisted of a glass coverslip and the reflected beam was focussed into a power meter. The $\lambda/2_{(1)}$ retarder was used to control the laser power of *Trap1*. This allowed the laser to be operated well above its lasing threshold ensuring good beam stability and intensity. The power of the stable beam at the back focal plane was determined by the pick-off mirror.

***Trap2***

The optical components in the beam path of *Trap2* and their uses are much the same as they were for *Trap1* with a few caveats.

A galvo-mounted mirror and a beam relay was used in the same way as for *Trap1* where the mirror was conjugate to the BFP of the lens. The additional optical components used in this beam path were needed to control the power of the laser beam whilst retaining good beam stability and intensity.
An additional $\lambda/2$ retarder was placed before the beam relay, this retarder ($\lambda/2_{(2)}$) was used to rotate the linear polarisation of *Trap2*'s beam without changing the beam power. A second polarising beam splitter was used to split the polarisation after the retarder into its linear components, one component was sent to a beam dump and the other formed the optical trap that was referred to as *Trap2*.

The 4% pick-off mirror for *Trap2* had to be placed before the $\lambda/2_{(2)}$ retarder due to positional constraints of the experimental system. Ideally it would be placed after the beam splitter and would give a measure on the laser power at the BFP of the objective. Instead a calibration of the $\lambda/2_{(2)}$ retarder as a function of angle and laser power had to be made.

When *Trap2* was used in conjunction with *Trap1* the laser powers of each trap needed to be adjusted to the required level. The power needed for *Trap1* would be determined and set using the retarder before the 'main' beam splitter. Once the power of *Trap1* had been set the $\lambda/2_{(2)}$ retarder in the 'arm' of *Trap2* would be rotated to reduce the power of *Trap2* to the required level.

### 3.2.2 Calibration of Pick-off Mirrors

As the pick-off mirrors that were used to monitor the laser power in each trap were not placed at the back focal plane of the objective the assumption that the laser power being 'picked-off' is 4% of the beam at the BFP is no longer valid. The optical components in the beam path after the pick-offs (mirrors, apertures and lenses) would absorb some of the laser energy and reduce the laser power. How the pick-off power relates to trap stiffness and sensitivity was required to characterise the optical traps. Knowledge of

the power at the back focal plane is useful, not merely from a safety point of view (how much laser radiation is passing through the system) but also useful when balancing the stiffnesses of the two optical traps.

For *Trap1* the process was relatively simple. The objective lens was removed, a laser power meter was mounted in its place and the ray path for *Trap2* was blocked off leaving only the laser light from *Trap1* arriving at the BFP. The power at the BFP was recorded with varying power at the pick off, figure 3.4.
The characterisation for *Trap2* was not as straightforward as the $\lambda/2_{(2)}$ retarder had to be calibrated first. The power measured at the BFP for *Trap2* was a function of the retarder angle and the initial laser power in *Trap2*'s 'arm'. If the retarder was aligned to the same optic axis as the beam splitter/beam dump then the maximum laser power at the BFP would correspond to an angle of 0° or 90°, depending on polarisation. In an experimental system this is rarely the case. The offset angle of the retarder had to be determined. The laser power meter was again mounted at the BFP and the power was recorded with varying angle of the $\lambda/2_{(2)}$ retarder. This was repeated for several beam powers determined by the pick-off for *Trap2* to ensure that a consistent change in the laser power at the BFP was possible using the retarder. The power at the BFP was plotted as a function of angle, $\theta$. A $\sin^2[2(\theta + \theta_0)]$ function was fitted to the data to determine that the offset angle $[\theta_0 = 84°]$ figure 3.3.

With the offset angle determined the power at the BFP for *Trap2* was determined. The $\lambda/2_{(2)}$ retarder was rotated to the offset angle and a maximum power confirmed at the BFP. The power at the BFP was determined in the same manner as that for *Trap1*, figure 3.4, where the gradients of the lines are $5.32 \pm 0.01$ and $5.02 \pm 0.01$ for *Trap1* and *Trap2* respectively.

## 3.3 Imaging and Position Detectors

The two trapping beams passed through the objective lens and into the sample, giving two independent, steerable optical traps in the image plane. The trapping beams were focussed by a Nikon 100× oil immersion lens that had a numerical aperture, $\mathrm{NA}_{objective} = 1.4$. A high numerical aperture gives a stronger gradient force to the optical trap (see Chapter 2) leading to a strong axial trap [29]. A lower objective NA will give a stronger trap in the lateral direction ($z$ direction along the axis of the beam) [30]. The condenser lens that collected the scattered and unscattered laser light down stream of the optical trap was also an oil immersion lens made by Nikon and had a numerical aperture, $\mathrm{NA}_{Condenser} = 1.4$. The high numerical aperture of the condenser was required for the high-resolution particle tracking [31] used in this research.

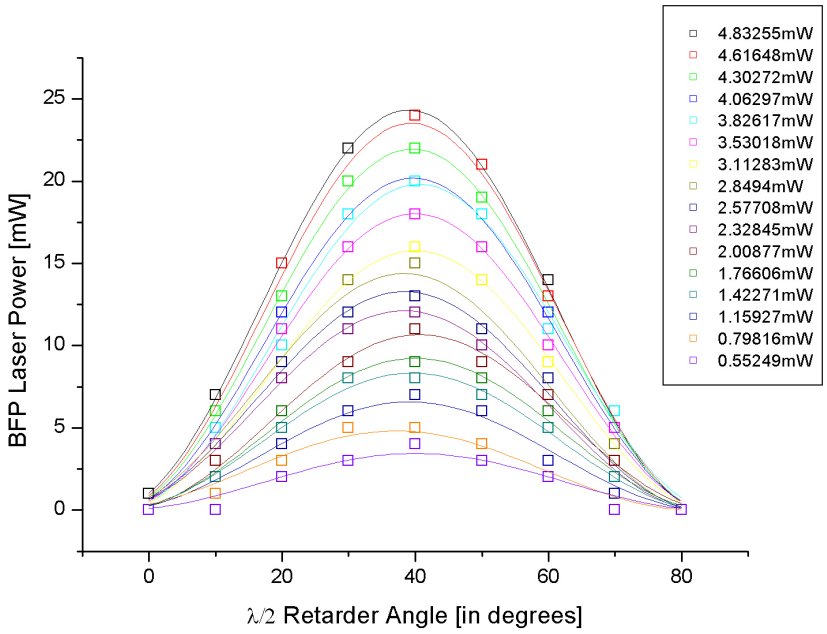


Figure 3.3: Laser power at the BFP as a function of angle where the lines are the fits to the function $\sin^2[2(\theta + \theta_0)]$ with $\theta_0 = 84°$.

The samples used had a refractive index of $n_{sample} \sim 1.49$ which is close to that of glass reducing any optical aberrations caused by refractive index differences at the interfaces. As a result of such small optical aberration the trap stiffness was still strong when (focussed) deep in the sample. The close match also meant that there was very little divergence of the light at the interface of the glass-oil-condenser side of the sample, thereby collecting as much light as possible from the sample.

### 3.3.1 Imaging

The condenser and objective lens arrangement were used to image the sample, as can be seen in figure 3.2. For general imaging of the sample a filament lamp was used as a white light source and focussed through the sample from the condenser side. Upon exiting the back aperture of the objective the white light passed through a dichroic mirror and was focussed into a CCD (charge coupled device) camera conected to a computer that was capable of capturing images.
When epi-fluorescence imaging was needed, the white light was turned off and a blue LED was used instead. The blue light was introduced with a dichroic mirror and followed the same optical path as that of the white light. The resulting fluorescent

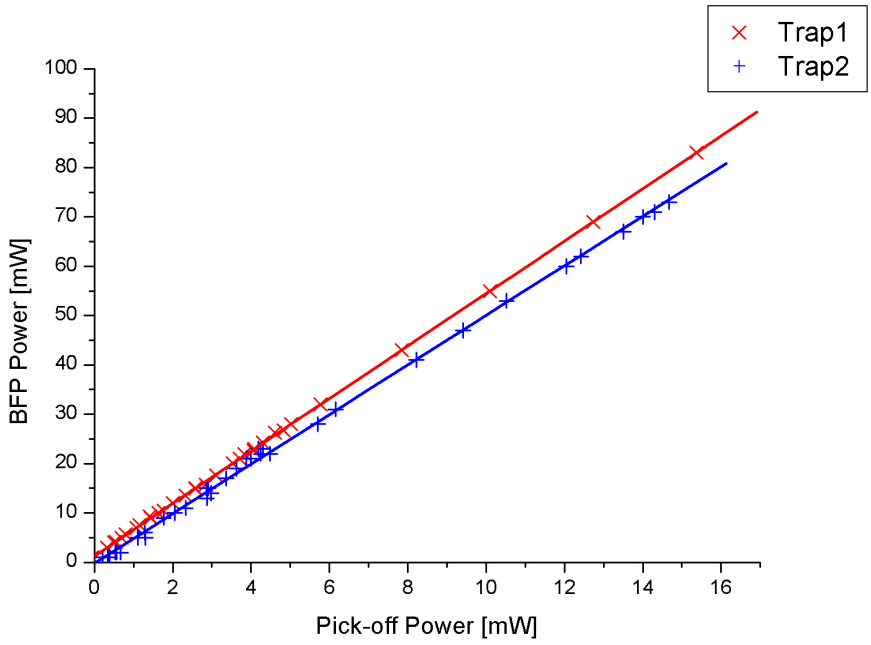


Figure 3.4: Laser power at the BFP as a function of pick-off powers for *Trap1* and *Trap2* with $\lambda/2_{(2)}$ retarder in the arm of *Trap2* at an angle of 84°.

light was focussed into the same camera.

The resolution of the CCD camera was determined using a calibrated Richardson slide. An image of the slide was taken and a plot of pixel intensity was made across the length of the scale bars in the image was made.

From this the resolution of the camera was calculated and found to have pixel size of $x = 0.046627\mu$m pixel$^{-1}$ and $y = 0.04572\mu$m pixel$^{-1}$ in the $x$ and $y$ directions respectively.

### 3.3.2 Position Detectors

#### Separating the Traps

The laser light from each optical trap was orthogonally polarised with respect to each other. A third and final polarising beam splitter was used after the condenser to separate the collected light into its two component polarisations. This separation relies on the axes of the beam splitter being aligned along the same axes as the polarisations of *Trap1* and *Trap2*. To ensure this was the case a final $\lambda/2$ retarder was placed at the back aperture of the objective lens and rotated until the axes were aligned.
The calibration of this retarder ($\lambda/2_{(3)}$) was straightforward, *Trap2* was blocked off

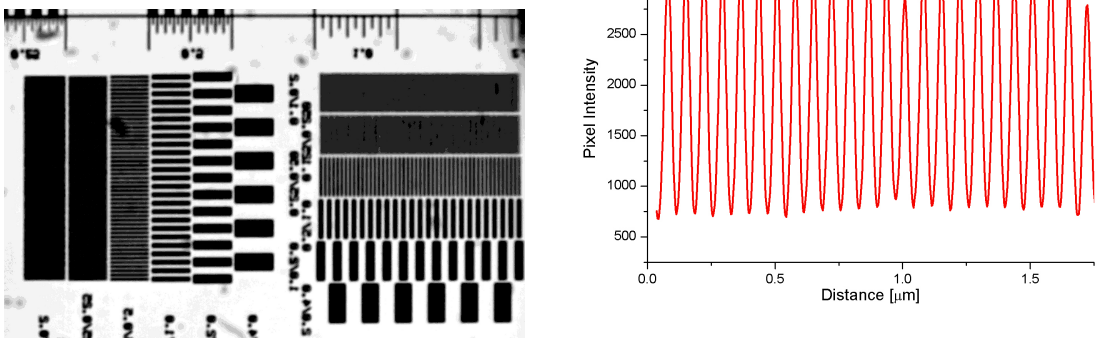


(a) (b)

Figure 3.5: (a) Image of the Richardson slide with scale bars used to determine the resolution of the imaging camera used. (b) An example of a graph of pixel intensity across the scale bars that was used to determine the imaging camera's resolution.

so that only light from *Trap1* would be detected. A power meter was placed on the output paths of the beam splitter and the power monitored as the retarder was rotated. The retarder was rotated until the output on one arm reached a maximum whilst simultaneously reaching a minimum on the other arm. To confirm that the axes were then aligned *Trap2* was unblocked and *Trap1* was blocked off. If aligned, the maximum previously measured on one arm would now be a minimum and vice versa.

The light for *Trap2* passed out of the beam splitter and into *Detector2* and the light for *Trap1* passed through a dichroic mirror (needed for optical alignment reasons) and into *Detector1*. *Detector1* and *Detector2* were identical in design but had operational differences between each other. They could readily be remounted and act as detectors for either optical trap once they had been appropriately calibrated for the optical trap.

### Detectors

Each detector consisted of an $xy$ translation stage used to align the detector to the beam path of the laser light, a lens to demagnify the image from the back focal plane of the condenser and a quadrant photodiode (QPD) to measure the incident laser light from the trap. The lens focussed the light onto the area of the QPD (a Hamamatsu S7479 model) which was under strong reverse bias.

The light from the particle that was collected from the back focal plane of the condenser was made up of scattered and unscattered light, which produced an interference pattern on the QPD. This interference pattern is in effect the Fourier

transform of the particle's image. The motion and intensity of the interference pattern on the QPD allows three dimensional tracking of the optically trapped particle.
If the particle moves laterally in the image plane then the interference pattern will shift laterally across the surface of the QPD. The QPD is split into quadrants and by adding and subtracting the voltages (induced by the photocurrent of the laser light) the displacement could be determined, figure 3.6. Any axial displacement of the particle in

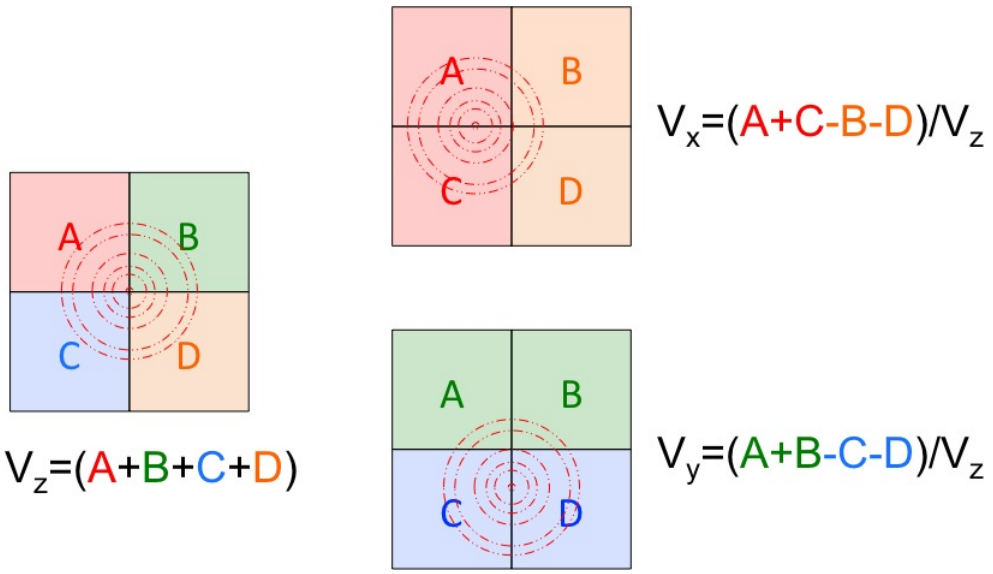


Figure 3.6: A schematic diagram of how the induced photo-current voltages are used to determine the displacement of the optically trapped particle.

the optical trap will result in a Gouy phase shift in the unscattered light and will change in the intensity of the light that falls on the QPD [32, 33]. As such the displacement in the $z$ direction is determined by the total voltage produced by the QPD.

The voltage produced by each quadrant on both the detectors was recorded by a 12-bit National Instruments data acquisition system (National Instruments PCI-MIO0=16E-4) using a LabView frontend[2]. The data acquisition routine made the appropriate additions and subtractions to give the $x$, $y$ and $z$ displacements for each trap (where each translation direction is referred to as a channel after here). The data from each channel was recorded as a byte stream of digitisation levels with a range of 0 to 4095. The voltage corresponding to one digitisation level could be set to ensure that the entire signal was recorded in the full digitisation range (*i.e.* the signal did not saturate) and an optimal resolution obtained.

[2]The data acquisition routines were written by *Dr. Jochen Arlt.*

The $x$ and $y$ channels for each detector were typically set as to have a range of $-0.25V$ to $+0.25V$ for two point passive and was increased to $-1V$ to $+1V$ for one point active measurements, dependant on trap stiffness (for an explanation of active and passive measurements see Chapter 5). The $z$ channels for all measurements typically had a range of $0V$ to $10V$.

If the laser intensity was great enough to saturate the QPD (high trap stiffnesses) then neutral density filters were placed in the path of the laser light between the $xy$ stage and the focussing lens of the detectors.

## 3.4 Detection of Particle Position

An initial calibration of the voltage response with particle displacement was required to convert the measured voltage into nanometres[3]. The calibration method used was the same as that found in [24]. In an ideal situation the photo-induced current on the QPD would produce a current that scales linearly across its surface [34]. For the QPDs used in this system this was not the case. The voltage response could only considered to be linear at small displacements[4] of the particle from equilibrium and became non-linear at larger displacements. This is because the intensity of the interference pattern of the forward scattered light when the particle was far from equilibrium can no longer be described by small angle approximations, with the result being that the QPD would overestimate the displacement of the particle from its equilibrium position. The calibration of the QPD was therefore divided into two parts; small displacements (generally associated with passive micro-rheology) and larger displacements (associated with active micro-rheology). These are described in the next subsections.

### 3.4.1 Small Displacements from Equilibrium

For small particle displacements ($< 0.2\mu$m) the Brownian motion of a single trapped particle was used. In Chapter 2 the power spectrum of an optically trapped particle's Brownian displacements was given by the Lorentzian:

$$S_x(f) = \frac{D_0}{\pi^2} \frac{1}{(f_c^2 + f^2)}, \tag{3.1}$$

[3]Whilst *Dr. Laurence Wilson* had measured the sensitivities and stiffnesses (see later) associated with *Trap1* for his doctoral thesis, the measurements had to be remade due to the additional optical components that were required for *Trap2*.

[4]Proof of this statement applied to this specific system can be found again in [24].

where $D_0$ is the free diffusion coefficient of the particle, $f$ is frequency and $f_c$ is the corner frequency, equation 2.17 & 3.1. In the of limit high frequency (short time scales) the particle can be considered to be freely diffusing and does not experience a trapping force:

$$\lim_{f \gg f_c} S_x(f) \rightarrow \frac{D_0}{\pi^2 f^2}. \tag{3.2}$$

In the small particle displacement limit, the voltage response of the QPD is linear and

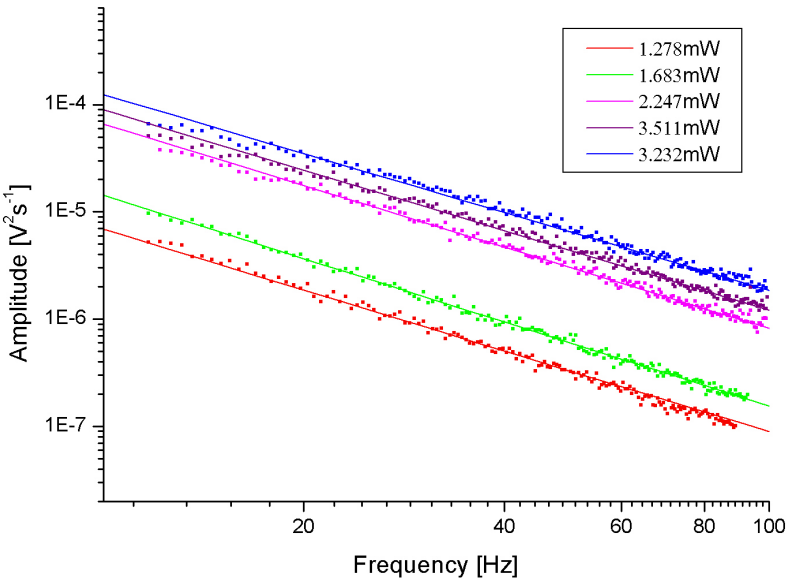


Figure 3.7: High-frequency limit of the power spectrum of a trapped particle with varying laser powers used to calculate conversion of volts to nanometres.

is only dependant on the photo-current produced by the laser light, where more intense laser light will produce a greater photo-current.
The amplitude of the power spectrum calculated from the experiment has the units of $V^2$ $s^{-1}$ and was dependant on the induced photo-current. The diffusion constant in equation 3.2 has the units of diffusion $m^2$ $s^{-1}$ and was used as a conversion (sensitivity) from volts to nanometres. The output voltage was varied by varying the input laser power for the trap to obtain the data needed for the calibration (see figures 3.7 & 3.8). The sensitivities of the traps were determined by the gradient of the linear fits shown in figure 3.8 and are summarised in table 3.1.

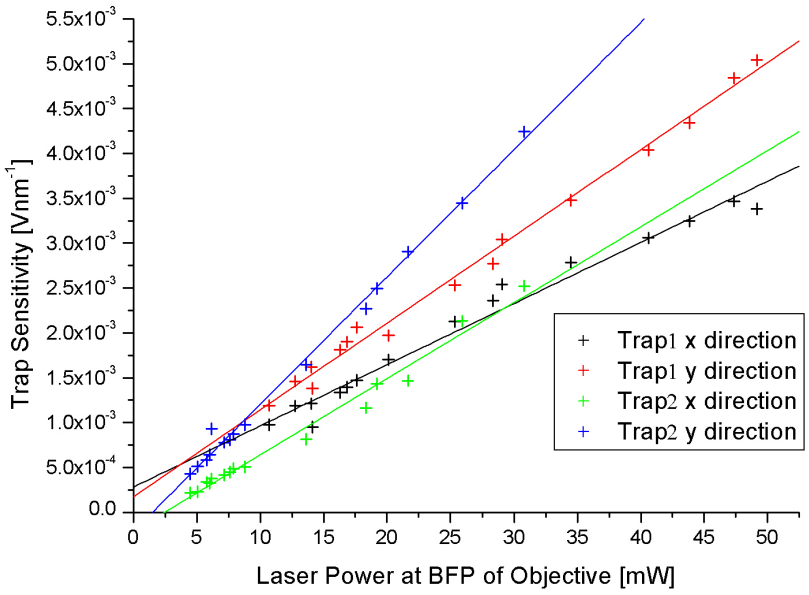


Figure 3.8: $x$ and $y$ channel sensitivities of *Trap1* and *Trap2* as a function of the laser power at the back focal plane of the objective.

| Optical Trap | $S_x$ [mV nm$^{-1}$ mW$^{-1}$] | $S_y$ [mV nm$^{-1}$ mW$^{-1}$] |
|---|---|---|
| *Trap1* | $6.817(3) \times 10^{-5}$ | $9.677(5) \times 10^{-5}$ |
| *Trap2* | $8.481(1) \times 10^{-5}$ | $1.418(7) \times 10^{-4}$ |

Table 3.1: List of sensitivities for the channels of each trap.

### 3.4.2 Large Displacements from Equilibrium

For active micro-rheology the displacement of the particle from equilibrium was used to to determine the viscosity of the system. As such the position must unambiguously be measured. At displacements larger than $0.35\mu m$ the response of the QPD became non-linear and needed to be corrected for to ensure that the calculated viscosity was not overestimated.

The calibration of the QPD in the detector for *Trap1* had been made by *Dr. Laurence Wilson* using a video microscopy method [24]. In this method a particle was held in the optical trap and the stage was oscillated with a triangular waveform using a piezo transducer that had a total travelling distance of $\sim 150\mu m$. By varying the frequency of oscillation and thereby the speed of the stage the particle could be displaced from equilibrium by an average distance. A series of images of these oscillating runs were made and analysed to determine the particle's displacement from equilibrium.

Simultaneously the displacement measured from the QPD was recorded. Histograms of the reported position of the particle by the QPD were plotted and fitted to determine the mean reported position of the particle from equilibrium. A plot of the particle's reported displacement by the QPD, $x_{r(1)}$, against actual displacement, $x_{a(1)}$, could be made allowing for the non-linearity of the QPD to be accounted for, see figure 3.9.

When calibrating the detector for *Trap2* changes had been made to the optical set-up. A dedicated image capture camera had been integrated into the system. This allowed a longer series of images to be acquired and stored. A different analysis method was also used for determining the actual position of the trapped particle. A LabView routine provided by *Dr. Jochen Arlt* which utilised threshold matching allowed the particle's displacement within the series of images to be determined. A sample image of the particle would be used and matched to each frame of the movie and the co-ordinates of the particle's position in each frame was determined. Using the same oscillation method, a series of movies were made in which the trapped particle had a different average displacement from equilibrium. Histograms of the particle's actual displacement were plotted and fitted to provide a value for the actual mean displacement from equilibrium, $x_{a(2)}$. Histograms for the mean reported displacement, $x_{r(2)}$, were made using the same method as *Dr. Laurence Wilson*. A similar plot of reported position and actual position was made and a similar fit was used to determine the non-linearity of the QPD in the detector that was used for *Trap2*, figure 3.9.
Identical non-linearities are not expected due to the inherent differences in the electronic components that make up each of the detectors.

The non-linearities for the reported position (indicated by the subscript letter $r$) with respect to the actual position (indicated by the subscript letter $a$) in the QPDs for *Trap1* and *Trap2* are noted below. The bracketed subscript numbers indicate the particular trap.

$$x_{r(1)} = (2.10(6) \times 10^{-6})x_{a(1)}^3 + x_{a(1)}, \tag{3.3}$$

$$x_{r(2)} = (9.78(6) \times 10^{-7})x_{a(2)}^3 + x_{a(2)}. \tag{3.4}$$

### 3.4.3 Detector Crosstalk

When both optical traps are in use some of the laser light from *Trap1* may end up being collected by the detector of *Trap2* and vice versa due to imperfections in the optics. To determine how much light from one trap spilled into the detector of the other a calibration of the 'cross talk' was carried out.
A single particle was held in one of the optical traps and the beam path to the other

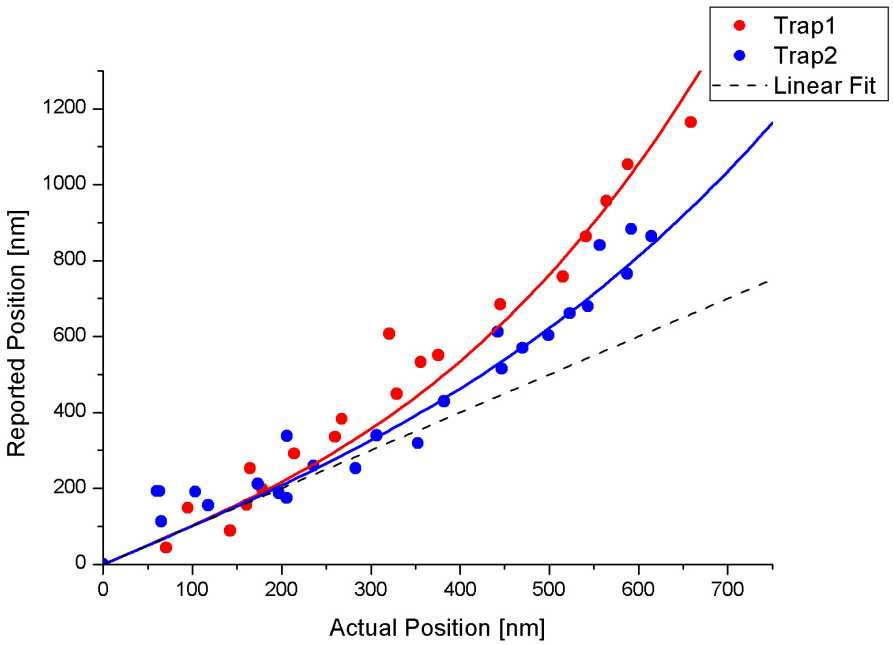


Figure 3.9: The reported position of the trapped particles for both QPDs as a function of the actual position. Fits are the solid lines.

was blocked. The output signals of both detectors were recorded. The same probe was transferred to the other optical trap and the process was repeated.
The resultant output signals from the two detectors were divided by one another and the amplitude of the overspill relative to a full signal was calculated. The amplitude in both case was found to be 3 orders of magnitude smaller than recorded signal of a trapped particle.
In the two point micro-rheology experiments the cross-correlation of two trapped particles was calculated (see Chapter 2 for details of the calculation). In a completely uncorrelated system the cross-correlation calculation would give a 'false' correlated signal associated light 'overspill'. A cross-correlation analysis was therefore carried out to determine amplitude of the cross-correlation between the detectors. The amplitude of the cross-correlation was found to be 49 times smaller than the cross-correlations calculated in Chapter 6 and lost in the background noise of the correlated signals.

## 3.5 Force Calibration

For the optical tweezers to be used for rheology the force that is experienced by the particle in the optical trap needs to be determined. Like the calibration of the

| Optical Trap | $\kappa_x$ [pN nm$^{-1}$ mW$^{-1}$] | $\kappa_y$ [pN nm$^{-1}$ mW$^{-1}$] |
|---|---|---|
| *Trap1* | $1.891(8) \times 10^{-4}$ | $1.672(2) \times 10^{-4}$ |
| *Trap2* | $1.675(5) \times 10^{-4}$ | $2.919(2) \times 10^{-4}$ |

Table 3.2: List of stiffnesses for the channels of each trap.

displacement measured by the QPDs the calibration of the stiffness of the force provided by the optical trap has to be broken up into a linear regime (small displacements) and a non-linear part (large displacements). The potential of the optical trap is not perfectly harmonic and the anharmonicity becomes noticeable at large displacements.

The optical potential of the trap is described as being harmonic and as such is modelled as a spring with a restoring force characterised by a stiffness $\kappa$ for small displacements, see Chapter 2 for details. As the gradient force scales with laser intensity it is reasonable to assume that increasing the laser intensity will produce a stiffer/tighter trap. The relationship between laser intensity and trap stiffness was calibrated using the same information as the volts to nanometre conversion. Equation 3.1 gives the power spectrum of the Brownian motion where the corner frequency $f_c$ is defined as (see Chapter 2 for details):

$$f_c = \frac{\kappa}{2\pi\xi_0}. \tag{3.5}$$

By fitting the power spectra for the corner frequency for varying laser powers at the back focal plane of the objective the stiffness of the each trap can be determined and a conversion of pico-newtons to nanometres can be made, figures 3.10 & 3.11.
The differences in the stiffnesses in the $x$ and $y$ directions can be explained due to optical alignment and that *Trap2* has more optical components in its laser beam path and will incur more loses.
The trap stiffnesses are summarised in table 3.2:

### 3.5.1 Calibration of Trap Anharmonicity

The optical trap potential is not perfectly harmonic. There are higher order terms that need to be determined and corrected for. As the optical potential describes the restoring force that the particle feels then by applying a known force to the probe the optical potential can be determined.
In a Newtonian liquid the drag force on a sphere is described by the Stokes equation,

$$F_{Stokes} = 6\pi\eta a v, \tag{3.6}$$

where $v$ is the speed at which he sphere is dragged. We can equate the Stokes drag force to the restoring force, $F_{Trap}$, that a particle experiences when being dragged through a

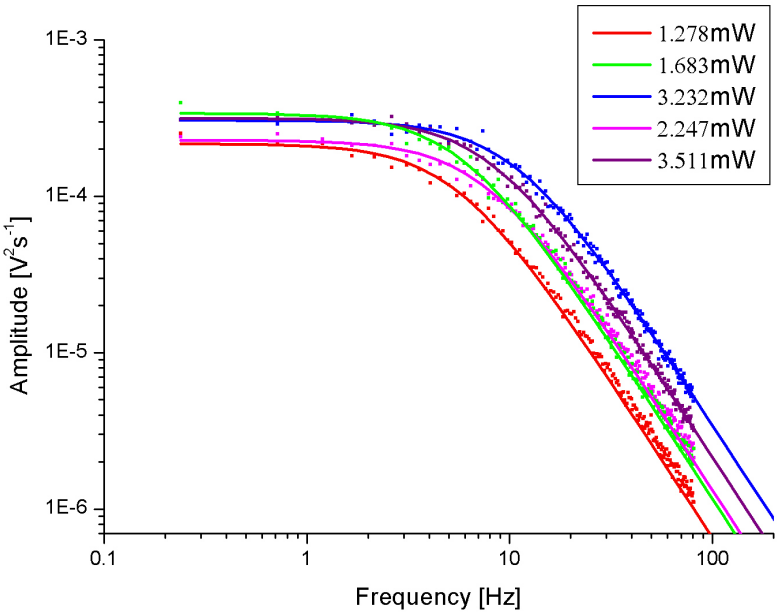


Figure 3.10: Power spectra of a trapped particle with varying laser powers used to calculate the trap stiffnesses.

Newtonian liquid by an optical trap, where the stiffness is a function of displacement:

$$\begin{aligned} F_{Stokes} &= F_{Trap} \\ 6\pi\eta a v &= x\kappa(x) \end{aligned} \tag{3.7}$$

The displacement $x$ was determined from the calibrated QPDs. The drag speed was provided using the same piezo transducer to oscillate the stage as described earlier.

A graph of displacement as a function of drag speed (force) could be plotted and the higher order terms fitted, figure 3.12. It was found the the restoring force of *Trap1* [24] could be described with a linear term (valid for small displacements) and a cubic term for larger displacements,

$$F = \kappa x + \vartheta x^3. \tag{3.8}$$

A cubic correction was found to be consistent with the characterisation of the anharmonicity of *Trap2* but the terms were not found to be equal.

The pre-factors of the cubic terms were found to be $\vartheta_{(1)} = -4.102 \times 10^{-9}$ pN nm$^{-3}$ and $\vartheta_{(2)} = -8.898 \times 10^{-9}$ pN nm$^{-3}$ for *Trap1* and *Trap2* respectively.

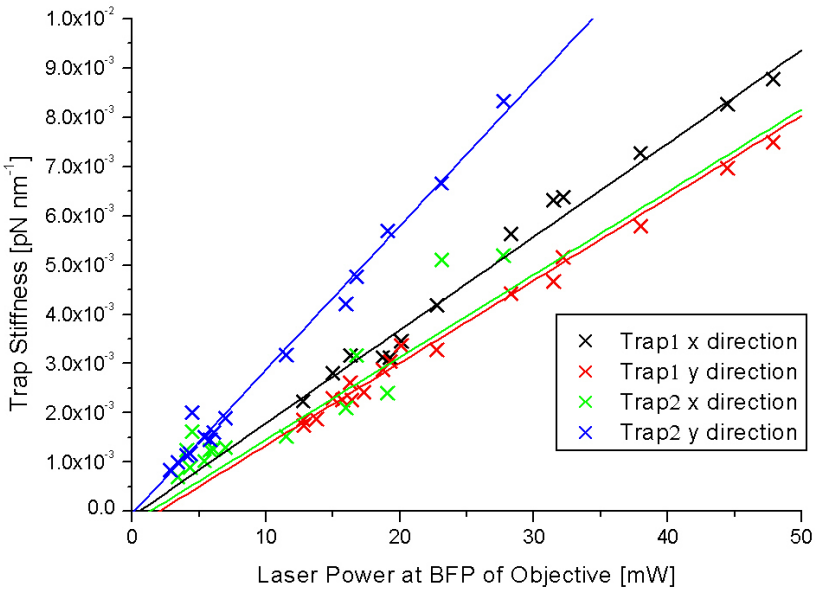


Figure 3.11: Trap stiffness as a function of laser power at the back focal plane of the objective lens for *Trap1* and *Trap2*.

## 3.6 Calibration of Angular Offsets

In the optical set-up there are three frames of reference that can be used to define a trapped particle's position: (1) the image plane with axes defined by the image captured by the CCD-camera, (2) the projection of the particle's scattered light onto the QPDs which has axes defined by the addition and subtraction of the appropriate quadrants and (3) the $x$ and $y$ directions defined by the motion of the stage. Imperfect alignments in the optical set-up means that the axes of these frames may not coincide with each other.
In the calibration, and in the active rheology experiments described in Chapter 5, the position of the optical trap was held constant and the stage was moved. Accordingly it was the stage's frame of reference that was used to define the particle positions in these experiments.

In two particle rheology experiments angular corrections needed to be made to the images and to the displacements measured by the QPDs. For both calibration experiments a particle was held in a very stiff optical trap and the stage oscillated in the $x$ direction with the fastest possible speed whilst ensuring that the particle remained in the trap. This ensured the maximum displacement and deviation from the axes of

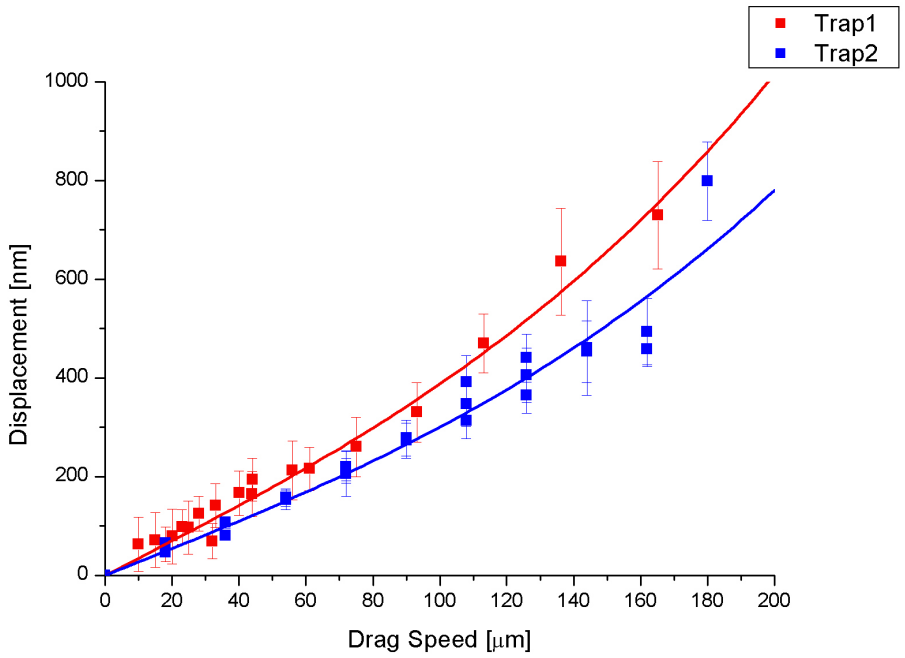


Figure 3.12: Mean particle displacement from equilibrium as a function of drag speed to determine the anharmonicities of *Trap1* and *Trap2*.

the reference frame being considered, see figure 3.13(a).

### 3.6.1 Angular Offset of the Image Plane

A series of images were captured using the same method outlined earlier where the stage was oscillated at varying speeds in the $x$ direction. The position co-ordinates of the particle in each frame were extracted and used to create a two dimensional histogram of the particle's position in the image. The position of the maxima allows the determination of any angular offset.

If the axes of the image plane were parallel to the stage then the two maxima in the histogram would be aligned along the $x$ direction of the image with one maxima either side of the equilibrium position of the optical trap. If the axes were not parallel the maxima in histogram would be displaced in the $y$ direction and again each maxima would be found either side of the equilibrium position of the optical trap. An example of this situation can be seen in the diagram of figure 3.13.

In the case of the optical set-up used any deviation in the $y$ direction was unresolvable from the histograms produced. From this it was assumed that the axes of the stage and the axes of the images produced by the CCD-camera were aligned. This

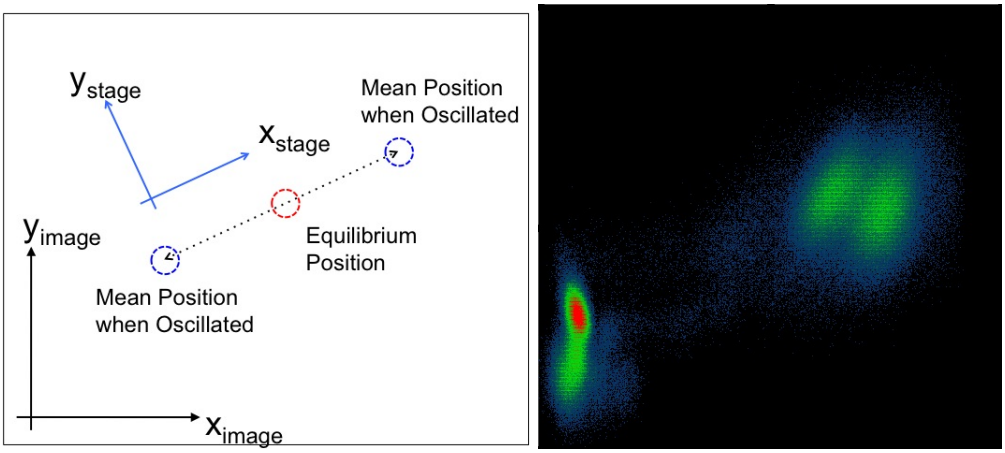


(a) (b)

Figure 3.13: (a) Schematic showing the mean positions of an oscillating particle in the image plane when the oscillation direction is not aligned with the $x$ direction of the image. (b) A $2-D$ histogram that has been exaggerated to show an offset in the angular alignment of the image reference frame with respect to the stage reference frame. Brighter colours correspond to larger amplitudes.

allowed for straight forward calibrations of the angular offsets of the detectors for each trap relative to the imaging plane that were used in Chapter 6.

### 3.6.2 Angular Offset of the Detectors

The calibration of the angular offset for each detector was carried out separately for each detector.

The detectors were likely to have some angular offset. Several components could contribute to an offset in the angle, such as the QPD's mounting to the circuit board, the circuit board's mounting to the $xy$ stage of the detector and the alignment of the optical components that focus the laser light onto the QPD. The particle was oscillated in the $x$ direction of the stage and two-dimensional histograms of the displacement measured by the detectors were made, figure 3.13(b). The co-ordinates of the maxima of the histograms were determined and using the relation $\tan\psi = y/x$ the angular offset of each QPD was determined.

The offset angles of the QPDs were found to be $\psi_{(1)} = -5.5°$ and $\psi_{(2)} = -7.5°$ for *Trap1* and *Trap2* respectively.

The angular offset of each of the detectors and its calibration is of great importance when the cross-correlation of the motion of two optically trapped particles is calculated (see Chapter 6). If it is not taken into account the cross-correlation of the motion in

| | *Trap1* | *Trap2* | [units] |
|---|---|---|---|
| Pick-off:BFP | 5.31679 | 5.02056 | – |
| $x$ Sensitivity, $S_x$ | $6.81729 \times 10^{-5}$ | $8.4811 \times 10^{-5}$ | V nm$^{-1}$ mW$^{-1}$ |
| $y$ Sensitivity, $S_y$ | $9.67754 \times 10^{-5}$ | $1.41872 \times 10^{-4}$ | V nm$^{-1}$ mW$^{-1}$ |
| $x$ Stiffness, $\kappa_x$ | $1.89179 \times 10^{-4}$ | $1.67558 \times 10^{-4}$ | pN nm$^{-1}$ W$^{-1}$ |
| $y$ Stiffness, $\kappa_y$ | $1.67226 \times 10^{-4}$ | $2.91925 \times 10^{-4}$ | pN nm$^{-1}$ mW$^{-1}$ |
| Anharmonicity, $\vartheta$ | $-4.102 \times 10^{-9}$ | $-8.898 \times 10^{-9}$ | pN nm$^{-3}$ |
| QPD (non-linearity) | $2.10608 \times 10^{-6}$ | $9.7861 \times 10^{-7}$ | nm$^{-2}$ |
| QPD Angular Offset, $\psi$ | $-5.5$ | $-7.5$ | $^\circ$ |

Table 3.3: Table summarising the calibrated variables for each trap.

the $x$ direction would be underestimated.

## 3.7 Calibration Summary

The results of the calibrations described are noted below.

The imaging pixel resolution of the camera was calculated to be $x = 0.046627\mu$m pixel$^{-1}$ and $y = 0.04572\mu$m pixel$^{-1}$ for the $x$ and $y$ directions respectively.

The offset angle for the $\lambda/2$ retarder used to regulate the laser power of *Trap2* was found to be $\theta_0 = 84^\circ$.

The cross-talk between the detectors was calculated to be 1 part in 1000.
The cross-correlation of the cross-talk was found to have an amplitude of 0.004 in normalised volts, which is comparable to the noise associated with the calculated cross-correlations made in Chapter 6.

Table 3.3 summaries all the variables associated with each trap and states the units for the variable.

# Chapter 4

# Colloids

A colloidal suspension consists of a homogeneous medium with particulate matter dispersed throughout; the particles size ranges between 1nm and 1$\mu$m. These tow limits cover a range of sizes that can describe simple molecules in the smallest case and particles that can be seen with the naked eye in the largest. Objects in this size range are large enough that the constituent atoms or molecules of the medium that they are suspended in can be considered as a continuum but are small enough that interactions with the medium are larger than the force due to gravity. Examples of such materials are smoke; solid particles suspended in air, emulsions; liquid droplets suspended in another liquid, and coffee; solid particle suspended in a liquid. Due to the small size of colloidal particles they experience thermal Brownian motion but are not so small that quantum mechanical effects will come into play.

From the previous examples of colloidal suspensions the industrial applications of academic studies can range from paint stabilisation (emulsions), smokestack dynamics, food (coffee, chocolate, whipped cream) and cosmetics (creams, makeup). However from a theoretical point of view colloids can be used as 'big atoms' [35, 36]. For example, Perrin used the sedimentation of colloidal particles to make a measure of Avogadro's number [37]. Colloidal suspension can also be used as a suitable model system for simple atomic and molecular dynamics, where because of the size of the particles the dynamics are slowed down to a timescale that is observable with a microscope.

This research deals with one particular type of colloidal suspension – the hard sphere system. This chapter describes the nature of a hard sphere colloidal system, how a hard sphere system is achieved in an experimental system, the characterisation of the system components and the experimental methods used to do so and the use of this system in rheological studies.

## 4.1 Colloids

There are many types of colloidal particles that are utilised in soft matter physics; discs like laponite, needle shape titania particles [38] and spheres, to name but a few.

This thesis is concerned with spherical colloidal particles that can be treated as having hard sphere interactions only. To obtain spherical particles that have these characteristics poly-methyl-mathacraylate (PMMA) particles were used.

## 4.2 Hard Sphere Colloids

### 4.2.1 Synthesis of Hard Sphere Colloidal Particles

The PMMA spheres were synthesised by *Dr Andrew B. Schofield* using the polymerisation of methyl-methacrylate (MMA) with methacrylic acid (MAA) and the methods described in [39]. In order to obtain spheres that had a radius of approximately $1\mu m$ the concentration of methyl-methacralate was determined using the information in *Antl et al* [40]. Poly-hydroxy-steric acid (PHSA) chains (approximately $10nm$ long) were locked onto the surface of the particles to provide steric repulsion between the particles. The particles were also fluorescently tagged using NBD-dye, this enabled them to be used in conjunction with confocal microscopy. The dye can be excited by a blue laser ($\lambda = 488nm$) and will emit photons of wavelength, $\lambda_{emission} = 525nm$, figure 4.1.

The particles suspended in their synthesis solvent were 'cleaned' so that they were suspended in dodecane. This was carried out via centrifugation where the PMMA spheres sedimented and the supernatant was poured off and replaced with dodecane. The particles were resuspended via vigourous shaking and replaced in the centrifuge. This process was repeated until a sample of supernatant had a refractive index equal to that of dodecane ($n \approx 1.422$), as measured by an Abbe refractometer. The locking of the PHSA chains onto the surface provides the repulsion at close range that was needed to give the hard sphere interaction [41], figure 4.3.

The inclusion of the NBD-dye to the MAA results in the dye being distributed throughout the particle, this enables the particles to be used in conjunction with confocal microscopy and epifluorescence microscopy techniques.

### 4.2.2 Density Matching

In a system where the density of the colloid equals that of the host that it is dispersed in, the particles neither sediment nor cream. When this is the case the particles behave like a Brownian gas and can be used as a model system with no net external driving forces (such as gravity), only hydrodynamic and thermal Brownian interactions are

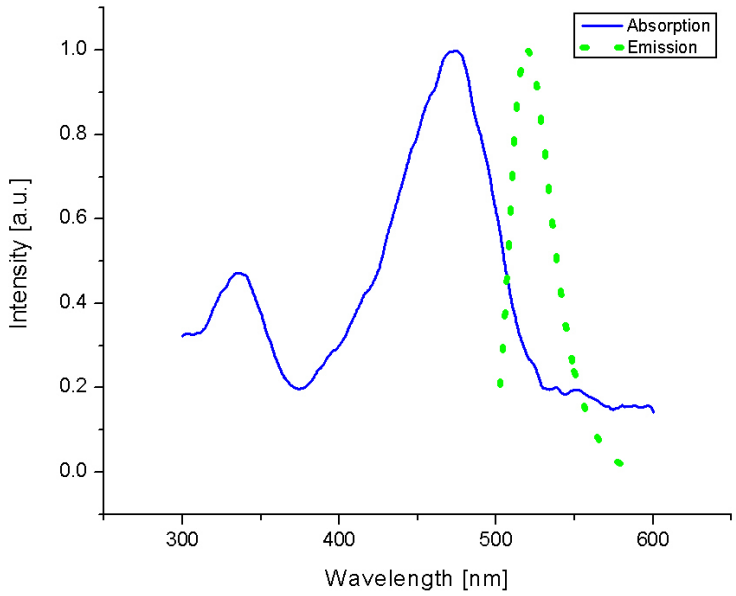


Figure 4.1: A graph of the absorbance (Blue solid line) and resultant phosphorescent emission (Green dotted line) of the NBD-Dye that is used to track the particles in confocal microscopy. The main absorption maxima is located at a wavelength of $488nm$ and the emission maximum is located at $525nm$. Graph reproduced from [1].

present in the system (and the interparticle collisions behave like hard spheres).

The particles synthesised are suspended in dodecane which does not have the same density as that of the PMMA particles. However it is known [42] that a mixture of *cis* and *trans*-decalin (chemical name decahydronaphthalene) with cyclo-heptyl brominde (CHB) can be used as a density matching fluid. The dodecane that the particles were initially suspended in was removed by centrifugation using the same method that was used to 'clean' them in the synthesis process. This time decalin was poured onto the sediment and the particles were redispersed. The process was repeated until the refractive index of the supernatant matched the refractive index of a sample of decalin freshly poured from the stock bottle ($n_{Decalin} = 1.4740$), to within the error of the instrument used. This took 7 washes on average.

Cyclo-heptyl bromide was distilled to ensure a high purity, a well defined density ($\rho_{CHB} = 1.30576$g cm$^{-3}$ at 22°C) and refractive index ($\eta_{CHB} = 1.5044$). Once the samples were clean of dodecane and had only decalin as their host some CHB was added and the PMMA particles were redispersed in this mixture. The samples were placed in a temperature controlled centrifuge and centrifuged at a rate of 7500 rpm at a

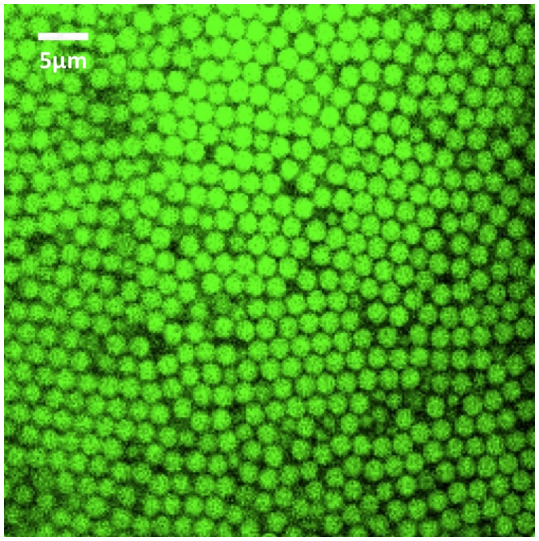


Figure 4.2: A confocal image of a sediment of the PMMA particles that were synthesised.

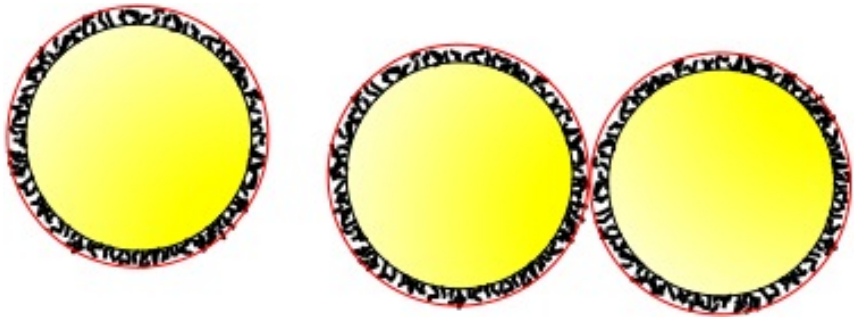

Figure 4.3: Schematic of the PHSA 'hair' on the colloidal spheres. Red line indicates effective radius of the particle extending from the PMMA core.

temperature of 22°C. If the sample sedimented more CHB was added and the particles redispersed and centrifuged again. If the sample creamed (the colloidal particles rose to the surface of the host) more decalin was added and the particles redispersed and centrifuged again at a constant temperature of 22°C. When neither sediment or cream formed after an hour of centrifugation the samples were considered to be density matched.

### 4.2.3 Steric Stabilisation

As only hard sphere interactions between the colloidal particles is desired any charge that is in the system, either present in the colloidal particles or in the host solvent, must

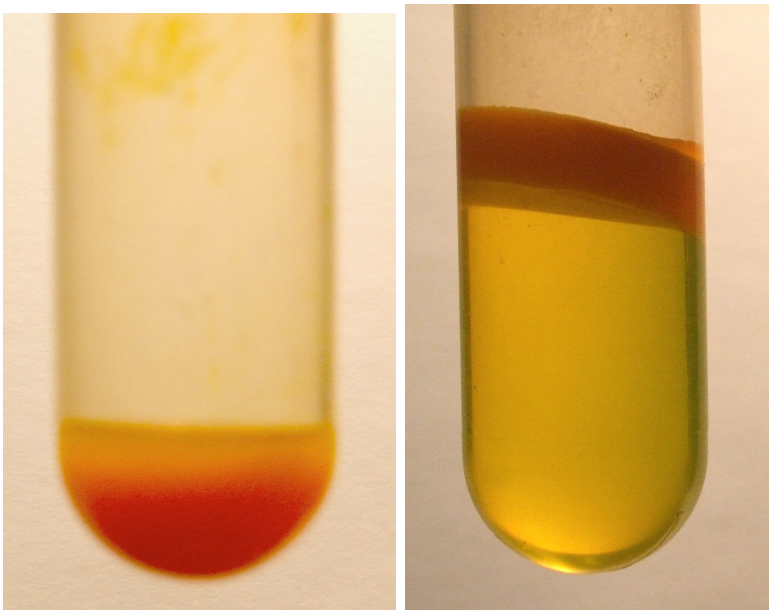

(a) (b)

Figure 4.4: (a) An image of sedimented colloid in a centrifuge tube. (b) An image where the colloid has creamed after an hour in the centrifuge.

be neutralised to ensure that it does not play a role in the interparticle interactions in the suspension.

During the polymerisation process in the synthesis of the PMMA spheres charges can develop that are not uniformly distributed across all the particles. To counter the charges developed by the particles salt can be dissolved in the suspension. The salt ions are attracted to the surfaces of the particles and form an ionic layer that screen the particle charges, making the suspension charge screened.

To screen the charges on the PMMA particles tetra-butyl-ammonium chloride (salt) was added to the density matched supernatant. The addition of the salt to the colloidal suspensions was achieved by first placing the density matched samples in a hot centrifuge and leaving them until the colloid had formed a sediment. Once sedimented the entire supernatant was poured off, filtered to remove any particles that were still suspended in the solvents and held as a stock for dilution of the PMMA sediment to suitable volume fractions used in the experiments of this research. The refractive index and density of the supernatant was measured to check that the addition of salt did not significantly change either the density or the refractive index of the suspension. In order to screen the charges in the system 1 mg of tetra-butyl-ammonium chloride was needed for every millilitre of fluid [43, 44]. The volume of supernatant was measured

Figure 4.5: A reproduction of the picture presented in [2] showing the phase behaviour of hard sphere system.

and a suitable mass of tetra-butyl-ammonium chloride was added. The salt was left to dissolve and was dispersed by vigourous shaking over a period of twenty four hours. Once the salt had been disolved a measurement of the refractive index and density of the supernatant was made and found to be $n_{solvent} = 1.495$ and $\rho_{solvent} = 1.178$ g cm$^{-3}$ respectively, both of which agree with the previous measurements of density and refractive index to three significant figures. The effective screening of the charges on the PMMA was confirmed using a commercial zeta sizer, see section 4.4.4.

van der Waals interactions were suppressed by matching the refractive index of the particles to that of the CHB/Declain mixture [43, 45].

### 4.2.4 Phase Behaviour

The phase behaviour of a hard-sphere colloid has been well studied. It was established that hard-sphere colloidal systems had distinct phases dependent on the volume fraction of the suspension [2].

Figure 4.5 shows from left to right the fluid phase, fluid crystal coexistence, crystallisation and the glass phase. This picture can be better understood in terms of a phase diagram (figure 4.6) where the phase changes that occur have been measured. The fluid-crystal coexistence phase is bounded by volume fractions $\phi_f = 0.494$ and $\phi_m = 0.545$ the freezing and melting points respectively. The glassy phase occurs at

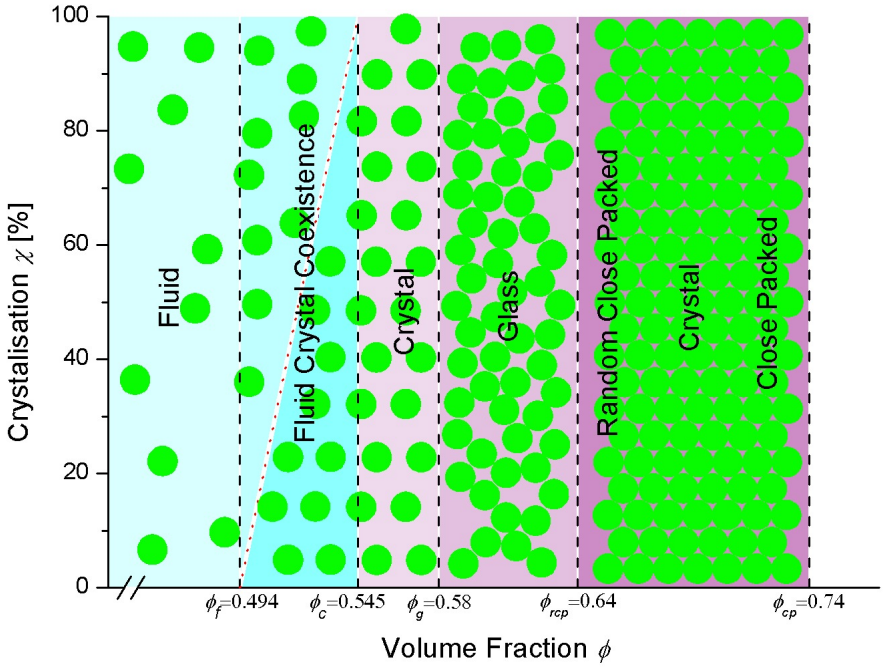


Figure 4.6: Phase diagram showing where the fluid-crystal coexistence, glassy and close packed phases occur.

$\phi_g \approx 0.58$ with an upper boundary of $\phi_{rcp} = 0.64$ (random close packed). The glass phase is metastable in the sense that the colloidal particles are 'stuck' in a configuration that suppresses crystallisation but each particle diffuses with Brownian motion in the region confined by its nearest neighbours, so that the particle is 'caged'.

## 4.3 Experimental Techniques

Optical trapping techniques are not the only method used to study hard sphere colloids. Other experimental methods can be used to determine physical properties of the hard sphere system. These methods will be outlined and where appropriate their use in the production of this research will be explained.

Static light scattering has been used extensively in this field to determine the ensemble average properties of colloidal systems, determining their long and short time diffusion. Confocal microscopy is another technique that can be used to build a three dimensional representation of particles that have been tagged with a suitable fluorescent dye, which can give information on the short range structural order of a system under

different situations. Video microscopy can be used to track particles that are not index matched to their surroundings.

### 4.3.1 Static Light Scattering

Light scattering experiments have been used extensively for many years to probe the structure of materials, particularly in crystallography where x ray radiation is scattered off of the crystal and the interference patterns formed give information on the structure of the crystal [46]. In colloidal science the radiation needs to have a wavelength comparable to size of the PMMA particles that are being used as the scattering medium, this places the wavelength of radiation in the optical part of the spectrum.

When a photon, with wavevector $k_i$, scatters off of a particle (figure 4.7(a)) it is assumed that the interaction is elastic, this is justified as the momentum imparted to the colloid is several orders of magnitude smaller than the thermal Brownian forces that colloidal particle experiences from the surrounding medium.

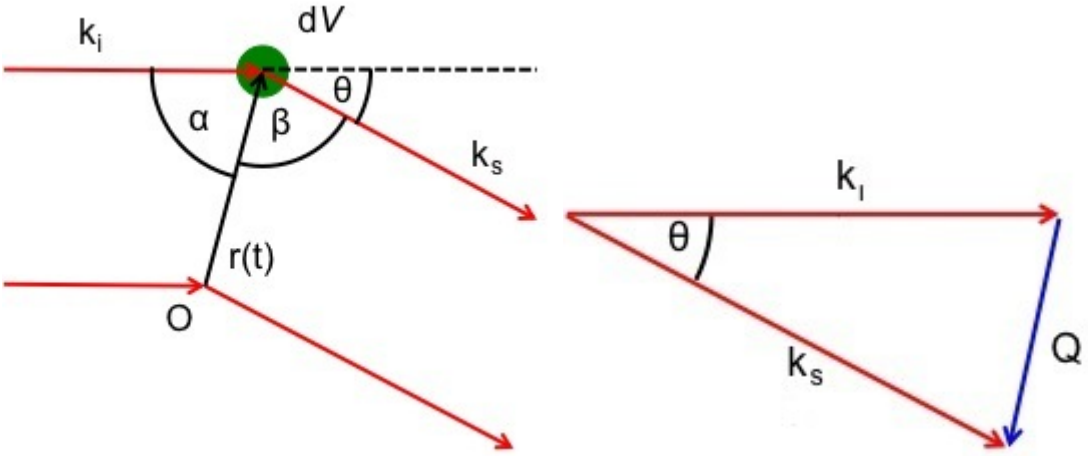


(a) (b)

Figure 4.7: (a) Diagram of an elemental volume scattering an incident beam of wavevector $k_s$. (b) Vector diagram showing the vector **Q** as the difference between the scattered and incident wavevectors.

The intensity of the scattered light as a function of scattering angle can be determined from the calculated electric field of the scattered light and the information defined in the figure 4.7(a).

The primary application of the scattering experiments used here was to characterise the core radius of the particles used, this is best done using static light scattering methods described in [47] to determine the form factor of an ensemble of particles with

identical radius,

$$P(Q,a) = \frac{9}{(Qa)^6}(\sin Qa - Qa\cos Qa)^2. \tag{4.1}$$

An ideal curve for the form factor as a function of $Qa$ is shown in figure 4.8 and the predicted minima for a particle with radius $a$ have the numerical values,

$$Qa = \tan Qa = 4.49, \quad 7.73, \quad 10.90, \ldots . \tag{4.2}$$

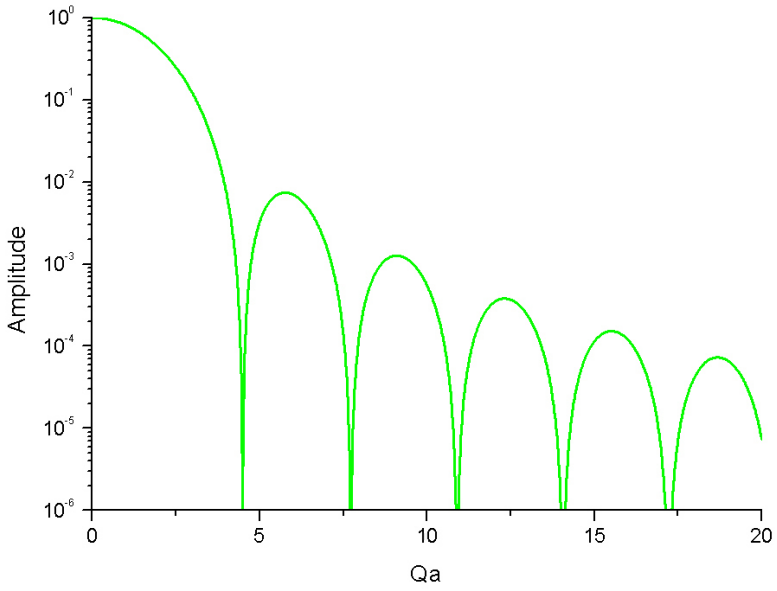


Figure 4.8: Theoretical curve predicted for the form factor described in equation 4.1 with a particle radius $a = 1$.

One caveat should be noted that the form factor that has been derived is for a monodisperse suspension, if the particles have slight polydispersity equation 4.1 will have to be derived for a range of particle sizes with the result that the minima in the will occur at varying values of $Q$, resulting in the minima of the form factor being filled in and no longer going to zero.

### 4.3.2 Confocal Microscopy

Confocal microscopy has become a more extensively used tool in colloidal physics [48, 49, 50] more recently as the increased precision of the instrument gives resolution of

less than $40nm$ and the increased computer technology that allows the analysis of large numbers of images.

Confocal microscopy uses a fluorescently tagged system where the dye can be excited by a specific wavelength of a photon. To excite the dye a laser is generally used. An area can be viewed by focussing the laser on a certain location and the fluorescent dye will be excited (figure 4.9), resulting in fluorescent emission of a certain wavelength, $\lambda_e$, however the emission will be in all directions. Due to the optical layout of the confocal set-up only photons emitted at the focal point of the excitation laser which have travelled back along the path of the laser will be detected, figure 4.10.

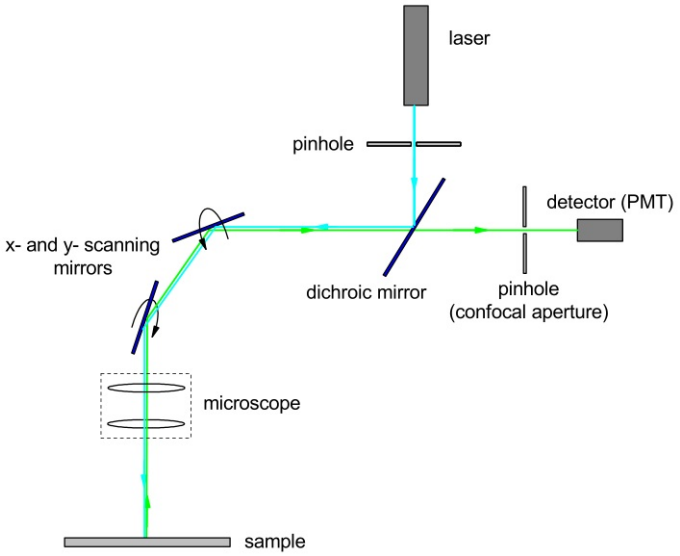


Figure 4.9: Ray optical for a typical confocal microscope setup with components. Blue ray-path indicates the the laser beam used to photo-excite the sample. Green ray-path is the photo-excitation path emitted from the sample to the detector. Diagram reproduced from [3].

Confocal microscopy is not used as a primary analytical tool in this research but has been used to confirm the volume fractions of the samples that were used in the optical tweezers experiments. This was done by taking a series of image 'stacks' in several locations and using image analysis software the particle centres were found and a Voronoi volume was calculated. Several locations were used to ensure that density variations across the sample were averaged out.

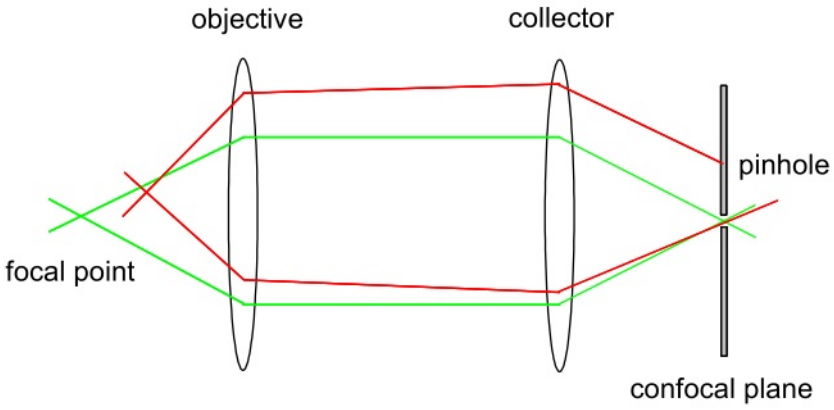


Figure 4.10: Simplified ray optics diagram of a confocal microscope set-up showing that only light from the focal point is imaged. Green ray-path is the the emitted light from the focal point of the objective lens (and hence laser). Red ray-path for light emitted away from the focal point of the objective showing that it is not detected. Diagram reproduced from [3].

### 4.3.3 Epi-Fluorescence

Epi-Fluorescence is a similar system to confocal microscopy in that light is used to photo-excite a fluorescently dyed system and the excitation photons are viewed. In this case instead of using a laser focussed on a specific location the entire sample is illuminated by a light source. A broad filter centred on the excitation wavelength of the dye is generally used as part of the illumination set-up and a second broad filter centred on the emission wavelength of the dye is placed in the optics of the viewing system. This system does not have as great a resolution as that of the confocal microscopy system and in general cannot be used in dense systems where it becomes hard to differntiate between the image plane and particles out with the focal plane. If a low density is used the system can be used as a rough method of particle tracking of bath particles in an index matched system using video tracking microscopy. The primary purpose of this technique was to determine if the area being investigated was 'typical' of the sample. It was also used to determine if any PMMA particles were located between the tracer particles that were being used as probes.

### 4.3.4 Video Tracking Microscopy

Video tracking techniques have been extensively used in the field of microscopy [51] and have been used in tracking colloidal particles. Limitations on this method have previously been that the image capture rates have not been fast enough to collect

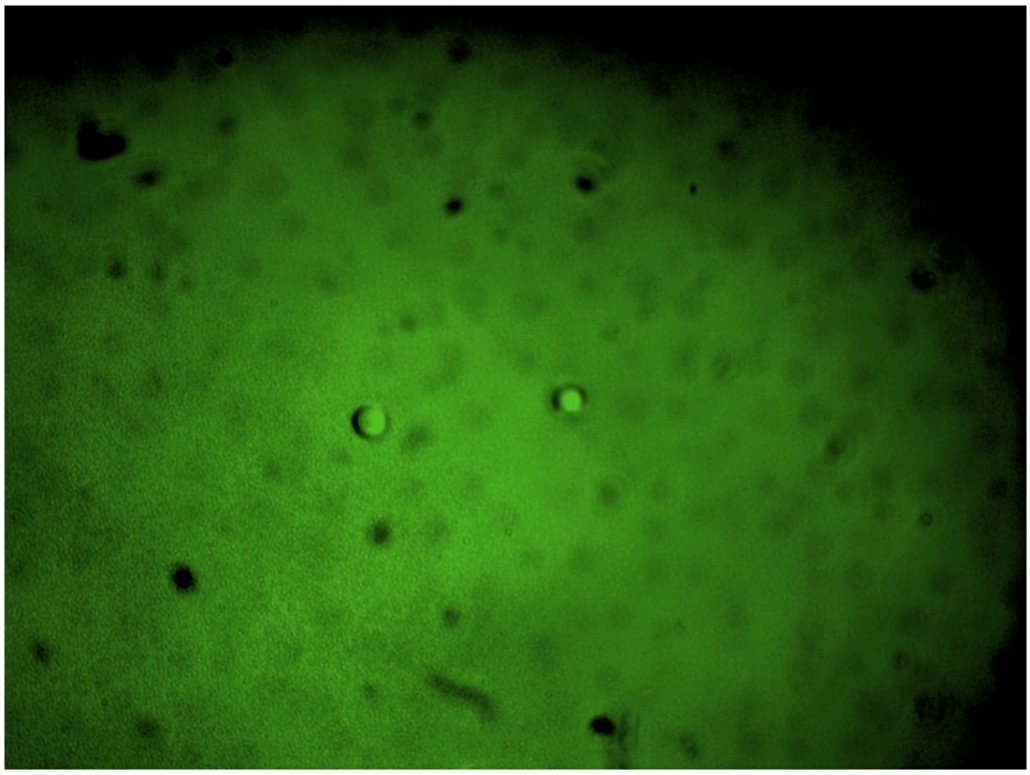

Figure 4.11: Image showing two tracers in held in optical traps in a suspension with volume fraction of $\phi = 0.05$. Darker smudges is the fluorescent emissions from the bath particles. False colour (green) has been added to the image to show bath particles more clearly.

data on the faster dynamics that particles undergo in the sample. This limitation however is being reduced with the advent of fast image CCD (charge coupled device) cameras which can now take images at a rate of $\sim 10000$ images a second, giving a time resolution of $\Delta t = 0.1ms$. Although the speed of these cameras has improved they are still several orders of magnitude behind the time resolution found in optical trapping. Also the resolution in displacement is dependant on the magnification of the optics and the size of the pixels of the camera placing the best resolution at the diffraction limit of the system, optical traps are not limited by the diffraction limit as an interference pattern is used to determine the displacement.

A further limitation of conventional video tracking in the use of the systems considered in this research is that the PMMA particles are density matched, this results in them also being nearly index matched and without a difference in refractive index they cannot be resolved in the image place of the objective lens. This does not mean that video tracking was not used, as the melamine tracer particles that were used (see

tracer characterisation) had a refractive index different to that of the CHB-decalin host they could be resolved and tracked. Video tracking of the melamine tracer particles was used in multiple instances in the calibration of the optical traps and their set-up, for details on these instances see Chapter 3.

### 4.3.5 Differential Dynamic Microscopy

Differential dynamic microscopy (DDM) is new method that has recently been developed that allows information on particle dynamics to be measured using a bright field microscope when the particle size is smaller than the diffraction limit of the microscope. The technique has only been possible to develop and deploy due to the improvement in the capture rate of images from a camera and computing ability to process a large number of images in a reasonable amount of time.

Cerbino and Trappe [52] were the first to explicitly use the DDM technique to confirm the radius of colloidal particles both above and below the diffraction limit of their microscope. The method involves subtracting the pixel intensities of a series of images as a function of increasing time separation, $\tau$, to give the fluctuations of pixel intensity. The two dimensional Fourier transform of the result is calculated of the fluctuation of the image $D(x, y, \tau)$,

$$\mathcal{F}_{2D} = \int D(x, y, \tau) e^{-i2\pi(u_x x + u_y)} \mathrm{d}x\mathrm{d}y. \tag{4.3}$$

The Brownian diffusion each Fourier mode will decay exponentially with a characteristic decay time, $\Delta t(q)$, where $\Delta t(q) = 1/D^{(Short)}q^2$ and $D^{(Short)}$ is the self diffusion of the colloidal particles. Giavazzi *et al.* [53] explicitly show that power spectrum will show this characteristic decay time:

$$|\mathcal{F}_{2D}(q, \tau)|^2 = A(q)\left[1 - e^{-\tau/\Delta t(q)}\right] + B(q), \tag{4.4}$$

where $A(q)$ and $B(q)$ can be treated as parameters if $q$ is fixed.
The radius of the particles can be calculated as equation 4.4 at fixed $q$ will be a function of the characteristic decay time $\Delta t(q)$ which as stated is related to the self diffusion of the particles, $D^{(Short)}$, which can then be used to determine the particle radius:

$$D^{(Short)} = \frac{k_B T}{6\pi\eta_m a}. \tag{4.5}$$

## 4.4 Characterisation of Colloidal System

### 4.4.1 Characterisation of Dispersion Medium

To determine the viscosity of the CHB/Decalin mixture a sample of supernatant was used to fill a rheometer's double couette geometry (concentric cylinders) and was used to measure the viscosity of the host and ensure that it had a Newtonian behaviour for the shear rates that would be used in the microrheology experiments that will be discussed in chapters 5, 6 and 7. A shear ramp was used at constant temperature to measure the viscosity and multiple temperatures were recorded to establish stability of the supernatant with temperature. The variation found at shear stresses of less

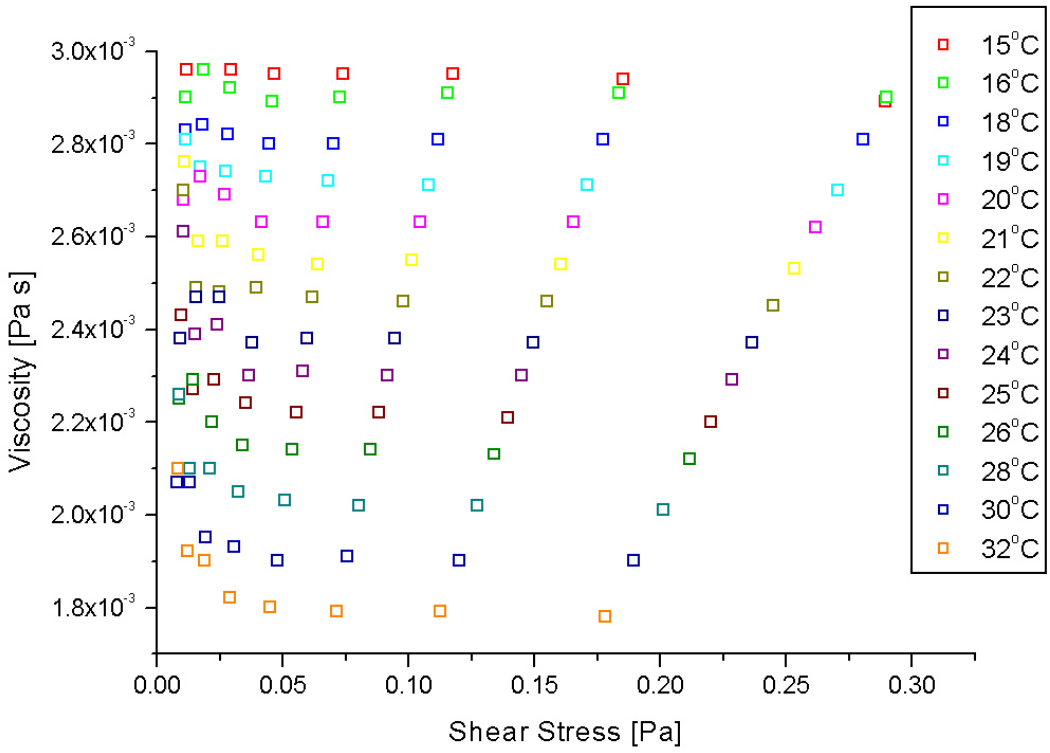


Figure 4.12: Measurements of the viscosity of a mixture of CHB and decalin for a series of temperatures. Viscosity at a temperature of 22°C is $\eta_0 = 2.504$mPa s.

that $0.025Pa$ are associated with the resoltion limit of the rheometer used to make the measurements. The measured viscosity above this limit as a function of shear stress is constant shows that the supernatant can be treated as as Newtonian liquid. The viscosity is also shown not to shear thin temperature range that the samples

experienced in any experiment carried out in this research. The viscosity of the fluid was found to be 2.5mPa s at a temperature of 22°C.

The stock was sealed in jars and placed in a fridge to increase the lifetime of the mixture as the bromide atoms in the cyco-heptyl bromide would eventually break free if exposed to warmth and light on a time scale of weeks if not months.

### 4.4.2 Characterisation of Colloid Radius

Once the PMMA particles had been density matched a sample of volume fraction $\phi < 0.01$ was prepared. This sample was used in a static light scattering experiment and via fitting of the resulting form factor the ensemble average of the particle radii was calculated, see figure 4.13. The radius and polydispersity was determined by fitting theoretical form factors with polydispersity as a parameter to the data using a program provided by *Assoc. Prof. Gary Bryant* and the technical assistance of *Dr. Vincent Martinez*. The radius found to be $a = 0.90 \pm 0.05 \mu$m with a polydispersity $\sigma = 3.5 \pm 0.1\%$ .

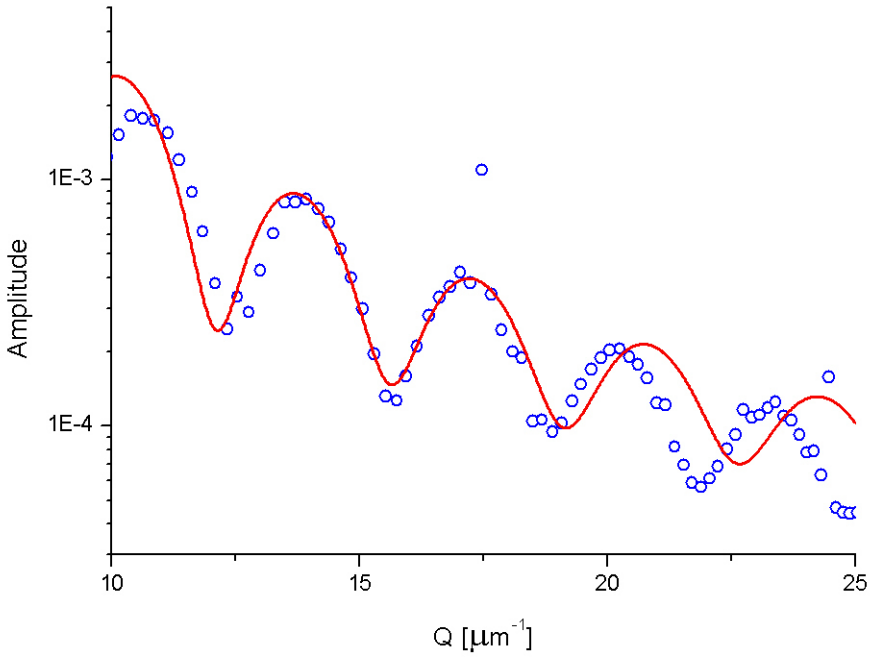


Figure 4.13: Static light scatter measurements and the form factor for measurements made of the PMMA particles used in this research giving a particle radius of 0.90$\mu$m.

### 4.4.3 Characterisation of Tracer Particles

Given that the PMMA particles were in a suspension that was density matched to that of the PMMA this resulted in the refractive index of the PMMA being nearly identical to that of the CHB/Decalin mixture (to suppress the van der Waals interaction). With this being the case the individual PMMA particles are unable to be confined by the optical trapping methods as discussed in Chapter 2. In order to probe the properties of the suspension (using optical tweezers) tracer particles that had a higher refractive index were needed to act as 'handles' for the optical trap. For this tracer particles made of melamine resin were obtained from Microparticles GmbH with a refractive index of $n_{melamine} = 1.7$, stated by the vendor. The tracer particles were characterised also by the vendor using scanning electron microscopy and had a radius (before PHSA was grafted to their surface, see below) of, $a = 0.95\mu m$ and a polydispersity of 4.7%. The tracers were very chemically inert and impermeable to most organic solvents, particularly those used in suspensions of the PMMA particles; they are reported to be damaged only by hot sulphuric acid [24].

To ensure that these tracer particles interacted with the PMMA particles in an identical manner to that the PMMA particles with each other PHSA strands were also grafted onto their surface. This gave the melamine particles the same steric stabilisation as the PMMA particles, this process was also carried out by *Dr. Andrew B. Schofield*. To confirm that the PHSA 'hair' had successfully been attached to the tracer particle's surface the backbone of the PHSA molecule was tagged with NBD dye (the same that is used to make the PMMA particle fluorescent) and confocal images[5] of a sediment were taken. The PHSA had to be tagged as the melamine was inert to the dye. The PHSA can be seen as the halo of emission around the empty space where the tracer particle sits. It can also be seen that none of the PHSA has penetrated into the centre of the melamine particle. The high refractive index of the melamine particles allows them to be optically trapped and used to probe the properties of density matched suspensions of PMMA particles.

In addition to the confocal images of the sediment of melamine particles DDM measurements, figure 4.15, were taken to determine the radius of the particles with the addition of the PHSA 'hair'. Differential dynamic microscopy was used as the melamine particles which are more dense than PMMA particles would sediment during the time it would take for a static light scattering experiment to be completed. In addition to the sedimentation was the high refractive index difference between the melamine and the solvent meant that there was a much higher chance of multiple scattering in any light scattering experiment (Dynamic Light Scattering). The diffusion of the melamine

[5]Image was acquired with the assistence of *Dr. Job Thijssen.*

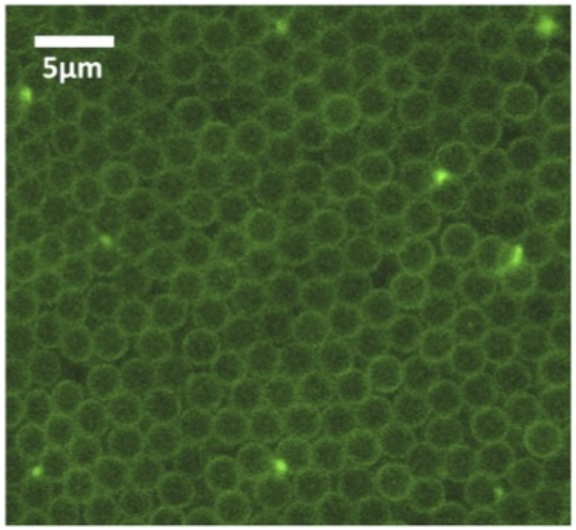


Figure 4.14: Confocal image of a sediment of melamine tracer particles with fourescently tagged PHSA grafted to their surface.

particles was $D_{melamine} = 0.1144$ resulting in a radius of $a = 969$nm showing an increase of 19nm compared to that of the initial radius stated by the vendor, figure 4.15.

To suspend the melamine tracer particles in a suspension of PMMA particles an initial sample of the melamine was placed in a clean jar and left under vacuum to remove all suspension solvent. A sample of the density matched fluid was poured over the dried melamine particles and the particles were resuspended by vigourous shaking. A small amount of these particles were then added to the sedimented PMMA samples at a mass fraction of less than 0.1%. This ensured that in all samples the number of melamine particles in the PMMA was very low and that in any experiment the probability of another melamine particle diffusing into the optical trap (which would ruin an experimental run) was vanishingly small.

### 4.4.4 Characterisation of Colloidal Charge

A commercial zeta sizer was used to identify if there was any residual charge on both the PMMA spheres and the melamine spheres. The zeta sizer determines the residual charge on the colloidal particles by using laser doppler velocimetry (LDV) to determine the electrophoretic mobility, $U_E$ [54]:

$$U_E = \frac{2\varepsilon_r \varepsilon_0 \zeta f(\kappa)}{3\eta}, \tag{4.6}$$

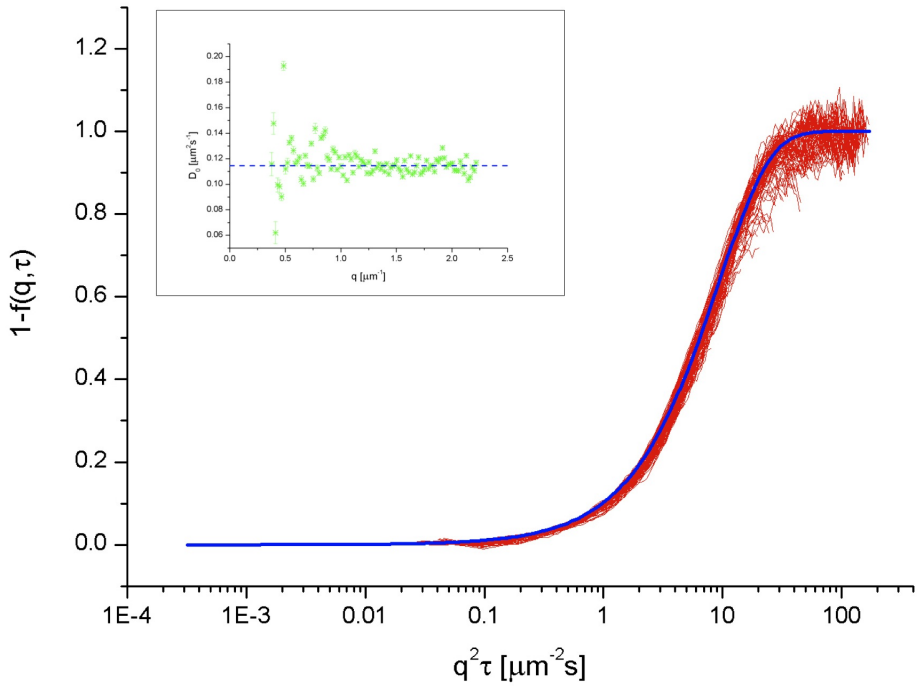


Figure 4.15: Differential dynamic microscopy analysis of a 30s long movie of a suspension of tracer particles in Decalin for various $q$ values. A fit to the data is shown in blue. Inset shows the determined diffusion from each data set, with the mean of $D_{melamine} = 0.1144\mu\text{m}^2\text{s}^{-1}$ shown by blue dashed line.

where $\varepsilon_r$ is the dielectric constant of the host suspension, $\varepsilon_0$ is the permittivity of free space, $f(K)$ is Henry's formula, $\eta$ is viscosity of the host and $\zeta$ is the zeta potential of the colloidal particles. To determine the electrophoretic mobility an oscillating potential is applied across the sample and laser is shone through sample. The oscillating potential causes the charged colloidal particles to move towards the oppositely charge electrode and when the particles move they scatter the laser light. The intensity of the scattered light is measured at an angle of 17° and the intensity of the scattered light is proportional to the fluctuation rate of the particles. The value of $\varepsilon_r$ for a mixture of CHB and Decalin was given in [55] and the Henry function was taken to be $f(\kappa) = 1.0$, which is the Huckel approximation [54]. The viscosity is that of the mixture of CHB and Decalin as stated in a previous section $\eta = 2.5$mPa s, figure 4.12.

Before the addition of salt the average zeta potential was measured to be $\zeta_0 = 11.2 \pm 0.6$mV, figure 4.16 red line.

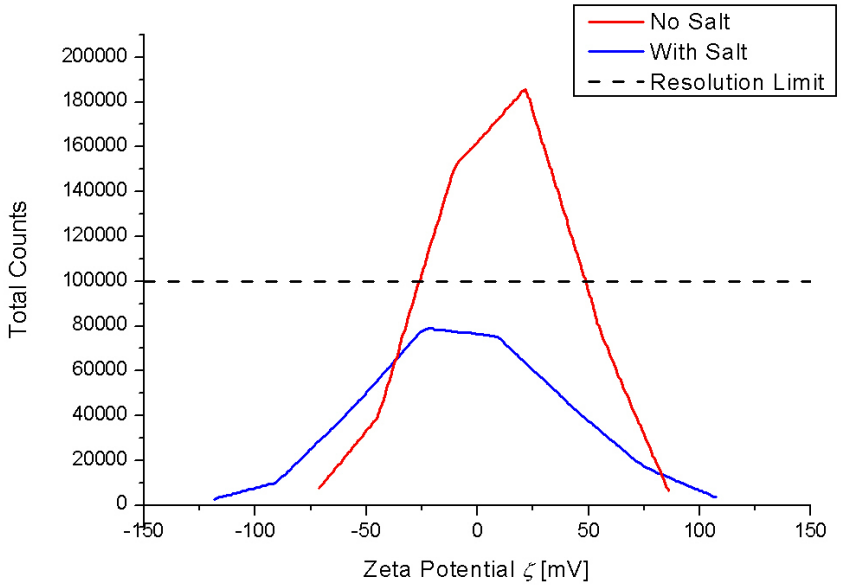


Figure 4.16: The zeta potential of PMMA particles in a mixture of CHB and Decalin with and without salt. The zeta potential determined to be $\zeta_0 = 11.2$mV and $\zeta_{salt} = -4.32 \pm 0.3$mV respectively.

To confirm that the charges on the PMMA particles were screened and that the particles were charge stabilised the zeta potential of the PMMA particles in the same mixture of CHB and Decalin was made but included the addition of the tetra-butyl-ammonium chloride (salt). The zeta potential was found to be $\zeta_{salt} = -4.32mV$, figure 4.16 blue line. Whilst $|\zeta_{salt}|/|\zeta_0| \approx 0.38$ is not an insignificant fraction the number of counts that was used to determine $\zeta_{salt}$ is in the resolution limit of the instrument and when the spread gives a value that is consistent with zero.

## 4.5 Sample Preparation

### 4.5.1 Determination of Volume Fraction

Once the PMMA particles had been density matched, charge screened and doped with melamine tracer particles they were resuspended by vigourous shaking and placed back into a warm centrifuge until they had sedimented again. This ensured that the melamine particles were part of the random close packed sediment at the bottom of the centrifuge tube and not sitting in a loose layer on top of the PMMA particles,

confirmed by confocal microscopy. The supernatant was again poured off and filtered to remove any particles that were still suspended.

As the PMMA and the CHB-decalin host had the same density the volume fraction, $\phi_V$ of a suspension would have an identical mass fraction, $\phi_m$:

$$\phi_m = \frac{m_c}{m} \quad ; \quad \phi_V = \frac{V_c}{V}, \tag{4.7}$$

where $m_c$ is the total mass of the colloidal particles in the suspension, $m$ is the total mass of the entire suspension likewise $V_c$ and $V$ are the volume of the colloidal particles and the total volume of the suspension respectively. Density is defined as $\rho = m/V$ and we have two densities in the system, the density of the colloid, $\rho_c$ and the density of the supernatant $\rho_\ell$. Taking the case of the supernatant first,

$$\begin{aligned} \rho_\ell &= \frac{m_\ell}{V_\ell} \\ &= \frac{m - m_c}{V - V_c}. \end{aligned} \tag{4.8}$$

Rearranging and substituting the volume fractions in equation 4.7 gives:

$$\begin{aligned} \rho_\ell &= \frac{m - m\phi_m}{V - V\phi_V} \\ &= \frac{m}{V}\left(\frac{1-\phi_m}{1-\phi_V}\right) \\ &= \rho\left(\frac{1-\phi_m}{1-\phi_V}\right). \end{aligned} \tag{4.9}$$

From equation 4.9 we can see that $\rho_\ell$ will only equal the density $\rho$ when the mass fraction, $\phi_m$, and the volume fraction $\phi_V$ are equal.
If we now consider the case for the density of the colloids, $\rho_c$, using the same substitutions for $m_c$ and $V_c$ as previously:

$$\begin{aligned} \rho_c &= \frac{m_c}{V_c} \\ &= \frac{m\phi_m}{V\phi_V} \\ &= \rho\frac{\phi_m}{\phi_V}. \end{aligned} \tag{4.10}$$

Again we can see that for if $\phi_m$ and $\phi_V$ are equal then $\rho_c$ reduces to $\rho$. Rearranging equations 4.9 and 4.10 for $\rho$ we can see explicitly their relationships to $\phi_m$ and $\phi_V$:

$$\rho = \rho_\ell\left(\frac{1-\phi_V}{1-\phi_m}\right) = \rho_c\frac{\phi_V}{\phi_m}. \tag{4.11}$$

If $\phi_m = \phi_V$ then equation 4.11 reduces to:

$$\rho = \rho_\ell = \rho_c. \tag{4.12}$$

Proving that when the density of the supernatant is equal to that of the suspended colloid the mass fraction must be the same as the volume fraction, allowing volume fractions to be determined by calculating the mass fraction.

Samples of suitable volume fractions were made by taking the sediment that was left at the end of the density matching process (see earlier) and measuring its mass. Assuming the volume fraction of random close packing, $\phi_{rcp}$, to be 0.64 the mass of the colloid in the sediment was determined. A mass of suspended melamine particles was then added (to have a mass fraction of less than 0.1%) to the sediment, the mass of fluid added was noted. With the mass of the colloid known (including the addition of the melamine) and the mass of the supernatant left in the sediment (the other 36% of the mass and the fluid that was added with the melamine) the mass of fluid needed to be added to give the desired volume fraction could be calculated. The diluted sample of known volume fraction could then be diluted further for other lower volume fractions.

### 4.5.2 Sample Cells

Two types of sample cell were used with the optical tweezers set-up[6]. The choice of which cell was used was based on the lifetime of the sample and on volume fraction concentration of the sample concerned. It has been found [56] that above a volume fraction of $\phi \sim 0.49$ jamming occurs. This is where a suspension being pulled (or pushed) through a narrow capillary will result in a jammed arrangement through which the colloidal particles do not move quickly but the solvent can be drawn through the gaps between the jammed particles. The main methodology used to transfer the samples to the cells was to use a pipette, however when dealing with samples that were $\phi = 0.30$ or higher a spatula was used to ensure that the volume fraction of the sample was not less than what would be expected (as the case would be if a pipette was used and jamming occured). When this was the case a 'bucket cell' (figure 4.17) was used, often it was easier to slowly pour the sample from a 'stock jar' into sample cell in these cases. For the lower volume fractions that were investigated capillary cells were used, figure 4.18.

[6]The cells used are modified versions of those that were used in [24].

### 4.5.3 Bucket Cell

The bucket cell design was used when volume fractions were high enough that jamming became a concern when filling a cell by capillary action, as mentioned above. They were also used for samples that needed to be kept for a long time. The bucket cell

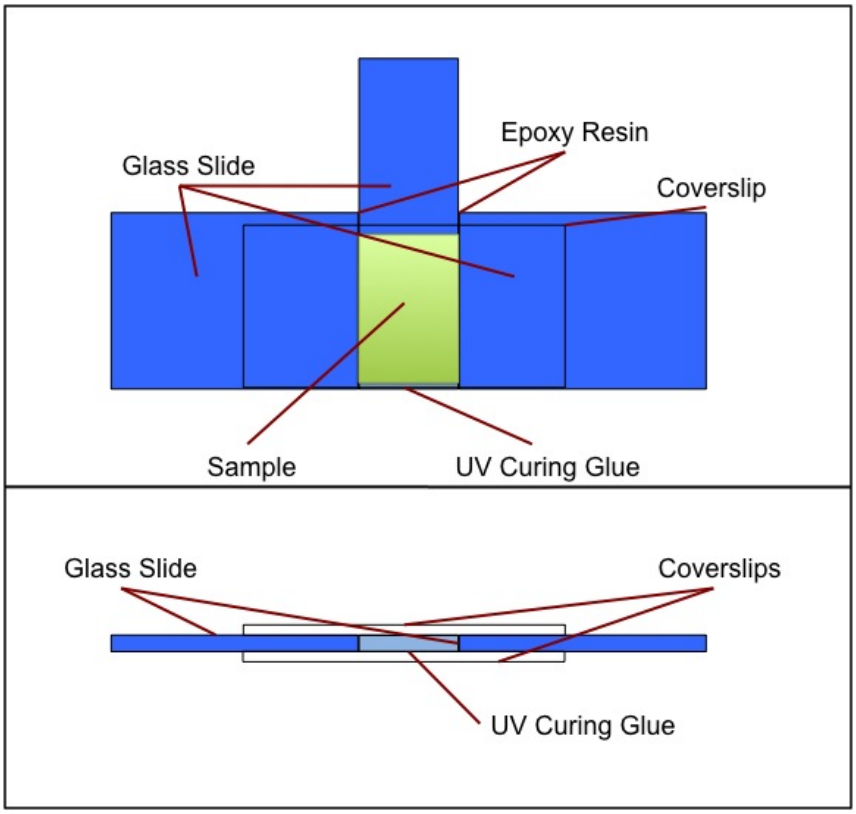


Figure 4.17: Schematic of the bucket cell used for the dense suspensions. Above the planer view of the sample cell, below is an end on view of the cell.

consisted of a standard 1mm thick microscope slide that had been cut in half, the clean edges where placed side by side with a space of about a centimetre between them. A coverslip was glued using UV curing glue to each half of the slide across the gap. A second coverslip was glued in the same manner on the opposite side of the glass slide, creating a glass tube with channel thickness of $\sim$ 1mm, width of $\sim$ 1cm and a length of $\sim$ 3cm. The bottom end of the tube was also sealed using UV curing glue to create the cavity or 'bucket' that would hold the sample. Finally a wedge of glass was cut to fit the cavity. Once the cavity was filled the wedge was inserted into the top of the bucket and fixed in place using rapid setting epoxy resin. The use of the glass wedge reduced the contact the sample had with the epoxy resin and ensured the sample remained

uncontaminated for a long period of time and as air tight as possible.

For samples that had a volume fraction where crystallisation may occur in the interval between the samples being used in experiments some lengths of nickel wire (of the order of a few millimetres) were added to the suspension. Before each experimental run a magnet was used to draw the metal filaments through the sample to break up any crystals or crystallites present. The wires were then drawn to the bottom and side of the sample chamber to ensure they did not affect any of the subsequent measurements.

### 4.5.4 Capillary Cell

A capillary cell design was used for the lower volume fractions and for the more disposable samples. In this case a single microscope slide had two half size cover slips glued to one side using UV curing glue to act as spacers. A final full-size coverslip was glued on top of these spacers, creating a bridge over the cavity, see figure 4.18. The cell was filled using capillary action, where an excess of the suspension would be placed on a clean microscope slide and the capillary cell placed with an open end on top of the

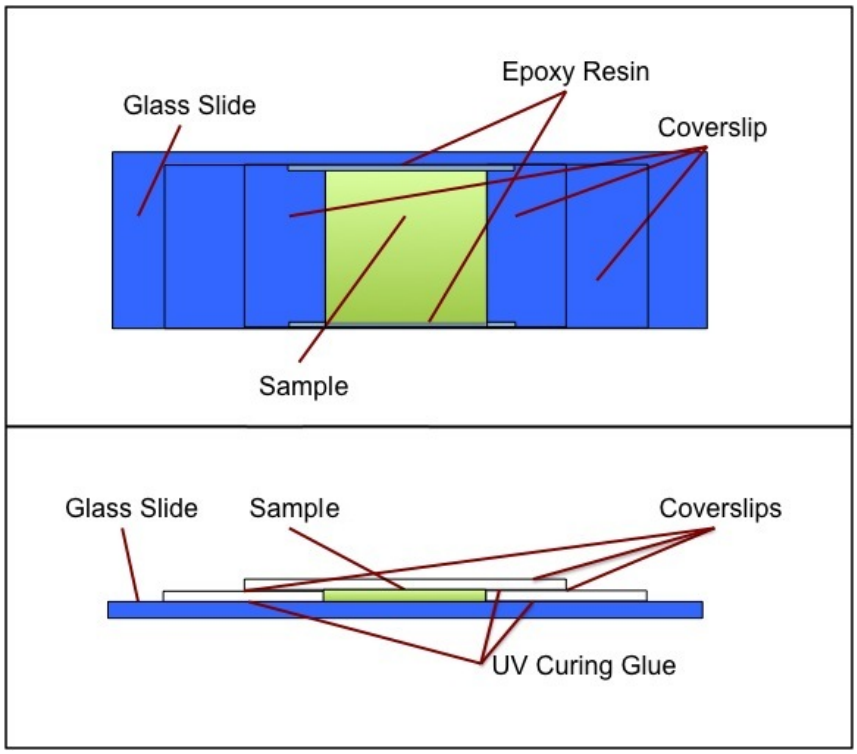


Figure 4.18: Schematic of the capillary cell used for low volume fraction suspensions. Above the planer view of the sample cell, below is an end on view of the cell.

suspension. Once the sample cell was full, quick setting epoxy resin was used to seal both ends immediately. Given that sample had contact with the epoxy resin at each end of the capillary cell, the solvent of the suspension would react slowly with it and the sample would slowly become contaminated. The contamination was noticeable after several days as faint particles diffusing throughout the sample cell. The contamination was negligible on the timescale of experimental runs. Thus, a new cell was generally used each day for the dilute, more readily prepared samples. If a specific low volume fraction sample was needed over a time period of greater than a day, a bucket cell was generally used and the cell examined for contamination before each run.

## 4.6 Rheology

Rheology is the study of how a material deforms and flows under stresses and strains [57]. In the case of a perfect solid the material will deform and store the energy internally and will be released as the material relaxes back to it's original conformation, this is the elastic response regime.

For systems that are in the elastic response regime the shear modulus $G$ can be


Figure 4.19: Illustration of a shear deformation from an applied stress, $\sigma$.

described in terms of the applied stress and the resulting shear strain, $\gamma$,

$$G = \frac{\sigma}{\gamma} \tag{4.13}$$

There is, however, a point where the stress applied, $\sigma_{yield}$, to the solid will result in an irreversible deformation, this is the elastic limit. The irreversible deformations are referred to as being plastic and the system is elastoplastic.

Unlike solids, ideal liquids have neither shear modulus or elastic modulus and offer no resistance to either an applied stress. Instead, it will respond by flowing. The fluid viscosity, $\eta$, can be determined from the applied stress and the resulting shear rate, $\dot{\gamma}$:

$$\eta = \frac{\sigma}{\dot{\gamma}}. \tag{4.14}$$

A fluid that satisfies equation 4.14 is called a Newtonian fluid.

Most materials do not exhibit completely elastic or purely viscous behaviour, but instead show a combination of the two under an applied stress; if they do not permanently deform, they are referred to as viscoelastic. The shear modulus of a viscoelatic material can therefore be decomposed into an elastic part, $G'$ (also known as the storage modulus), and a viscous part, $G''$ (loss modulus) [57]:

$$G^* = G' + iG'' \tag{4.15}$$

The proportions of the storage modulus and the loss modulus that make up the shear modulus are usually dependant on the frequency of the applied stress,

$$\sigma(\omega) = \gamma(\omega)\left[G'(\omega) + iG''(\omega)\right]. \tag{4.16}$$

### 4.6.1 Macro-rheology

Macro-rheology deals with the bulk properties of a material, where in general a suspension can be treated as a continuous medium because the volume of material that is sheared is very much greater than the size of the colloidal particles. The shear rates in macro-rheology are best described by the Péclet number, which is a dimensionless quantity defined in terms of a Brownian time $\tau_B$ and a shear time $\tau_{\dot{\gamma}}$:

$$Pe = \frac{\tau_B}{\tau_{\dot{\gamma}}}. \tag{4.17}$$

The Brownian time, $\tau_B$, is the time it takes a particle to freely diffuse its own radius, whilst $\tau_{\dot{\gamma}}$ is the time it takes to separate two particles by the same distance by mechanical shearing. thus,

$$Pe_{Macro} = \frac{\dot{\gamma}a^2}{2D_0}. \tag{4.18}$$

The definition of the Péclet number allows two regimes to be described. When $Pe < 1$ the Brownian time is smaller than the shearing time where in the suspension the Brownian motion is able to relax any deformations induced by the applied shear rate. Once the shear rate gets sufficiently large enough that $\tau_{\dot{\gamma}} < \tau_B$ and $Pe > 1$ then the Brownian motion is no longer fast enough to allow the deformations to relax back to equilibrium.

In hard sphere colloids there have been several investigations of how the rheology of a suspension changes with volume fraction [58], [59, 60, 61, 62]. For volume fractions where $0 < \phi < 0.4$ (the fluid phase) the suspension was found to behave as a Newtonian fluid with constant viscosity but the value of the viscosity increases with increasing volume fraction. The authors of [4] (figure 4.20) showed that for the region between

fluid and glass phases the suspension would still behave as a Newtonian fluid for low Péclet numbers. When the Péclet number was increased the suspension shear thinned. The onset of shear thinning for each volume fraction depends on the volume fraction of the suspension, figure 4.20 shows that the onset of shear thinning occurs at lower Péclet numbers as the volume fraction increases.

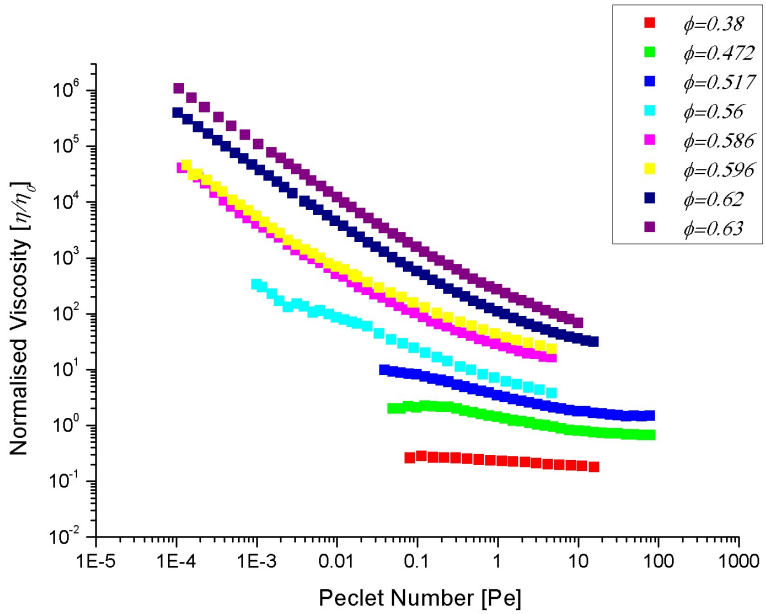


Figure 4.20: Data taken from [4] and replotted to give normalised viscosity as a function of Péclet number.

Above the glass transition, $\phi_g$, the viscosity at low $Pe$ diverges from the Newtonian plateau indicating the presence of a yield stress. This is approximately where the loss modulus $G''$ in equation 4.15 becomes smaller than the storage modulus.

### 4.6.2 Micro-rheology

Micro-rheology is the microscopic counterpart to macro-rheology, instead of the bulk rheological properties of the material being probed a much smaller volume is probed.

The methods used in this thesis to study the micro-rheology of hard sphere suspensions uses the optical tweezers set-up outlined in chapter 2. The main difference between optical tweezer micro-rheology and macro-rheology is that the optical tweezers trap and shear at most two particles (lengthscale of order $\mu m$) rather than shearing the entire suspension (of order $cm$).

Single particle active micro-rheology involves trapping one tracer and dragging it

through the colloidal suspension in order to measure the normalised micro-viscosity as a function of Péclet number. However the Péclet number defined in equation 4.18 is no longer valid as the entire sample is not being sheared at a specific rate, only 1 particle and the area surrounding it is being sheared. Instead using equation 4.17 and redefining the shear time $\tau_{\dot{\gamma}}$ for a single particle to traverse its radius moving with constant velocity in a suspension of particles with identical radius, a micro-Péclet number can be defined, $Pe_{\mu}$,

$$Pe_{\mu} = \frac{2Ua}{D_0}. \tag{4.19}$$

Research by Brady and co-workers [63] have predicted the same shear thinning behaviour as a function of micro-Péclet number that was found in macro-rheology experiments. Furst has also shown shear thinning behaviour [13] in a suspension where the tracer particles are $\sim 3$ times larger than the bath particles. The experiments shown in the next chapter are for the measurement of the microviscosity when the tracer particles are roughly the same size as the bath particles.

# Chapter 5

# One Point Micro-Rheology

This chapter details the one point micro-rheology measurements made using the optical tweezers and compares the passive results to established DLS data and compares the active results to bulk macro-rheology measurements.

The first and second parts of this chapter detail the measurement of the passive and active microviscosities of hard-sphere colloidal suspensions with volume fractions below the glass transition. A detailed description is given on the observation of shear thinning for Péclet numbers greater than 1 followed by measurements of the low shear plateau for similar volume fractions measured in the high shear limit.

A comparison is made between the micro-rheology measurements made here to the established measurements of shear thinning found in macro-rheology experiments. Corrections that can be made to account for the difference between the two regimes are explained and the corrected micro-rheology data compared to the bulk macro-rheology data.

The final part describes the construction of a parallel plate shear cell built with the intention of being used in conjunction with the optical tweezers to obtain information on the interparticle forces experienced by a colloidal suspension when it is sheared. This proved to be impractical mainly due to the operational constraints of the optical tweezers in their current form, full details of which are described in the body of the shear cell section.

## 5.1 From Macro-Rheology to Micro-Rheology

Complex fluids are often investigated using macro-rheological techniques and methods. These methods often require large volumes of the material to be probed. These may not be readily available, for cases such as new synthetic materials and biological materials. New techniques to measure the micro-rheology of materials such as video tracking

microscopy, differential dynamic microscopy, confocal microscopy and optical tweezers have all been developed where only a small volume of material is needed to make a measurement.

There is however the issue of whether the micro-rheology will match the bulk rheology of the material. The micro-rheology might not agree as only a small volume of the sample is being perturbed (a few particles, polymers *etc*) and the macro-rheology is measured by perturbing the entire bulk of the sample. If they do not agree there must be some length scale on which the two systems do agree. To this end the optical tweezers experiments have been used to determine the microviscosities of hard sphere colloids and compare these measurements to the established bulk measurements that can be found in the literature [18].

## 5.2 One Point Mirco-rheology with Optical Tweezers

Optical tweezers can be used to make one point active and one point passive micro-rheological measurements of a colloidal system. In a one point passive measurements, a single tracer particle is held in an optical trap and the particle's fluctuations are recorded and used to yield information on the rheology of the material immediately surrounding the particle. In a one point active micro-rheology, a single particle is held in an optical trap and the particle is actively translated through the material it is suspended in. Measurement of the velocity of the trapped particle and the force it experiences then yield rheological information about the medium through which the particle is dragged.

The advantage of micro-rheology is that only a small quantity of the samples are required compared to bulk rheological measurements. However, relating micro-rheology and bulk rheology is highly non-trivial, and indeed is one of the main themes of the remainder of this thesis.

The one point passive and some of the one point active micro-rheology experimental work that is described next was carried out in collaboration with *Dr. Laurence Wilson* who did the initial work on this area. Here I have added more volume fractions to his passive results. I have also added more results to his high shear active results but all the low shear active results were measured by myself and I have collected all the one point microviscosity results here.

## 5.3 One Point Passive Micro-Rheology

There is no trivial relation between the microviscosity and the bulk viscosity hard spheres and DLS measurements of the microviscosity do not in general agree with the

bulk viscosity. This is described by Fan *et al.* [64] and the references therein, for a sphere in a polymer solution. It shows that there is a depletion layer around the sphere that is not representative of the bulk viscosity (has no polymers) and as such the fluctuations of the particle's position that DLS techniques use to determine the microviscosity of the suspension will not agree with the bulk viscosity measured by a rheometer. For these reasons the microviscosities measured by the optical tweezers should be compared to the microviscosities measured using DLS.

As outlined in Chapters 2 and 3 the power spectrum of the fluctuations of a trapped particle's displacement can be used to determine the short time diffusion co-efficient $D_0$ for a particle in bare solvent,

$$\begin{aligned} S_x(f) &= \frac{D_0}{\pi^2}\frac{1}{(f_c^2+f^2)} \\ \lim_{f\gg f_c} S_x(f) &\rightarrow \frac{D_0}{\pi^2 f^2}. \end{aligned} \tag{5.1}$$

Using the same method to analyse the fluctuations of a trapped particle in a suspension of colloidal particles the short time diffusion $D^{(Short)}$ of the trapped particle can be determined. The passive microviscosity $\eta_\mu^{(Passive)}$ of the suspension can then be calculated using a Stokes-Einstein relation,

$$D^{(Short)} = \frac{k_B T}{6\pi\eta_\mu^{(Passive)} a}, \tag{5.2}$$

where $a$ is the radius of the trapped particle. It has been found that the power spectrum of colloidal suspensions become non-Lorentzian at low frequencies, however as stated in equation 5.1 we are considering the high frequency limit where the power spectrum can still be described as Lorentzian.

### 5.3.1 Passive Experimental Method

Two batches of quasi-monodisperse PMMA particles were used as the 'bath' in the determination of the passive micro-viscosity of colloidal dispersions with volume fractions less than the glass transition. Both batches were measured using static light scattering and had radii of $a^{(1)} = 0.90 \pm 0.05\mu$m and $a^{(2)} = 0.86 \pm 0.07\mu$m with polydispersities of $\sigma^{(1)} = 3.5 \pm 0.1\%$ and $\sigma^{(2)} = 8.0 \pm 0.1\%$ respectively. Each batch was doped with the same melamine tracer particles. Each batch was used independently of each other and neither of the batches were mixed with each other[7]. The ratios $\alpha$ of the batches of bath particles to the tracer particles were 1.07 and 1.13 respectively. There was no systematic difference between the data recorded using either set of particles and

as such the results were treated together.

Suitable volume fractions with a range of $\phi = 0.10$ to $\phi = 0.57$ were made using the methods outlined in Chapter 4 and loaded into cells that were then sealed with epoxy resin. Capillary cells were used for samples with volume fractions of less than $\phi = 0.40$ and bucket cells were used for the other volume fractions for reasons that were stated in Chapter 4. For samples that were more dense, $\phi > 0.40$, a magnet was used to perturb magnetic pieces of wire placed inside the cell to break up any crystallites that may have formed. This ensured that the sample was as homogenous as possible. The sample was then placed under the optical tweezers and the condenser and objective lens focussed to a region $20\mu$m from the lower coverslip. This reduced any hydrodynamic wall effects that the coverslip would have provided. The Faxén correction to the solvent's viscosity [65] gives a quantifiable effect that the chamber walls have as a function of height away from the closest wall $h$. For tracer particles with radius $a = 0.969\mu$m at a height of $20\mu$m and a cell thickness, $t$, of 0.5mm was calculated at most to be,

$$\begin{aligned}\xi &= \frac{1}{\left[1 - \frac{9}{16}\left(\frac{a}{h}\right) + \frac{1}{8}\left(\frac{a}{h}\right)^3 - \frac{45}{256}\left(\frac{a}{h}\right)^4 - \frac{1}{10}\left(\frac{a}{h}\right)^5\right]} + \\ &\quad \frac{1}{\left[1 - \frac{9}{16}\left(\frac{a}{t-h}\right) + \frac{1}{8}\left(\frac{a}{t-h}\right)^3 - \frac{45}{256}\left(\frac{a}{t-h}\right)^4 - \frac{1}{10}\left(\frac{a}{t-h}\right)^5\right]} - 1 \\ &= 1.02914. \end{aligned} \tag{5.3}$$

At most there would be an increase in the measured viscosity of 3%. This value is less than what was later found to be the greater source of systematic error of the system, the error associated with the radius of the tracer particle. We therefore ignore this correction.

The following experimental protocol was used for each sample. An isolated tracer particle was selected and trapped, the particle was moved to a height of $20\mu$m above the coverslip. The sample was then left to equilibrate typically for 15 minutes to half an hour, depending on volume fraction. This allowed any stress that had been induced in filling the cell and when moving the trapped probe time to relax fully.

Once equilibrated the voltage range on the detector was set to give the optimum resolution of the fluctuations in the trapped particle's displacement. A recording of the fluctuations was made and the signal monitored to ensure there was no drift in the sample caused by either the sample not being fully equilibrated or not having been

[7]The batch of particles with radius of $a^{(2)} = 0.86\mu$m belonged to *Dr. Laurence Wilson* and a description of their full characterisation can be found in [24].

mounted properly to the optical stage. Several measurements were made of each volume

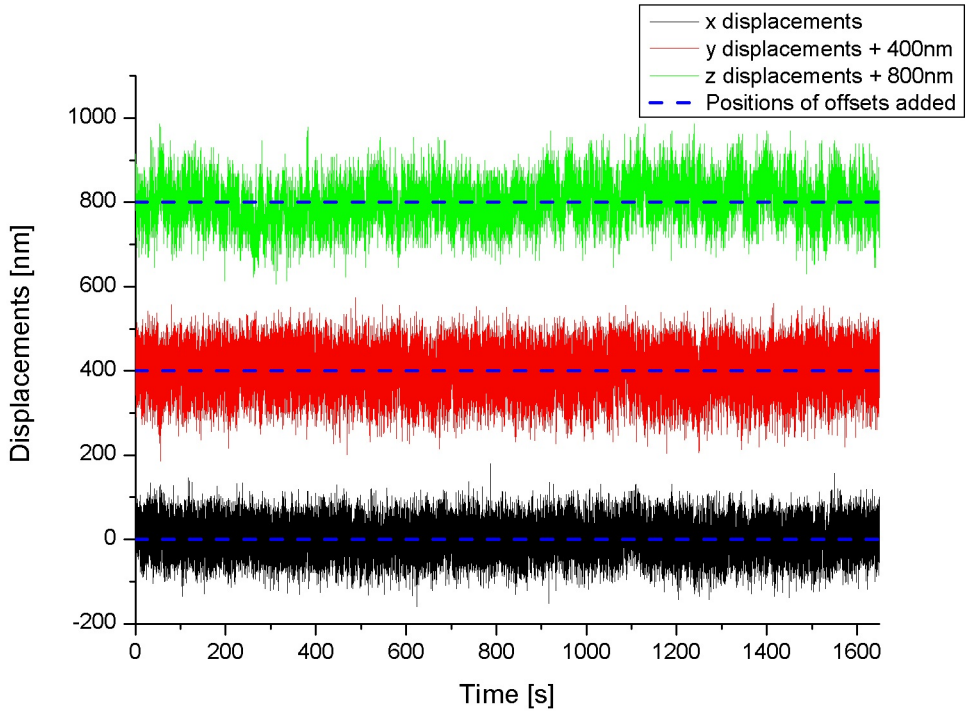


Figure 5.1: Displacements over time of a trapped particle in a suspension of volume fraction $\phi = 0.20$. The black trace is the displacement in the $x$ direction, the red trace is the displacement in the $y$ direction and the green trace is the displacement in the $z$ direction. An offset of $400nm$ and $600nm$ has been added to the $y$ and $z$ displacements respectively to differentiate their traces for presentation purposes. Blue dashed lines indicate the offsets that have been added to the displacements

fraction with different trap stiffnesses, to determine whether the trap stiffness changed the interaction of the tracer with the surrounding bath particles. Measurements were also made in several locations to reduce any effects that density fluctuations in the sample may have had on the measurement.

### 5.3.2 Passive One Point Micro-Rheology Results

To analyse the data a fast fourier transform was performed on the voltage signal recorded representing the trapped particle's displacement. This gave the power spectrum of the particle's displacement in $V^2 s^{-1}$. The voltage was converted to $nm$ using the conversion factors determined in Chapter 3 and the data was fitted using a Lorentzian, where $D^{(Short)}$ was extracted from the fit.

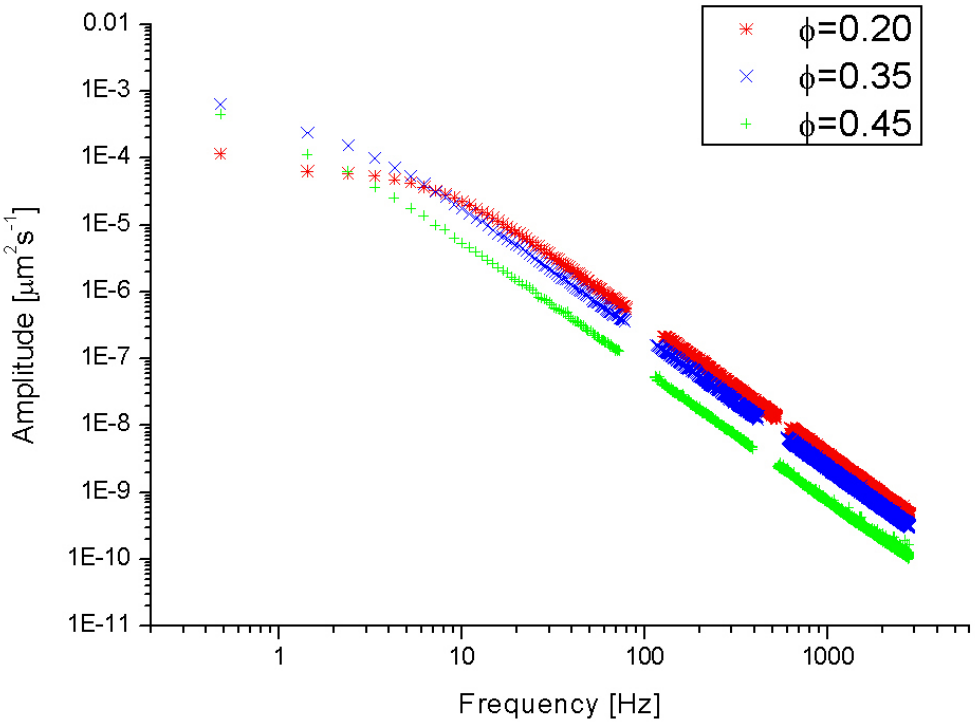


Figure 5.2: Fourier transforms of the particle displacements for volume fractions $\phi = 0.20$ (red), $\phi = 0.35$ (blue) and $\phi = 0.45$ (Green) with approximate trap stiffness of $\kappa = 6 \times 10^{-4}$pN nm$^{-1}$. Gaps in the data sets are due to removed noise peaks that are associated with mains frequency interference. All data sets here were collected and analysed by myself.

It can be seen in figure 5.2 that at high frequencies the amplitude decreases with increasing volume fraction, where the amplitude is directly related to the short time diffusion for the sample. It can also be seen in figure 5.2 that the variation in the low frequency increases and becomes progressively non-Lorentzian with increasing volume fraction. The decreasing diffusion would correlate with an increasing viscosity which is expected for a suspension of hard-spheres.

Once $D^{(Short)}$ was determined from the fit the passive micro-viscosity, $\eta_{\mu}^{(Passive)}$, for each volume fraction was calculated, full details of the error analysis used can be found in Appendix C. The passive microviscosity was normalised by the viscosity of the bare solvent and a plot of microviscosity as a function of volume fraction was made, figure 5.3[8]. No variation was found in the passive micro-viscosity calculated from different

trap stiffnesses.

The passive microviscosity measured by the optical tweezers shows good agreement

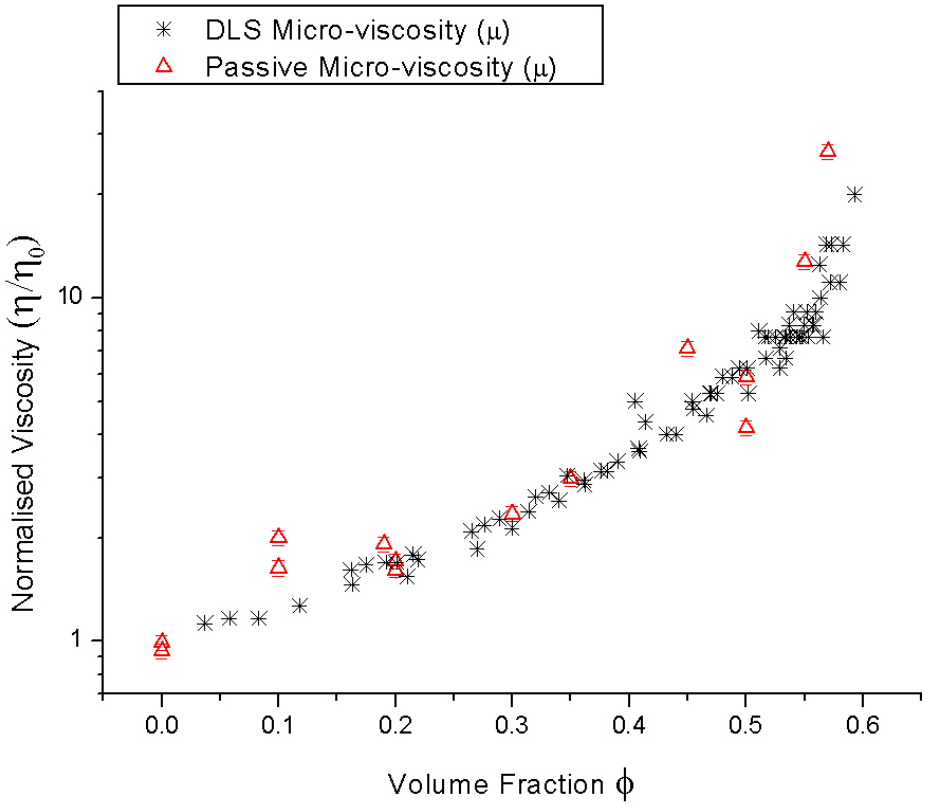


Figure 5.3: Measure of normalised passive microviscosities $\eta_{\mu}^{(Passive)}$ (red open triangles) as a function of volume fraction with normalised microviscosity measured by DLS reproduced from [5] (black asterisks).

with the established passive microviscosity for a similar system measured by DLS. The two points for volume fraction $\phi = 0.10$ for the optical tweezers are greater than their corresponding DLS microviscosity. However, DLS takes an ensemble average over many particles in the sample and the optical tweezers only deals with one particle at a time it is perhaps not surprising that the optical tweezers are not as precise in some cases. Particularly good agreement is found at volume fractions $\phi > 0.45$ and show the increase in viscosity expected as the volume fraction approaches the glass transition.

[8] Volume fractions $\phi = 0.10$, $\phi = 0.50$, $\phi = 0.56$ and $\phi = 0.57$ were measured by *Dr. Laurence Wilson* the rest were measured by myself.

### 5.3.3 Conclusions from One Point Passive Micro-Rhelogy

The optical tweezers can be used to determine the passive microviscosity $\eta_{\mu}^{(Passive)}$ for a range of volume fractions from $0.10 < \phi < 0.57$. It was found that the passive microviscosity agrees to within one standard deviation with the established microviscosity measured by DLS in a similar system of hard-sphere PMMA particles. Particularly good agreement was found for volume fractions of $\phi > 0.45$.

## 5.4 One Point Active Micro-Rheology

In macro-rheology where a stress is applied to the entire sample it has been found that suspensions of hard spheres will shear thin [4].

The next step is to determine whether the microviscosity behaves in a similar manner, exhibiting shear thinning. In this case the stress would be applied by dragging a single particle through the suspension, figure 5.4. Whilst a system may show shear thinning it is not obvious that the passive microviscosity will match the macroviscosity in the same way as the system is not being probed on the same lengthscale.

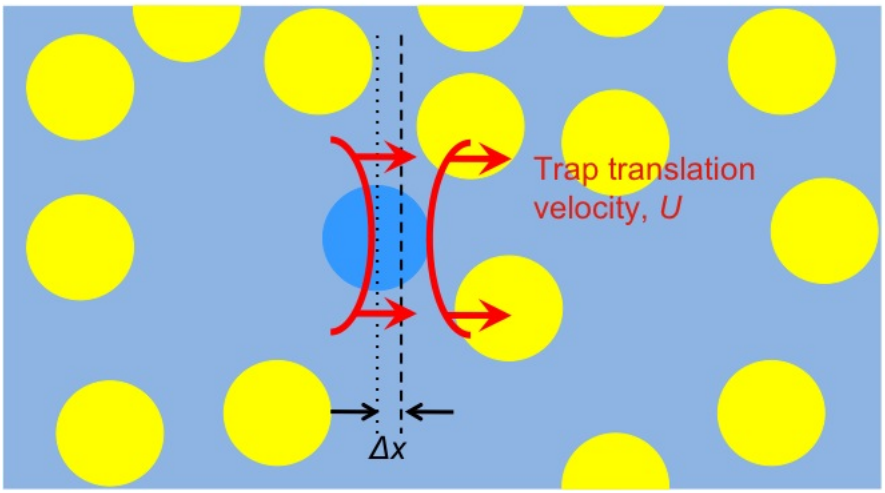


Figure 5.4: Schematic showing a tracer particle being dragged through a suspension of colloidal particles with a translational velocity, $U$, that produces a displacement of $\Delta x$ of the tracer from equilibrium.

Theoretical work and simulations by Brady and co-workers [66, 67, 68, 69] suggest that the active microviscosity to agree with the macroviscosity. In a dispersion of very dilute hard-sphere colloidal particles ($\phi < 0.10$) shear thinning should occur for Péclet numbers greater than 1. Meyer *et al.* [13] showed shear thinning of both the

macro- and microviscosities of a suspension of teflon particles. The microviscosity was measured using constant velocity optical tweezers and the macroviscosity was measured in a commercial rheometer but the two data sets did not agree. The macro-rheology performed on the teflon particles indicated that they behaved like hard-spheres but the information presented showed that on a microscopic level they were only quasi-spherical. The viscosity of the teflon particles with volume fraction grew faster than hard spheres indicating possible interparticle attractions. Habdas *et al.* [70] have also carried out an experimental comparison of the macro- and microviscosity for a hard sphere colloidal suspension. They used PMMA hard-spheres and dragged a magnetic bead through their suspension with a constant force provided by a magnetic field. They presented agreement between the macro- and the microviscosity for a suspension with volume fraction of $\phi = 0.29$ but gave no other quantitative comparison for other volume fractions.

In both the experimental cases mentioned the ratio of the tracer particle to the bath particles $\alpha$ was greater than 2 and as such the tracer particle cannot be treated as being representative of the colloidal fluid that it is suspended in, nor can it be treated as being suspended in a fluid that can be described as a continuum.

In the cases presented above the active micro-viscosity in the high shear limit ($Pe > 1$) was determined using the generalised Stokes-Einstein relation outlined in the preceding chapter.

$$\eta_{\mu}^{(Active)} = \frac{F}{6\pi v a} \tag{5.4}$$

where is $F$ is the force the particle experiences, $a$ is the particle radius and $v$ is the velocity at which the particle is dragged. It should be noted that this expression is certainly valid in the continuum limit but it should not be expected to remain accurate for when the size of the probe particles is similar to that of the bath particles that they are suspended in, *i.e* when $\alpha \to 1$.

### 5.4.1 Active Experimental Method

The same batches of PMMA particles that were used the passive measurements, were used for measuring the active microviscosity. The same volume fractions were also used to allow a direct unambiguous comparison between the two microviscosities measured.

Once the cell had been placed on the tweezers and the condenser had been focussed to a height of 20$\mu$m above the coverslip, a check was made of the surrounding area to confirm that there was a dilute dispersion of tracer particles. This check was to ensure that during any experimental run the likelihood of another tracer either being

directly in the path of the optical trap or diffusing into the optical trap was low. An isolated tracer was positioned at a height of 20$\mu$m above the lower coverslip and left to equilibrate as for the passive micro-viscosity measurements.

For each measurement the tracer was held in a stationary position for approximately 3 minutes. The stage was then translated at a preselected speed in the $x$ direction for 24 minutes then stopped. A further 3 minutes of stationary fluctuations of the tracer particle were recorded. The system was then left to equilibrate again.
The two 3 minutes sections at the beginning and end of each experimental run allowed a measure of the drift associated with the experimental system, sources being that the zero position of the optical trap could wander with time, relaxations in the mechanical springs and components of the stage and drift in the optical alignment.

The stage was driven at speeds corresponding to micro Péclet numbers in the range of $3 < Pe < 600$, although for higher volume fractions, $\phi > 0.5$ Péclet numbers greater than 60 were not possible as the tracer particle was forced out of the optical trap by the suspension at these speeds. Péclet numbers were calculated using equation 4.19 stated in Chapter 4,

$$Pe = \frac{2Ua}{D_0}. \tag{5.5}$$

To determine the maximum drag speed an initial experimental run was carried out but was not recorded. The speed of the stage would gradually be increased and the voltage signals of the displacements noted. When the tracer particle was pushed out of the trap the drag speed was noted and not exceeded during the subsequent experimental runs. The probe would be moved to a new location and the sample left to equilibrate once more. This also gave an estimate for the voltage range that would need to be set on the detector to ensure good resolution of the displacements the individual drag runs.

Care was taken to ensure that the tracer particle was not dragged back through a region it had already perturbed, when the tracer had traversed the length of the cell it would be dragged to a new location, the system left to equilibrate and the experiment continued in the new region, thereby removing any hysteresis present in the analysed data. By sampling several regions with the same drag speeds the effects of density fluctuations through out the cell were reduced.

The recorded voltage signal of the detector was converted into two data sets one of nano-metres and the other of pico-newtons using the voltage conversions described in Chapter 3. The displacement of the particle was plotted as a function of time for the experiment, see figure 5.5.

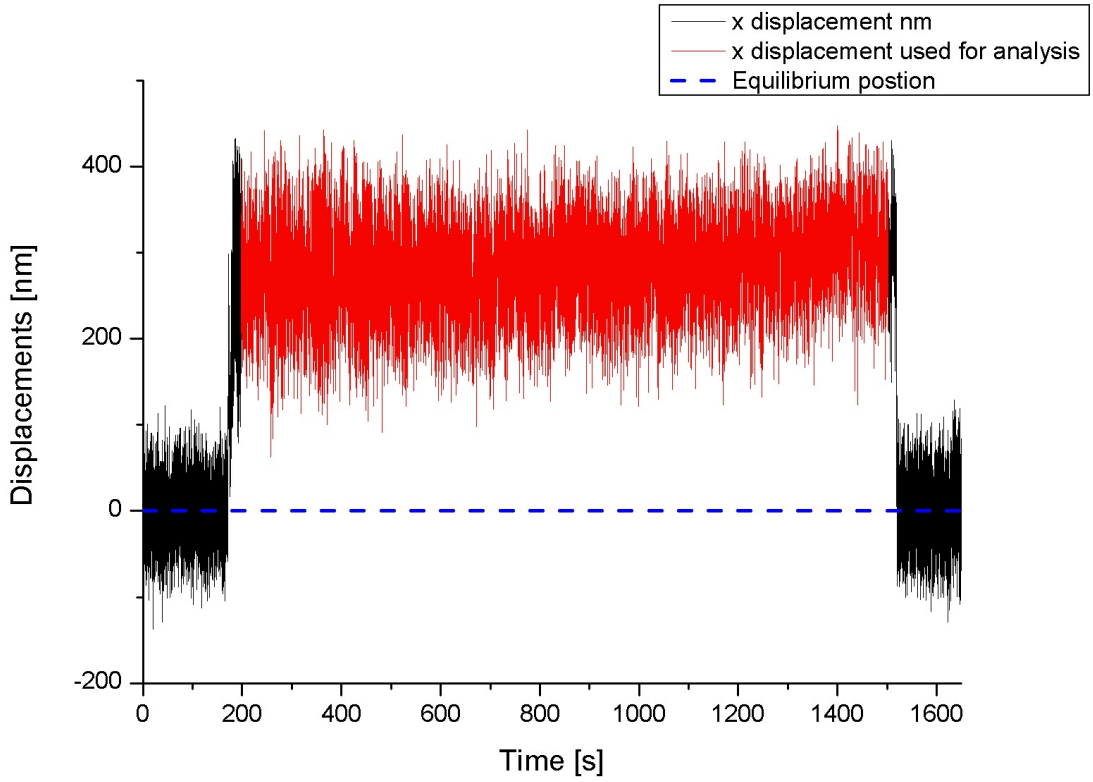


Figure 5.5: Tracer displacement from equilibrium position as a function of time for a sample with volume fraction $\phi = 0.30$ dragged with a velocity of $v = 6.0\mu ms^{-1}$. The fluctuations around the equilibrium position (indicated by the dashed blue line) at the beginning and end of the run were used to determine the drift of the experimental system and the error on the displacement that was used to determine the microvisosity. The displacement marked in red is the section that was used to determine the tracer's displacement from equilibrium.

The displacement of the particle from equilibrium, indicated in red in figure 5.5, was measured relative to the average position of the particle when it was stationary in the first 3 minutes of the experimental run. Measurements were made relative to the first three minutes to be consistent across all samples and experimental runs as concerns were that the system may not have returned fully to equilibrium in last three minutes of the recording for the more dense samples as the mean of the last three minutes was not always equal to zero.

The displaced section of the tracer's displacement was isolated and a histogram of

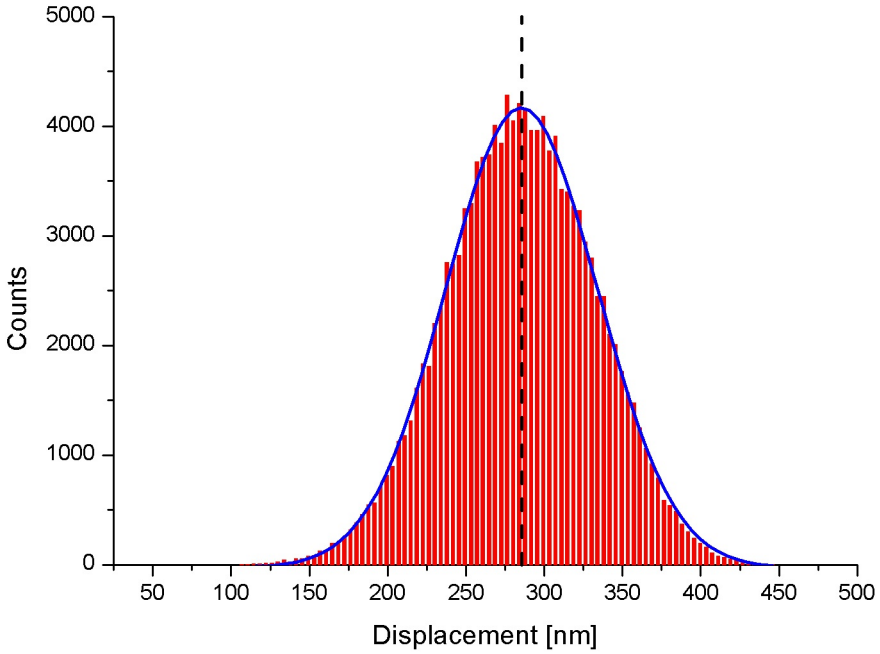


Figure 5.6: Typical histogram of the fluctuations of the tracer particle around its mean displacement for a sample of $\phi = 0.30$ and a drag speed of $v = 6.0\mu ms^{-1}$ corresponding to a $Pe = 130$. The blue line is the Gaussian curve that was fitted to the histogram and the black dashed line indicates the mean displacement of the particle in the optical trap.

the fluctuation around its average position plotted, figure 5.6. A Gaussian curve was fitted to the fluctuations and the mean displacement and its associated error determined for each experimental run.

### 5.4.2 One Point Active Micro-Rheology Results

Using the displacement histograms to determine the mean force that was exerted upon the tracer particle by the colloidal suspension and the generalised Stokes-Einstein, equation 5.4, the microviscosity as a function of Péclet number was calculated for each volume fraction.

The microviscosites calculated were normalised by the bare solvent viscosity, $\eta_0$, and plotted as a function of Péclet number on a *log-log* plot.

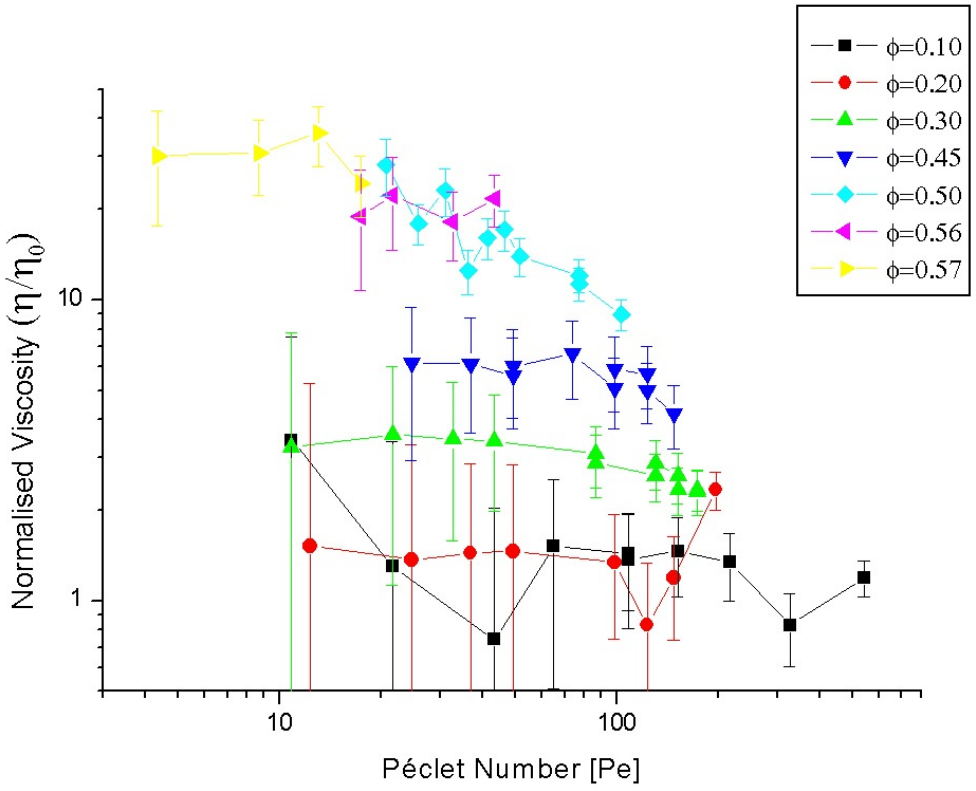


Figure 5.7: Normalised active microviscosities of a series of colloidal suspensions as a function of Péclet number

A description of the error analysis that was used to determine these results can be found in Appendix C. The measurement and analysis of volume fractions $\phi = 0.10$, $\phi = 0.56$ and $\phi = 0.57$ was carried out by *Dr. Laurence Wilson*. The measurement and analysis of $\phi = 0.19$, $\phi = 0.45$ and $\phi = 0.50$ were carried out by myself. The measurement of $\phi = 0.30$ was carried out by myself and analysed by *Dr. Laurence Wilson*.

Before the data can be interpreted and compared with macroviscosity the division between the high and low shear regimes should be considered.

A good division between the two regimes can be found by considering the time scales associate with the interparticle interactions. The macro-rheological definition of Péclet number in Chapter 4, equation 4.17, is:

$$Pe = \frac{\tau_B}{\tau_{\dot{\gamma}}}. \tag{5.6}$$

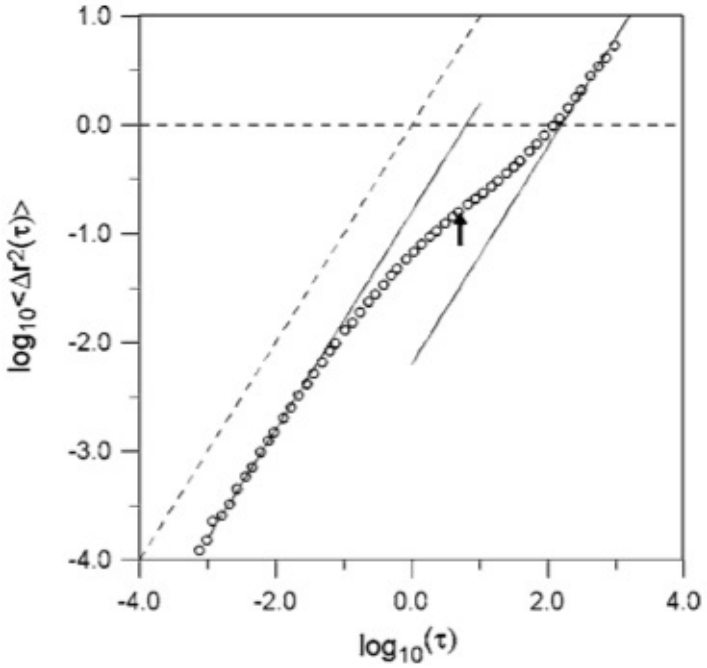


Figure 5.8: Reproduction of mean squared displacements for an ideal dilute suspension found in [6], where the arrow at the inflection point indicates a measure of the cage lifetime.

Considering the Brownian time $\tau_B$, *"the time it takes a single particle to diffuse a distance of its own radius in bare solvent"* would be,

$$\tau_B = \frac{a^2}{6D_0} = \frac{\pi\eta_0 a^3}{k_B T}. \tag{5.7}$$

Another time scale is the so-called 'cage' lifetime. In a suspension a single particle will be surrounded by a collection of nearest neighbours that can be described as a cage around it. The time it takes for this particle to diffuse into another cage is referred to as the cage lifetime, $\tau_{Cage}$. It was found in [6] that $\tau_{Cage} \approx 4\tau_B$ for $\phi < 0.50$. For volume fractions of greater than $\phi = 0.50$ the cage lifetime, $\tau_{Cage}$ diverges to be much greater than $4\tau_B$.

The length scale of the 'cage' can be determined by using the root mean squared displacements of the particles at the time equal to $\tau_{Cage}$, figure 5.8.
The time indicated can be interpreted as the point at which the 'caged' particle comes between two particles of the cage, in effect half a cage length. Therefore 'size' of a cage can be described as being $R_{Cage} = 2\sqrt{\langle \Delta r^2(\tau_{Cage})\rangle}$. The size of the cage was also found to be fitted to $R_{Cage} = (1.1 - 1.8\phi)a$ for volume fractions $\phi < 0.50$.

To apply this information to define a Péclet number at which shear thinning will occur can be found by considering the time it will take for a trapped particle to be dragged with speed $U$ to traverse through a single cage,

$$\tau_{Probe} = \frac{R_{Cage}}{U}. \tag{5.8}$$

It stands to reason that shear thinning will occur when the tracer particle is being dragged through the suspension faster than it would diffuse into a new cage;

$$\begin{aligned} \tau_{Probe} &> \tau_{Cage} \\ \Rightarrow \tau_{Probe} &> 4\tau_B \\ \Rightarrow \frac{R_{Cage}}{U} &> \frac{4a^2}{6D_0}. \end{aligned} \tag{5.9}$$

Substituting for $R_{Cage}$ and replacing and rearranging equation 5.5 for $U$ can define a Péclet number at which we expect shear thinning to occur,

$$Pe_c > 3.3 - 5.4\phi. \tag{5.10}$$

The critical Péclet numbers can be found in table 5.1 although for $\phi > 0.50$ the values cannot be viewed as definitive due to the divergence of the cage lifetime.

| $\phi$ | $Pe_c$ |
|---|---|
| 0.10 | 2.76 |
| 0.20 | 2.22 |
| 0.30 | 1.68 |
| 0.45 | 0.87 |
| 0.50 | 0.60 |
| 0.56 | 0.28 |
| 0.57 | 0.22 |

Table 5.1: Péclet numbers above at which shear thinning is expected to occur for a suspensions of hard-sphere colloids.

All the measurements made in figure 5.7 are above these thresholds for their respective volume fractions. this means that we are in fact in the high shear viscosity plateau.

The viscosities in figure 5.7 are mostly constant with a few caveats that shall be addressed in this section.

It can be seen that in the shear thinned viscosity plateau (high Péclet number data) increases with volume fraction and appears to be converging to a maximum located at

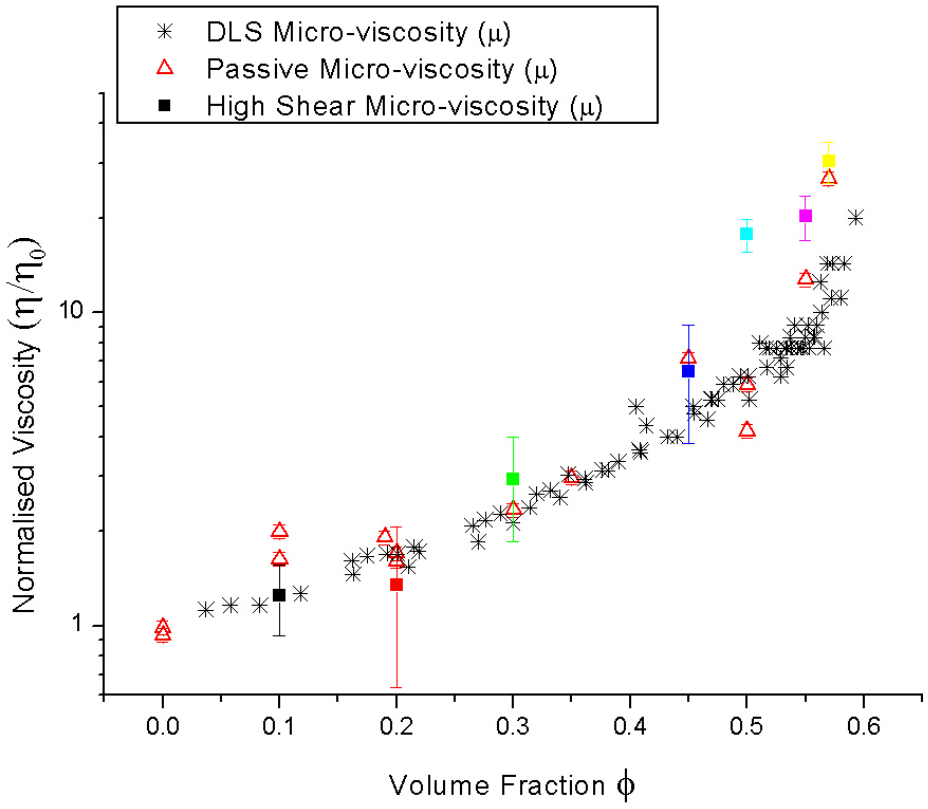


Figure 5.9: Normalised active and passive microviscosities of hard spheres plotted as a function of volume fraction determined using optical trapping techniques. Passive optical tweezer data and DLS from [5] has also been plotted for comparison. The colours of the high shear data matches the colours used for the samples in figure 5.7 for easy identification and comparison.

the glass transition. For Péclet numbers greater than 50 no data is presented for volume fractions $\phi = 0.56$ and $\phi = 0.57$. This is because that at these high drag speeds the tracer particle was pushed out of the trap.

To determine the active microviscosity of the suspensions their means were calculated. Figure 5.9 shows the measured active microviscosities as a function of volume fraction alongside the passive optical tweezer data and DLS data showing the passive microviscosity of hard sphere colloidal suspensions.

The high shear active microviscosity can be seen to be greater than both the passive micro and macroviscosities in the higher volume fractions. For volume fractions $\phi \lesssim 0.30$ the passive and active microviscosities are indistinguishable from each other within experimental uncertainties and as such any measurement of shear thinning between these two regimes is questionable. It can also be noted that the error on

the active microviscosities for the higher volume fractions is less than those for the passive microviscosity.

It is perhaps no surprise that the active microviscosity does not agree with the passive viscosities as the active case is being sheared or perturbed in some way that induces flows in the sample, whereas passive rheology experiments do not. However it does confirm that we expect the active microviscosity to be greater than the passive viscosities.

A direct comparison to the active macroviscosity can be made to the work by Phan *et al.* [18] who has measured both the high (shear thinned) and low shear macroviscosities of hard sphere suspensions. Figure 5.10 shows the shear thinned macroviscosities measured by Phan *et al.* as a function of volume fraction alongside the measured active microviscosities presented here.

We can see that the active microviscosities measured at above $Pe_c$ using the optical

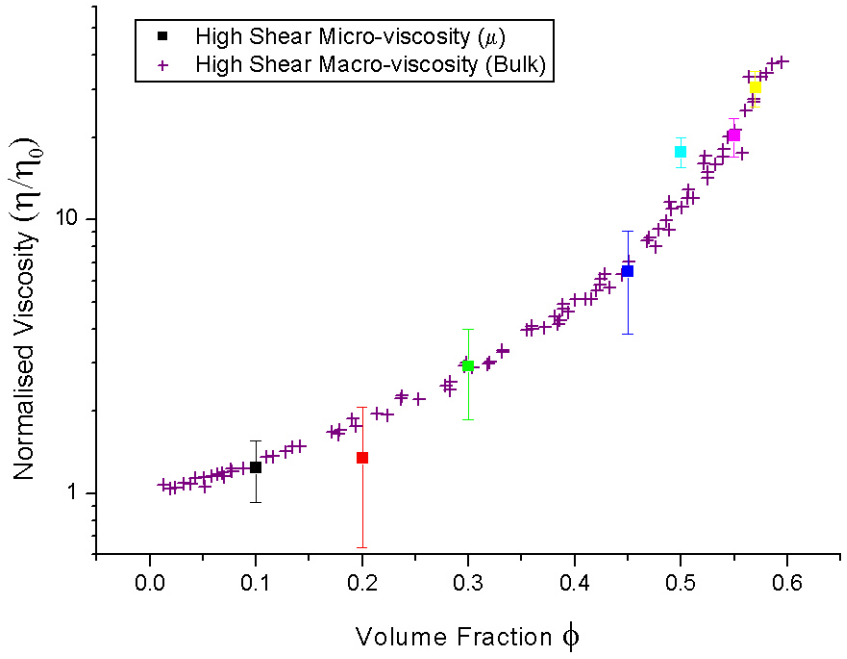


Figure 5.10: Active macro- and microviscosities of shear thinned hard sphere colloidal suspensions as a function of volume fraction, where the colours of the microviscosities match the volume fractions presented in figure 5.7.

tweezers are in good agreement with measurements of the macroviscosities in the equivalent regime.

### 5.4.3 Conclusions from the High Shear Limit

The measurement of the active microviscosity of a hard sphere suspension found no evidence of shear thinning below a volume fraction of $\phi = 0.30$ due to being indistinguishable from the passive microviscosity, $\eta_{\mu}^{(Passive)}$.

All the active microviscosities are in good agreement with shear thinned macroviscosities for the same range of Péclet numbers which can be found in the literature.

## 5.5 Low Shear Regime

The previous section showed that the optical tweezers can be used to measure the microviscosity at Péclet numbers where the suspension is expected to experience shear thinning. At lower Péclet numbers the viscosity is expected to be greater. Being able to measure the low shear plateau with optical tweezers would give a microrehological tool that could measure the full range of microviscosities expected for hard sphere suspensions.

The measurement of the viscosity will come from the tracer particle impacting the bath particles, forcing the bath particles along the path of the tracer particle to yield and diffuse around it.

This constant velocity dragging is in stark contrast with constant force optical tweezers, where in this slow shear regime the tracer particle would have to diffuse around the bath particles rather than continue along its drag direction or wait until the bath particles diffuse out of its path.

All material in this section was collected, measured and analysed by myself.

### 5.5.1 Low Shear Experimental Method

The motor used to drive the stage for the high shear experiments had a minimum drive speed of $0.1\mu$m s$^{-1}$ which corresponded to a minimum Péclet number of approximately 2.5. A slower motor was required to drive the stage if Péclet numbers less than 1 were to be reached.

A piezo actuator was mounted to the stage instead of the motor and a waveform signal generated to drive the translation displacement. An initial problem with driving the piezo at low frequencies was that the motion of the stage and hence the trapped particle appeared to be stepping. The source of the stepping was found to be the

waveform signal generator and not the piezo actuator [71]. The waveform generator was found to digitise the voltage signal being sent to the piezo rather than sending an analogue stream of voltages. To smooth out the digitised signal an integrating circuit was designed and built by the in house electronics technicians, figure 5.11.

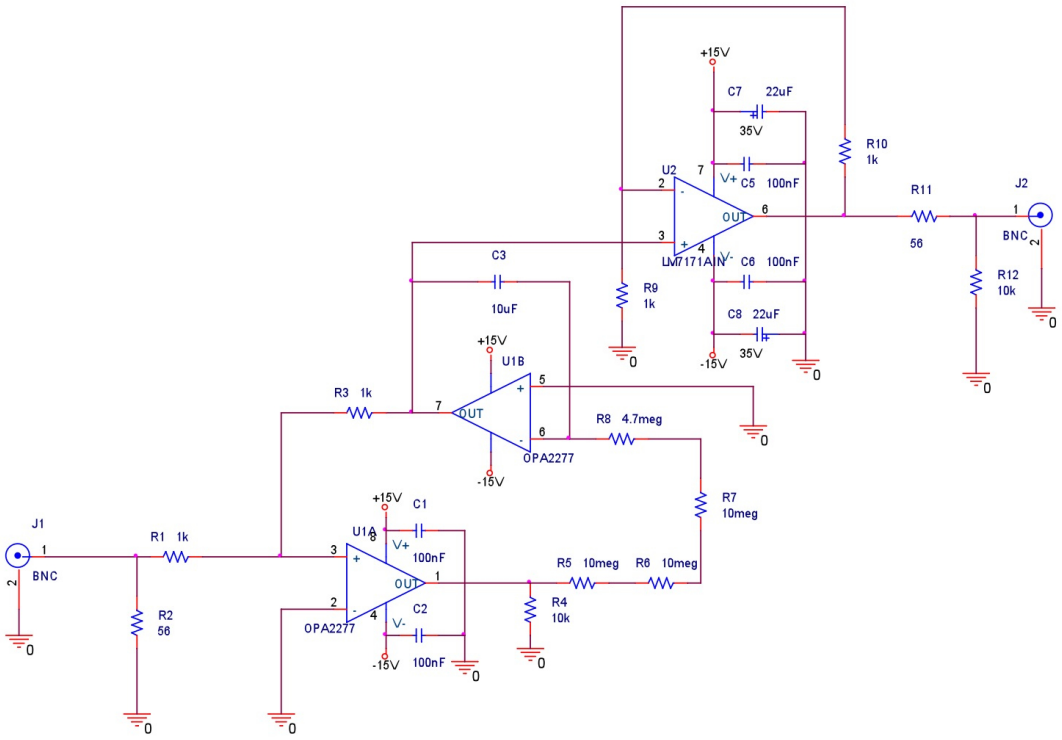


Figure 5.11: Circuit diagram of the integrating circuit that was used to smooth the digitised voltage signal from the waveform generator.

To confirm that the circuit was smoothing the motion of the piezo the laser focus of the optical tweezers was scanned through a tracer particle that had become stuck to the coverslip of a sample cell. The measured output signal should be the same as that presented in [31], [23] which can be also used to measure the non-linear response of a detector, figure 5.12. With the motion of the piezo driving the stage smoothly the low shear microviscosity could be measured by the optical tweezers.

A range of volume fractions were prepared to correspond with the previous data sets for the high shear viscosity measurements. In addition a very dense volume fraction $\phi = 0.62$ was made, this dense glassy sample was used to establish if slow dragging

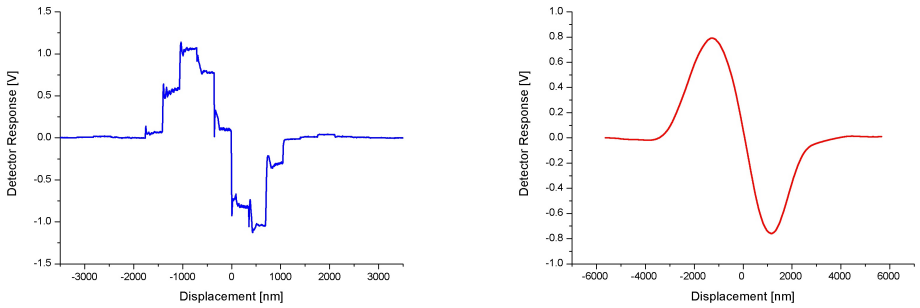


(a) (b)

Figure 5.12: Detector response as the laser focus is passed through a tracer particle stuck to the surface of a coverslip (a) without the integrating circuit and (b) with the integrating circuit.

was possible in the glass phase. Normally the force needed to make the system yield in such a sample would have pushed the tracer particle out of the trap. The samples were loaded into bucket cells as the samples needed to be kept for long periods of time. The samples were placed on the tweezers, the condenser lens focussed and the sample left to equilibrate. The focussing of the objective and condenser, the selection of a single tracer particle and sample equilibration was carried out in the same manner as has already been described in the high shear experiments. With a tracer particle trapped the particle was also held in position for the first and last 3 minutes of the recorded run. The piezo was driven by an oscillating triangular wave with a frequency that would move the particle with a Péclet number of 10 or less. The particle was translated with a speed slow enough that the area that had been perturbed by the particle had time to relax and return to equilibrium before the particle traversed through the same region on the return journey. As such hysteresis effects were negligible provided the data analysed was not located at a point where the particle experienced a change in direction, figure 5.13. The driven fluctuations of the particle's motion were isolated and analysed in a similar manner to the high shear measurements.

### 5.5.2 Micro-Rheology Results (Low Shear)

The active microviscosities for $0.4 < Pe < 10$ for volume fractions $\phi = 0.10$ to $\phi = 0.62$ are shown in figure 5.14.

The dotted line shown in figure 5.14 corresponds to a conservative estimate of the operational systematic error associates with the optical tweezers, where the drift in

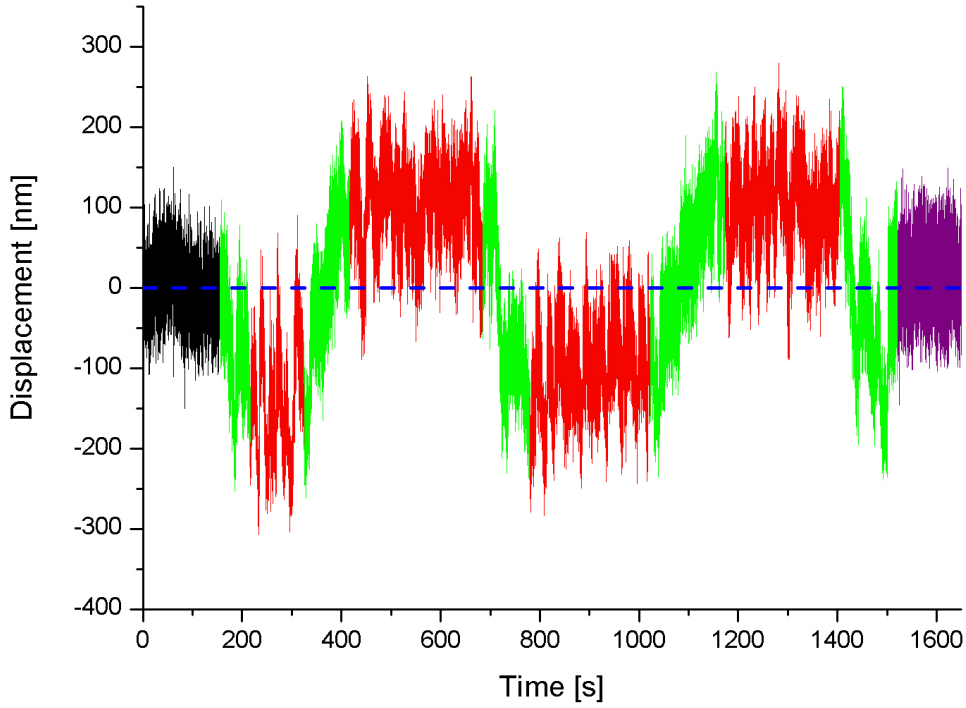


Figure 5.13: Displacements of a trapped particle with the stage being driven by a triangular waveform. Only sections marked in red were used to determine the displacement form equilibrium. The black section was used to give the base line and the difference between the black and purple sections was used in the determination of how much the centre of the optical trap drifted with time.

the optical trap is $10nm$ over an extended time period. The systematic error was determined only after the large number of data sets presented here and elsewhere had been obtained. Full details of how this was determined can be found in Appendix D. Values in this region of uncertainty should be treated with caution. A method of determining the validity of these measurements will be described at the end of this chapter.

The initial feature of figure 5.14 are the size of the error bars associated with each data point, particularly for the data corresponding to volume fractions $\phi = 0.10$ and $\phi = 0.20$. In these two data sets the values cross-over and appear to be identical.

The low shear viscosities appear to be increasing as is expected and if the shapes of the data sets are to be believed they are exhibiting shear thinning in the region of $2 < Pe < 10$.

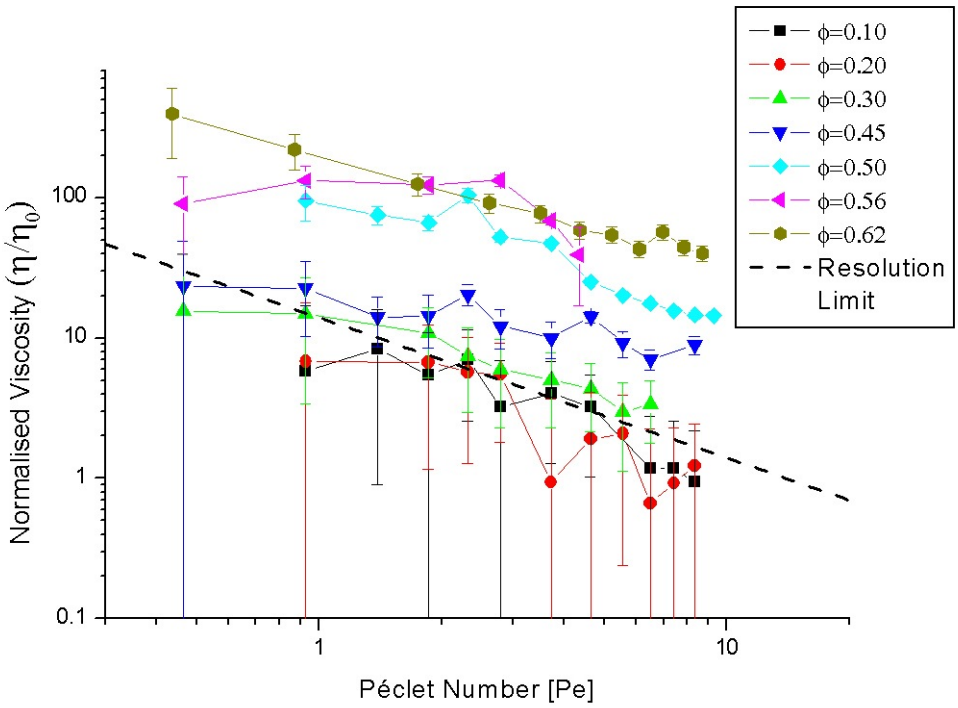


Figure 5.14: Active microviscosities, $\eta_\mu$, for several volume fractions in the low shear regime measure by constant velocity optical tweezers. The diagonal dotted line represents the systematic uncertainty associated with the instrument.

The glassy sample, with volume fraction $\phi = 0.62$, appears to be showing the yielding behaviour that would expected in a colloidal glass.

A consistency check on the data sets is to compare how well the low shear data matches up with the high shear data for the same volume fractions. Due to the size of the error bars and the closely spaced data points each volume fraction has been plotted separately, with the exceptions of the data sets for volume fractions $\phi = 0.55$, $\phi = 0.56$, and $\phi = 0.57$ which have all been plotted on the same graph, figures 5.15, 5.16, 5.17 and 5.18. A graph with all the data can be found in Appendix E.

The individual data sets show good agreement between the two overlapping regimes, *i.e.* $5 < Pe < 30$.

In [72] it was shown that the macroviscostiy of hard-sphere suspensions can be described by the following Krieger-Doughery equation,

$$\eta(Pe) = \frac{\eta_\ell - \eta_\infty}{1 - \left(\frac{Pe}{Pe_c}\right)^2} + \eta_\infty. \tag{5.11}$$

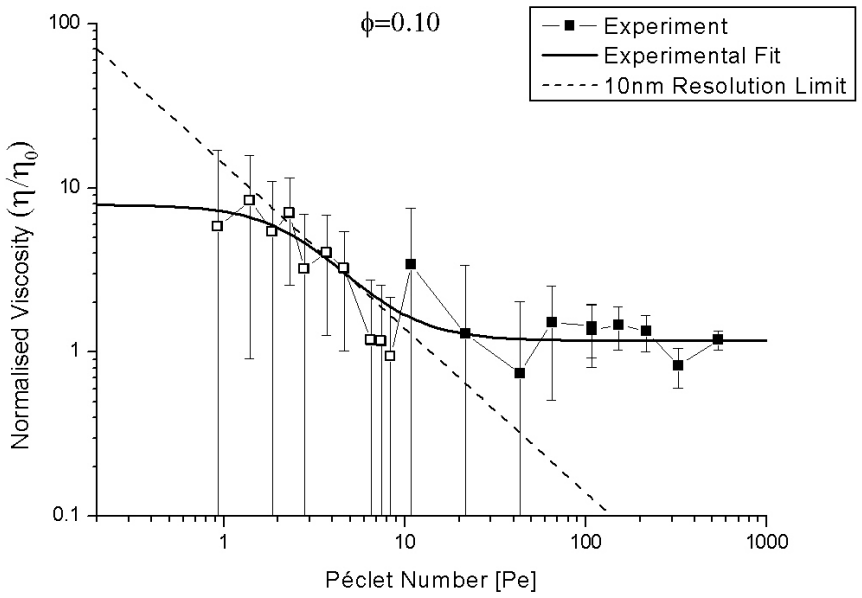


(a)

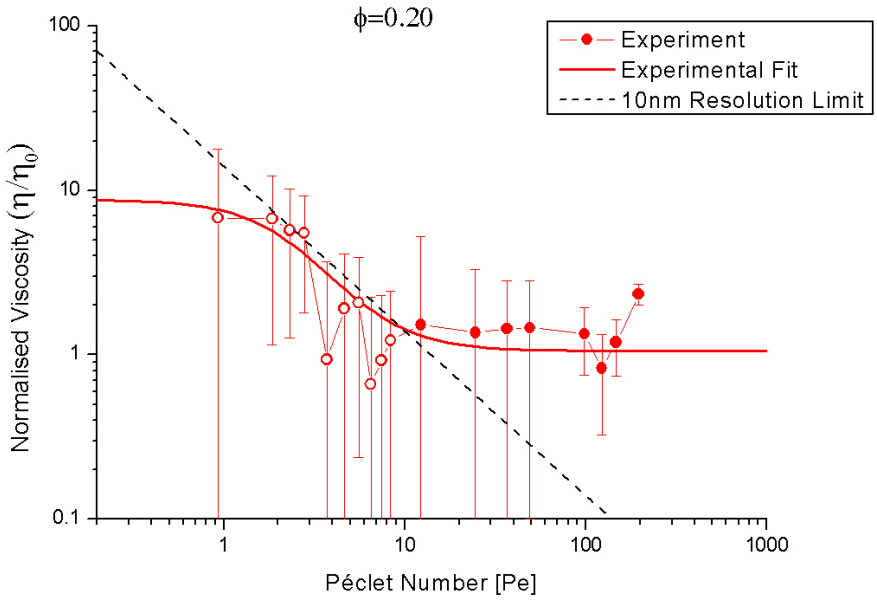


(b)

Figure 5.15: All active microviscosity, $\eta_{\mu}^{(Active)}$, measurements for volume fractions (a) $\phi = 0.10$ (b) $\phi = 0.20$. Low shear data plotted as open symbols.

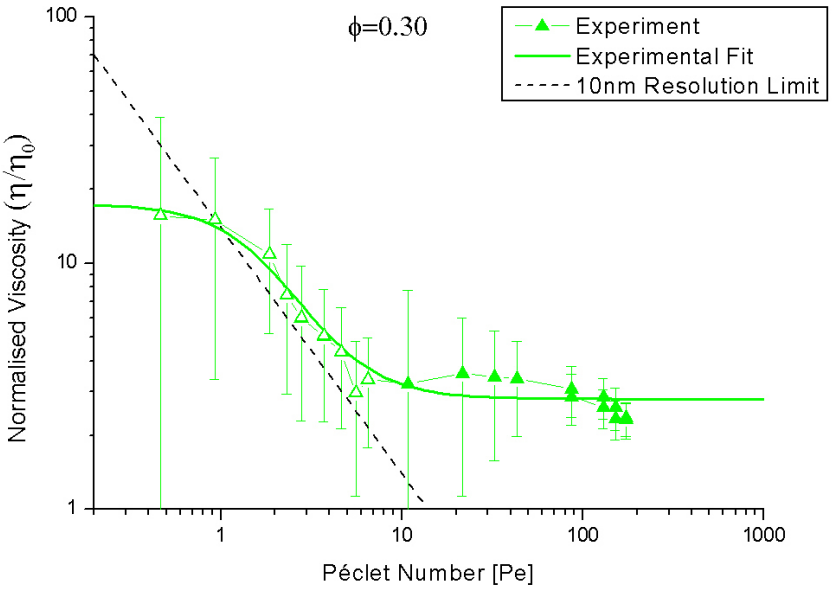


(a)

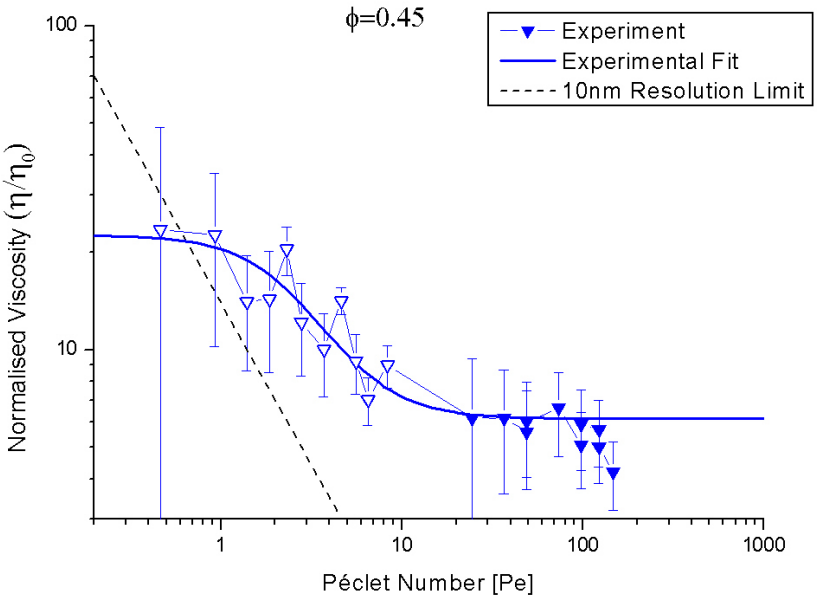


(b)

Figure 5.16: All active microviscosity, $\eta_{\mu}^{(Active)}$, measurements for volume fractions (a) $\phi = 0.30$ (b) $\phi = 0.45$. Low shear data plotted as open symbols.

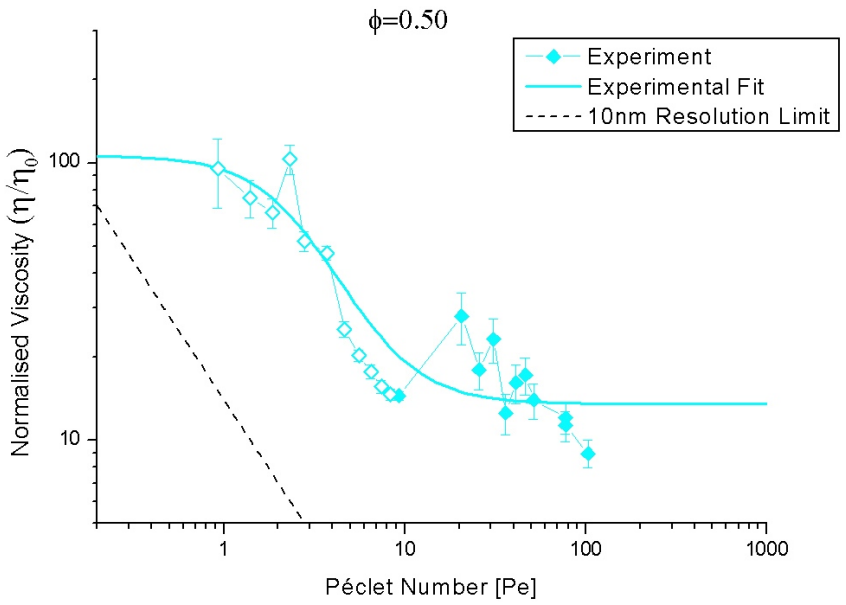


(a)

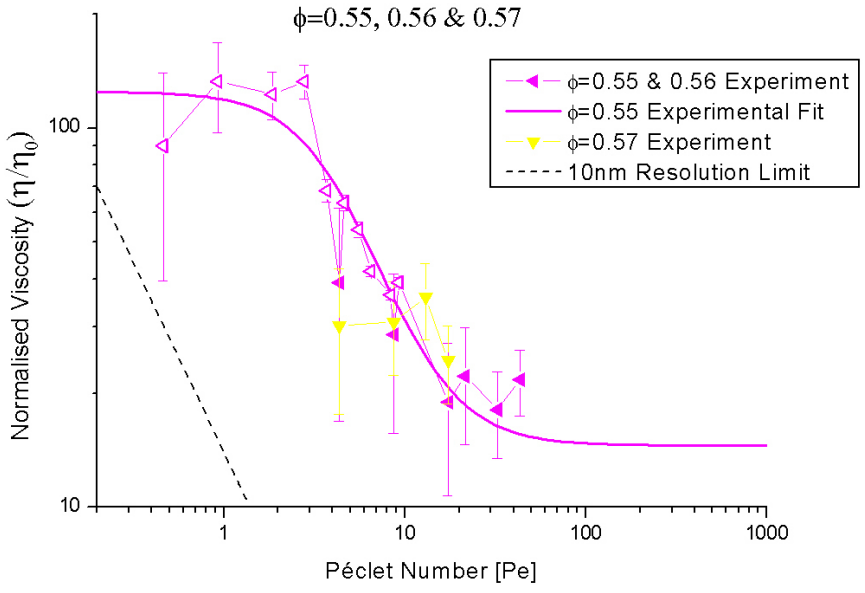


(b)

Figure 5.17: All active microviscosity, $\eta_{\mu}^{(Active)}$, measurements for volume fractions (a) $\phi = 0.50$ (b) $\phi = 0.55$, $\phi = 0.56$ and $\phi = 0.57$. Low shear data plotted as open symbols.

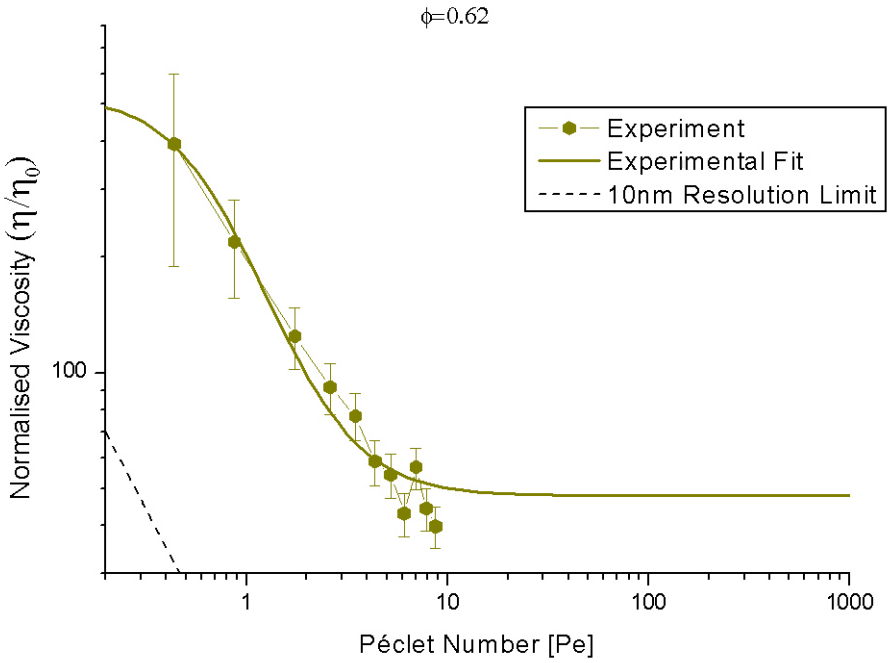


Figure 5.18: All active microviscosity, $\eta_{\mu}^{(Active)}$, measurements for volume fraction $\phi = 0.62$. Low shear data plotted as open symbols.

Where $\eta(Pe)$ is the effective viscosity of the suspension as a function of Péclet number, $\eta_{\ell}$ is value of the low shear viscosity plateau, $\eta_{\infty}$ is the value of the high shear viscosity and $Pe_c$ is the value at which the curve turns and can be associated with our definition the onset of shear thinning.

A fit was carried out to the complete data sets with volume fractions of $\phi = 0.10$, $\phi = 0.20$, $\phi = 0.30$, $\phi = 0.45$, $\phi = 0.50$, $\phi \approx 0.55$ and $\phi = 0.620$ using the Krieger-dougherty viscosity equation where the free parameters were, $\eta_{\ell}$, $\eta_{\infty}$ and $Pe_c$. The motivation to leave the critical Péclet number, $Pe_c$, free was to determine the accuracy of the values predicted in table 5.1.

### 5.5.3 High Shear Fit Results

The values determined by the fits for the high shear viscosity, $\eta_{\infty}$, for the data sets agree with the values determined in the previous section (as would be expected) but has reduced the error on the higher volume fraction, figure 5.19.

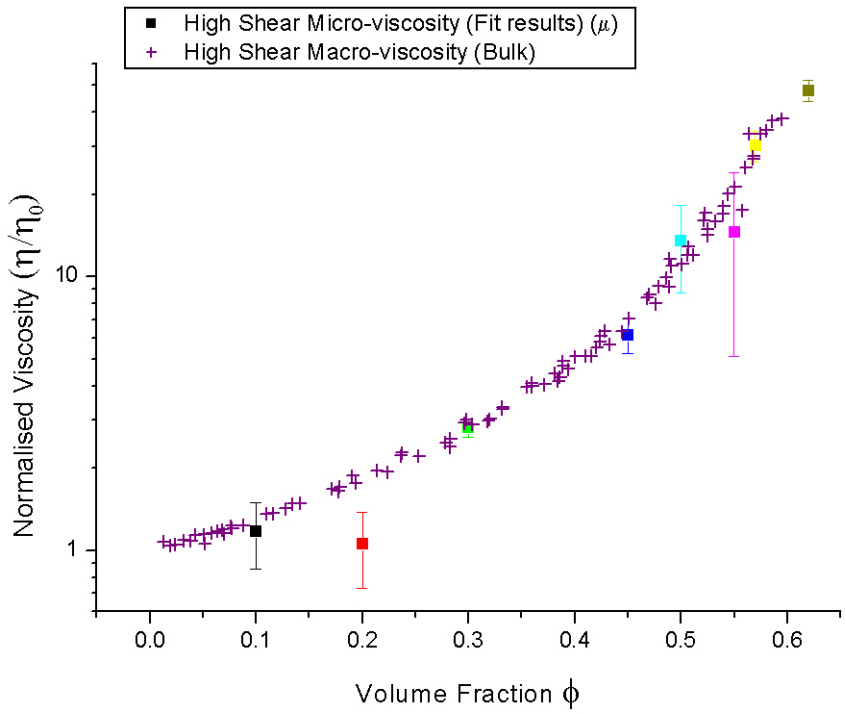


Figure 5.19: Active macro- and microviscosities of shear thinned hard sphere colloidal suspensions as a function of volume fraction, where the microviscosity values have been determined using a fit to equation 5.11.

### 5.5.4 Low Shear Fit Results

The values for the low shear microviscosity, $\eta_\ell$, determined by the fit are shown in figure 5.20 along side the low shear macroviscosities determined by Phan *et al.* [18] for a similar range of volume fractions.

It can be seen that all the microviscosities measured do not agree with the macroviscosity with the exceptions of the volume fractions $\phi = 0.45$ and $\phi \approx 0.55$, where the $\phi = 0.45$ is greater than macrorheology.

Whilst it may be that for low shear rates the microviscosity will not agree with the low shear macroviscosity for colloidal hard spheres, we should consider any reasons why the microviscosity could be overestimated. In a macro-rheology experiment a constant stress, $\sigma$ or a constant shear rate, $\dot{\gamma}$ is generally applied to the suspension. The viscosities measured by these two methods are identical for hard-sphere suspensions in both the high and low shear regimes.

Using optical tweezers for micro-rheology the analogous processes to the two macro-rheological methods would be to drag a particle through the suspension with constant

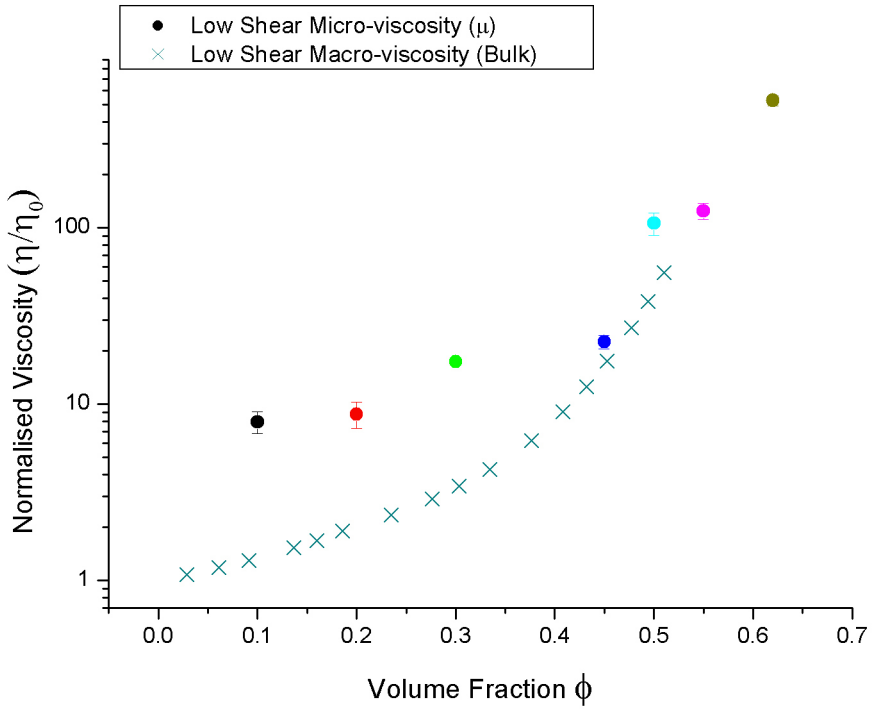


Figure 5.20: Low shear active macro- and microviscosities of hard sphere colloidal suspensions as a function of volume fraction, where the colours of the microviscosities match the volume fractions presented in figures 5.15, 5.16, 5.17 and 5.18

.

force (constant stress) or constant velocity (constant shear rate). The mode used here was dragging with constant velocity. As outlined in Chapter 3 there are fundamental differences in how the trapped particle will interact with the bath particles in constant velocity and constant force modes. As such the question has to be asked, would the two modes measure the same microviscosities?

If we consider how Péclet number is defined; for constant velocity it is,

$$Pe_{\mu}^{U} = \frac{2Ua}{D_0}. \tag{5.12}$$

and for constant force is is typically defined as [68],

$$Pe_{\mu}^{F} = \frac{Fa}{k_B T}. \tag{5.13}$$

At high Péclet numbers at constant velocity ($U \gtrsim D_0$), the trapped particle will be dragged through the suspension and will 'bulldoze' its way through the suspension,

breaking through many cages in an experimental run. For the same range of Péclet numbers but when the trapped particle is being dragged with constant force, specifically when $F \gtrsim k_B T$, the trapped particle may slow down slightly on impact with a bath particle but will be dragged with such force that it to will also effectively 'bulldoze' its way through the suspension.

Therefore in the high shear regime, where the suspension is shear thinned, constant force dragging experiments and constant velocity dragging experiments with optical tweezers will measure the same active microviscosity,

$$\eta_\mu^{(F)}(Pe \gg 10) \equiv \eta_\mu^{(U)}(Pe \gg 10). \tag{5.14}$$

For low Péclet numbers at constant velocity ($U \lesssim D_0$) the trapped particle will no longer 'bulldoze' its way through the suspension, it will instead be moving so slowly that the bath particles can diffuse around it, or in the case of dense samples the bath particles will push the trapped particle back into a stronger optical potential until the trapped particle is able to exert a force large enough to make the bath particles yield to its motion, figure 5.21 (a)-(d).

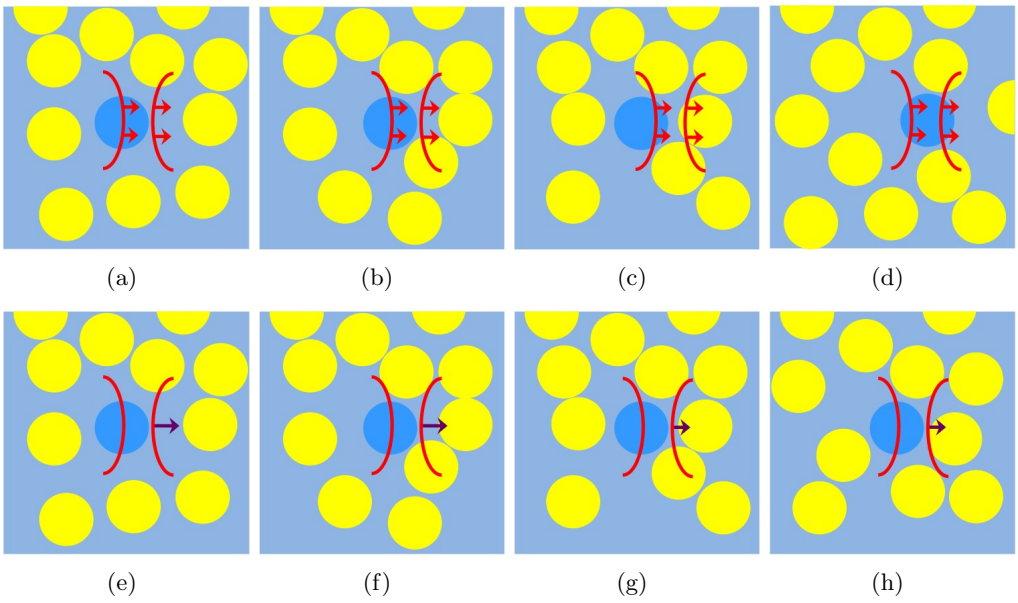


Figure 5.21: Examples of trapped particles being dragged through suspensions in the low shear regime at constant velocity (a)-(d) and at constant force (e)-(h).

In the case of constant force at low Péclet numbers the trapped particle will be moved but will never exert a yielding force on a bath particle. Instead the tracer will always slowly diffuse its way around the bath particle.

It is clear from the ways that the trapped particles interact with the bath particles that the constant velocity case will measure a greater microviscosity than the constant force case, particularly if the trapped particle is exerting a yield force on the bath particles. Specifically the constant velocity case will measure a microviscosity that is related to the constant force microviscosity by [68], where both viscosities have been normalised by the viscosity of the solvent,

$$\frac{\eta_\mu^{(U)}}{\eta_0} = 2\frac{\eta_\mu^{(F)}}{\eta_0} - 1. \tag{5.15}$$

Whilst constant force and constant velocity measurements will not match which of either of them should match the macroviscosity?

For a constant stress macro-rheology experiment a stress is applied across the sample, where each bath particle will experience some stress. This is analogous to a constant force being applied to a trapped particle in one point micro-rheology experiments. In both cases the suspension is not made to yield until the stress applied places the sample in the high shear regime.

In a constant shear rate experiment for macro-rheology the bath particles will experience some force driving them along a specific direction but will also be free to move in both the vorticity and shear gradient directions. Whereas in the analogous constant velocity case for optical tweezers only the trapped particle has a drive direction and when the trapped particle encounters a bath particle the optical potential holds the tracer such that it cannot move in the 'vorticity' ($y$) or the 'gradient' ($z$) directions as the analogue could in the macro-rheological case. Instead the trapped particle has to push a bath particle out of its path. Second the optical potential allows the tracer to impart a yielding force if it has been held up for a long enough period of time. In the macro-rheological case it is unlikely that a single particle would impart a yield force on another particle, instead the particles are more likely to slip past each other and move either in the vorticity or gradient directions. If dense enough (*i.e.* a glass) the particles are likely to slip through the suspension as group.

For both of these reasons we can say that constant velocity optical tweezer micro-viscosity measurements are not truly analogous to constant shear rate macroviscosity measurements. As such if either of the two modes of the optical tweezers were to be used to compare to macro-rheology it should be experiments that have been made using constant force optical tweezers. Constant force optical tweezers apply a stress to a single particle in an analogous manner to bulk rheology where the stress is applied to the entire sample.

Figure 5.22 shows the microviscosities of the low shear microviscosity data presented in figure 5.20 that has been corrected, using equation 5.15, to give the values that

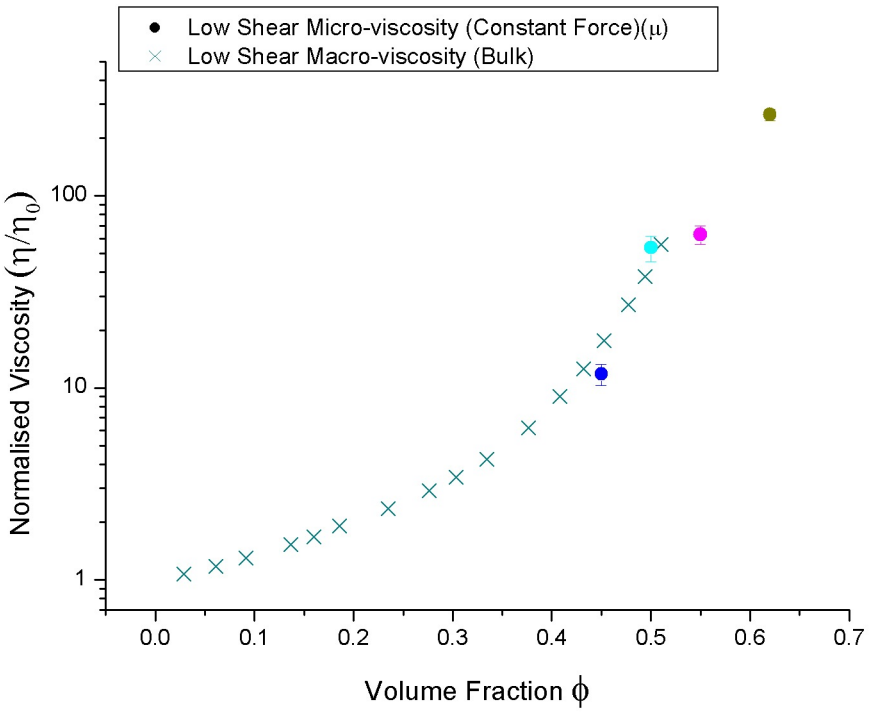


Figure 5.22: Low shear active microviscosities as a function of volume fraction if they had been measured using constant force optical tweezers instead, alongside the low shear macroviscosities.

constant force optical tweezers would have measured.

The low shear microviscosities for constant force match the low shear macroviscosities for $\phi \geqslant 0.45$. The values for volume fractions $\phi = 0.10$, $\phi = 0.20$ and $\phi = 0.30$ are questionable as their original measured values are in the region associated with the systematic resolution of the optical tweezers.

### 5.5.5 Critical Péclet Number Fit

The position at which the hard sphere suspensions are said to shear thin, given in equation 5.10, is not dependant on the mode in which the measurement is made. As such the values that were determined by the Krieger-Dougherty fits to the full data sets are shown in figure 5.23 alongside the line predicted by equation 5.10.

It is perhaps surprising that the prediction line fits so well to the data points that correspond to the the volume fractions $\phi = 0.10$, $\phi = 0.20$ and $\phi = 0.30$ when the low shear data in particular falls in the region associated with the systematic uncertainty of the optical tweezers. The data points that correspond to volume fractions $\phi \geqslant 0.50$ are

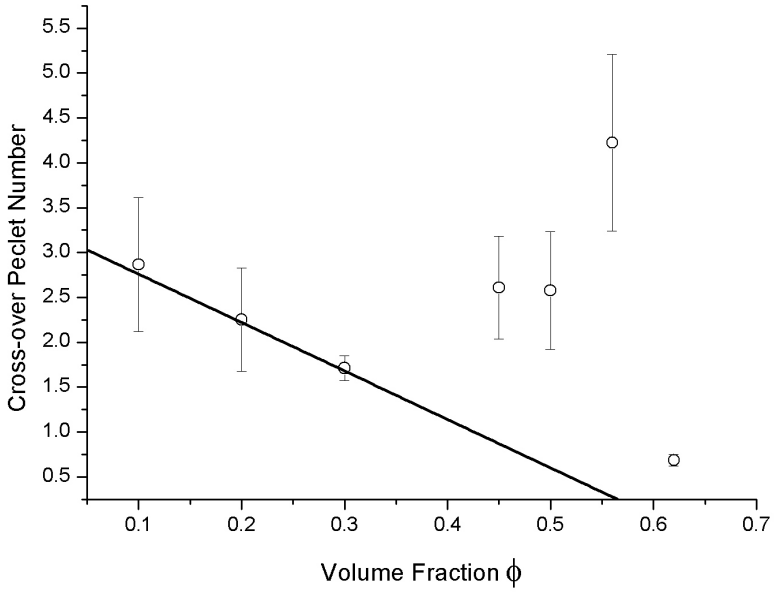


Figure 5.23: Critical Péclet number, $Pe_c$, determined from fits to the data sets as a function of volume fraction $\phi$. The black line is the prediction made by equation 5.10.

not expected to agree with equation 5.10 due to the divergence of the 'cage' lifetime at these volume fractions that was used to derive the equation. Of concern is the data point associated with a volume fraction of $\phi = 0.45$ that does not agree with the predicted value and is below the divergence threshold of the 'cage' lifetime. At time of production of this research no definitive reason can be given for this lack agreement to the prediction when the lower volume fractions (which maybe should not be expected to) agree so well with the prediction.

## 5.6 One Point Microviscosity Summary and Conclusions

One point micro-rheology can be used to measure the microviscosities of hard sphere systems for both passive and active systems.

The passive measurements for the microviscosity agree well with dynamic light scattering macroviscosity measurements carried out by van Megen [5].

Using optical tweezers to probe the active microviscosity, $\eta_\mu^{(Active)}$, of a hard sphere suspension is possible in in the high shear regime $Pe > 10$ for all volume fractions in the range $0.10 \leqslant \phi < \phi_g \approx 0.58$. However it is not possible to observe difference between the high shear active microviscosity and the passive microviscosity, $\eta_\mu^{(Passive)}$

for volume fractions $\phi \leqslant 0.30$ mainly due to the error associated with determining the size of the tracer particle that is used.

The measurement of the active microviscosity in the low shear regime, $Pe < 2$, was more complex. For agreement to be found with macroviscosities measured in the equivalent regime the microviscosity measurements had to be converted to the values that would have been determined if constant force tweezers had been used. Once the conversion had been made agreement of the low shear microviscosity with the low shear macroviscosity was found for volume fractions $\phi > 0.45$. The microviscosities below this threshold are all greater than their equivalent macroviscosities but these measurements are located in the regime associated with the operational systematic uncertainty of the optical tweezers, where the displacement needed for agreement with macro-rheology is less than or order of the average wandering displacement of the optical trap.

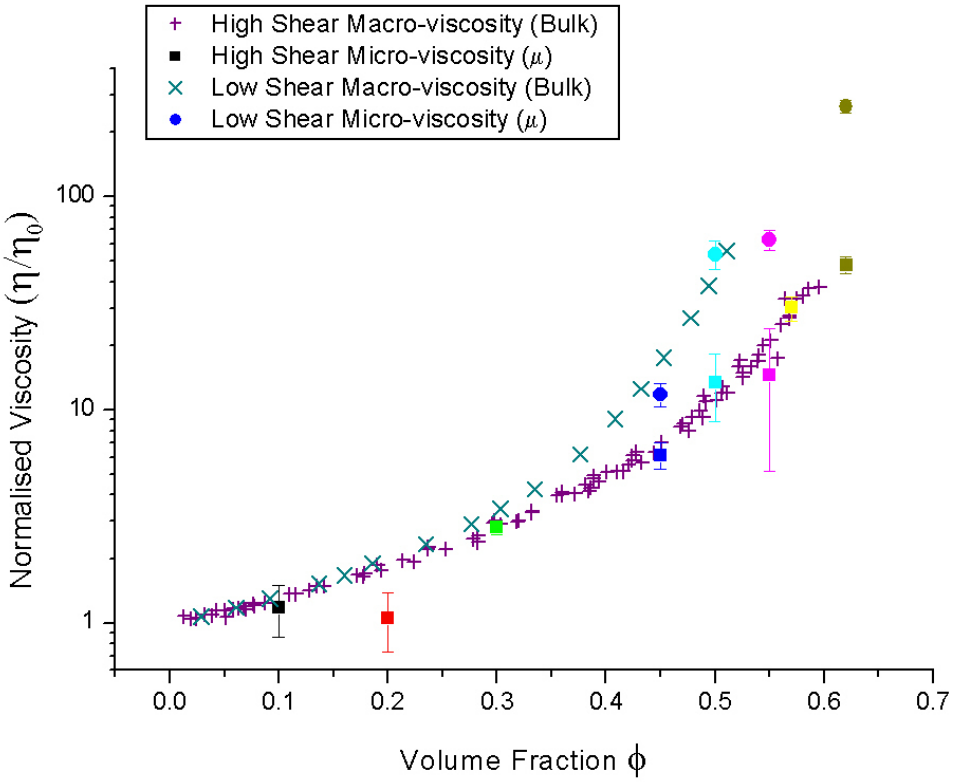


Figure 5.24: High and corrected low shear active microviscosities measured as a function of volume fraction, along side the macroviscosities for the high and low shear regimes.

### 5.6.1 Future Work

The measurement of the low shear active microviscosities for volume fractions $\phi \leqslant 0.30$ needs to be determined with more certainty than has been possible to do here. A system that could be used to measure these volume fractions would be to use a host solvent with a greater viscosity. Increasing the solvent viscosity would result in greater displacements of the trapped particle in the optical trap when being dragged allowing the active displacement to be resolved out with the region of systematic uncertainty. Complications with such a system arise with determining a liquid (or a mixture of liquids) with a great enough viscosity that could be used to index match (and density) the bath particles that would be used as the hard-sphere suspension used.

## 5.7 Shear cell

This section describes and experimental set-up that would use the optical tweezers to measure the microviscosity that single particle experiences whilst the rest of the sample is being sheared in an attempt to link the micro- and macroviscosities of hard spheres.

The macro-rheology of hard sphere colloid has been investigated using methods such as DLS, confocal microscopy and as stated in the preceding chapter through the use of commercial rheometers [73, 74, 75].

Besseling *et al.* [76] have used confocal microscopy in conjunction with a parallel plate shear cell to investigate a colloidal glass under steady shear. The colloidal particles were PMMA particles. The shear cell used consisted of two parallel plates that could be driven in anti-phase to one another creating a shear gradient between the two plates, see figure 5.25.

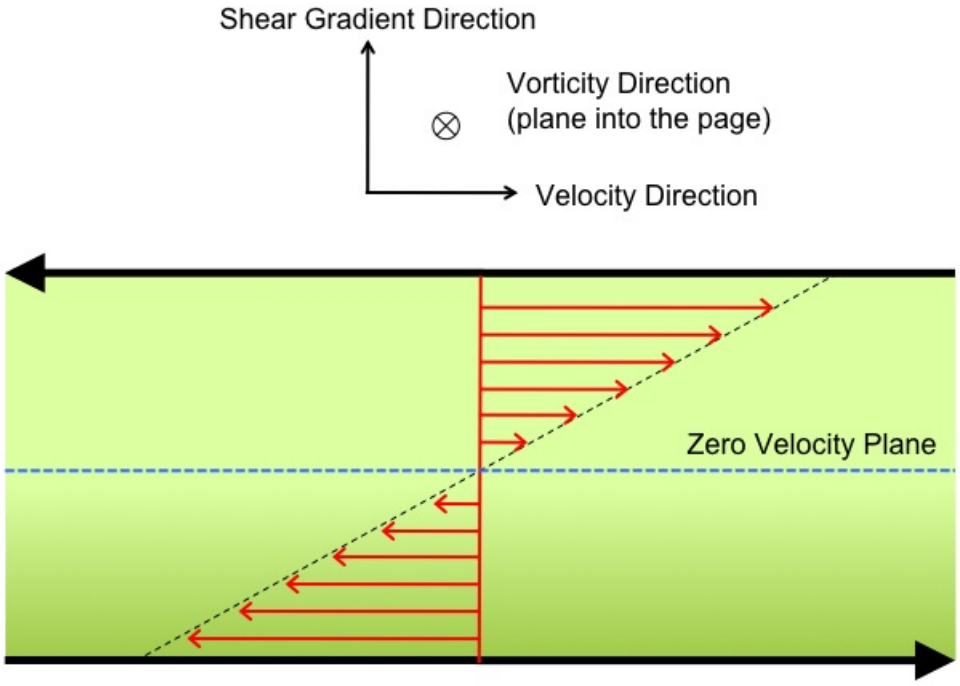


Figure 5.25: Schematic diagram stating the velocity, vorticity and shear gradient directions and illustrating the shear gradient that can be induced by a parallel plate shear cell.

Using a fast confocal microscope the particle positions could be tracked in three dimensions as as function of time. From the position information the trajectories of the particles when sheared were determined and the relaxation time, $\tau_\alpha$, and the

diffusion constant, $D$, was calculated. The measured shear-thinned diffusion was found be related to the shear rate by a power law, $D \propto \dot{\gamma}^{0.8}$. The bulk rheology of the colloidal glass was measured using a cone and plate rheometer and found to exhibit Hershel-Bulkey behaviour. Showing a contrast between bulk (macro-rheology) obtained from a rheometer and the micro-rheology determined by the confocal imaging.

Optical tweezers can be used to probe the micro-rheology of a material and have been used to measure the short-time diffusion of a single particle in a colloidal glass [24]. A logical step to gain more information on the forces that are exerted between the particles would be to optically trap a particle and measure the forces it experiences whilst the surrounding system is being sheared, figure 5.26. In this case the system would be actively sheared and the tweezers would be measuring the active micro-rheology of colloidal glasses.

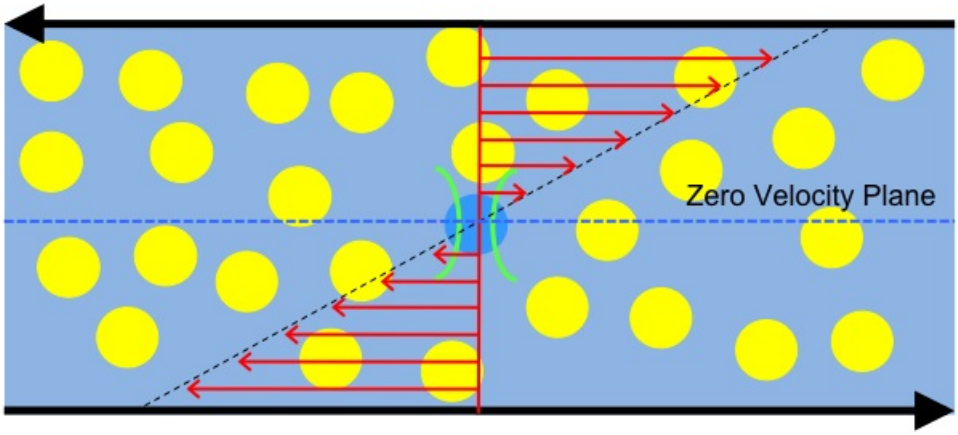


Figure 5.26: Schematic diagram showing colloidal suspension being sheared, with an optically trapped particle being held in the zero velocity plane.

### 5.7.1 Shear Cell Design

A suitable shear cell had to be designed[9] that would be compatible with the spatial and positional constraints of the optical tweezers. Copper clad silicone fibre board (the same material that is used for printed circuit boards) was used as it had a high rigidity and was manufactured with near uniform flatness. The rigidity is important as the plates must not buckle or bend to ensure that a uniform shear is applied. The flatness is crucial to ensure that the plates can be aligned parallel to each other to a high degree of accuracy. Apertures were cut in the fibre boards and thin glass coverslips were glued

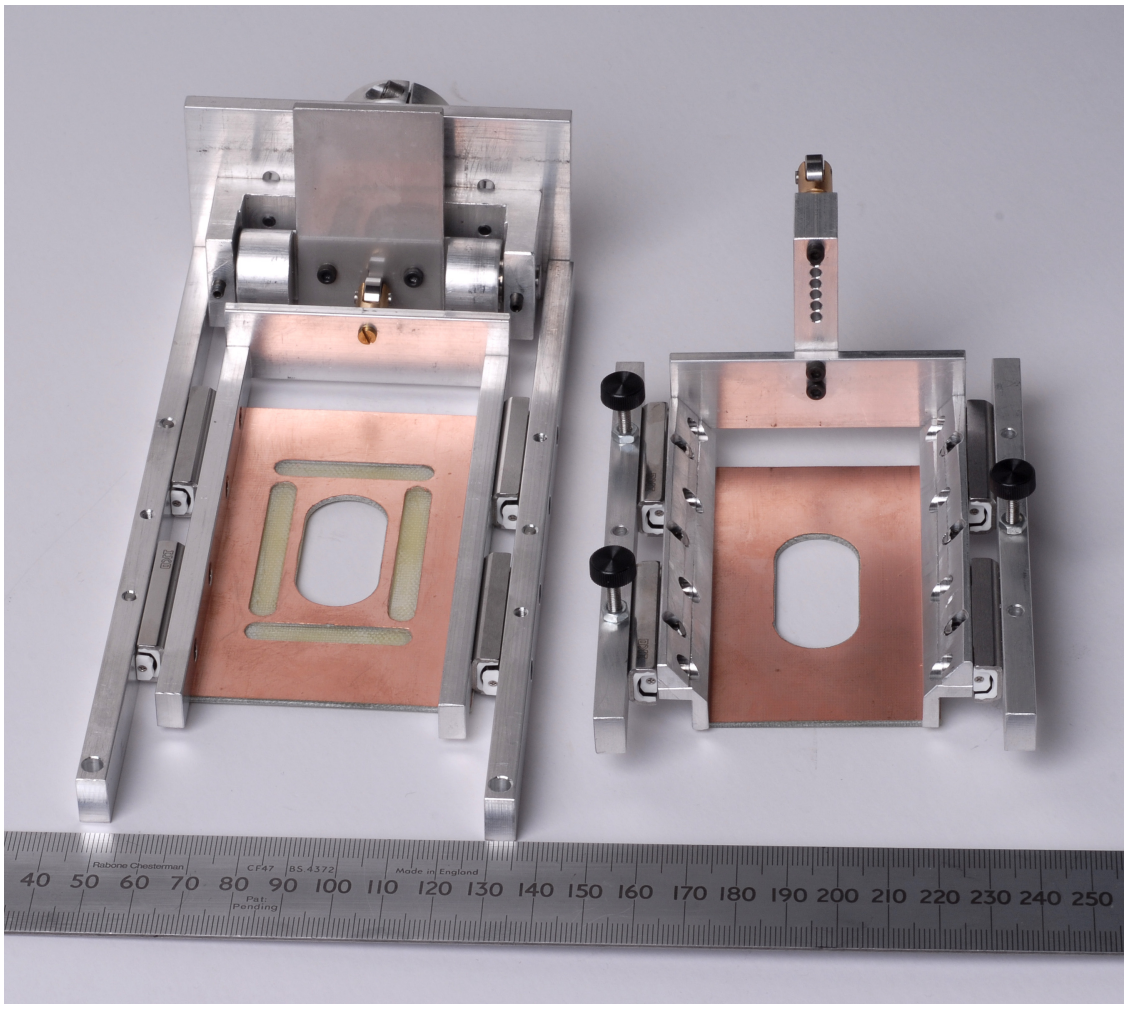


Figure 5.27: Picture showing the lower (left) and upper (right) plates of the shear cell designed for use with the optical tweezers.

over the apertures, figure 5.27. The ellipsoidal pits that can be seen in the lower shear plate on the left of figure 5.27 are solvent traps to ensure there is as little evaporation as possible of the sample when the shear cell was loaded. To ensure that there was no slip between the loaded suspension and the shearing plates, the coverslips were coated with a layer of colloidal particles using a spin-coater. The coverslips were held on the spin-coater and a dilute dispersion of colloidal particles were placed on the surface. The spin-coater rotated the cover-slip at speed such that the colloidal dispersion flowed across the surface of the coverslip and the host solvent evaporated off. The coating was then baked in place by placing the coverslips on a hot-plate for approximately

[9]The shear cell was designed and manufactured by *Mr. Andrew Downie* with input and suggested modifications made by myself.

30 seconds at a temperature of $100°C$. A check was made to ensure that coating the coverslips with a layer of colloidal particles did not affect the trapping power of the optical tweezers by creating a bucket cell with two coated coverslips. The bucket cell was filled with a dilute suspension of tracer particles suspended in the CHB/Decalin mixture. A measurement of the trap stiffness and sensitivity was made and compared to the calibrations described in Chapter 3 and found to be in agreement to within the error of the instrument.

The plates were mounted to linear bearings that had been fixed to a metal frame. The bearings were mounted such that they ran parallel to each other when in operation. The smooth running of these bearings was integral to the functional use of the shear cell, as such the entire shear cell was immersed in alcohol and cleaned using sonication prior to use.

To drive the upper and lower plates in anti-phase a lever connecting the upper and lower plates was used. The lever could be driven by a piezo actuator connected to a signal generator to produce oscillatory shear. Two springs were placed between the end of the lower plate and the shear cell's frame to provide the restoring force for the lower plate. The restoring force for the upper plate was provided by two springs located at the lever end of the shear cell, these springs were removable to facilitate the reloading of the cell. The displacements of each plate could be varied by changing the contact point of the plate with the lever. The lower plate was fixed to the shear cell's frame. To change the displacement that it could be driven at the height of the lever could be changed, figure 5.28(c).

The upper plate's displacement could be varied by changing the height at which the contact wheel was located 5.28(b). It could also be varied by changing the height at which the upper plate was mounted. This in practice was not ideal as a specific height of plate separation was normally wanted and that the maximum separation available was of the order of a few $mm$. The maximum separation was set by the working distance between the objective lens and the condenser lens of the optical tweezers.

### 5.7.2 Parallelity

The material that the shear plates were made of was chosen because of its high degree of flatness that would ensure that the two shear plates were as parallel as possible. Before every experiment the parrallelity of the plates had to be aligned. This was done using a confocal microscope.

As the coverslips had been coated with a layer of colloidal particles the layer could be imaged with the confocal to find the variation in the height of the plate across its surface. The general method, used on both plates was to focus on an area of the

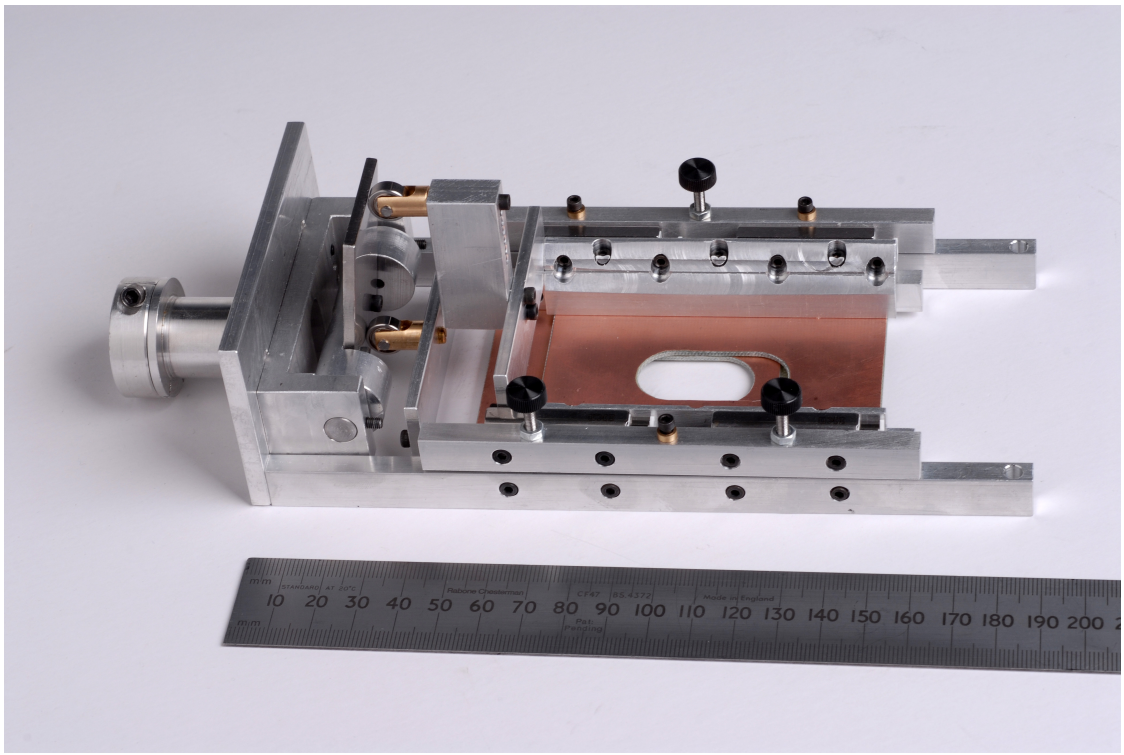


(a)

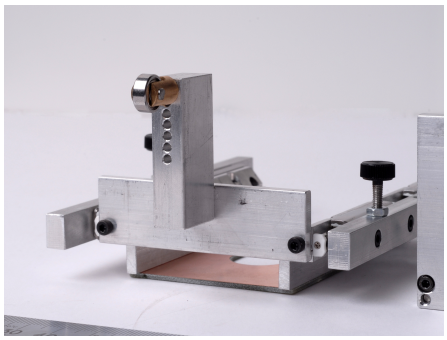

(b)

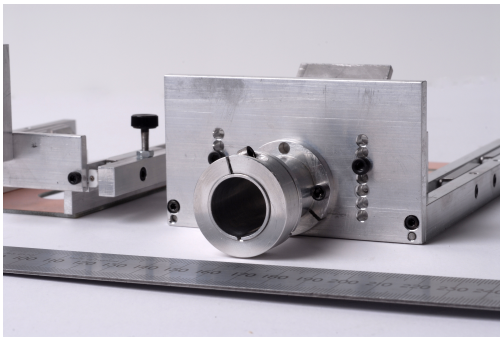

(c)

Figure 5.28: (a) Picture showing the assembled shear cell. (b) Picture showing the mounting positions for the contact wheel of the upper plate. (c) Picture showing the mounting positions of the driving lever.

coated layer, the cell would be translated and the height of the plate being imaged adjusted until the layer came into focus. This was repeated in several locations until the measured heights were in agreement, within the resolution of the vertical stage for the objective. The ability to adjust the top and bottom plates was not identical. The bottom plate would be adjusted first as it was mounted on the shear cells frame, as such there was no way to directly adjust its alignment. Instead the shear cell was bolted onto a mounting plate and three grub screws located at points in the shear cell's frame could be turned to lift the cell up. By careful tuning of these screws the bottom plate could be set flat. The top plate was then mounted on the shear cell and the focal point of the objective lens raised to the desired plate separation. The height of the top plate would be adjusted, using the three grub screw shown in figure 5.29, until the coated layer came into focus. The three grub screws could also be used to adjust the parallelity of the top plate. The nuts on the grub screws were used to ensure that the height of each screw remained constant once calibrated. They were tightened then coated with wax to hold them in place.

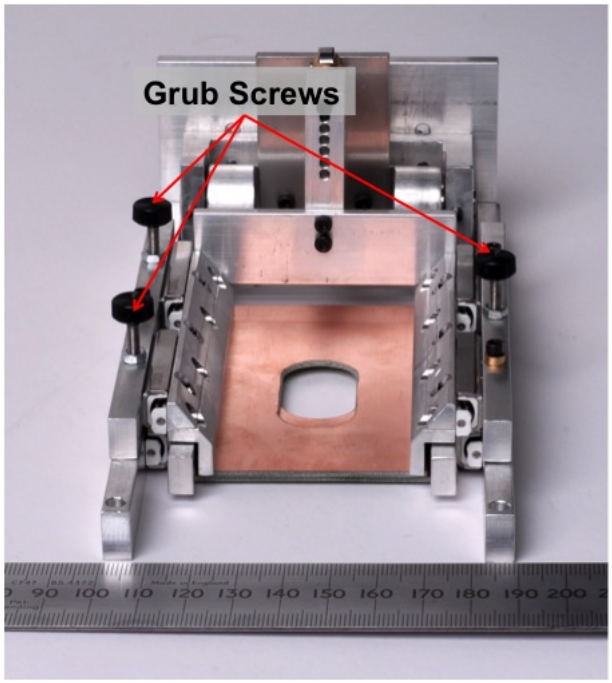


Figure 5.29: Picture showing the three grub screws that were used to adjust the parallelity of the top plate and to set the plate separation of the assembled shear cell.

### 5.7.3 Calibration

The next step in the characterisation of the shear cell was to test that the applied shear would produce a shear gradient across the plate separation, like that shown in figure 5.25.

The upper and lower plates were set parallel with a plate separation of roughly $400\mu m$. The shear cell was then loaded with a dilute dispersion of colloidal particles ($\phi \sim 0.05$) and the driving lever was set such that the ratio of displacement of the upper plate to the lower plate was roughly $5:1$. The plate separation and lever ratio were chosen such that the zero velocity plane would be expected to be found between the lower plate and $100\mu m$ into the cell. This was the operational translation of the objective mounted on the optical tweezers.

Confocal imaging was used to measure the velocity of the suspended particles as a function of height for various oscillation frequencies and amplitudes. The average absolute velocity of the particles in the $x$ and $y$ directions of the images was was determined by *Dr. Pierre Ballesta* using IDL particle tracking programs. The $x$ direction corresponded to the oscillation direction of the shear cell (velocity) and the $y$ direction corresponds to the vorticity (neutral) direction.

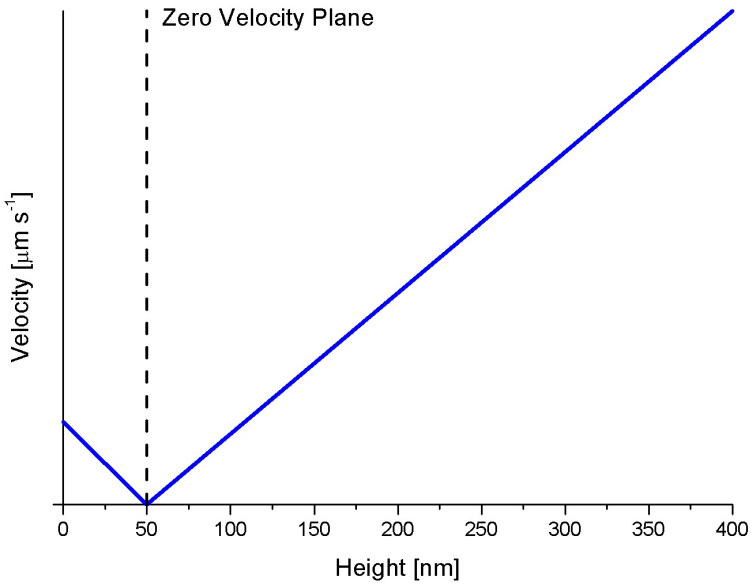


Figure 5.30: Example of the idealised absolute particle velocity for the shear cell.

An example of the ideal velocity profile that was expected to be measured can be seen

in figure 5.30 which shows the zero velocity plane at a height of $50\mu m$ above the lower plate.

Oscillation frequencies of $0.01Hz$ or greater were chosen as below this level the frequency generator that was used gave a noticeably digitised signal that would result in stepping in the motion of the piezo. The amplitude of the voltage used to drive the translation of the piezo was chosen to be less than than $5V$ (the maximum driving amplitude) to avoid hysteresis effects in the length of translation.

It can be seen in figures 5.31(a) and 5.31(b) that no clear zero velocity plane is observed but there is evidence of a possible zero velocity plane in figure 5.31(c) at a height of approximately $50\mu m$ and a clear zero velocity plane at the same position in figure 5.31(d). Suggesting that a zero velocity plane was only observable at shear rates of $0.1Hz$ or greater.

The absolute velocity of the particles in the vorticity direction was also measured. For a purely Brownian system that is sheared in the velocity direction the absolute velocity of the vorticity direction should be zero. In an experimental system this is rarely the case as there is often some inherent systematic drift. Knowing how much drift there is in the system is important for the analysis. Figure 5.32 shows the measured velocity in the vorticity direction for the same data sets shown in figure 5.31.

In all cases presented here (and when measured) the absolute velocity in the vorticity direction was not zero and can be seen to increase across the gap spacing of shear cell. Of great concern is that the measured flow in the vorticity direction is comparable to the induced flow in the velocity direction in the region between the lower plate and up to a height of $100\mu m$. As such any measurement using the optical tweezers of the forces experienced by the particle will not be directed along the shear direction alone.

A possible explanation for this observed increase in the flow in the vorticity direction with increasing height could be that objective lens of the confocal microscope is bending the glass coverslip, see figure 5.33. When the cell is being sheared the position of the hump in the coverslip will move and cause an induced flow in both the vorticity and the velocity directions. As such no zero velocity plane would be observed either.

If this were the case the same bending would be present in the optical tweezers system but there would be additional bending of the top coverslip caused by the condenser lens. Another explanation is that there may be some inhomogeneity in either the glass surface or the coating layer that is causing the flow in the vorticity direction. The effect this of this inhomogeneity could be reduced by increasing the gap separation of the plates. This solution presents its own problems in that the separation that has been presented is already close to the maximum separation allowable by the spatial constraints of the imaging parts of the optical tweezers and the working distance constraints for the condenser lens. Also increasing the separation further would have

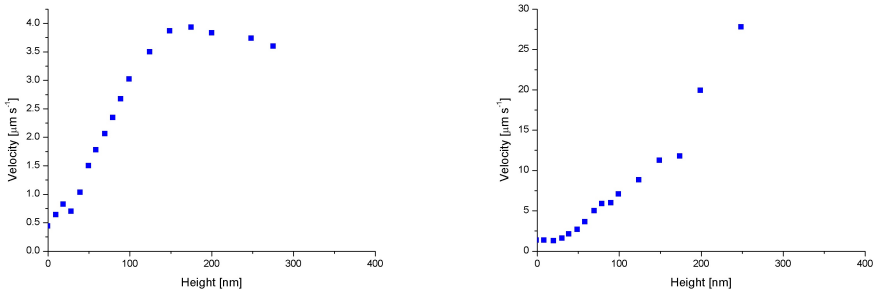


(a)




(b)

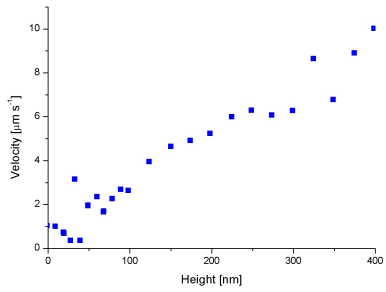


(c)

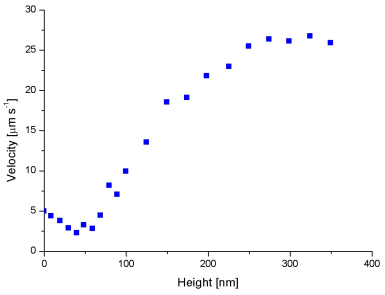


(d)

Figure 5.31: Absolute velocity profiles in the velocity direction for a dilute dispersion of particles with increasing distance from lower plate for (a) oscillation frequency of $0.01Hz$ and $1V$ driving amplitude; (b) oscillation frequency of $0.01Hz$ and $4V$ driving amplitude; (c) oscillation frequency of $0.1Hz$ and $1V$ driving amplitude; (d) oscillation frequency of $0.1Hz$ and $4V$ driving amplitude.

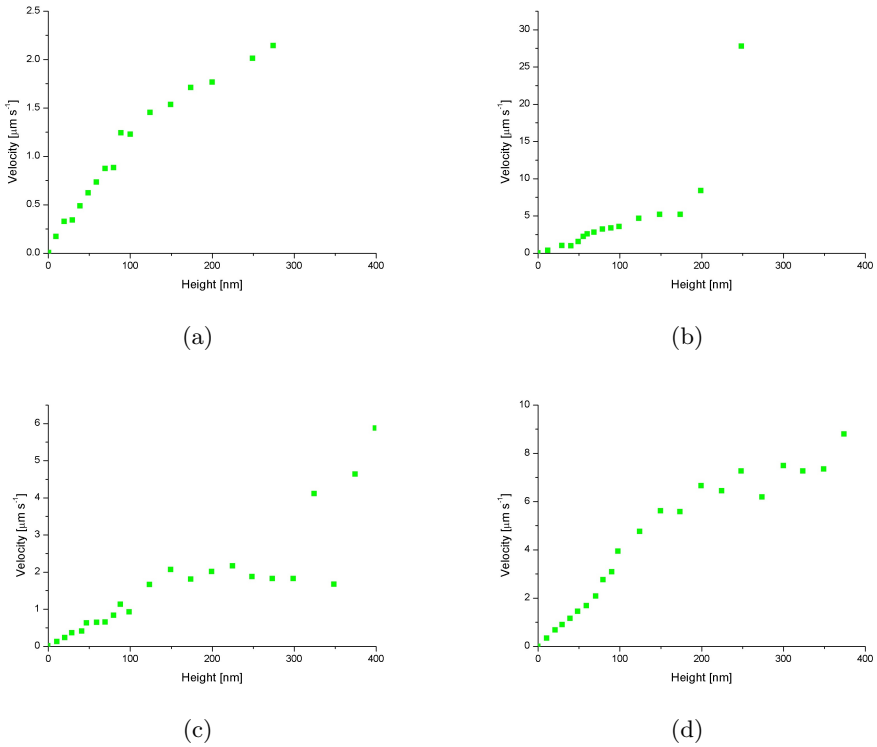


Figure 5.32: Absolute velocity profiles in the vorticity direction for a dilute dispersion of particles with increasing distance from lower plate with an (a) oscillation frequency of $0.01Hz$ and $1V$ driving amplitude; (b) oscillation frequency of $0.01Hz$ and $4V$ driving amplitude; (c) oscillation frequency of $0.1Hz$ and $1V$ driving amplitude; (d) oscillation frequency of $0.1Hz$ and $4V$ driving amplitude.

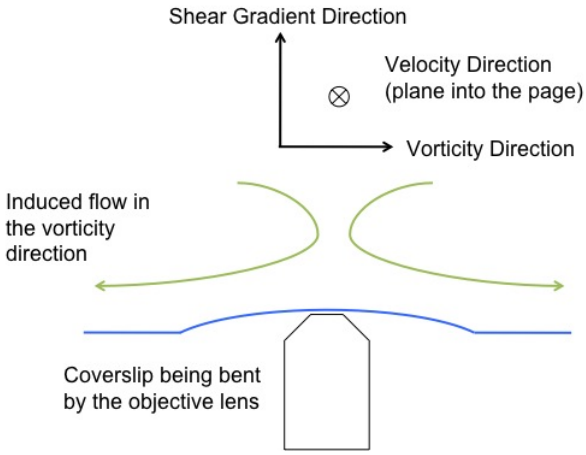


Figure 5.33: Illustration showing possible bending of the coverslip by an objective lens causing an induced flow in the vorticity direction.

placed the upper plate beyond the range of travel for the stage controlling the objective lens on the confocal. As such it would be impossible to measure the parallelity of the top plate without almost certainly deforming or even cracking the lower coverslip with objective's vertical motion. The confocal can be setup such that samples may be imaged from above, but without a point of reference it would not be possible to measure the gap separation or the parallelity of each plate relative to the other. Also increasing the gap separation would increase the height at which the zero velocity plane could be found. The ratio of the displacement of the upper plate to that of the lower plate would have to be increased to be greater than $5:1$ which would mean that the upper plate would be reliant on the linear bearings to be able to run smoothly over a greater displacement. The greater displacement would also increase the likelihood of particles of dirt to get into the bearings reducing their ability to run smoothly, compromising the ability to produce a linear shear across the whole sample (which is the same problem that increasing the gap separation attempts to solve).

### 5.7.4 Shear Cell Conclusions

The shear cell was found to be impractical for use in conjunction with the optical tweezers. The main reason for this was the inability to arrest the induced flow in the vorticity direction when a suspension was sheared, whilst retaining a small enough gap separation such that a particle could be imaged and trapped in the zero velocity plane of the suspension. The shear cell has been kept as it can be used by other researchers, it is compatible with most commercial microscopes currently used within the research group.

There are however several points that should be considered for anyone who wishes to carry out similar research with a shear cell.

A method has to be found to measure the parallelity of the shear plates, confocal imaging of a coated coverslip was used here and found to be quite effective. Coating the coverslips also provided the no-slip boundary condition and did not prevent the optical tweezers from trapping a particle. The gap separation must be able to be determined well enough to calculate the displacement ratio of the upper and lower plate. If the plates used do not have layer of colloid then another method for measuring the parallelity and plate separation will have to be found.

The problem of the flow in the vorticity direction can be arrested by increasing the gap separation of the two plates however for the shear cell to be used in conjunction with a set of optical tweezers the objective lens will probably need to have an extra long working distance and not make contact with the lower plate, to ensure there is no bending. This will reduce the numerical aperture of the system and introduce spherical aberrations common in systems where the light travels through materials with varying refractive indices. This will also reduce the trapping strength of the optical trap to a level such that it cannot be used with viscous systems. An additional constraint on the long working distance objective lens will be that it must have a magnification large enough such that probes of a suitable size can still be imaged and trapped within the cell.
The condenser lens will also need to be replaced for similar reasons, reducing the amount of the scattered laser light used for particle detection and result in a reduction in the resolution of the instrument.

A dedicated confocal microscope is recommended to allow calibration of the parallelity and gap separation to be determined on this modified system (provided that optical trapping is still possible). This would allow the shear cell to be fully calibrated for an experiment without the need to move it from a lab where a confocal is located to the one where the optical tweezers are[10].

[10]The modifications mentioned are technically possible but due to the multiuser nature of the microscopes were not implemented.

# Chapter 6

# Passive Micro-Rheology with Two Optical Traps

This chapter deals with the implementation of two point passive micro-rheology experiments using the optical tweezers described in Chapter 3.

First an initial description is given of how the two point system can be used to measure the hydrodynamic interaction between two particles that are suspended in a solvent of fixed viscosity. This measurement is subsequently used to show predictions made from the Oseen tensor is independent of viscosity.

The same methods are then applied to suspensions of colloidal particles with volume fractions $\phi = 0.02$ where the resultant cross-correlations can be used to determine the size of the particles. The coupled motion of the two particles is then used to determine the friction co-efficients of $\xi^{\parallel}_{1,1}$ and $\xi^{\parallel}_{1,2}$ of the particles in the suspension, which can then be used to explain the deviations of the experimental data from the predictions made from the Oseen tensor when used in conjunction with the Einstein correction to viscosity.

## 6.1 Two Trap Passive Micro-Rheology

In the previous chapter one point passive micro-rheology was used to measure the fluctuations in the position of a single particle in a colloidal suspension. The fluctuations of the particle are a result of Brownian forces and hydrodynamic forces and a measurement of the hydrodynamic forces can be made using optical tweezers using two optical traps instead of just one [12], [7], [8], [77].

In a suspension of hard sphere colloidal particles a single particle will experience thermal brownian forces and hydrodynamic forces caused by the other particles. When a particle moves it will displace the surrounding fluid and produce a vorticity flow field

that will diffuse through the fluid at a rate that is controlled by the kinematic viscosity of the fluid, $\nu = \frac{\eta_0}{\rho}$. When this flow field encounters the surface of another particle some of the momentum of the flow field will be transferred to the particle and the particle will experience a force. In this way the motion of each particle will be coupled with some time delay to the motion of all the other particles in the fluid. In effect the motion of all the particles in the suspension will be embedded in the motion of each individual particle in the suspension. Theoretically by measuring the motion of one particle and knowing how it interacts with all other particles the full bulk dynamics of the suspension could be determined, but understanding how a single particle interacts with all the others is the limiting factor of this situation.

The problem can be simplified to an initial two body problem by using two particles where each particle can be held in an optical trap and their displacements measured. Using the fluctuations of their displacements in the presence of each other the coupled motion can be determined and their hydrodynamic forces calculated. By using the two body data as a baseline the system can be scaled up to a more complex situation by introducing bath particles and determining if this produces additional hydrodynamic forces or suppresses the existing interactions between the two particles.

As well as determining the hydrodynamic interactions there are other predicted benefits from using two point micro rheology. Levine and Lubensky [78] have provided the theoretical framework for both one and two point micro-rheology. It is expected that any measurements made using two point micro-rheology are more likely to agree with the bulk rheology of the system than one point measurements. The two point micro-rheology is more likely to yield results that are similar to the bulk rheology because of the length-scales associated with the measurement. One point passive micro-rheology will only probe a suspension up to a distance of roughly a particle radius whereas two point micro-rheology will probe a distance equal to the separation of the two particles, which reflects the bulk more than a single particle radius does.

The far-field hydrodynamic flow produced by a single particle when it moves in an incompressible fluid at low Reynolds number can be described by the Oseen tensor [79]. A vector plot of the vorticity field produced for a fluid experiencing a point force located at the origin, can be seen in figure 6.1.

If the the flow is induced by a particle located at the origin the induced force on a second particle located at some distance $R$ can be determined and the resultant displacement of the second particle calculated. This method has been used by Meiners and Quake [7] and by Bartlett *et al.* [8] to determine the correlated motion of two particles suspended in a fluid being held by optical traps. Meiners and Quake solved the coupled equations of motion of the particles using the first order terms of the Oseen

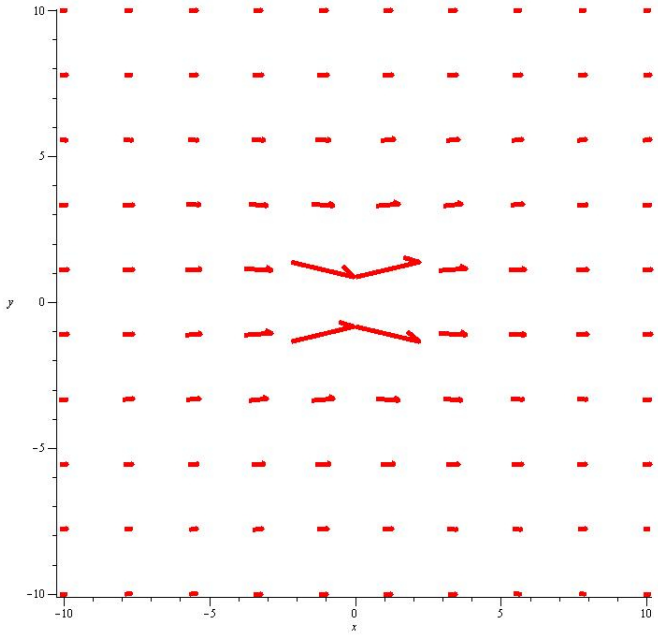


Figure 6.1: Flow field predicted by the Oseen tensor for a fluid experiencing a point force located at the origin directed along the $x$ axis with a magnitude of 1. All units have been normalised to particle size for ease of computation.

tensor and found the predicted cross-correlated motion to be,

$$\langle x_{(1)}(t)x_{(2)}(t+\tau)\rangle = \frac{k_B T}{2\kappa}\left(e^{-\frac{\tau\kappa}{6\pi\eta_0 a}(1+\epsilon)} - e^{-\frac{\tau\kappa}{6\pi\eta_0 a}(1-\epsilon)}\right), \tag{6.1}$$

where $\epsilon = \frac{3a}{2R}$ (for cross-correlations carried out along the longitudinal direction) where $R$ is the centre to centre separation between the two particles. The cross-correlation for the motion in the transverse direction has a similar form except that the value of $\epsilon$ takes the form $\epsilon = \frac{3a}{4R}$, however focus is mainly given to the motion acting along the longitudinal direction. A complete derivation of how the Oseen tensor can be used to determine this cross-correlation can be found in [80].

Bartlett *et al.* used derived a similar equation that included the higher order terms of the Oseen tensor and was also normalised by the mean square displacements of the particles [8],

$$\frac{\langle x_{(1)}(t)x_{(2)}(t+\tau)\rangle}{\sqrt{\langle x^2_{(1)}\rangle\langle x^2_{(2)}\rangle}} = \frac{1}{2}\left(e^{-\frac{\kappa\tau}{\xi_+}} - e^{-\frac{\kappa\tau}{\xi_-}}\right) \tag{6.2}$$

The exponential terms in equation 6.1 and 6.2 describe the decays of correlated and anti-correlated modes of the two particles which are shown in figure 6.2.

The reason why the anti-correlated mode decays slower is due to the time it takes

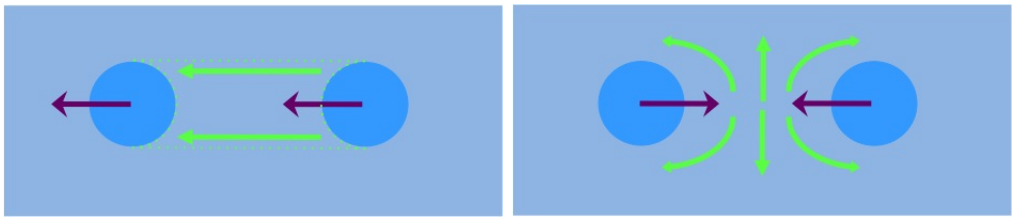

(a) (b)

Figure 6.2: Schematic showing (a) correlated motion of two particles displacing the fluid in the same direction and (b) anti-correlated motion of two particle squeezing the fluid between them.

for the fluid to flow back into the space between the particles. In the correlated case the particles effectively displace the fluid between them in the same direction that they are both moving in, figure 6.2. The example shown in figure 6.3 has been normalised by the mean square displacements of the trapped particles to remove prefactor in equation 6.1. Normalising equation 6.1 by the mean square displacements of both particles produces,

$$\frac{\langle x_{(1)}(t)x_{(2)}(t+\tau)\rangle}{\sqrt{\langle x_{(1)}^2\rangle\langle x_{(2)}^2\rangle}} = \frac{1}{2}\left(e^{-\frac{\tau\kappa}{6\pi\eta_0 a}(1+\epsilon)} - e^{-\frac{\tau\kappa}{6\pi\eta_0 a}(1-\epsilon)}\right). \tag{6.3}$$

The resulting normalised equation gives a function where amplitude of the anti-correlation is only dependant on the particle separations. An investigation of how the amplitude evolves with particle separation can be found in [7] and a more detailed investigation will follow in a later section of this chapter.

It also tell us that the correlation time $\tau_{min}$ that the anti-correlation occurs at is dependant on trap stiffness $\kappa$, particle size $a$, solvent viscosity $\eta_0$ and particle separation. This allows the investigation of the viscosity as a function of separation or the coefficients of the friction tensor could be determined instead [8].

It should be noted that the derivations from the Oseen tensor and all subsequent mathematics and predictions are in the dilute limit and for particles that are well separated. It is therefore expected that there will come a point when the increase in volume fraction of the suspensions and when the particles come close together will result in the assumptions used to no longer being valid. The question arises how far will the dilute limit hold and how close can finite particles be brought together before the predictions break down?

Predictions from the Oseen tensor show that the depth of the minima in the cross-correlated motion will decrease with increasing particle separation. To determine how the minima evolves with particle separation, the derivative of equation 6.3 was taken

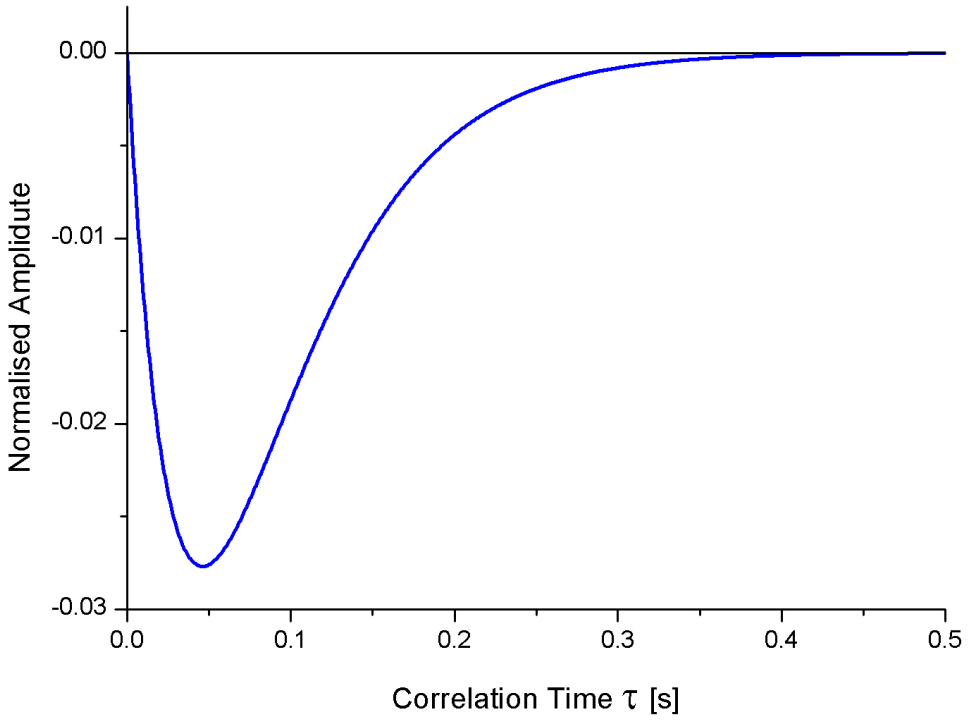


Figure 6.3: Example of predicted cross-correlation from equation 6.1 of two particles with radius $a = 0.969\mu$m in a solvent with viscosity $\eta_0 = 2.5mPa\ s$ held in independent optical traps with stiffnesses of $1 \times 10^{-3} pNnm^{-1}$ and a centre to centre separation of $4.5a$.

with respect to correlation time, $\tau$,

$$\frac{\mathrm{d}}{\mathrm{d}\tau}\left(\frac{\langle x_{(1)}(t)x_{(2)}(t+\tau)\rangle}{\sqrt{\langle x_{(1)}^2\rangle\langle x_{(2)}^2\rangle}}\right) = \frac{6\pi\eta a}{2\kappa}\left(-(1+\epsilon)e^{-\frac{\tau\kappa}{6\pi\eta_0 a}(1+\epsilon)} + (1-\epsilon)e^{-\frac{\tau\kappa}{6\pi\eta_0 a}(1-\epsilon)}\right). \tag{6.4}$$

Solving equation 6.4 for $\tau = 0$ gives the time that the minima occurs, $\tau_{min}$,

$$\tau_{min} = -\frac{6\pi\eta_0 a}{2\kappa\epsilon}\ln\left(-\frac{-1+\epsilon}{1+\epsilon}\right), \tag{6.5}$$

replacing $\tau$ in the starting correlation equation 6.3 with the above solution for $\tau_{min}$,

$$\frac{\langle x_{(1)}(t)x_{(2)}(t+\tau_{min})\rangle}{\sqrt{\langle x_{(1)}^2\rangle\langle x_{(2)}^2\rangle}} = \frac{1}{2}\left(e^{(1+\epsilon)\ln\left(-\frac{-1+\epsilon}{1+\epsilon}\right)/2\epsilon} - e^{(1-\epsilon)\ln\left(-\frac{-1+\epsilon}{1+\epsilon}\right)/2\epsilon}\right). \tag{6.6}$$

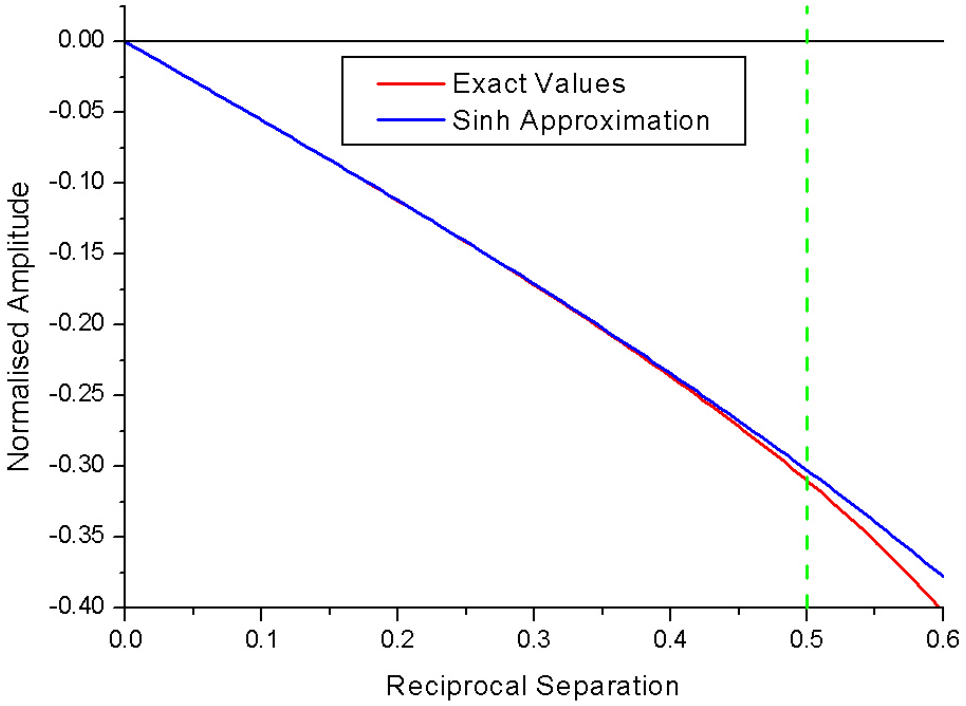


Figure 6.4: Equations 6.6 (red) and 6.7 (blue) plotted as a function of reciprocal particle separation. Closest approach of the two particles indicated by the green dotted line at $a/R = 0.5$.

The most notable feature of equation 6.6 is that it is only dependant on $\epsilon$, which in turn is only dependant on the particle separations. Effectively the measured amplitude should be constant no matter what stiffness of optical trap is used or what solvent the particles are suspended in, giving an ideal function with which to calibrate any two point micro-rheology set-up. Using the same methods that were used in [7]equation 6.6 can be approximated to,

$$\frac{\langle x_{(1)}(t)x_{(2)}(t+\tau_{min})\rangle}{\sqrt{\langle x^2_{(1)}\rangle\langle x^2_{(2)}\rangle}} \approx -\frac{1}{e}\sinh(\epsilon) \tag{6.7}$$

The difference between equations 6.6 and 6.7 can be seen by plotting the two functions of normalised reciprocal separation, $a/R$. Deviations become noticeable at $a/R = 0.4$ which corresponds to a gap of half one particle radius between the two surfaces of the particles which is where it is likely that the predictions made from the Oseen tensor

will begin to break down.

With this tool the two point passive system was calibrated using a very dilute suspension of melamine probes in various solvents. The cross-correlation of the longitudinal motion was measured and the minima determined and checked to agree with equation 6.7.

A small sample of the melamine particles, as in Chapter 4, were poured into jars and placed under vacuum at a temperature of $40°C$ to evaporate the solvent that the particles came suspended in. Complete evaporation was confirmed when no variation in the mass of each sample jar was found. Three solvents were chosen that had varying viscosity, decalin $\eta_{decalin} = 1.948mPa\ s$, CHB/decalin mixture $\eta_{CHB/decalin} = 2.504mPa\ s$ and Cyclopentyl Bromide $\eta_{CPB} \approx 3.2mPa\ s$. Each solvent was poured over the dried tracer particles to produce a suspension with volume fraction $\phi \sim 0.001$. The tracer particles were resuspended in the solvent via vigourous shaking. Once suspended a capillary cell was filled, sealed and used immediately with the optical tweezers.

### Experimental Method

The sample was placed under the optical tweezers and the condenser and objective lenses focussed at a depth of $20\mu$m above the coverslip of the cell. Two tracer particles were found and trapped and the system was left to equilibrate for about an hour. This also ensured that any suspended tracer particles would sediment to the coverslip and would not diffuse into the optical traps during the course of the experimental runs. In the case of decalin the tracer particles became stuck to the coverslip upon sedimentation. The focussing of the lenses and the trapping of two tracer particles had to be carried out in the short time before this happened.

Once the system had been left to equilibrate the optical traps had to be balanced to ensure that the particles experienced identical stiffnesses. A short 3 minute recording was made of each of the particles motion. The mean squared displacments (MSDs) of each particle were calculated and the corner time, $\tau_c$, for each particle was determined using the methods described in Chapter 2 where $\tau_c$ was given in equation 2.23,

$$\tau_c = \frac{\xi_0 \sigma^2}{k_B T} \tag{6.8}$$

Once $\tau_c$ was calculated for each trap they would be compared and the half waveplate retarder $\lambda/2_{(2)}$ that controlled the laser power of *Trap2* would be adjusted accordingly. Another 3 minutes would be recorded and the MSDs compared again. This procedure was repeated until the calculated stiffnesses for each trap were in agreement to within

5%, the error associated with the radius of the tracer particles, figure 6.5.

The particles were aligned roughly with the $x$ direction of the image to give a longitudinal separation of roughly 20$\mu$m. The laser power to both traps was increased to give as stiff traps as possible and but still maintain the balance in stiffness of the optical traps by increasing the initial output power of the laser. An image of the particles was taken to determine the longitudinal separation and the relative angle between the two particles. The laser power was reduced to its original output level and a $\sim 30$ minute recording of the particles' positions taken. The particles were then brought closer together and the positions determined. This process was repeated until the particles were as close to each other as possible without the particles becoming confined by the same optical trap. The detectors recorded with a sample rate of 20kHz, faster rates were possible but the positional information from each trap could no longer be assumed to be simultaneous and would result in errors in the crosscorrelation calculations.

### Longitudinal Separation and Angle

The location of the particle positions in the image were determined using the same threshold imaging programme used in Chapter 3 to determine the trap anharmonicity. With the particle locations known the longitudinal separation was calculated and the angle of the longitudinal separation relative to the image $x$ axis was determined, see figure 6.6.

The longitudinal angle was determined by taking the tangent of the relative $x$ and $y$ separations of the two particles, $\beta = \tan(y/x)$. An additional angular transform of the data from each detector was made such that the output $x$ channels were aligned with the longitudinal separation of the particles. If this correction was not made then the calculated crosscorrelation would be underestimated.

### Predictions from Theory and Results from Experiment

The crosscorrelations were calculated using a LabVIEW routine using the analytical methods described in Chapter 2 and were normalised by the MSDs to remove the trap stiffness prefactors from the amplitude of the calculated crosscorrelation, equation 6.2.

As the stiffness of the optical traps was known along with the particles' longitudinal separations, predictions of the crosscorrelations could be made and the measured cross correlations compared, see figures 6.7.

As can be seen, the cross-correlations agree well with the predictions derived from the Oseen tensor until the centre to centre separation $R < 5a$, at which point the measured cross-correlations have minima that are less than those predicted.

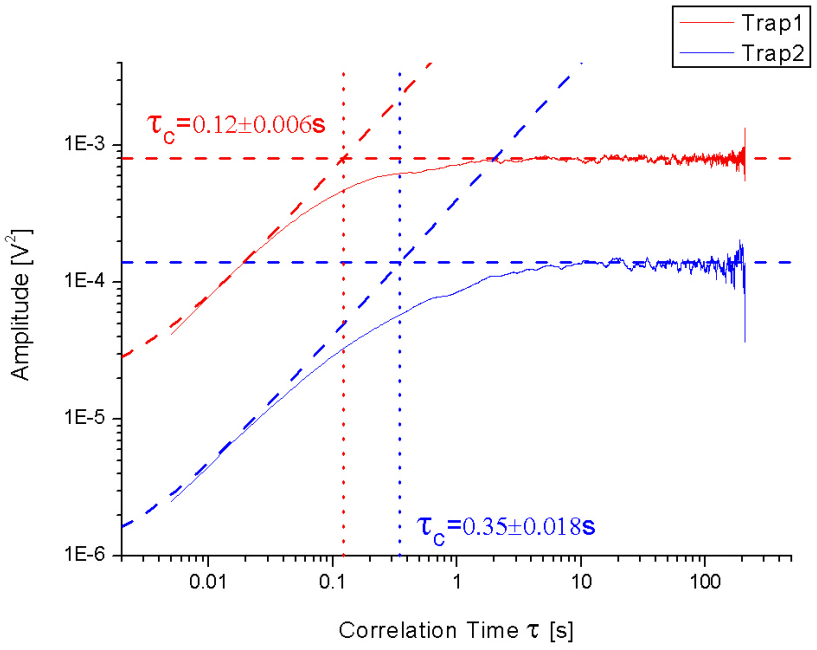


(a)

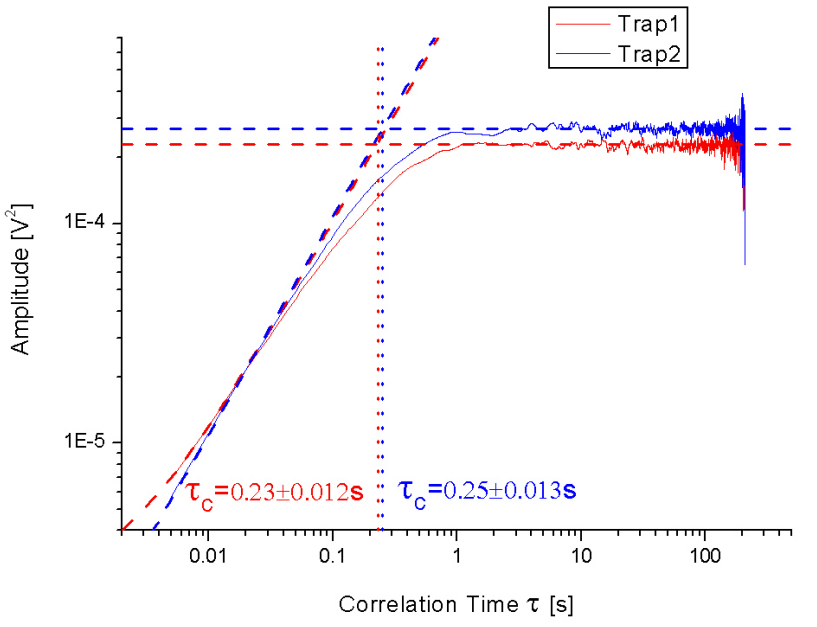


(b)

Figure 6.5: Mean squared displacements of two optically trapped particles where (a) the traps have unequal stiffnesses and (b) when the traps have equal stiffness, evidenced by the corner times $\tau_c$ of the mean square displacements being approximately equal.

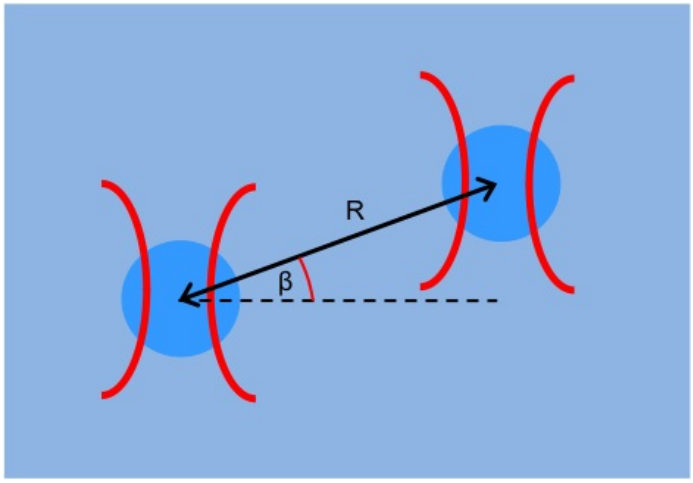


Figure 6.6: Schematic diagram showing the transverse and longitudinal directions associated with particle spearation and the angle $\beta$ defining the longitudinal separation relative to the image $x$ axis.

### Cross-Correlation Minima Results

In order to determine the exact minimum, all data sets were fitted using a double exponential with the form (fits are shown in figures 6.7 as dashed lines),

$$y = A\left(e^{(-tB)} - e^{(-tD)}\right) + c \tag{6.9}$$

where $A, B, D$ and $c$ were all adjustable parameters and $t$ was the correlation time. The resultant fit equation was solved in a similar manner as equation 6.3. The value of the minima for each of the separations was determined for each solvent.

The values of the minima are plotted against normalised reciprocal separation with the hyperbolic sine approximation, equation 6.7, shown as the red line in figure 6.8.

It can be see that good agreement with the approximation is found for normalised reciprocal separations of $\frac{a}{R} < 0.25$, above this point the minima deviate from the approximation. However graph of the residuals relative the approximation shows that the data is consistently less that what is expected as the particles are brought closer to each other for the well fitting region, figure 6.9.

Possible sources for this systematic offset could be that the approximation is not sensitive enough to accuately map the actual prediction, crosscorrelation overspill from the transverse direction, detector crosstalk, wall effects from the coverslip 20$\mu$m away, higher order corrections to the Oseen tensor or that because the particles are have finite

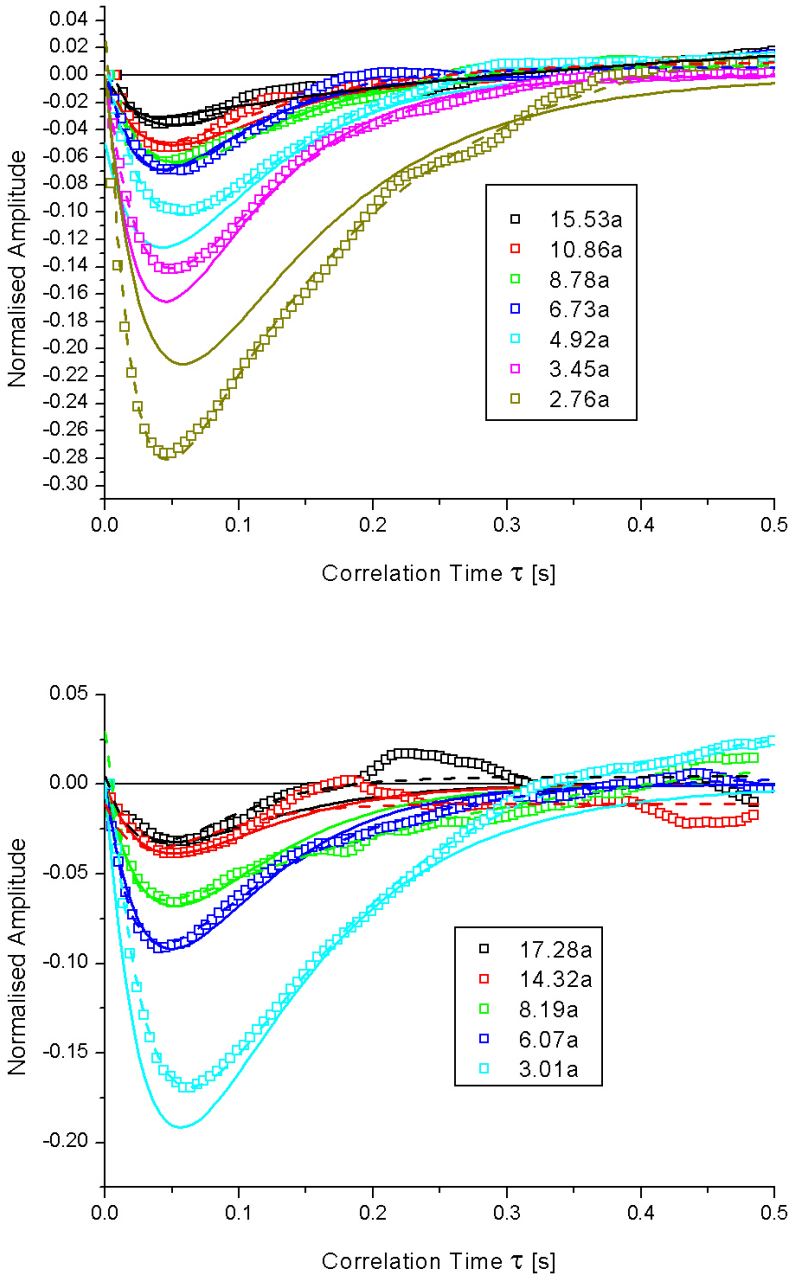


Figure 6.7: Measured longitudinal crosscorrelations for CHB/decalin mixture where the solid lines are the predictions derived from the Oseen tensor and dashed lines are double exponential fits to the data. Every 10th point is plotted for the experimental data shown. Data has been plotted over two graphs for clarity purposes.

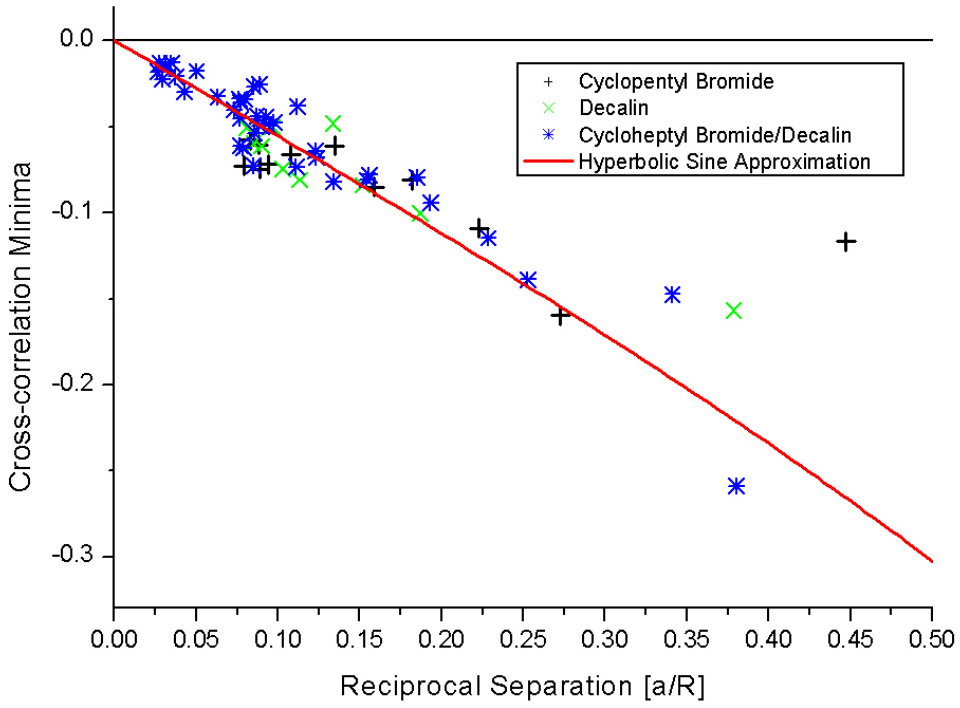


Figure 6.8: Longitudinal crosscorrelation minima as a function of normalised reciprocal separation with hyperbolic sine approximation in red.

size they will interact with each other in ways that the Oseen tensor does not account for.

Figure 6.4 shows the deviation of the hyperbolic sine approximation to the actual function described by equation 6.6. This deviation is in the positive direction, so in actual fact the underestimation is actually greater than what the Oseen tensor predicts what it should be. The observed deviation from the hyperbolic sine function, equation 6.7, is shown in the residuals plot in figure 6.9. Also the residuals become dominantly positive for all data sets at normalised reciprocal separations of $\frac{a}{R} > 0.15$ which is when there is no discernible difference between the approximation and the values determined by equation 6.6.

Detector crosstalk can be ruled out as it was found in Chapter 3 that the normalised amplitude of the crosstalk between the two detectors was less than 0.001 which is not large enough to have an observable effect. If it were observable the detector crosstalk would cause the crosscorrelation to be overestimated rather than

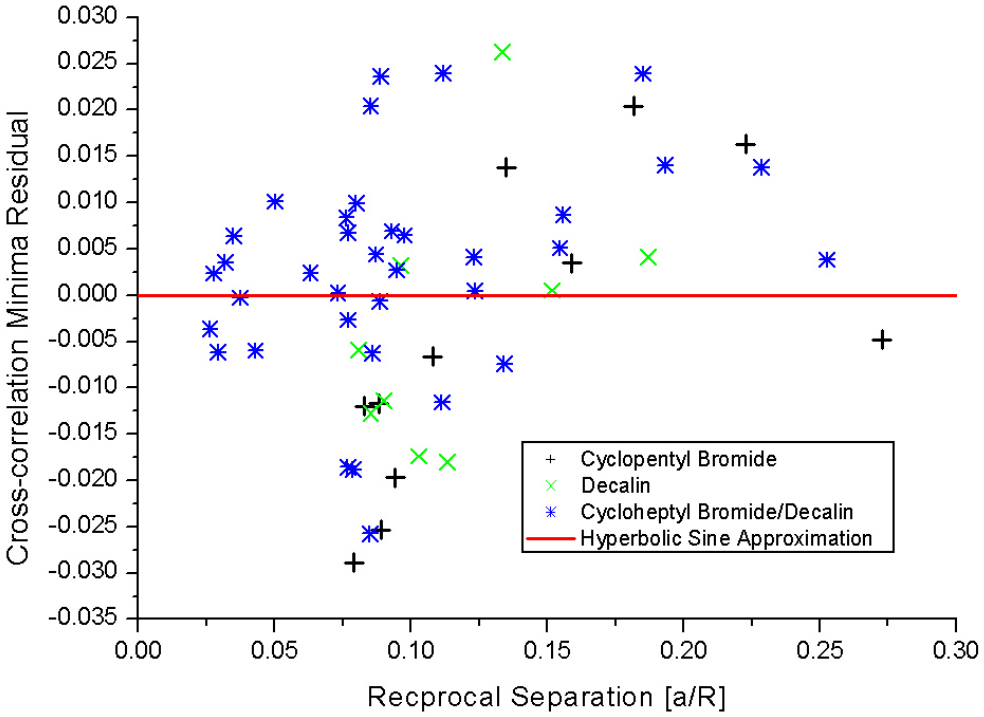


Figure 6.9: The residuals for the data presented in figure 6.8 relative to hyperbolic sine approximation showing a systematic underestimation of the crosscorrelation minimum as the particles come closer together. The data point of closest approach has been omitted for clarity purposes.

systematically underestimated.

Crosscorrelation overspill from the transverse direction was ruled out by calculating the crosscorrelation for varying angles around the longitudinal direction and confirmed that longitudinal direction had minimum value for the calculated crosscorrelation, figure 6.10.

It can be seen that the correct angle for the angular transforms has been used. Accordingly that at a height of 20$\mu$m above the coverslip the hyperbolic sine approximation works for large separations but for closer separations it will overestimate the value of the anti-correlation.

To discount the possibility of wall effects a series of crosscorrelations of melamine in CHB-decaline mixture were recorded at a height of 40$\mu$m above the coverslip. The minima of these crosscorrelations were also determined and shown in figure 6.11.

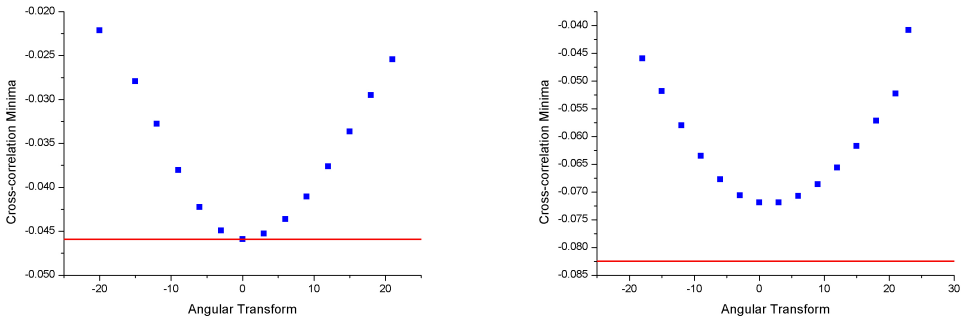


(a) (b)

Figure 6.10: (a) Crosscorrelation minima as a function of angular transform for a normalised reciprocal separations of $\frac{a}{R} = 0.16$, showing a minima at the angle associated with the longitudinal separation that agrees with the hyperbolic sine approximation, equation 6.7. (b) Similar crosscorrelation minima for a normalised reciprocal separations of $\frac{a}{R} = 0.29$ showing that the minima does not reach the value expected form the hyperbolic sine approximation.

At a height of 40$\mu$m there is better agreement with equation 6.7 suggesting that the underestimation of the values could be down to wall effects.

Another possible explanation for the underestimation would be the higher order correction terms of the Oseen tensor. The higher order corrections to the Oseen tensor were derived by *Dr. Alexander Morozov*, a complete description of the derivation that he used can be found in Appendix F. For clarity the higher order corrections have been plotted with the hyperbolic sine approximation and the measurements made using the particles suspended in the mixture of CHB and decalin, figure 6.12.

It can be seen that the higher order corrections to the Oseen Tensor are not large enough to correct for the systematic underestimation in the minima of the longitudinal crosscorrelation.

It should be noted that the underestimation is not an artefact of the optical tweezers that have been used here as a similar underestimation has been observed by Meiners and Quake [7] but was not addressed by them. A reproduction of their data presented can be found alongside the CHB/decalin data that has been presented in this section in figure 6.13.

There is a similar deviation from the hyperbolic sine approximation that was observed in figure 6.8. The data collected by Meiners and Quake was measured at

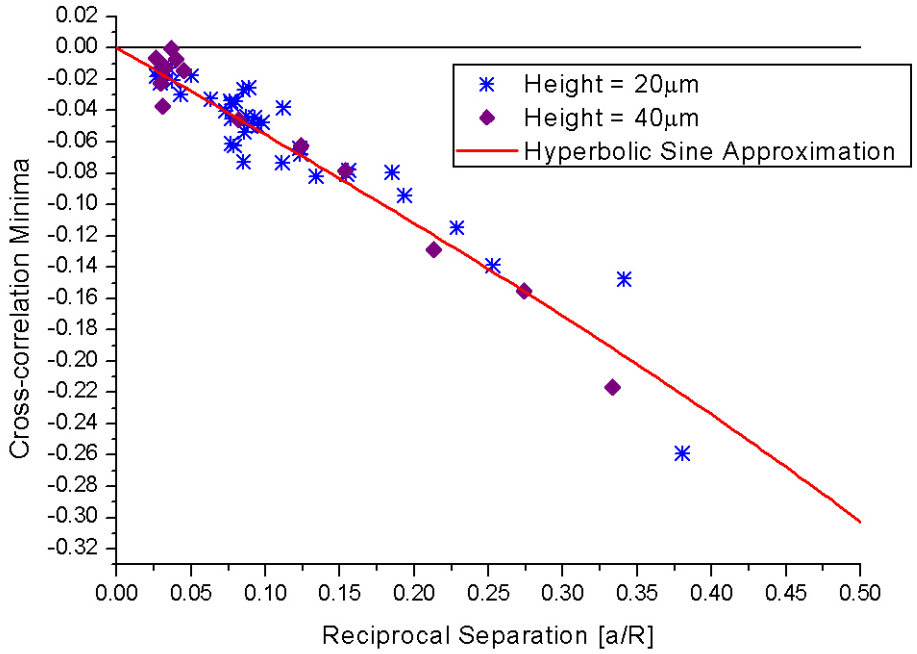


Figure 6.11: Measured longitudinal crosscorrelations for melamine particles suspended in CHB/decalin mixture at heights of 20$\mu$m and 40$\mu$m. Hyperbolic sine prediction shown as the red line.

a height of 40 particle radii from the nearest wall. Which is an equivalent distance to the data that is presented in figure 6.11 where not as much deviation was observed casting doubt on the deviation to be solely due to wall effects of the sample chamber.

The calibration of the two point passive optical tweezers has been found to agree with the predicted theory when the two particles have a centre to centre separation $R > 6.5a$.

Measurements of bare solvent in this limit allow the optical tweezers to be tested that they are functioning as expected as the results should be independent of the host viscosity.

Deviation from the predicted theory occurs when the particles have a centre to centre separation $R < 6.5a$ where the measurement of the absolute value of the anti-correlation made by experiment will typically be lower than that predicted by the solutions derived from the Oseen tensor. There is evidence that this may be due to wall effects although the case for this is not strong as similar experiments carried out elsewhere with similar boundary conditions observed a systematic underestimation of

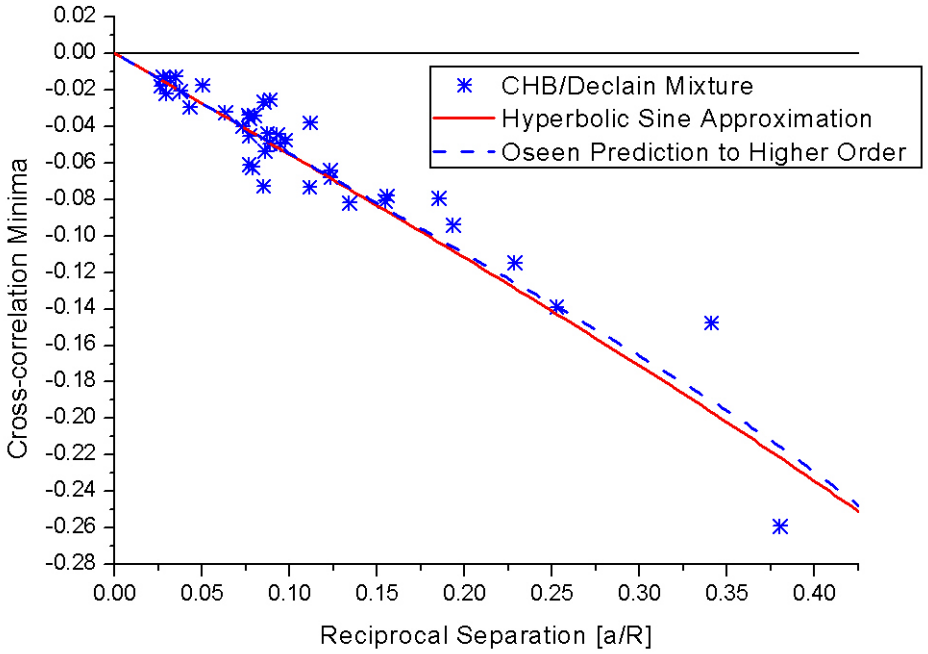


Figure 6.12: Graph showing the measured crosscorrelations for CHB/Declain along with the hyperbolic sine prediction in red and the higher order corrections from the Oseen tensor in blue.

the anti-correlation.

### 6.1.1 Friction Coefficients

The amplitude of the anti-correlation give a useful benchmark from which to check that set of dual trap optical tweezers has been suitably calibrated but cross-correlated motion of the two particles allows us to measure the friction coefficients of the friction tensor,

$$\begin{pmatrix} \xi_{1,1} & \xi_{1,2} \\ \xi_{1,2} & \xi_{1,1} \end{pmatrix}. \tag{6.10}$$

As stated Bartlett *et al.* [8] split the cross-correlated displacements into its two modes,

$$\frac{\langle x_{(1)}(t)x_{(2)}(t+\tau)\rangle}{\sqrt{\langle x_{(1)}^2\rangle\langle x_{(2)}^2\rangle}} = \frac{1}{2}\left(e^{-\frac{\kappa\tau}{\xi_+}} - e^{-\frac{\kappa\tau}{\xi_-}}\right) \tag{6.11}$$

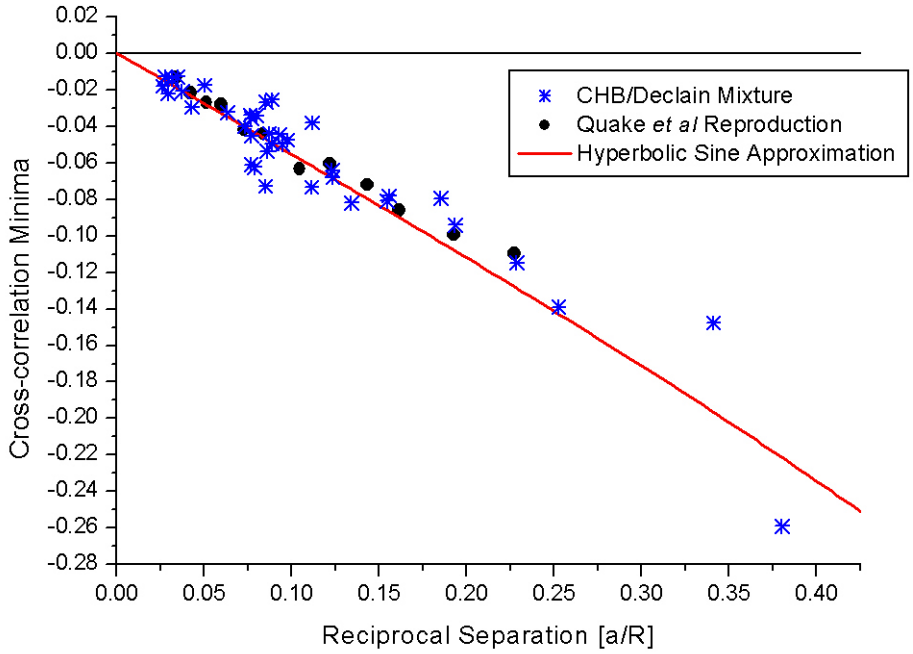


Figure 6.13: A reproduction of the data found in [7] that has been normalised to be comparable to data presented here and all data that has been presented. The data presented showing a similar deviation from the approximation line.

with the correlated decay rate given by $\frac{\kappa}{\xi_+}$ and the anti-correlated decay rate by $\frac{\kappa}{\xi_-}$, where $\xi_+$ and $\xi_-$ are given by,

$$\xi_+ = \xi_{1,1} + \xi_{1,2}, \tag{6.12}$$

$$\xi_- = \xi_{1,1} - \xi_{1,2}. \tag{6.13}$$

The equivalence of the decay rates to first order stated here and the ones given in equation 6.1 can be found in appendix F equations F.6 to F.13.

From the analytical fits to the data the normalised longitudinal friction coefficients (normalised by $\xi_0 = 6\pi\eta_0 a$) can be calculated and are shown in figures 6.14 and 6.15.

The measurements of both friction coefficients show good agreement with the predicted theory up to normalised reciprocal separations of $\frac{a}{R} \sim 0.25$ corresponding to a centre to centre separation of $4a$, which is when the two particles have surface separation equal to a particle diameter. Above a normalised reciprocal separation of $\frac{a}{R} \sim 0.25$ the measured friction coefficients begin to diverge from the predicted

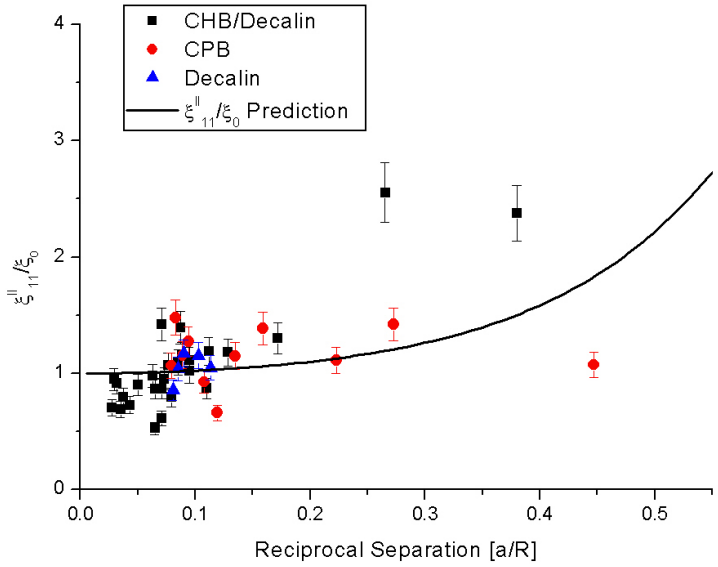


Figure 6.14: $\xi^{\parallel}_{1,1}/\xi_0$ friction coefficients as a function of normalised reciprocal separation for the data that has been presented in figure 6.8.

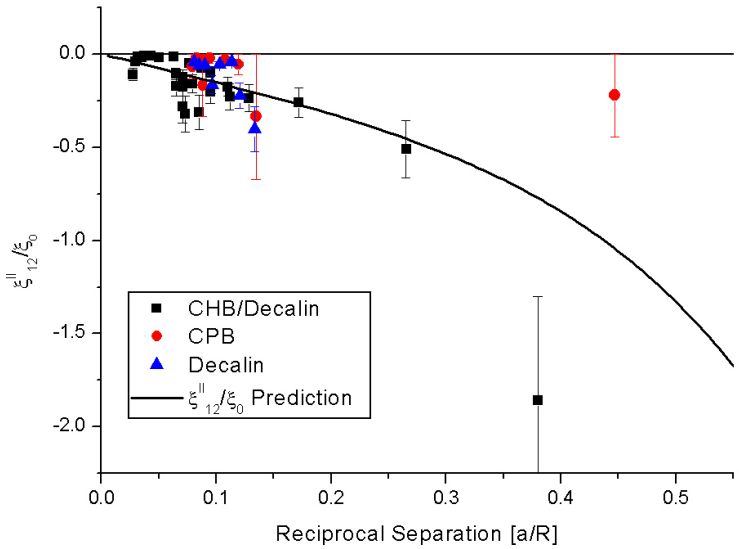


Figure 6.15: $\xi^{\parallel}_{1,2}/\xi_0$ friction coefficients as a function of normalised reciprocal separation for the data that has been presented in figure 6.14.

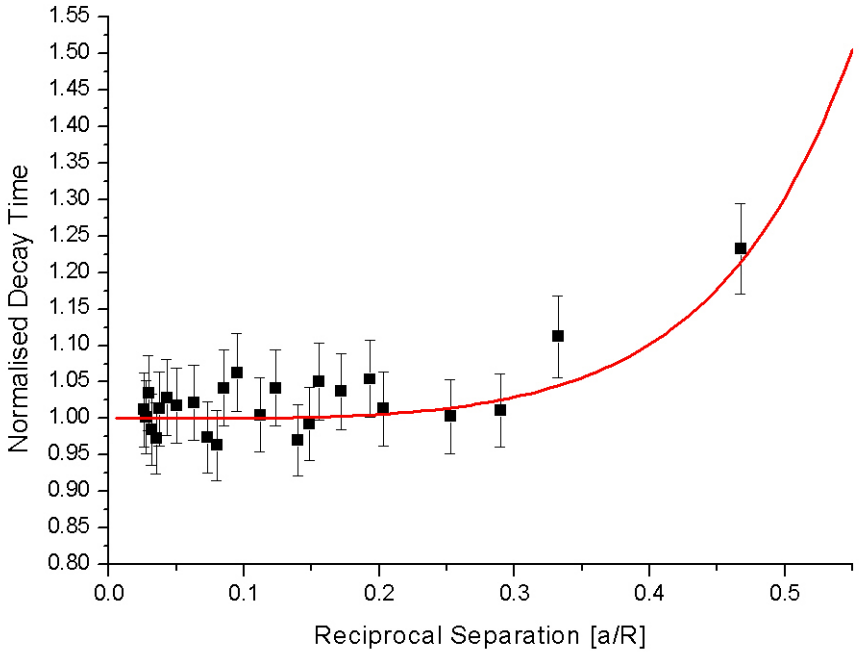


Figure 6.16: Normalised initial decay time of the autocorrelation function of a particle in the presence of a second particle as a function of normalised reciprocal separation. Red line is the theoretical values found in [8].

theoretical values.

The autocorrelations of the trapped particles will also deviate from a single exponential decay and instead be described by a double exponential decay, where the exponential terms in equation 6.2 are added together,

$$h_{1,1}(\tau) = \frac{1}{2}\left(e^{-\frac{\kappa\tau}{\xi_+}} - e^{-\frac{\kappa\tau}{\xi_-}}\right). \tag{6.14}$$

The friction coefficients can be extracted from fits to the autocorrelation function specifically by using the initial decay time, $\tau_s$, where $\tau < 50$ms. The decay time is expected to have the form [8],

$$\frac{\tau_s}{\tau_0} = \frac{\xi^{\parallel}_{1,1}}{\xi_0}\left(1 - \left[\frac{\xi^{\parallel}_{1,2}}{\xi^{\parallel}_{1,1}}\right]^2\right). \tag{6.15}$$

The decay time has been normalised by the decay time of the autocorrelation of a single particle not in the presence of any other particles, $\tau_0 = \xi/\kappa$. The decay times for bare

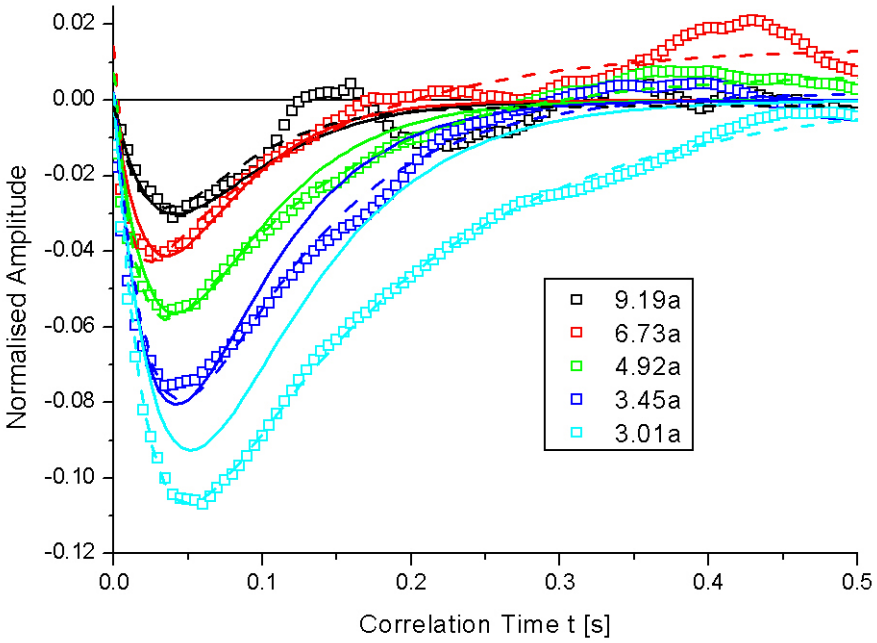


Figure 6.17: Cross-correlated motion of the two particles in the transverse direction. Showing a lower amplitude than the cross-correlated motion in longitudinal direction. Solid lines are the predictions derived from the Oseen tensor and dashed lines are double exponential fits to the data. Every 10th point is plotted for the experimental data shown.

solvents are shown in figure 6.16.

The data shows good agreement with the predicted values although using this method is less sensitive as fewer data points are used to determine the coefficients and the error on the measurement is large enough that only at normalised reciprocal separations of $\frac{a}{R} > 0.4$ would the prediction is greater than a standard deviation for a measurement made at much smaller reciprocal separations.

The cross-correlated motion of the particles in the transverse direction was measured (figure 6.17) and the friction coefficients (figures 6.18 and 6.19) and decay times for two particle the autocorrelation function (figure 6.20 this direction were determined.

The friction coefficients in the transverse direction also show good agreement with the theoretical predictions in the same region as the longitudinal direction and the deviations are also in the same region and deviate in the same direction as the those found in the longitudinal direction. This agreement also confirms that there is no overspill of the transverse cross-correlated motion during the measurement of the cross-

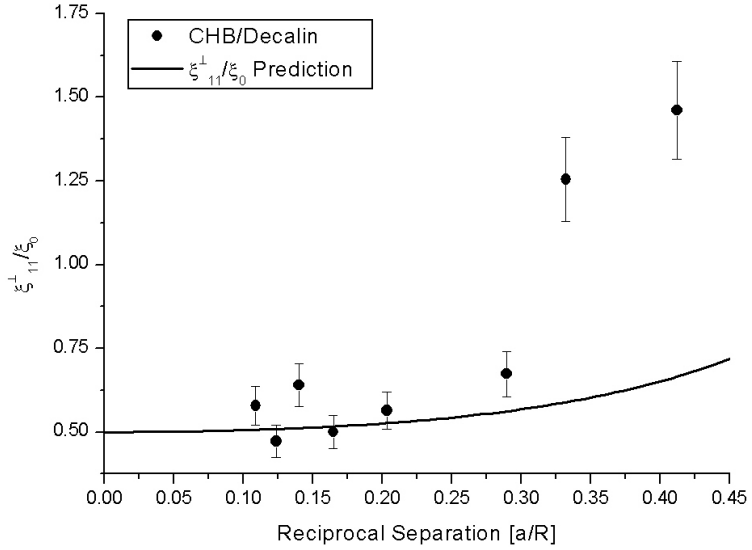


Figure 6.18: Friction coefficient $\xi^{\perp}_{1,1}$ in the transverse direction as a function of normalised longitudinal reciprocal separation $\frac{a}{R}$.

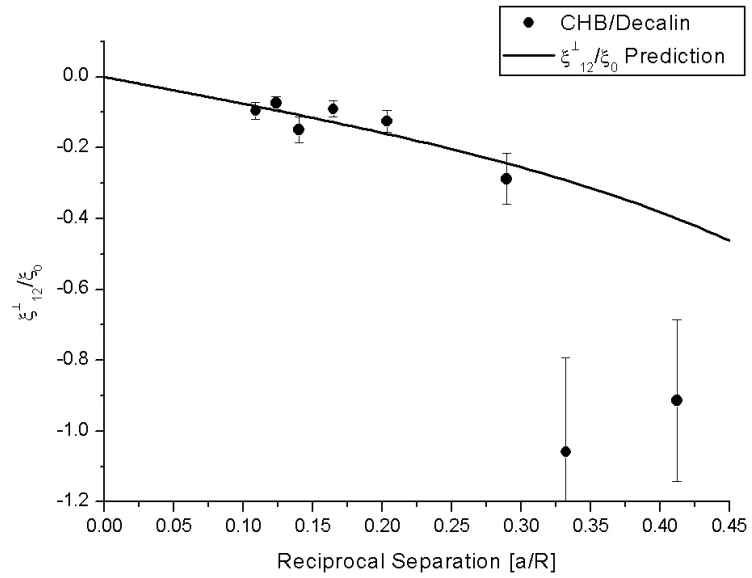


Figure 6.19: Friction coefficient $\xi^{\perp}_{1,2}$ in the transverse direction as a function of normalised longitudinal reciprocal separation $\frac{a}{R}$.

correlated motion in the longitudinal direction.

The decay times of the autocorrelations agree with the theoretical values across the full range of normalised reciprocal separations but the error on the measurement is as large as the deviation expected across the full range.

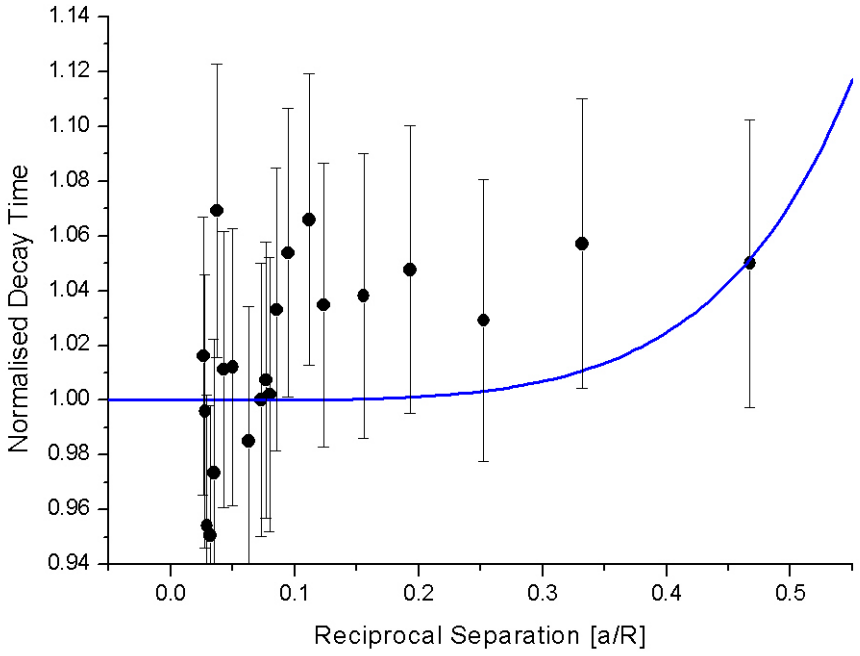


Figure 6.20: Normalised initial decay time of the autocorrelation function of a particle in the presence of a second particle in the transverse direction as a function of normalised longitudinal reciprocal separation. Blue line is the theoretical values found in [8].

The crosscorrelations in the vertical direction were not calculated as the potential of the optical trap in this direction was not symmetrical. Symmetry in the optical trap is required for the solutions of the Oseen tensor that have been used to determine the cross-correlated motion of the two tracer particles.

Two point passive micro-rheology using the cross-correlated motion of two particles of finite size can be used to measure the friction coefficients of the friction tensor provided the particles have a centre to centre separation $R > 4a$.

## 6.2 Finite Volume Fraction

In the last section the very dilute ($\phi \sim 10^{-4}$) suspensions of melamine particle were used to measure the cross-correlated motion of two particles, and from the cross correlation determine how the hydrodynamic interactions between the particles develop as they are brought closer together. In order to determine the hydrodynamic interactions that exist in hard sphere suspensions a second probe particle can be used and cross-correlated motion calculated, using the methods that have been outlined in the previous section.

In an attempt to determine when the use of equation 6.3 no longer holds the experiments were repeated with a suspension of small bath particles.

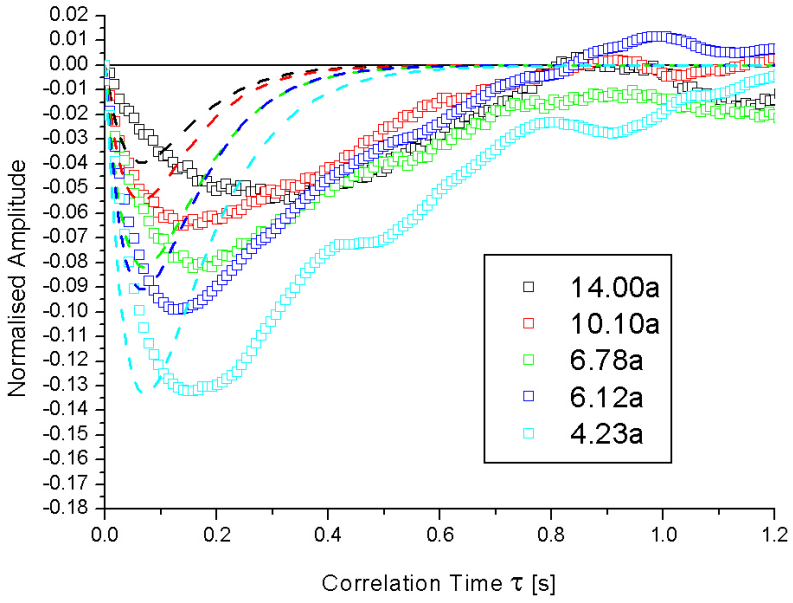


Figure 6.21: Cross-correlations for a selection of separations for two melamine particles with radius $a_{Melamine} = 0.969\mu$m in a suspension of bath particles with volume fraction $\phi = 0.02$ and radius $a_{small} = 133$nm. Solid lines are the predictions derived from the Oseen tensor and dashed lines are double exponential fits to the data. Every 10th point is plotted for the experimental data shown.

The small particles that were chosen were also synthesised by *Dr. Andrew Schofield*. The particles had also been previously characterised by him using static light scattering and were determined to have a radius of $a_{small} = 133$nm, more than seven times smaller that the melamine tracer particles that they were using in conjunction with.

As has been established the viscosity should have no effect on the amplitude of the anti-correlation and the first test would be use a suspension of hard-spheres with low

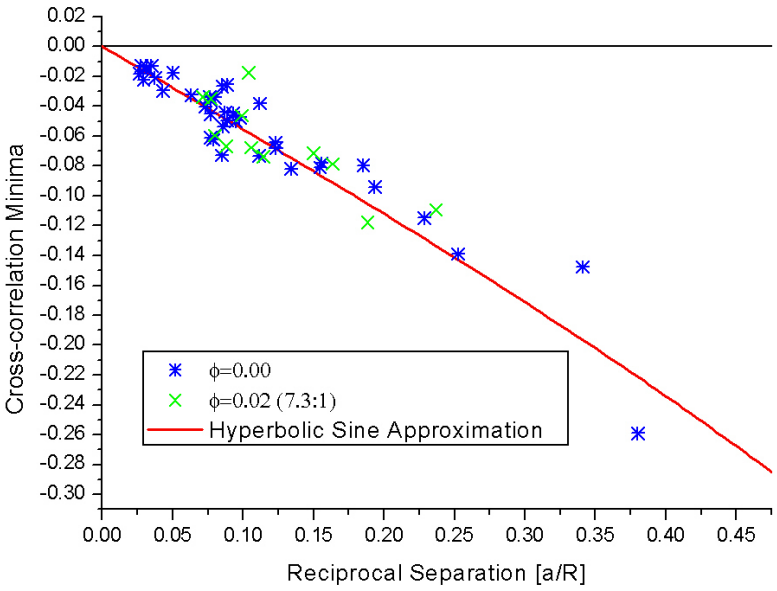


Figure 6.22: Minima of the anti-correlation of two particles in different suspensions. Blue asterisks correspond to probe particles suspended in solvent only. Red crosses correspond to a volume fraction $\phi = 0.02$ with bath and probe particles of approximately equal size.

volume fraction and calculate the maximum anti-correlation as a function of separation. A suspension of the small PMMA particles was prepared and doped with a dilute number of melamine particles using the methods described in chapter 4 and was then diluted down to a suspension with volume fraction $\phi = 0.02$ where the host solvent was the CHB/decalin mixture. A volume fraction of $\phi = 0.02$ was chosen as in this limit the Einstein correction to the viscosity of the suspension is valid for the bulk viscosity and in the case for the system that was used this corresponded to an increase in bulk viscosity of 5% [74].

$$\frac{\eta_{eff}}{\eta_0} = (1 + 2.5\phi) \tag{6.16}$$

The resultant crosscorrelations measured are shown in figure 6.21 alongside the predictions that were calculated from the Einstein viscosity and equation 6.3.

The first most noticeable feature is that the predictions do not give the correct time at which the anti-correlated minima occurs. Normally a shift in the position of $\tau_{min}$ in figure 6.28 would be explained by the optical traps having a weaker stiffness, this was not the case where the stiffnesses were kept roughly the same for all experiments

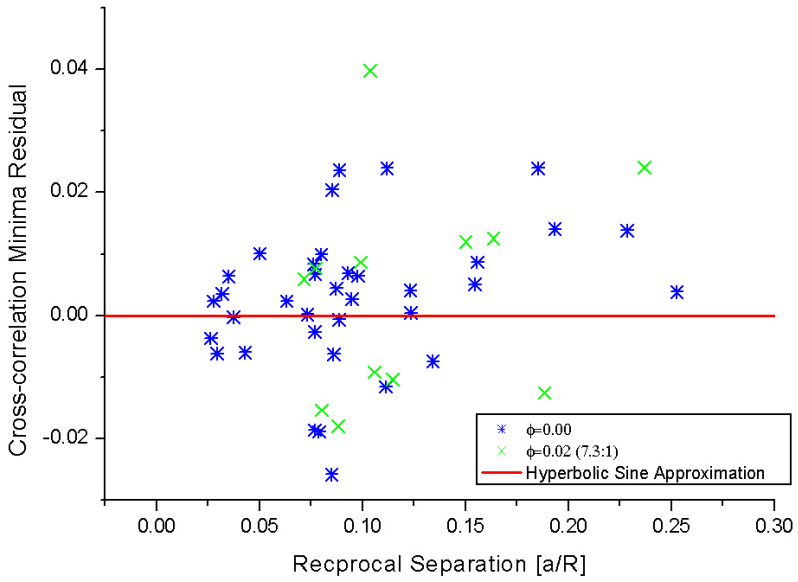


Figure 6.23: Residuals of the data presented in figure 6.22

.

described here. That the time has shifted in the positive direction may not be too surprising as whilst the bath particles are smaller than the two melamine particles the bath particles still cannot be considered as point-like particles as the solvent particles can. The addition of colloidal particles to the system increases the time it takes for the anti-correlation minima to occur than it would for a system with out the particles but of an equivalent viscosity. The other striking feature is that the amplitude of the anti-correlations that are predicted is quite close to the values determined by the experiment confirming the that the amplitude of anti-correlation should be independent of the fluid viscosity. This can be seen and confirmed in figure 6.22.

The minima for the smaller particles shows good agreement with equation 6.7 which shows that the predictions derived from the Oseen tensor for the minima of the anti-correlation are valid for the continuum limit.

The shift in the time where, the anti-correlation occurs in both figures 6.7 and 6.21 gives an easily identified feature of cross-correlation analysis that can determine if a dilute dispersion of colloidal particles is present in a system, that may not be readily visible in a microscope. Anti-correlation minima time, $\tau_{min}$ as a function of normalised reciprocal separation for the smaller particles is shown in figure 6.24.

The anti-correlation time minima for the suspension with small bath particles

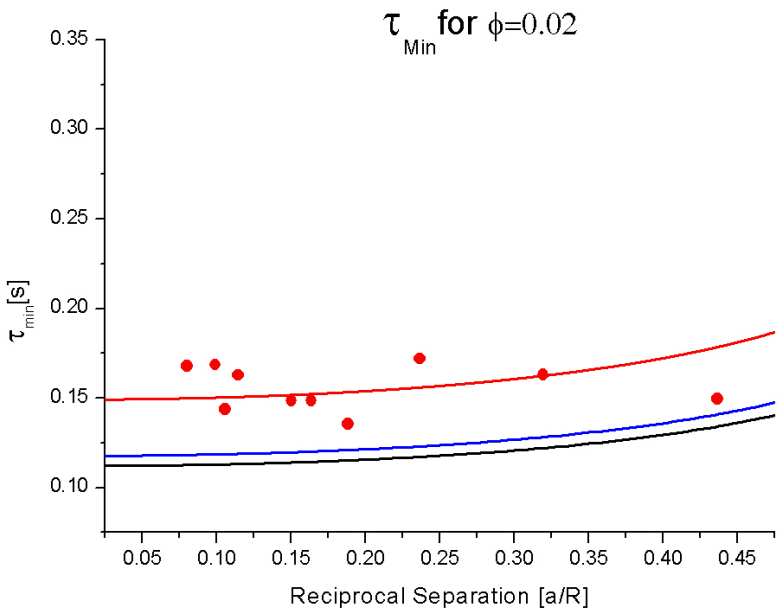


Figure 6.24: Anti-correlation time minima $\tau_{min}$ for bath particles with radius $a$ = 133nm (red circles) where a fit has been used to find the red line.

remains roughly constant. Simple modifications to include the relative particle sizes in equation 6.5 did not produce a curve that agreed with the data. Instead a numerical fit was made from the theoretical form of the prediction for a suspension with volume fraction $\phi = 0.02$ but with a variable amplitude term, which in figure 6.24 was determined to be 1.267s.

### 6.2.1 Friction Coefficients for Finite Volume Fraction

From the information that has been presented so far it can be said that modifications to equation 6.3 using the Einstein approximation for viscosity (equation 6.16) to determine the cross-correlated motions between two particles in a dilute suspension of bath particles is not valid due the change in the correlation time that the anti-correlation appears at, $\tau_{min}$. The friction coefficients of this system should give information that could explain why there are deviations from theoretical predictions.

The longitudinal friction coefficients $\xi^{\parallel}_{1,1}$ and $\xi^{\parallel}_{1,2}$ were calculated from a double exponential fit (equation 6.9) in the same way as they were for bare solvent.

The longitudinal friction coefficients for the sample that had a volume fraction of $\phi = 0.02$ and bath particles with radius $a$ = 133nm are shown in figures 6.25 and 6.26.

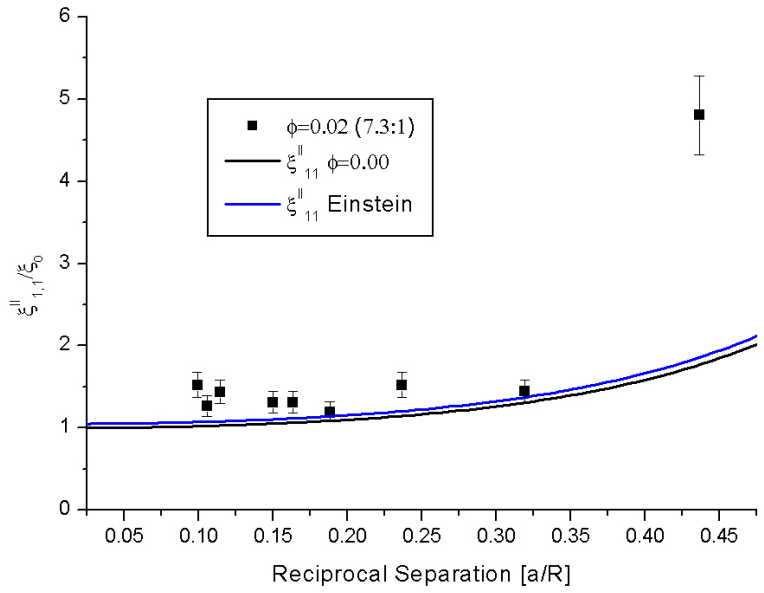


Figure 6.25: Longitudinal friction coefficient $\xi^{\parallel}_{1,1}$ for small particles showing a slight deviation from the theoretical values predicted for bare solvent (black line) and for Einstein correction to viscosity (blue line).

Both $\xi^{\parallel}_{1,1}$ and $\xi^{\parallel}_{1,2}$ appear to have reached a constant value with the exception of the last data point in figure 6.25 where it has been established that much greater deviations are expected, the associated data point in figure 6.26 has not been included as it is more negative than the range shown. The slight deviation of $\xi^{\parallel}_{1,1}$ tells us that the suspension of colloidal particles causes a trapped particle to experience greater hydrodynamic force caused by itself. The much larger deviation of $\xi^{\parallel}_{1,2}$ tells us that the solvent particles suppress the hydrodynamic forces that one particle experts upon another. In effect the small bath particles are reflecting some of the hydrodynamic forces back to the trapped particles and absorbing the some of the hydrodynamic forces between the two trapped particles.

The normalised decay time of the autocorrelations are shown in figure 6.27 which show that the decay time agrees with the theoretical values to within error. This is not surprising given that the normalised decay time, $\tau_s/\tau_0$, (equation 6.15) is more dependant on $\xi_{1,1}$ for small values of $\xi^{\parallel}_{1,2}$.

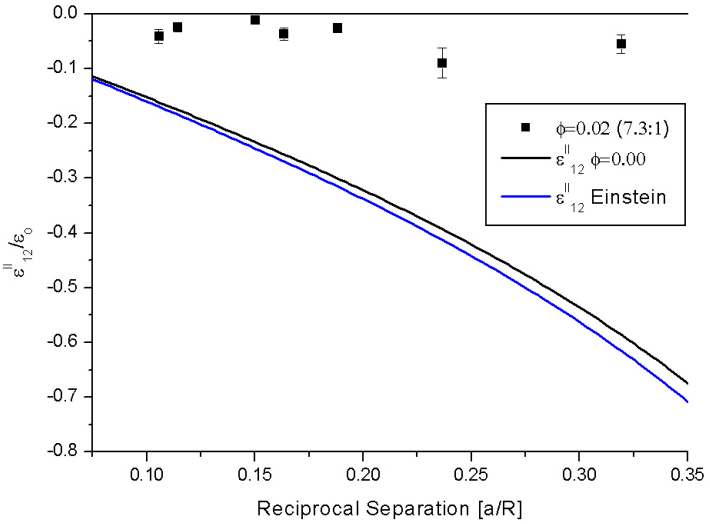


Figure 6.26: Longitudinal friction coefficient $\xi^{\parallel}_{1,2}$ for small particles showing a slight deviation from the theoretical values predicted for bare solvent (black line) and for Einstein correction to viscosity (blue line).

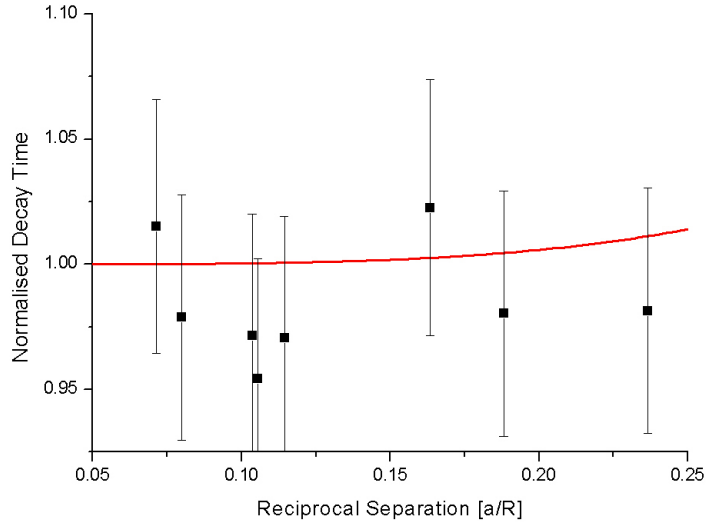


Figure 6.27: Normalised initial decay time of the autocorrelation function of a trapped particle in a suspension of hard spheres with radius $a = 133$nm and a volume fraction of 0.02 in the presence of a second trapped particle for the longitudinal direction as a function of normalised longitudinal reciprocal separation.

## 6.3 Larger Bath Particles

The suspension with bath particles that are smaller that the trapped particles has shown that the amplitude of the minima of anti-correlation is independent of viscosity holds for the continuum limit but the time that the anti-correlation increases from what is expected and the friction coefficients deviate from the theoretical predictions. Are these deviations typical for when there are colloidal particles in the suspension? Another suspension also with volume fraction $\phi = 0.02$ was made using bath particles that had a radii that were roughly the same as the melamine particles, the same bath particles that were used in chapter 5 and characterised in chapter 4.

The cross correlations for this suspension is shown in figure 6.28.

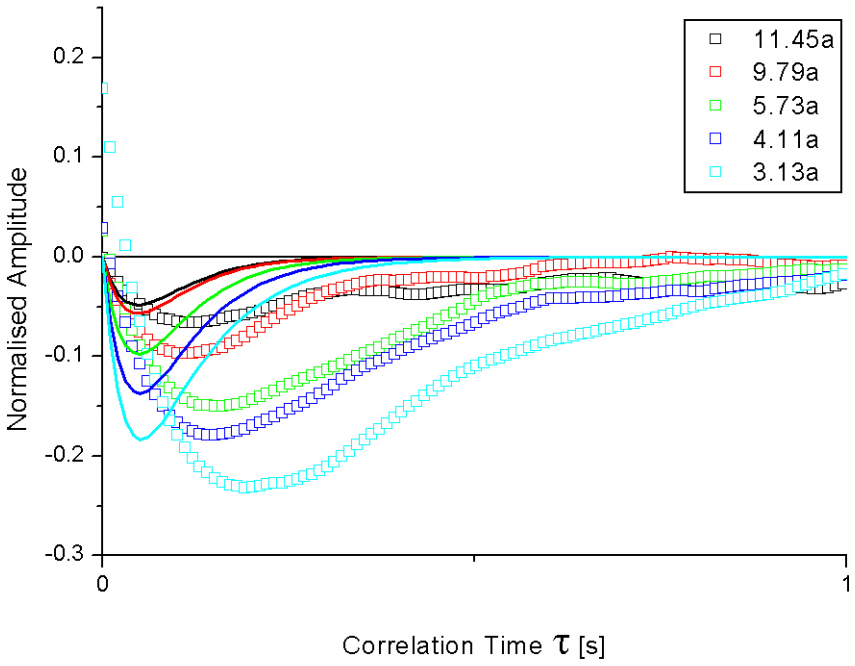


Figure 6.28: Longitudinal cross-correlated motion of two particles in a suspension of colloidal particles with a volume fraction $\phi = 0.02$ with the predicted curves of hydrodynamic coupling in a continuum described by equation 6.3 shown as solid lines. Every $10th$ point plotted for clarity.

Like the cross-correlations for the suspension with small particles there is a noticeable deviation from the predictions in the time at which the anti-correlation should occur. Giving a clear indicator that a dilute suspension of colloidal particles are present in the fluid. The second feature is that the amplitude of the anti-correlation

is deeper than what is expected. The presence of the larger bath particles either slows the anti-correlated relaxation of the two particles or enhances the correlated relaxation. The final feature that is just noticeable is that at very short correlation times $\tau < 0.04$s the cross correlated motion of the two particles is positive, this is not an artefact of a single data set but reproducible effect. Figure 6.29 shows this feature in detail where the absolute values of the cross-correlated motion has been plotted on a log-log plot.

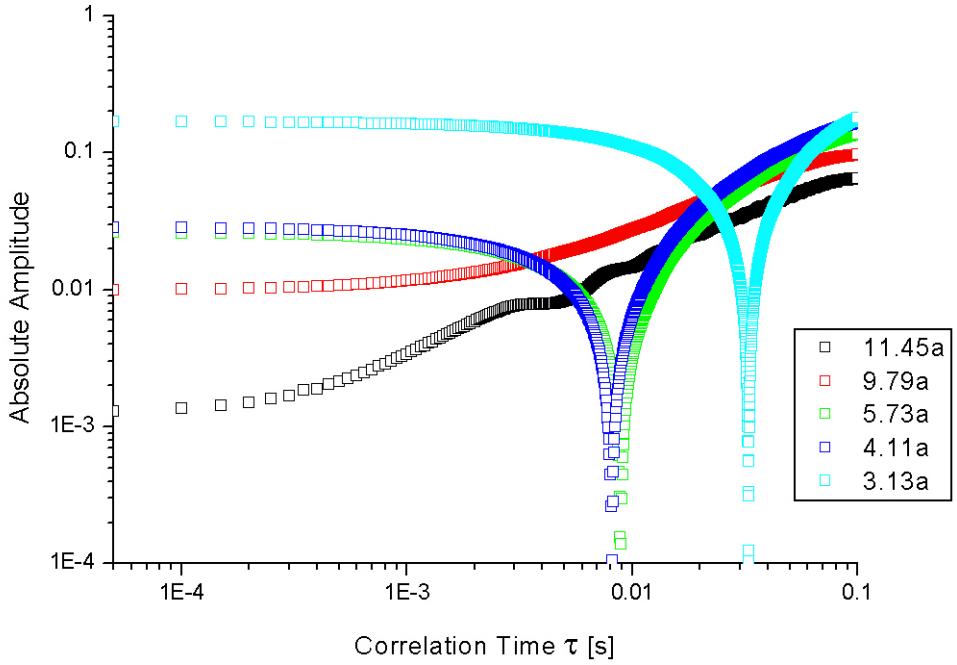


Figure 6.29: Enlarged section of the data shown in figure 6.28 for correlation times $0.00s < \tau < 0.04s$.

It appears that at zero correlation time $\tau = 0$s correlated motion is tending towards a constant value that is increasing as the centre to centre separation decreases and for a short period of time the two particles correlated motions. This would imply that at any instance during the measurement both particles will be moving in the same direction (but not necessarily with same magnitude). This has the problem that the second particle is moving before the hydrodynamic wave, induced by the first particle, arrives at its surface. This of course defies the laws of causality. The only interpretation is that the cross-correlated motion does indeed have zero amplitude at correlation time, $\tau = 0s$, but the hydrodynamic coupling propagates faster than is resolvable by the

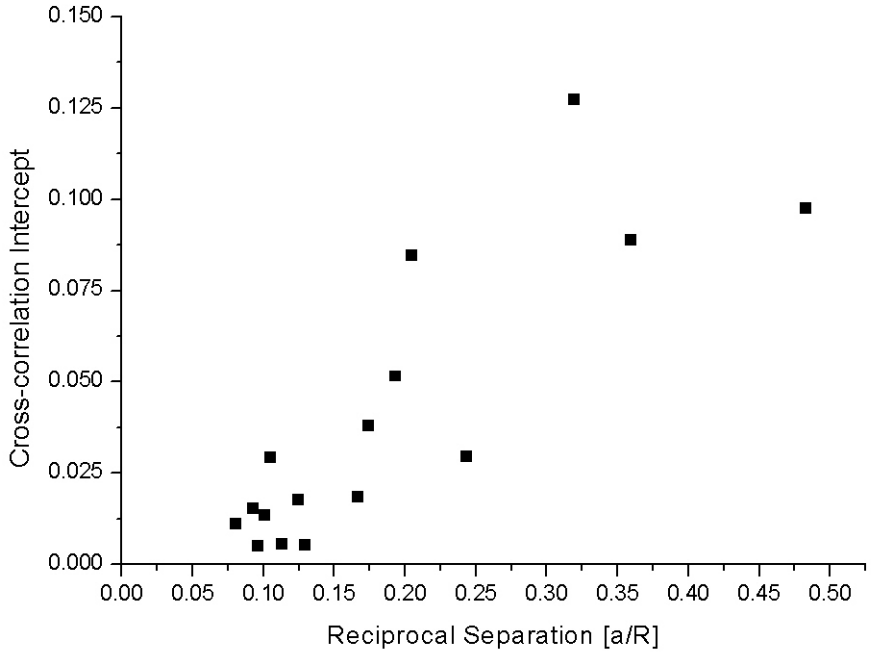


Figure 6.30: Intercepts of the cross-correlated motion with the correlation axis of two particles in a suspension with volume fraction $\phi = 0.02$ as a function of normalised reciprocal separation.

system ($\sim 10^{-5}s$). Larger bath particles cause a delay in the relaxation of the correlated mode between the two particles at short correlation times.

In order to determine how the correlated motion develops a plot of the intercept with the correlation axis was made as a function of reciprocal position.

The intercept can be seen to be increasing the closer the particles are and a suggestion from the last two data points that it will reach a plateau value where the initial correlated motion is approximately the same as the amplitude of the anti-correlation minima for when the particles are at their closest approach. However there is a large amount of scatter that makes the determination of any relation difficult.

The previous suspension in the continuum limit showed no variation in the amplitude of the anti-correlation this is not the case for when the bath particles are the same size as the trapped particles, figures 6.31 and 6.32 show the minima and their residuals respectively. The residuals of the minima show that for normalised reciprocal separations $\frac{a}{R} < 0.15$ the minima agree with the minima measured for bare solvent. Above this threshold where the minima of the bare solvent deviated from equation 6.7

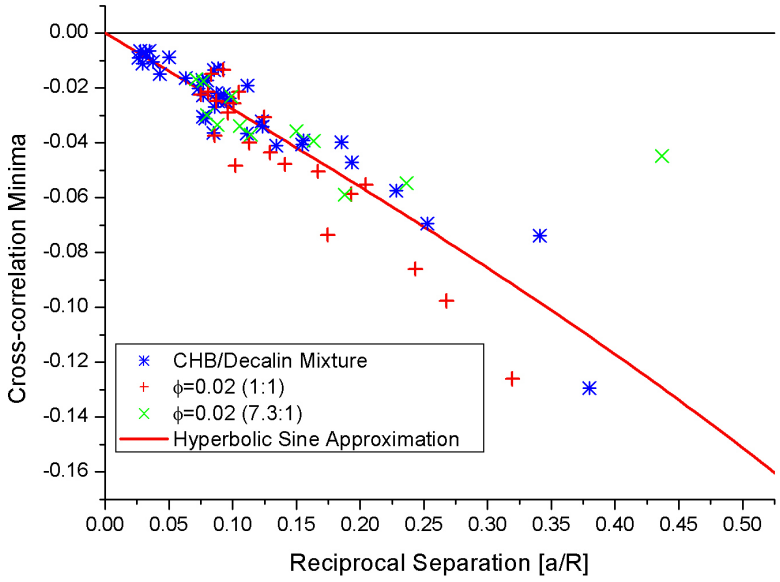


Figure 6.31: Minima of the anti-correlation of two particles in different suspensions. Blue asterisks correspond to probe particles suspended in solvent only. Red crosses correspond to a volume fraction $\phi = 0.02$ with bath and probe particles of approximately equal size. Green $\times$'s correspond to a volume fraction $\phi - 0.02$ with bath particles $\sim 7.3$ times smaller than the probe particles. The large particles show a deeper minima.

in the positive direction we see instead that the deviations in the sample with volume fraction $\phi = 0.02$ are in the negative direction. This shows that the addition of larger bath particles no longer means that the anti-correlation produced is independent of the suspensions viscosity. It also shows that the evolution of the minima with normalised reciprocal separation is only sensitive to the relative size difference of the probe particles to the bath particles.

Figure 6.33 shows how $\tau_{min}$ increases with normalised reciprocal separation in comparison to the predicted values determine by equation 6.5.

As can be seen $\tau_{min}$ begins to strongly deviate from the predicted values at normalised reciprocal separations of $\frac{a}{R} > 0.15$ (centre to centre separation of $R \approx 6.5a$), which corresponds to when the minima for the cross-correlations deviate from their predicted values for bare solvent. Given the form of equation 6.5 it is possible that the viscosity of the suspension in these close regions may not be equivalent to the bulk of the system. Future work would be to determine at what size of bath particles would

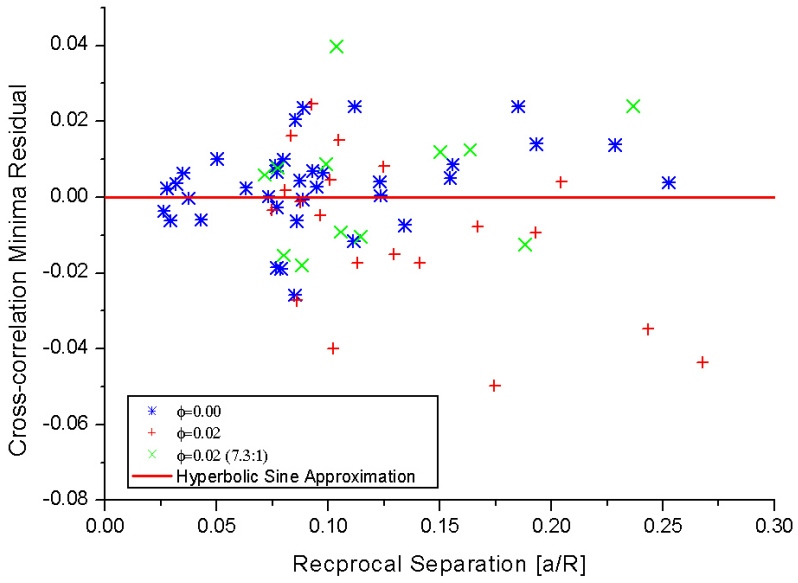


Figure 6.32: Residuals for the the amplitude of the minima for bare solvent and for suspensions with volume fraction $\phi = 0.02$.

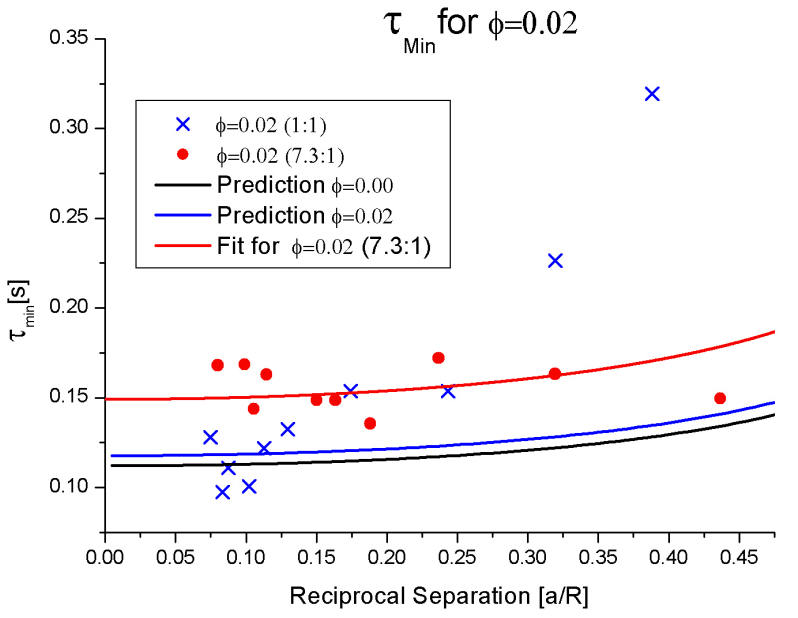


Figure 6.33: Anti-correlation time minima $\tau_{min}$ for both large bath particles (blues $\times$'s) and the smaller particles (red circles) where a fit has been used to find the red line.

greater deviation from a roughly constant value be observed. However whether the bath particles are the same size as the probe particles or if they are smaller than them neither data set agrees fully agrees with the predictions made by equation 6.5.

### 6.3.1 Friction Coefficients for Larger Particles

The longitudinal friction coefficients for the bath particles with radii approximately equal to the melamine particles $a \approx 0.9$ were measured and $\xi^{\parallel}_{1,1}$ and $\xi_{1,2}$ are shown in figures 6.34 and 6.35 respectively.

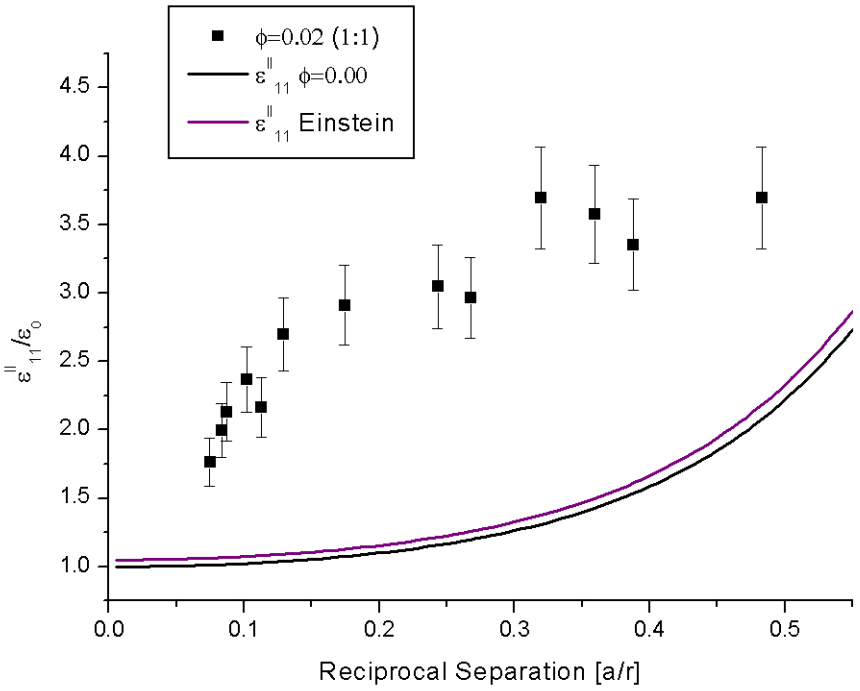


Figure 6.34: Longitudinal friction coefficient $\xi^{\parallel}_{1,1}$ where the bath particle have the same size as the probes, showing deviation from the theoretical values predicted for bare solvent (black line) and for Einstein correction to viscosity (purple line).

Both $\xi^{\parallel}_{1,1}$ and $\xi^{\parallel}_{1,2}$ deviate from theoretical values and both appear to be converging to a constant value when the particles become close. Given that the depth of the anti-correlated minima was deeper than for bare solvent and the time at which the anti-correlation was observed also did not agree with the predicted values the deviations observed in these results are not surprising. The large deviation in $\xi^{\parallel}_{1,1}$ tells us that the trapped particles experience stronger hydrodynamic forces caused by itself than when the in a suspension of smaller particles or when in bare solvent. Unlike the

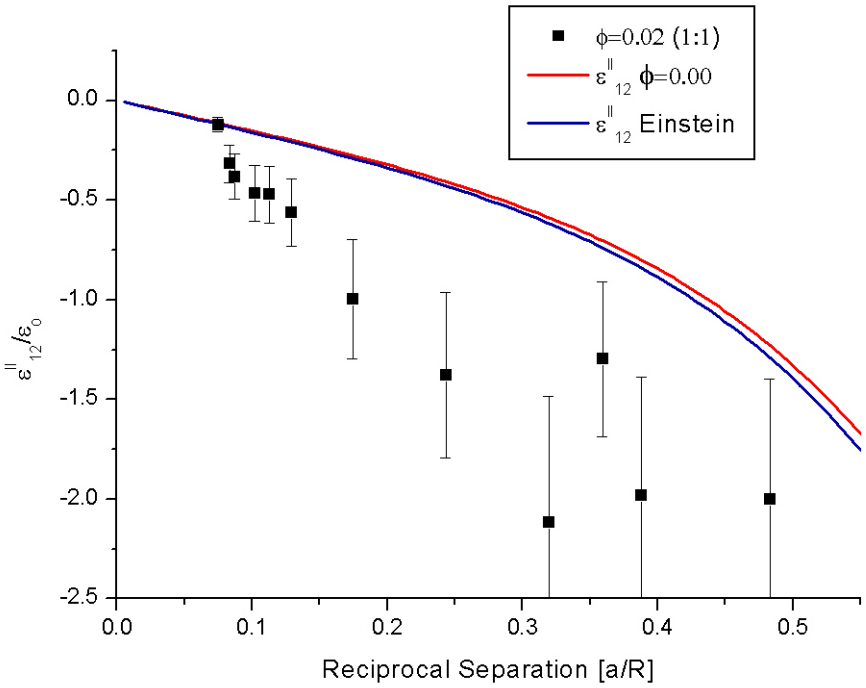


Figure 6.35: Longitudinal friction coefficient $\xi^{\parallel}_{1,2}$ where the bath particle have the same size as the probes, showing deviation from the theoretical values predicted for bare solvent (black line) and for Einstein correction to viscosity (red line).

case for a suspension with smaller particles the deviation from the theoretical values in $\xi^{\parallel}_{1,2}$ is in the negative direction and as such the hydrodynamic forces between the particles increases when the bath particles are approximately the same size as the trapped particles. It is conceivable that there is an intermediate size of particle that will give a friction coefficient $\xi^{\parallel}_{1,2}$ that agrees with the theoretical values for bare solvent, however the measurement of $\xi^{\parallel}_{1,1}$ for the intermediate size of particles will be greater than their theoretical values. With only two data sets to compare the radius of these particles cannot as yet be determined.

The decay times for the autocorrelations, figure 6.36, also deviate from the theoretical values for bare solvent and again is not surprising and shows that the presence of a dilute suspension of particles with radius approximately equal to that of the trapped particles can be detected using the initial time decay of the autocorrelation function.

Whilst $\xi^{\parallel}_{1,1}$ and $\xi^{\parallel}_{1,2}$ specifically tell us how how a particle interacts with itself and another particle it is perhaps intuitively easier to understand how the correlated

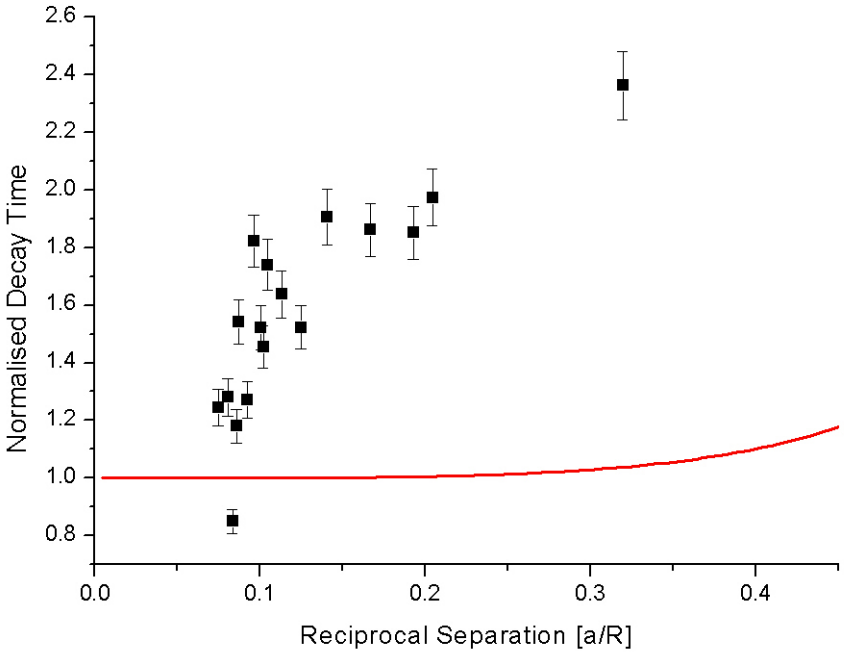


Figure 6.36: Normalised initial decay time of the autocorrelation function of a trapped particle in a suspension of hard spheres with volume fraction of 0.02 and in the presence of a second trapped particle for the longitudinal direction as a function of normalised longitudinal reciprocal separation.

and anti-correlated friction coefficients $\xi_+^{\parallel}$ and $\xi_-^{\parallel}$ behave as a function of normalised reciprocal separation.

### 6.3.2 $\xi_+^{\parallel}$ and $\xi_-^{\parallel}$ Friction Coefficients

For the small particles both $\xi_{1,1}^{\parallel}$ and $\xi_{1,2}^{\parallel}$ appeared to have reached a constant value and given how $\xi_+^{\parallel}$ and $\xi_-^{\parallel}$ are defined (equations 6.12 and 6.13) they would both be constant. The larger bath particles however show more deviation in $\xi_{1,1}^{\parallel}$ and $\xi_{1,2}^{\parallel}$ and their correlated and anti-correlated frictions should change as a function of normalised reciprocal separation, figure 6.37.

Both the correlated and anti-correlated frictions increase rapidly and seem to be converging to constant values with the anti-correlated friction being greater than the correlated friction. That the anti-correlated friction is greater because the anti-correlated motion of the two particles has to squeeze and the fluid located between the two particles unlike to correlated motion.

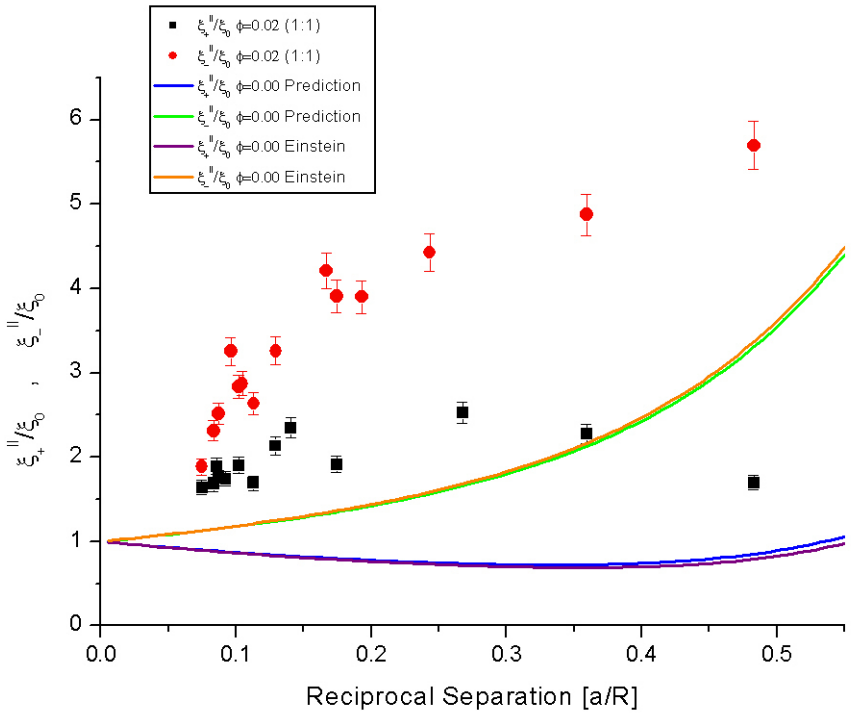


Figure 6.37: Normalised longitudinal friction coefficients for correlated motion (black squares) and anti-correlated motion (red circles) for a suspension of volume fraction $\phi = 0.02$ with radius $a = 0.90\mu$m.

The cross-correlated motion in the transverse direction was measured but found to exhibit noise that made fitting the double exponential to extract the friction coefficients difficult. Noise in the transverse direction has been reported for other systems using cross-correlation analysis [81] although an explanation for the additional noise has not been established.

Two point micro-rheology can be used to determine the friction coefficients for finite dilute suspension of hard spheres where the bath particles may not have the same radius as the particles held in the optical traps.

## 6.4 Screening limit

An attempt to extend to the techniques developed here to more concentrated suspensions of colloidal particles with the same size as the probe particles was made.

A volume fraction of $\phi = 0.10$ was made and measurements carried out in the same

manner as was outlined previously. The cross correlations were measured and shown in figure 6.38.

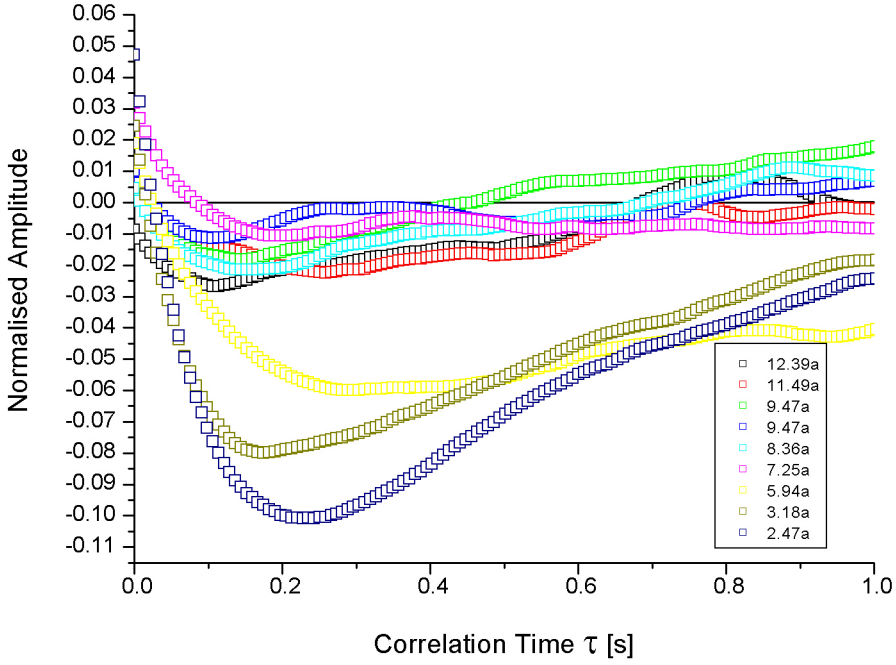


Figure 6.38: Cross-correlated motions of two particles in a suspension with volume fraction $\phi = 0.10$ at various separations.

The data for when the particles are far apart do not show curves of the form that would be expected, with very few showing an anti-correlation if any. Comparison of the green and the blue data sets, which have the same separation, show that the data is not reproducible. Once the particles come very close together the curves take on the form that is expected. Without data that resembles a double exponential the friction coefficients for this more dense suspension cannot be determined.

The two curves in figure 6.38 that show a clear correlation minima ($R = 3.18a$ & $R = 2.47a$) correspond to separations where a bath particle cannot fit between the two particles. The minima also agree well with the hyperbolic sine approximation, equation 6.7, but do not show any enhanced anti-correlation that was observed in the sample with volume fraction $\phi = 0.02$. There are only two points and further investigation of this region would be needed to determine when the cross-correlations become irreproducible.

The irreproducibility of the cross-correlations suggest that the surrounding particles effectively screen the hydrodynamic interactions between the two probe particles and it is not until the bath particles can no longer fit between the probes that this screening breaks down. However once in this region the surrounding bath particles effectively screen all the other particles in the system and as a result the two probes only measure the cross-correlations that would be associated with bare solvent.

Future work in this area would be to determine the maximum separation for the particles to experience the predicted anti-correlation and be reproducible and then to reduce the volume fraction to determine how the cross-correlated motions found in a volume fraction $\phi = 0.02$ gradually get suppressed.

## 6.5 Conclusions

If two point passive micro-rheology is to be carried out using the techniques that have been described in here the longitudinal angle $\beta$ between the two probe particles must be readily measurable to ensure that the cross-correlated motions of the probes are not diluted by contributions from the motions in the transverse directions.

In the case of bare solvent, when a very small number of probe particles are dispersed in a fluid without any particles the anti-correlation minima will agree with the hyperbolic sine prediction, equation 6.7, for centre to centre separations of $R < 6.5a$ for any solvent and is independent on the viscosity of the solvent used.

$$\frac{\langle x_{(1)}(t)x_{(2)}(t+\tau_{min})\rangle}{\sqrt{\langle x_{(1)}^2\rangle\langle x_{(2)}^2\rangle}} = -\frac{1}{e}\sinh(\epsilon)$$

For separations $R > 6.5a$ the anti-correlation will be less than the absolute value predicted. Higher order corrections to the Oseen tensor, from which the equation is derived, are insufficient to account for this difference. There is evidence in the system used here that the deviation could be due to wall effects but work carried out elsewhere with the same boundary conditions refute this. It is also possible that at these separations the particles begin to affect each other in ways not described by the Oseen tensor because the particles have a finite size and are not point like.

The friction coefficients $\xi_{1,1}$ and $\xi_{1,2}$ for both the transverse and longitudinal directions can be extracted from the cross-correlated motions of two particles and agrees with the theoretical values for bulk rheology.

In a dilute suspension of particles with volume fraction $\phi = 0.02$ and radius much

less than that of the probe particles the cross-correlated motion will show agreement with equation 6.7 for the value that the anti-correlated minima takes, but the time at which it occurs will be delayed. The delay time is suspected to be related to the relative size difference between the bath particles and probe particles that are used but no direct relation was found as only one size of small particles was investigated. The difference in the time at which the anti-correlation is expected to occur allows the technique to be used to determine if small colloidal particles are present in a fluid when they are may not be visible in a microscope.

The friction coefficients $\xi^{\parallel}_{1,1}$ and $\xi^{\parallel}_{1,2}$ for bath particles are constant across all separation ranges.

For a dilute suspension with volume fraction $\phi = 0.02$ and bath particles with the same radius as the probe particles the cross-correlations will not agree with predictions derived from the Oseen tensor when used in conjunction with the Einstein correction to the viscosity. The absolute value of the anti-correlation will be greater than the values predicted by equation 6.7. The time at which the anti-correlation occurs will also be greater than what is predicted. The combination of these two observations allows the determination of the presence of a dilute suspension of colloidal particles that are the same size as the probes in the solvent even if they have the same refractive index as the fluid.

The friction coefficients $\xi^{\parallel}_{1,1}$ and $\xi^{\parallel}_{1,2}$ for a dilute suspension can be extracted from the cross-correlated motions of two particles held in the optical traps where the bath particles may have radius equal to or less than the trapped particles, whereas the corresponding coefficients for bath particles roughly the same size as the trapped particles vary with particle separation.

The correlated and anti-correlatied friction coefficients, $\xi^{\parallel}_{+}$ and $\xi^{\parallel}_{-}$, was found to grow with decreasing particle separation until particles were separated by roughly $R = 6.5a$. At separations less than this friction coefficients appear to converge to a constant value. The anti-correlated friction is always greater than the correlated friction due to the correlated motion being dissipative than the anti-correlated motion where the particles have to squeeze the fluid in the gap between them.

# Chapter 7

# Conclusions and Future Work

This chapter summaries the conclusions that have been made from the material that has been presented in this thesis and goes on to describe future work that can be carried out to either improve or expand on the information that has already been gathered.

## 7.1 One Point Micro-Rheology

### 7.1.1 Passive Micro-Rheology

In chapter 5 the one point passive micro-rheology experiments to measure the microviscosity, $\eta_{\mu}^{(Passive)}$, of colloidal hard sphere suspensions with volume fraction below the glass transition, was shown to be in agreement to within one standard deviation of established microviscosity measurements using dynamic light scattering made by van Megen *et al.*[5].

### 7.1.2 Active Micro-Rheology

The full range of shear thinning behaviour in the active microviscosity, $\eta_{\mu}^{(Active)}$, for was observed for Péclet numbers in the range $0.3 < Pe < 200$ for suspensions with volume fractions $\phi > 0.45$. Below this volume fraction the low shear microviscosities were in the resolution limit of the optical tweezers but all high shear microviscosities were above this limit.

The microviscosities measured in the high shear regime have been found to agree with established measurements for the bulk viscosity of similar hard sphere systems that were made by Phan *et al.* [18].

The microviscosities measured in the low shear regime, above the resolution limit of the optical tweezers, were found to be in agreement with the established bulk viscosity measurements also found in [18] but only once the microviscosities had been converted

from the values determined by constant velocity dragging to those that would have been measured had constant force dragging been used instead. The conversion was made using equation 5.15 found in [68],

$$\frac{\eta_\mu^{(U)}}{\eta_0} = 2\frac{\eta_\mu^{(F)}}{\eta_0} - 1.$$

## 7.2 Two Point Micro-Rheology

### 7.2.1 Bare Solvent

In chapter 6 the cross-correlatied motion of two particles held in the optical traps that were suspended in various solvents, in all cases the amplitude of the minima agreed with the theoretical predictions for when the particles had a centre to centre separation of $R > 6.5a$ and was shown to be independent of viscosity. For particles with a centre to centre separation of $R < 6.5a$ the measured amplitude of the minima was found to deviate in the positive direction. This deviation is mostly caused by the fact that the particles that were used had finite size and at these close separations the particles interact with each other in a manner that is not described by the Oseen tensor alone.

The friction coefficients $\xi_{1,1}$ and $\xi_{1,2}$ in both the longitudinal and transverse directions were also found to agree with the theoretical predictions for centre to centre particle separations of greater than $R = 3.5a$ for the solvents that were used. The initial decay times of the autocorrelation function in the longitudinal direction, $\tau_s/\tau_0$, was also found to agree with theoretical predictions for the same range of particle separations before deviations were observed. The transverse initial decay time was found to agree with the predicted theoretical values for the full range of separations measured but the standard deviation of the data was roughly the same size as the expected deviation across the same range of particle separations.

### 7.2.2 Finite Volume Fraction

For a suspension of colloidal hard spheres with volume fraction $\phi = 0.02$ when the bath particles, where more than 7 times smaller $a_{bath} = 133$nm than the trapped particles ($a_{Melamine} = 0.96\mu$m), the amplitude of the minima of the cross-correlated motion remained unchanged for centre-to-centre particle separations of $6.5a$. However when bath particles with a radius of approximately the same as the trapped particles were used instead for the same volume fraction the amplitude of the cross-correlation minima became more negative over this region, indicating that the amplitude of the

cross-correlated motion is dependant on the relative particle sizes between the bath particles and the trapped particles.

A feature that was only found in the suspension with bath particles approximately the same size as the trapped particles was that at short correlation times $\tau < 0.4s$ the cross-correlated motion of the two particles was correlated. The initial correlated motion was found to be reproducible and grow with decreasing particle separation.

For both suspension the time at which the minimum of the cross-correlated motion occurred was found to be greater than the time time at which it occurred for bare solvent and was found to increase with decreasing particle separation. The suspension with bath particles of approximately the same size as the trapped particles had times that grew much more rapidly with decreasing particle separation than the suspension with smaller bath particles.

The longitudinal friction coefficients, $\xi^{\parallel}_{1,1}$ and $\xi^{\parallel}_{1,2}$, for the suspension with bath particles smaller than the the trapped particles were found to deviate from the predicted values. where the Einstein correction, equation 6.16, had been used to determine the fluid viscosity. They also appeared to have converged to constant values. In the case of $\xi^{\parallel}_{1,1}$ the deviation was in the positive direction indicating that the bath particles cause the trapped particle to experience a greater hydrodynamic forces induced by itself. The other friction coefficient, $\xi^{\parallel}_{1,2}$, also deviated from the predicted values in the positive direction but more strongly than $\xi^{\parallel}_{1,1}$ indicating that the bath particles are suppressing the hydrodynamic interactions between the trapped particles.

The equivalent longitudinal friction coefficients for the suspension with particles that had the approximately same radius as the trapped particles were also found to deviate from the predicted values but not in the same manner. The friction coefficient $\xi^{\parallel}_{1,1}$ deviated in the positive direction more strongly than the suspension with smaller bath particles. The friction was found to grow with decreasing centre to centre particle separation until a centre to centre separation of $R \approx 6.5a$ at which point it appeared to be converging towards a constant value. Again the friction that a trapped particle experience that has been induced by itself has been enhanced by the presence of the bath particles. $xi^{\parallel}_{1,2}$ deviated in the negative direction away from the predicted values becoming more negative until a centre to centre separation of $R \approx 6.5a$ where it also appeared to be converging towards a constant value. Unlike the case for the smaller particles the friction that a trapped particle experiences induced by a second trapped particle some distance away is stronger when the bath particles are approximately the same size at the trapped particles.

The initial decay times of the autocorrelations in the longitudinal direction for the suspension, $\tau_s/\tau_0$, with bath particles smaller than the trapped particles was found to be in agreement with predicted values to within the error of the instrument.

In the case of the suspension with bath particles approximately the same size at the trapped particles the initial decay times of the autocorrelations were found grow with deceasing centre to centre particle separations until a separation of $R \approx 6.5a$ where the initial decay time appeared to be converging towards a constant as would be expected as the friction coefficients for this suspension also behaved in a similar manner.

## 7.3 One Point Micro-Rheology Future Work

The one point micro-rheology could be improved by the inclusion of a confocal imaging system to determine the relaxation times of the structural deformations of the suspension when a single particle is being dragged through the suspension. It will also be able to determine how the particles in front of the probe are diffusing around it when the probe is being dragged at low shear rates; does the bath particles 'hold up' the tracer until it is in an area of the optical potential to bull doze its way through the build up?

The inclusion of the second optical trap during dragging experiments would allow a second particle to be dragged some distance behind the first to determine if there is any hysteresis caused by the first, such as whether or not it is harder or easier to move through an area that has previoulsy been dragged through.

Inclusion of a confocal imaging system would also allow the possible implementation of the shear cell that was described at the end of chapter 5 and be able to obtain information of the interparticle forces whilst the entire suspension is being sheared.

## 7.4 Two Point Micro-Rheology Future Work

The interactions between the two particles in the presence of bath colloids should be investigated to determine how the particle size of the bath particles affects the friction coefficients measured by the optical tweezers. The inclusion of a confocal imaging system should also be considered here as it would yield additional information on how the bath particles interact with the optically trapped particles.

# Appendix A

# Mean Square Displacement Corner Time Derivation

This appendix details the derivation of the corner time that was described in Chapter 2 but includes the laser power and sensitivity factors.

## A.1 Corner Time Derivation

The functional form of the mean squared displacements of an optically trapped particle is,

$$\langle \Delta x^2(\tau) \rangle = \frac{2k_B T}{\kappa} \left( 1 - e^{\frac{-\kappa\tau}{\varepsilon_0}} \right). \tag{A.1}$$

To determine the corner time $\tau_c$, the point at which the curve turns towards the long time plateau, equation A.1 was solved in the short time limit $\tau \ll 1$. In Chapter 2 this was done by expanding the exponential term,

$$\langle \Delta x^2(\tau) \rangle = \frac{2k_B T}{\kappa} \left( 1 - \left[ 1 + \frac{\left(\frac{-\kappa\tau}{\varepsilon_0}\right)}{1!} + \frac{\left(\frac{-\kappa\tau}{\varepsilon_0}\right)^2}{2!} + \ldots \right] \right). \tag{A.2}$$

The short time limit is given by the first order $\tau$ term from the expansion of the exponential term,

$$\begin{aligned} \lim_{\tau \to 0} \langle \Delta x^2(\tau) \rangle &= \frac{2k_B T}{\kappa} \left( 1 - \left[ 1 + \frac{-\kappa\tau}{\varepsilon_0} \right] \right) \\ &= \frac{2k_B T \kappa \tau}{\kappa \varepsilon_0} \\ &= \frac{2k_B T \tau}{\varepsilon_0}. \end{aligned} \tag{A.3}$$

It should be noted that in this limit the stiffness drops out of the expression and were we to include the actual description of the stiffness which is a function of laser power $\kappa(P)$ the two functions would still cancel.

The analytical expression for calculating the mean square displacements, equation 2.18 in Chapter 2, was evaluated in the long time limit $\tau \gg 1$ to determine the plateau value for the mean square displacements of a particle confined in an optical trap:

$$\langle \Delta x^2(\tau) \rangle = 2\sigma^2 - 2\langle x(t)x(t+\tau) \rangle. \tag{A.4}$$

The autocorrelation function is known to decay to zero in the long time limit as the longer in time the less a particle's original motion is likely to affect its current motion. Accordingly the autocorrelation is omitted in the long time limit,

$$\lim_{\tau \to \infty} \langle \Delta x^2(\tau) \rangle = 2\sigma^2. \tag{A.5}$$

In Chapter 2 it was at this point that equations A.3 and A.5 were equated and solved for $\tau$ to determine the corner time $\tau_c$. However the method that was used to balance the traps for the experiments described in Chapter 6 were made in volts not nano-metres and as each trap had differing sensitivities the expression in equation A.5 must be explored further.

## A.2 Conversion from Volts to Nano-metres

The definition of the variance of a data series of length $N$ is,

$$\sigma^2 = \frac{1}{N} \sum_{i=1}^{N} \left( x_i - \langle x \rangle \right)^2. \tag{A.6}$$

For the recorded data stream, that was used to balance the traps, the units of $x$ are volts. To convert this to nano-metrres the sensitivity $S$ of the trap needed to be used. The sensitivity like trap stiffness is a function of laser power $S(P)$, if we include this

in the definition of the variance we see that the sensitivity will be a simple prefactor:

$$\sigma^2 = \frac{1}{N}\sum_{i=1}^{N}\left(\frac{x_i}{S(P)} - \frac{\langle x\rangle}{S(P)}\right)^2 \tag{A.7}$$

$$= \frac{1}{N}\sum_{i=1}^{N}\frac{1}{S^2(P)}\left(x_i - \langle x\rangle\right)^2 \tag{A.8}$$

$$= \frac{1}{NS^2(P)}\sum_{i=1}^{N}\left(x_i - \langle x\rangle\right)^2 \tag{A.9}$$

$$\sigma^2 S^2(P) = \frac{1}{N}\sum_{i=1}^{N}\left(x_i - \langle x\rangle\right)^2. \tag{A.10}$$

Substituting the variance the variance in nano-metres into equation A.5 and equating it to equation A.3 and solving for $\tau$ to obtain $\tau_c$ gives,

$$2\sigma^2 S^2(P) = \frac{2k_B T\tau}{\varepsilon_0} \tag{A.11}$$

$$\tau_c = \frac{\sigma^2 S^2(P)\varepsilon_0}{k_B T}. \tag{A.12}$$

This give the corner time $\tau_c$ in the correct units.

## A.3 Equating Corner Times

To balance the stiffnesses of the two optical traps for the two point experiments described in Chapter 6 the corner times of the mean square displacements of each trap were equated. However as described in Chapter 3 the optical traps did not have identical functions of stiffness $\kappa(P)$ or sensitivity $S(P)$, although both were linear functions that will make the derivation easier.

As described earlier the stiffness of the optical trap cancels in the determination of the corner time but we are left with the sensitivity. The ratio of the corner times of each optical trap $\tau_{c(1)}$ and $\tau_{c(2)}$, where the subscript number denotes trap is,

$$\frac{\tau_{c(1)}}{\tau_{c(2)}} = \frac{\frac{\sigma^2_{(1)}S^2_{(1)}(P_{(1)})\varepsilon_0}{k_B T}}{\frac{\sigma^2_{(2)}S^2_{(2)}(P_{(2)})\varepsilon_0}{k_B T}} \tag{A.13}$$

$$= \frac{\sigma^2_{(1)}S^2_{(1)}(P_{(1)})}{\sigma^2_{(2)}S^2_{(2)}(P_{(2)})}. \tag{A.14}$$

When the corner times are equal and the two optical traps have identical stiffnesses the

ratio will be equal to unity,

$$\frac{\sigma^2_{(1)}S^2_{(1)}(P_{(1)})}{\sigma^2_{(2)}S^2_{(2)}(P_{(2)})} = 1 \tag{A.15}$$

$$\sigma^2_{(1)}S^2_{(1)}(P_{(1)}) = \sigma^2_{(2)}S^2_{(2)}(P_{(2)}) \tag{A.16}$$

$$\frac{\sigma^2_{(1)}}{\sigma^2_{(2)}} = \frac{S^2_{(2)}(P_{(2)})}{S^2_{(1)}(P_{(1)})}. \tag{A.17}$$

Accordingly the ratio of the variance (in volts) is inversely proportional to the ratio between the sensitivities of the optical traps.

In the method described in Chapter 6 the corner times that were calculated in volts was used denoted here by $\tau_c^{(V)}$:

$$\tau_c^{(V)} = \frac{\sigma^2\varepsilon_0}{k_BT}. \tag{A.18}$$

Taking the ratio of the corner times in volts and equating to unity gives,

$$\frac{\tau^{(V)}_{c(1)}}{\tau^{(V)}_{c(2)}} = \frac{\frac{\sigma^2_{(1)}\varepsilon_0}{k_BT}}{\frac{\sigma^2_{(2)}\varepsilon_0}{k_BT}} \tag{A.19}$$

$$1 = \frac{\sigma^2_{(1)}}{\sigma^2_{(2)}} \tag{A.20}$$

$$= \frac{S^2_{(2)}(P_{(2)})}{S^2_{(1)}(P_{(1)})}. \tag{A.21}$$

When the corner times are equal so are the sensitivities of the traps.

# Appendix B

# Cross-Correlation Intercept Proof

This appendix details the reason that when calculating the cross correlated motion the length of the data series used must be much larger than the length of the resultant data series, *i.e.* that if the correlated time scale of interest is $\sim 1s$ a data ceries of $> 10s$ must be used.

## B.1 Calculating the Mean

The Brownian forces experienced by a single particle in an optical trap must have a mean value of zero in the long time limit,

$$\lim_{t\to\infty} \langle F_B(t) \rangle = 0. \tag{B.1}$$

Resulting in the displacements of the particle, along any axis, as having a mean value of zero in the same limit,

$$\lim_{t\to\infty} \langle x(t) \rangle = 0. \tag{B.2}$$

From here onward the long time limit notation will be dropped and will be implied by the angular brackets.

This is the case for the ideal situation. The experimental situation is slightly different, the particle will indeed experience Brownian forces that will have a mean of zero in the long time limit but the recorded voltage will be offset from zero by some systematic offset inherent in the alignment of the QPD detector to the image of the particles' displacements. As such the recorded voltage signal will not have a mean of zero,

$$\langle x^{(V)}(t) \rangle \neq 0. \tag{B.3}$$

Where the superscript $(V)$ denotes the voltage signal recorded by the QPD. To remove the offset for each data set the mean of the entire data set is calculated and subtracted from each data point $x_i^{(V)}$ in the data set:

$$x_i = x_i^{(V)} - \langle x^{(V)}(t) \rangle. \tag{B.4}$$

This gives the resultant data set a mean value approximately equal to zero, although there will still be some small finite offset $\delta x$,

$$\begin{aligned} \langle x(t) - \langle x(t) \rangle \rangle &= \delta x & \text{(B.5)} \\ &\approx 0. & \text{(B.6)} \end{aligned}$$

This approximation is good enough for most of the data that has been presented but will cause problems if not accounted for in the cross-correlation analysis.

If we consider a perfect data time series $x(t)$ that does has a mean of some finite value $\langle x(t) \rangle = \alpha$. This perfect data set would then conform to the condition,

$$\langle x(t) - \langle x(t) \rangle \rangle = 0. \tag{B.7}$$

If we extract every $n$th data point in $x(t)$ to create another times series $x'(t)$ with a lower resolution. It stands to reason that the mean of $x'(t)$ not equal be exactly equal to $\alpha$, $\langle x'(t) \rangle \neq \alpha$, it instead will have some small offset similar to that described earlier for the numerical calculation of the mean for the recorded time series. The mean of the data set could then be described by,

$$\begin{aligned} \langle x'(t) \rangle &= \alpha - \delta x & \text{(B.8)} \\ &= \langle x(t) \rangle - \delta x. & \text{(B.9)} \end{aligned}$$

The value of $\delta x$ will be directly proportional to the number of data points omitted from the perfect data set *i.e.* the sample time of the recorded data set $\Delta t$:

$$\begin{aligned} \delta x &\propto \Delta t & \text{(B.10)} \\ \delta x &= K \Delta t, & \text{(B.11)} \end{aligned}$$

where $K$ is some constant of proportionality. Accordingly equation B.9 can be rewritten,

$$\begin{aligned} \langle x'(t) \rangle &= \langle x(t) \rangle - \delta x \\ &= \langle x(t) \rangle - K \Delta t. & \text{(B.12)} \end{aligned}$$

If consider what the effects equation B.12 are when we subtract the analytical mean from our data set with finite resolution $\Delta t$:

$$x'(t) - \langle x'(t)\rangle = x'(t) - [\langle x(t)\rangle - K\Delta t] \tag{B.13}$$

$$= x'(t) - \langle x(t)\rangle + K\Delta t. \tag{B.14}$$

Statistically, the analytical value for $\langle x'(t)\rangle$ is defined as,

$$\langle x'(t)\rangle = \frac{1}{N}\sum_{i=0}^{N} x'_i, \tag{B.15}$$

and will approach that of the perfect value $\langle x(t)\rangle$ as $N \to \infty$. In this long term limit the value of the offset $K\Delta x \to 0$.

## B.2 Calculating the Cross-correlation

The calculation of the cross-correlation between two times series, $x(t)$ and $y(t)$, is defined mathematically as,

$$\langle x(t)y(t+\tau)\rangle = \int_{-\infty}^{\infty} x^*(t)y_(t+\tau)\mathrm{d}\tau. \tag{B.16}$$

However the data that is recorded is a finite series of data and cannot readily be described with a functional form. Each data set will have a finite number of terms $N$ where $N$ can be related to the time by,

$$N = \frac{t}{\Delta t}. \tag{B.17}$$

where $\Delta t$ is the time between the recorded samples of the detector, *e.g.* for a typical sample rate of $20kHz$ the time between samples will be $\Delta t = 5 \times 10^{-5}s$. The cross-correlation $h$ can be calculated numerically as a function of time from the elements of the two data sets accordingly,

$$h_j = \frac{1}{M}\sum_{k=0}^{N-1} x_k y_{k+j}. \tag{B.18}$$

Where $j$ runs from $-(N-1)...(N-1)$. If the $k+j$th element does not exist the term is replaced with zero in the sum. The sum for each element is normalised by the number of non-zero elements present $M$.

An example of the analytical cross-correlation for two identical data sets is shown

in figure B.1 Here the cross-correlation runs from $-\tau$ to $+\tau$ this is due to the cross-correlation of two data sets of equal length. In the analysis that was used the data that corresponds to values $\tau < 0$ the data is flipped around the $y$ axis to give a data set with positive $\tau$ values. Then mean of the two data sets was calculated and used to give the final cross-correlations.

## B.3 Effect of a Non-zero Mean

If we consider the calculation for a single element of the cross-correlation between two finite series, $x_i$ and $y_j$, that have had an analytical mean subtracted from their data sets:

$$x_i = x'_i - \langle x', \rangle \tag{B.19}$$
$$y_j = y'_j - \langle y', \rangle \tag{B.20}$$

where $\langle x' \rangle \neq \langle x \rangle$ and $\langle y' \rangle \neq \langle y \rangle$ and instead are offset by some value,

$$x_i = x'_i - \langle x \rangle + K\Delta t \tag{B.21}$$
$$y_j = y'_j - \langle y \rangle + K\Delta t \tag{B.22}$$

Using these two data sets for the analytical definition of the cross-correlation,

$$\begin{aligned}
h_j &= \frac{1}{M}\sum_{k=0}^{N-1} x_k y_{k+j} \\
&= \frac{1}{M}\sum_{k=0}^{N-1} \left[x'_k - \langle x \rangle + K\Delta t\right] \times \left[y'_{k+j} - \langle y \rangle + K\Delta t\right] && \text{(B.23)} \\
&= \frac{1}{M}\sum_{k=0}^{N-1} x'_k y'_{k+j} - x'_k\langle y \rangle + x'_k K\Delta t - \langle x \rangle y'_{k+j} + \langle x \rangle\langle y \rangle \\
&\quad -\langle x \rangle K\Delta t + K\Delta t y'_{k+j} - K\Delta t\langle y \rangle + K^2(\Delta t)^2 && \text{(B.24)} \\
&= \frac{1}{M}\sum_{k=0}^{N-1} (x'_k - \langle x \rangle)(y'_{k+j} - \langle y \rangle) + x'_k K\Delta t - \langle x \rangle K\Delta t \\
&\quad +K\Delta t y'_{k+j} - K\Delta t\langle y \rangle + K^2(\Delta t)^2 && \text{(B.25)} \\
&= \frac{1}{M}\sum_{k=0}^{N-1} x_k y_{k+j} + K\Delta t(x'_k - \langle x \rangle + y'_{k+j} - \langle y \rangle + K\Delta t) && \text{(B.26)} \\
&= \frac{1}{M}\sum_{k=0}^{N-1} x_k y_{k+j} + K\Delta t(x_k + y_{k+j} + K\Delta t). && \text{(B.27)}
\end{aligned}$$

It can be seen from equation B.27 that if there is a slight offset in the subtraction of the mean from the data set then this offset will work its way through the cross-correlation calculation producing an offset that will that will cause a systematic offset to the calculation.

To limit the effect of this systematic offset there are two options, decrease sample time step $\Delta t$ by increasing the sample rate or increase the number of data points that are used to calculate the cross-correlation. Increasing the sample rate is possible on other systems but on the system that was used in this research a rate faster than $20kHz$ was not used as the recorded voltages from each detector could no longer be regarded as being simultaneous at these rates. Increasing the number of data points is limited by the memory capacity of the computer program used. The region of interest that has been presented here had a correlation time of $\tau < 1s$, to this end a minimum number of $2^{18} = 262144$ data points were used corresponding to a time of $\sim 13.10s$, an order of magnitude greater.

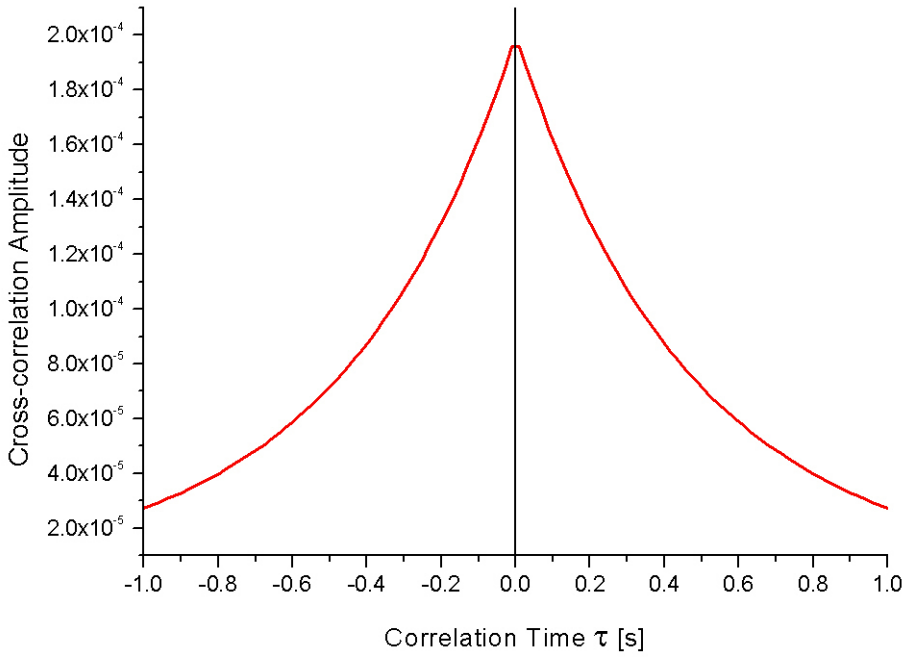


Figure B.1: Example of calculated cross-correlation of two identical data sets that run from correlation time $-\tau$ to $+\tau$ with a symmetry about the $y$ axis. This would not necessarily be the case for two independent data sets.

# Appendix C

# Error Analysis

This appendix deals with the error analysis that was used to analyse the data that has been presented throughout this research.

## C.1 Passive Micro-rheology Analysis

In the passive micro-rheology data a data set would be broken up into sections of with $2^{21} = 2097152$ data points. A the fast Fourier transform of a section of data was calculated and the mean over all sections was determined:

$$X_k = \frac{1}{N}\sum_{T=1}^{N} T_k. \tag{C.1}$$

where $X_k$ is the $k$th element in the final power spectrum calculated from $N$ sections, where $T$ represents one section of length 2097152 data points.

The standard deviation on a single data point can be defined as,

$$\sigma = \sqrt{\frac{1}{N}\sum_{i=1}^{N}(X_i - \langle X\rangle)^2}. \tag{C.2}$$

For the data that has been presented here $N > 16$ for all the analysis. The resulting data set consisted of series data series with length $\sim 10^4$ data points. That is then used to calculate the effective diffusion constant of the colloidal suspension.

The error on the values determined for $D^{(Short)}$ can be defined as being less than,

$$\Delta D^{(Short)} < \frac{1}{\sqrt{10^4}} D^{(Short)}. \tag{C.3}$$

Which as a percentage would give an error of less than $\Delta D^{(Short)} < 1\%$.

The Stokes-Einstein relation that was used to determine the effective viscosity is,

$$D = \frac{k_B T}{6\pi\eta a}, \tag{C.4}$$

which was rearranged to give the effective viscosity is,

$$\eta = \frac{k_B T}{6\pi D^{(Short)} a}. \tag{C.5}$$

The error on the effective viscosity $\eta$ can be calculated using the addition of errors in quadrature,

$$\frac{\Delta\eta}{\eta} = \sqrt{\left[\frac{\Delta T}{T}\right]^2 + \left[\frac{\Delta D^{(Short)}}{D^{(Short)}}\right]^2 + \left[\frac{\Delta a}{a}\right]^2}. \tag{C.6}$$

The uncertainty in the temperature of the lab was approximately $1^{\circ}C$ which would correspond to an uncertainty of 0.3% and as has been stated in Chapter 4 the uncertainty in the size of the tracer particles was given by the vendor as 5%. Using these numerical values in equation C.6 gives,

$$\begin{aligned} \frac{\Delta\eta_{eff}}{\eta_{eff}} &= \sqrt{0.003^2 + 0.01^2 + 0.05^2} && \text{(C.7)} \\ &= \sqrt{9\times10^{-4} + 1\times10^{-4} + 2.5\times10^{-3}} && \text{(C.8)} \\ &\approx 6\%. && \text{(C.9)} \end{aligned}$$

The error that had been calculated on the viscosity of the CHB/Decalin mixture was determined to be $4\times10^{-2} mPa\ s$ and as a percentage the uncertainty was found to be $\Delta\eta_0 = 1.6\%$. All viscosities that were presented in Chapter 5 had been normalised by the viscosity of the CHB/Declin mixture and as such the final error on the data points that were calculated was,

$$\begin{aligned} \frac{\Delta\frac{\eta_{eff}}{\eta_0}}{\frac{\eta_{eff}}{\eta_0}} &= \sqrt{\left[\frac{\Delta\eta_{eff}}{\eta_{eff}}\right]^2 + \left[\frac{\Delta\eta_0}{\eta_0}\right]^2} && \text{(C.10)} \\ &= \sqrt{3.6\times10^{-3} + 1\times10^{-4}} && \text{(C.11)} \\ &\approx 6.1\%. && \text{(C.12)} \end{aligned}$$

Which shows that the over-riding uncertainty on the determination of the viscosities calculated in Chapter 5 is the uncertainty associated with the radius of the tracer

particle that is used as a probe.

## C.2 Active Micro-rheology Analysis

For the active micro-rheology data analysis the displaced section of the time series is used. This section was typically a series of length $\sim 6 \times 10^5$ data points. The data was converted from Volts to either pico-Newtons or nanometers depending on the variable desired for the next stage in the analysis. Typically the data was converted into pico-Newtons as this corrected for the anharmonicity of the optical trap that was used. The conversion factor that was used had been determined from the straight line fits shown in Chapter 3 and relies on the assumption that the particle that is used in all experiments is the same size as the particle that was used in the calibration. This places a 5% error on the conversion of volts into pico-Newtons due to the error associated with the particle size.

A histogram was plotted of the force $F$ experienced by the tracer particle as it is being dragged through the suspension and fitted with a gaussian to determine the average force $\langle F \rangle$ experienced by the particle during the length of the drag run:

$$g(x) = \frac{1}{\sigma\sqrt{2\pi}} e^{-(F-\langle F \rangle)^2/2\sigma^2}. \tag{C.13}$$

The uncertainty associated with the fit of the value for $\langle F \rangle$ is not $\sigma$ as $\sigma$ describes the fluctuations in the force experienced by the particle over the displaced run. It is instead given by the number of points that were used to determine the mean,

$$\Delta\langle F \rangle = \frac{1}{\sqrt{6 \times 10^5}} \langle F \rangle \tag{C.14}$$

$$\approx 0.0013 \times \langle F \rangle. \tag{C.15}$$

By simple inspection it can be seen that the over-riding source of error on average force of the active displacements will be the assumption that the radius of the particle used for the calibrations is identical to the radius of the particle that was dragged through the colloidal suspension.

The equation that was used to determined the normalised active microviscosity was,

$$\frac{\eta_{eff}}{\eta_0} = \frac{\langle F \rangle}{6\pi a v \eta_0}. \tag{C.16}$$

Propagation of the error through the above equation yields where the slowest value for the drag velocity was used with an instrumental error of $5 \times 10^{-3} \mu s^{-1}$ and the error on the average force and the size of the particle cannot be regarded as independent as

they are dependant on the same variable,

$$\frac{\Delta\frac{\eta_{eff}}{\eta_0}}{\frac{\eta_{eff}}{\eta_0}} = \sqrt{\left[\frac{\Delta\langle F\rangle}{\langle F\rangle}\right]^2 + \left[\frac{\Delta v}{v}\right]^2 + \left[\frac{\Delta\eta_0}{\eta_0}\right]^2} \tag{C.17}$$

$$\leqslant \sqrt{0.05^2 + 0.01^2 + 0.016^2} \tag{C.18}$$

$$\leqslant 1.86\%. \tag{C.19}$$

Again the over-ridding error associated with the measurements that have been made to calculate the active microviscosities presented in Chapter 5 is the error on the radius of the tracer particle that was confined by the optical trap.

## C.3 Cross-correlation Analysis

The error associated with the cross-correlation analysis that was used in Chapter 6 is similar to the error that was calculated for the active micro-rehology on the data set.

The initial calibration that was carried out was to balance to the optical traps with the corner times of the mean square displacements to be less than 5%. This normalisation was carried out without the implicit knowledge of the optical trap stiffness needing to be known as the the derivation described in Appendix A has shown that when the corner times are equal the optical trap stiffnesses have to be equal as well.

With the stiffnesses of each trap normalised out the uncertainty in the stiffness has no effect on the amplitude of the cross-correlation as derivation of equation 6.7 shows.

The numerical error associated with with each data point in the cross-correlated motion is insignificantly small as each data point was calculated from the sum of approximately $33 \times 10^6$ data points for correlation times of $\tau < 1s$. This gives a the numerical error on any value of the correlated motion as approximately $1.7 \times 10^{-2}\%$.

## C.4 Coupled Diffusion Error Analysis

The error on the coupled diffusions for the correlated and anti-correlated mode is exactly the same as the error calculated for for the short time diffusion $D^{(Short)}$ given in section C.1. This is because the same generalised Stokes-Einstein relation is used and the same number of data points were used to calculated the initial slope of the the diffusion from the mean squared displacements.

# Appendix D

# Laser Position Fluctuations

This appendix describes how the systematic uncertainty in the position of the optical traps were determined from active drag experiments.

## D.1 Positional Offset

In Chapter 5 the active microviscosity of suspensions of colloidal particles were determined by dragging the tracer particle, confined in the optical trap, through the suspension. For the first three minutes the particle was held stationary experiencing Brownian motion around the equilibrium position of the optical trap. The particle was then dragged through the suspension for a period of time and held stationary again for the last three minutes. As the Brownian motion experienced by the particle at the beginning and end of the experimental run is about the centre of the optical trap this motion can be used to determine the drift of the laser with time. The mean of the particle's position in these two regions was calculated and the mean of the end section was subtracted from the beginning section. Once many data sets had been recorded a measurement of the average drift could be determined.

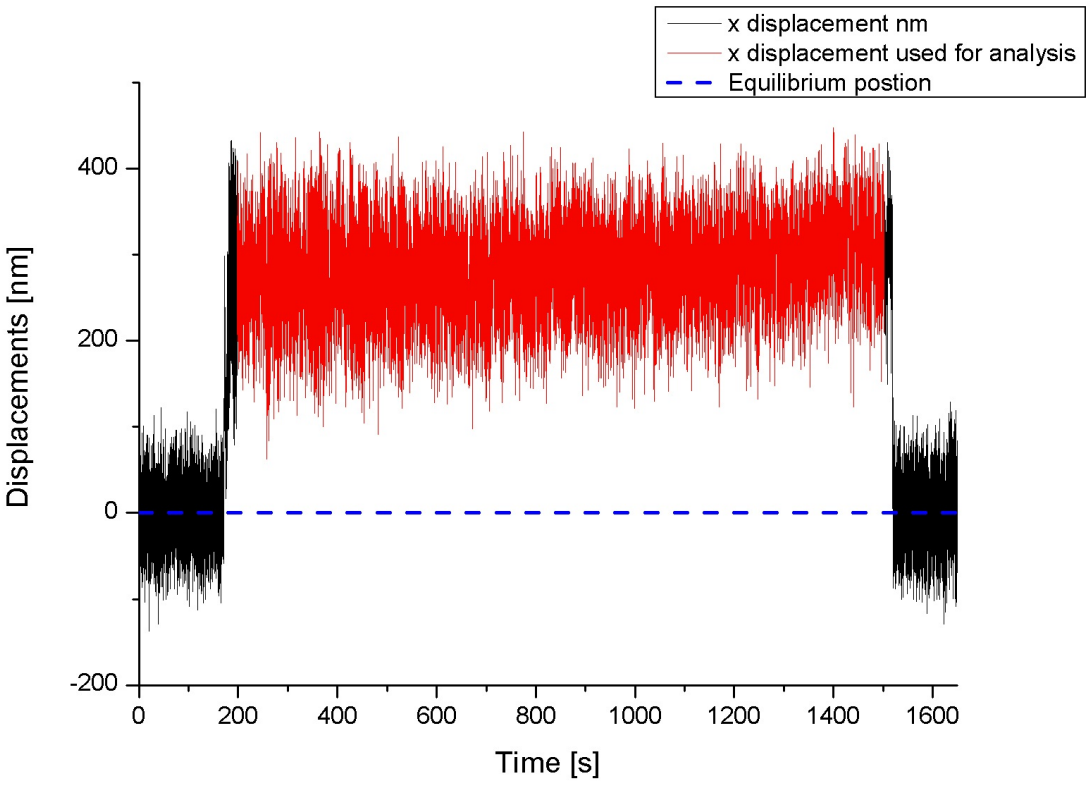


Figure D.1: Tracer displacement from equilibrium position as a function of time for a sample with volume fraction $\phi = 0.30$ dragged with a velocity of $v = 6.0\mu ms^{-1}$. The fluctuations around the equilibrium position (indicated by the dashed blue line) at the beginning and end of the run were used to determine the drift of the experimental system and the error on the displacement that was used to determine the microvisosity. The displacement marked in red is the section that was used to determine the tracer's displacement from equilibrium.

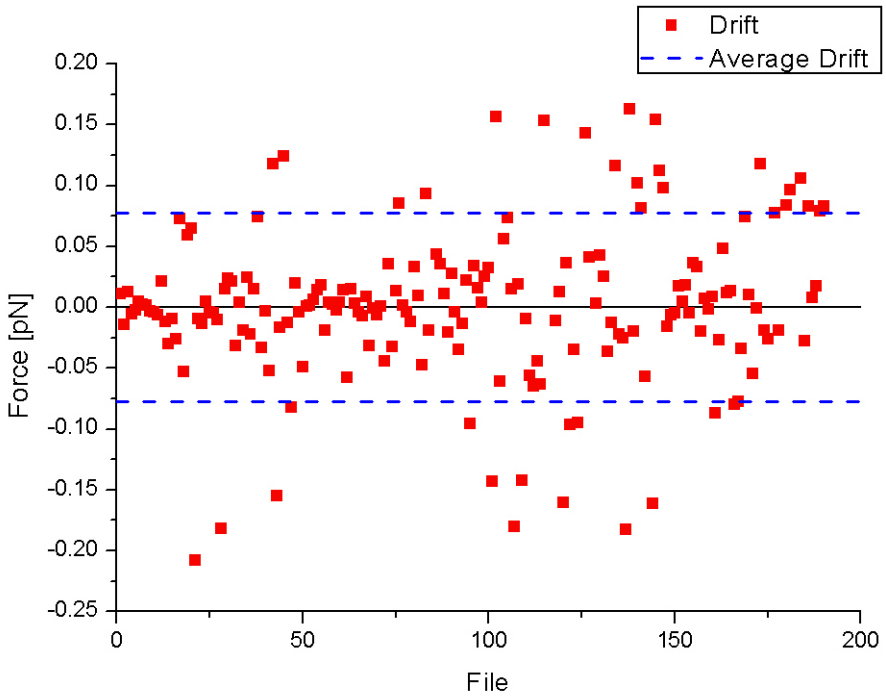


Figure D.2: Average force that is observed in the drift of the trapping laser.

# Appendix E

# Viscosity Graphs

This appendix shows a graph of all the normalised viscosities as functions of volume fraction for all the micro and macroviscosities that were presented in Chapter 5 where the simulation data has been modified to include hydrodynamics and all the low shear data (both experimental and simulations) have been corrected to the values that constant force tweezers would have measured. It also shows a graph with all the active micro-viscosities for high and low shear measured using constant velocity optical tweezers.

## E.1 Viscosity as a Function of Volume Fraction

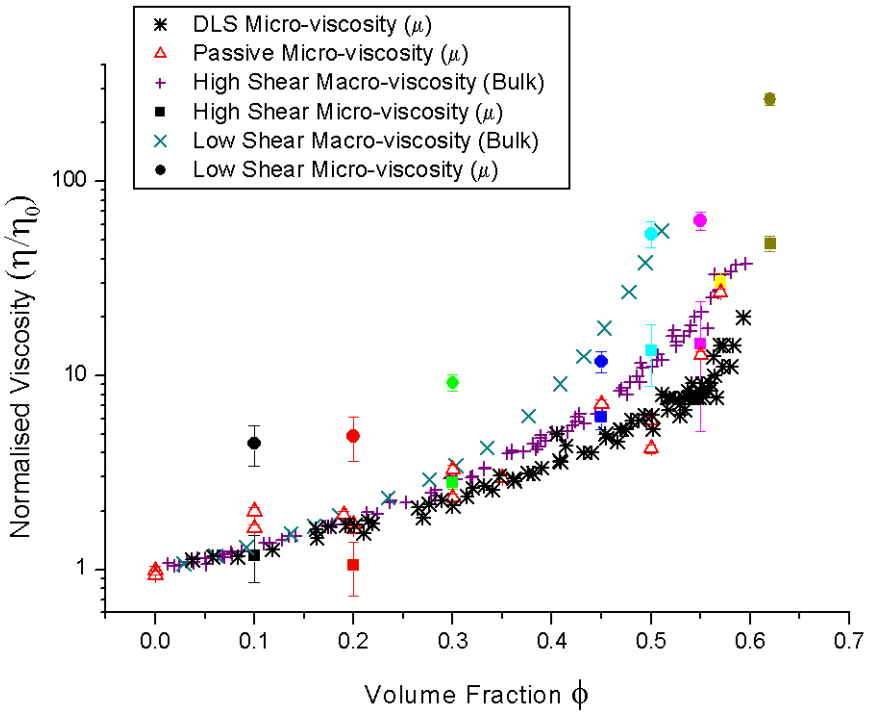


Figure E.1: Normalised viscosities presented in Chapter 5. High shear microviscosities are from fit results, low shear micro-viscosties have been modified to represent values measured if constant force tweezers had been used instead of constant velocity.

## E.2 Active Microviscosities as Functions of Péclet Number

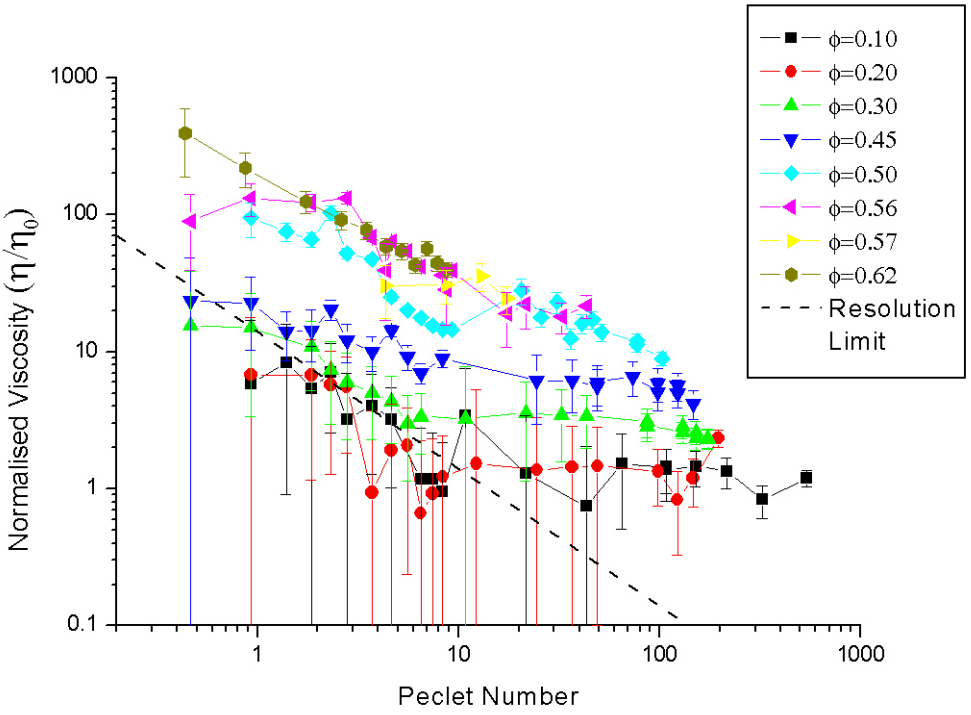


Figure E.2: High and low shear active microviscosities for volume fractions presented in Chapter 5 measured using constant velocity optical tweezers. No modifications have been made to any of the data presented here.

# Appendix F

# Higher Order Corrections to the Oseen Tensor

This appendix details the derivation that was carried out by *Dr. Alexander Morozov* to determine the second order corrections to the predicted minima used in figure 6.12.

## F.1 Derivation of 2nd order correction to Minima Prediction

In [8] the form of the cross correlation between two particles is described by,

$$h_{i,j}(t) = \frac{\langle x_i(t)x_j(0)\rangle}{\sqrt{\langle x_i^2\rangle\langle x_j^2\rangle}} \tag{F.1}$$

$$= \frac{1}{2}\left[e^{-\frac{\kappa t}{\xi_+}} - e^{-\frac{\kappa t}{\xi_-}}\right] \tag{F.2}$$

with the normalisation and the assumption that both traps have identical stiffnesses,

$$\langle x_i^2\rangle = \frac{2k_BT}{\kappa_i}, \tag{F.3}$$

and defining $\xi_+$ and $\xi_-$ by elements in the friction tensor of the two particles,

$$\xi_+ = \xi_{i,i} + \xi_{i,j}, \tag{F.4}$$

$$\xi_- = \xi_{i,i} - \xi_{i,j}. \tag{F.5}$$

Meiners and Quake [7] on the other hand defines the cross-correlation (to first order) as,

$$h_{ix,jx}(t) = \langle R_{ix}(t) R_{jx}(0) \rangle \tag{F.6}$$

$$= \frac{k_B T}{2\kappa_x} \left[ e^{-\frac{t(1+\xi_x)}{\tau_x}} - e^{-\frac{t(1-\xi_x)}{\tau_x}} \right], \tag{F.7}$$

where $R_i(t)$ are the three dimensional displacements of the $i$ particle. The subscript $x$ in equation F.7 denotes that the displacement in the $x$ (longitudinal) direction is being considered and $\tau_x$ and $\xi_x$ have the forms,

$$\tau_x = \frac{6\pi\eta_0 a}{\kappa_x} \tag{F.8}$$

$$\xi_x = \frac{3a}{2R}. \tag{F.9}$$

Where $R$ here, and from now on, is the centre to centre separation of the two particles. The equivalence of the exponents of the correlated mode in equation F.2 and F.7 can be shown by,

$$\frac{\kappa}{\xi_+} = \frac{1+\xi_x}{\tau_x} \tag{F.10}$$

$$= \frac{\kappa}{6\pi\eta_0 a} \left[ 1 + \frac{3a}{2R} \right] \tag{F.11}$$

$$= \frac{\kappa}{\xi_{1,1} + \xi_{1,2}}, \tag{F.12}$$

and the anti-correlated mode can be described as,

$$\frac{\kappa}{\xi_-} = \frac{\kappa}{6\pi\eta_0 a} \left[ 1 - \frac{3a}{2R} \right] \tag{F.13}$$

$$= \frac{\kappa}{\xi_{1,1} - \xi_{1,2}}, \tag{F.14}$$

where $\xi_{1,1}$ and $\xi_{1,2}$ in the longitudinal direction have the the forms [8],

$$\xi_{1,1} = \xi_0 \left( 1 + \frac{9}{4}\left(\frac{a}{R}\right)^2 + \frac{93}{16}\left(\frac{a}{R}\right)^4 + \frac{1197}{64}\left(\frac{a}{R}\right)^6 + \ldots \right), \tag{F.15}$$

$$\xi_{1,2} = \xi_0 \left( -\frac{3}{4}\left(\frac{a}{R}\right) - \frac{19}{8}\left(\frac{a}{R}\right)^3 - \frac{387}{32}\left(\frac{a}{R}\right)^5 + \ldots \right). \tag{F.16}$$

These can be approximated to first order and inserted into equations F.12 and F.14 and using a Taylor expansion on these two equations it can be shown that,

$$\frac{\kappa}{\xi_0\left[1-\frac{3R}{2a}\right]} \cong \frac{\kappa}{\xi_0\left[1-\frac{3R}{2a}\right]} \tag{F.17}$$

Replacing making the appropriate substitutions equation F.7 becomes,

$$\langle R_{ix}(t)R_{jx}(0)\rangle = \frac{k_BT}{2\kappa_x}\left[e^{-\frac{t\kappa}{\xi_+}} - e^{-\frac{t\kappa}{\xi_-}}\right]. \tag{F.18}$$

To determine the minima the derivative of the cross-correlation is solved for zero,

$$\begin{aligned}\frac{\mathrm{d}}{\mathrm{d}t}\langle R_{ix}(t)R_{jx}(0)\rangle &= \frac{k_BT}{2\kappa_x}\left[e^{-\frac{t\kappa}{\xi_+}} - e^{-\frac{t\kappa}{\xi_-}}\right] \\ &= -\frac{\kappa}{\xi_+}e^{-\frac{\kappa t}{\xi_+}} + \frac{\kappa}{\xi_-}e^{-\frac{\kappa t}{\xi_-}}. \end{aligned}\tag{F.19}$$

$$-\frac{\kappa}{\xi_+}e^{-\frac{\kappa t_{min}}{\xi_+}} + \frac{\kappa}{\xi_-}e^{-\frac{\kappa t_{min}}{\xi_-}} = 0 \tag{F.20}$$

$$\frac{\kappa}{\xi_-}e^{-\frac{\kappa t_{min}}{\xi_-}} = \frac{\kappa}{\xi_+}e^{-\frac{\kappa t_{min}}{\xi_+}} \tag{F.21}$$

$$\frac{\xi_+}{\xi_-} = e^{-\kappa t_{min}\left(\frac{1}{\xi_+}-\frac{1}{\xi_-}\right)} \tag{F.22}$$

$$\ln\frac{\xi_+}{\xi_-} = -\kappa t_{min}\left(\frac{1}{\xi_+}-\frac{1}{\xi_-}\right) \tag{F.23}$$

$$t_{min} = -\frac{1}{\kappa}\left(\frac{\xi_-\xi_+}{\xi_- - \xi_+}\right)\ln\frac{\xi_+}{\xi_-}. \tag{F.24}$$

The depth of the cross-correlation minima is,

$$\langle R_{ix}(t_{min})R_{jx}(0)\rangle = \frac{k_BT}{2\kappa}\left[e^{\left\{\left(\frac{\xi_-}{\xi_- - \xi_+}\right)\left(\ln\frac{\xi_+}{\xi_-}\right)\right\}} - e^{\left\{\left(\frac{\xi_+}{\xi_- - \xi_+}\right)\left(\ln\frac{\xi_+}{\xi_-}\right)\right\}}\right]. \tag{F.25}$$

By replacing $\xi_+$ and $\xi_-$ with their forms given in equations F.16 and expanding and the logarithms and then the exponentials an approximation for higher order corrections to the minima can be determined,

$$\langle R_{ix}(t_{min})R_{jx}(0)\rangle = \frac{k_BT}{2\kappa e}\left[-\frac{3a}{R} + \frac{7}{8}\left(\frac{a}{R}\right)^3 - \frac{6381}{640}\left(\frac{a}{R}\right)^5\right]. \tag{F.26}$$

Which when normalised by the mean square displacements of both particles in their optical traps becomes,

$$\langle R_{ix}(t_{min})R_{jx}(0)\rangle \;=\; \frac{1}{e}\left[-\frac{3a}{R}+\frac{7}{8}\left(\frac{a}{R}\right)^3-\frac{6381}{640}\left(\frac{a}{R}\right)^5\right]. \tag{F.27}$$

# Bibliography


[1] Roger Jardine. PhD thesis, School of Chemistry, The University of Bristol, 2000.

[2] P.N. Pusey and W van Megen. Phase-behavior of concentrated suspensions of nearly hard colloidal spheres. *Nature*, 320(6060):340–342, 1986.

[3] Lucio isa. *Capillary Flow of Dense Colloidal Suspensions.* PhD thesis, School of Physics, The University of Edinburgh, 2007.

[4] G. Petekidis, D. Vlassopoulos, and P. N. Pusey. Yielding and flow of sheared colloidal glasses. *Journal of Physics: Condensed Matter*, 16(38):S3955–S3963, 2004.

[5] W. van Megen, T. C. Mortensen, S. R. Williams, and J. Müller. Measurement of the self-intermediate scattering function of suspensions of hard spherical particles near the glass transition. *Physical Review E*, 58(5):6073–6085, 1998.

[6] W. van Megen. Random-Walk Analysis of Displacement Statistics of Particles in Concentrated Suspensions of Hard Spheres. *Physical Review E*, 73(1, Part 1), 2006.

[7] Jens-Christian Meiners and Stephen R. Quake. Direct measurement of hydrodynamic cross correlations between two particles in an external potential. *Physical Review Letters*, 82(10):2211–2214, 1999.

[8] Stuart Henderson, Steven Mitchell, and Paul Bartlett. Direct measurements of colloidal friction coefficients. *Physical Review E*, 64(6):061403, 2001.

[9] A. Ashkin, J. M. Dziedzic, J. E. Bjorkholm, and S. Chu. Observation of a single-beam gradient force optical trap for dielectric particles. *Optics Letters*, 11(5):288–290, 1986.

[10] P.J. Bronkhorst, G.J. Streekstra, J. Grimbergen, E.J. Nijhof, J.J. Sixma, and G.J. Brakenhoff. A new method to study shape recovery of red blood cells using multiple optical trapping. *Biophysical Journal*, 69(5):1666 – 1673, 1995.

[11] Graham D. Wright, Jochen Arlt, Wilson C.K. Poon, and Nick D. Read. Experimentally manipulating fungi with optical tweezers. *Mycoscience*, 48:15–19, 2007.

[12] S Henderson, S Mitchell, and P Bartlett. Position correlation microscopy: Probing single particle dynamics in colloidal suspensions. *Colloids and Surfaces A-Physicochemical and Engineering Aspects*, 190(1-2):81–88, 2001.

[13] A. Meyer, A. Marshall, B.G. Bush, and E.M. Furst. Laser Tweezer Microrheology of A Colloidal Suspension. *Journal of Rheology*, 50(1):77–92, 2006.

[14] M. Reicherter, T. Haist, E. U. Wagemann, and H. J. Tiziani. Optical particle trapping with computer-generated holograms written on a liquid-crystal display. *Optics Letters*, 24(9):608–610, 1999.

[15] K.C. Neuman and S.M. Block. Optical Trapping. *Review of Scientific instruments*, 75(9):2787–2809, 2004.

[16] J.E. Molloy, J.E. Burns, J.C. Sparrow, R.T. Tregear, J. Kendrickjones, and D.C.S. White. Single-molecule mechanics of heavy-meromyosin and s1 interacting with rabbit or drosophila actins using optical tweezers. *Biophysical Journal*, 68:S298–S305, 1995.

[17] Erik Fällman and Ove Axner. Design for fully steerable dual-trap optical tweezers. *Applied Optics*, 36(10):2107–2113, 1997.

[18] S.E. Phan, W.B. Russel, Z.D. Cheng, J.X. Zhu, P.M. Chaikin, J.H. Dunsmuir, and R.H. Ottewill. Phase Transition, Equation of State, and Limiting Shear Viscosities of Hard Sphere Dispersions. *Physical Review E*, 54(6):6633–6645, 1996.

[19] A Ashkin. Acceleration and trapping of particles by radiation pressure. *Physical Review Letters*, 24(4):156–160, 1970.

[20] J. E. Molloy and M. J. Padgett. Lights, action: Optical tweezers. *Contemporary Physics*, 43(4):241–258, 2002.

[21] A Mazolli, P. A. M. Neto, and H. M. Nussenzveig. Theory of trapping forces in optical tweezers. *Proceedings of The Royal Society of London Series A-Mathematical Physical and Engineering Sciences*, 459(2040), 2003.

[22] J. D. Jackson. *Classical Electrodynamic*. John Wiley and Sons inc., 2nd edition, 1975.

[23] T. Tlusty, A. Meller, and R. Bar-Ziv. Optical gradient forces of strongly localized fields. *Physical Review Letters*, 81(8):1738–1741, 1998.

[24] Laurence Wilson. *Optical Force Measurements in Concentrated Colloidal Suspensions*. PhD thesis, School of Physics, The University of Edinburgh, 2007.

[25] K. Berg-Sørensen and H Flyvbjerg. Power spectrum analysis for optical tweezers. *Review of Scientific instruments*, 75(3):594–612, 2004.

[26] F. Gittes and C. F. Schmidt. Signals and noise in micromechanical measurements. *Methods in Cell Biology*, 55:129–156, 1998.

[27] L. P. Ghislain, N. A. Switz, and W. W. Webb. Measurement of small forces using an optical trap. *Review of Scientific instruments*, 65(9):2762–2768, 1994.

[28] John C. Crocker and David G. Grier. Methods of digital video microscopy for colloidal studies. *Journal of Colloid and interface Science*, 179(1):298 – 310, 1996.

[29] W. H. Wright, G. J. Sonek, and M. W. Berns. Parametric study of the forces on microspheres held by optical tweezers. *Applied Optics*, 33(9):1735–1748, 1994.

[30] Pu Chun Ke and Min Gu. Characterization of trapping force in the presence of spherical aberration. *Journal of Modern Optics*, 45(10):2159 – 2168, 1998.

[31] F. Gittes and C. F. Schmidt. Interference model for back-focal-plane displacement detection in optical tweezers. *Optics Letters*, 23(1):7–9, 1998.

[32] A. Pralle, M. Prummer, E.-L. Florin, E.H.K. Stelzer, and J.K.H. Hörber. Three-dimensional high-resolution particle tracking for optical tweezers by forward scattered light. *Microscopy Research and Technique*, 44(5):378–386, 1999.

[33] A. Rohrback and K. Stelzer. Three-dimensional position detection of optically trapped dielectric particles. *Journal of Applied Physics*, 91(8):5474–5488, 2002.

[34] J. Huisstede, K. van der Werf, M. Bennink, and V. Subramaniam. Force detection in optical tweezers using backscattered light. *Opt. Express*, 13(4):1113–1123, 2005.

[35] P. N. Pusey. *Liquids, Freezing and The Glass Transition, Chapter 10*. Elsevier, 1991.

[36] Wilson Poon. Colloids as big atoms. *Science*, 304(5672):830–831, 2004.

[37] J Perrin. Mouvement brownien et molécule. *Journal De Physique*, 9(5), 1910.

[38] Ping Cheng, Jianxun Qiu, Mingyuan Gu, Yanping Jin, and Wenfeng Shangguan. Synthesis of shape-controlled titania particles from a precursor solution containing urea. *Materials Letters*, 58(29):3751 – 3755, 2004.

[39] Dr. andrew B. Schofield Private communication.

[40] L. Antl, J.W. Goodwin, R.D. Hill, R.H. Ottewill, S.M. Owens, S. Papworth, and J.A. Waters. The preparation of poly(methyl methacrylate) latices in non-aqueous media. *Colloids and Surfaces*, 17(1):67 – 78, 1986.

[41] S. M. Underwood, J. R. Taylor, and W. van Megen. Sterically stabilized colloidal particles as model hard spheres. *Langmuir*, 10:3550–3554, 1994.

[42] Paul Bartlett and Andrew I. Campbell. Three-dimensional binary superlattices of oppositely charged colloids. *Physical Review Letters*, 95(12):128302, 2005.

[43] J. N. israelachvili. *intramolecular and Surface Forces*. Academic Press, London, 2 edition, 1991.

[44] A. Yethiraj and A. van Blaaderen. A colloidal model system with an interaction tunable from hard sphere to soft and dipolar. *Nature*, 421(6922), 2003.

[45] D. C. Henry. The cataphoresis of suspended particles part i - the equation of cataphoresis. *Proceedings of the Royal Society London Series A*, 133(821):106–129, 1931.

[46] I.K. Robinson and D.J. Tweet. Surface x-ray diffraction. *Reports On Progress in Physics*, 55(5):599–651, 1992.

[47] David John Fairhurst. *Polydispersity in Colloidal Phase Tansitions*. PhD thesis, Department of Physics and Astronomy, The University of Edinburgh, 1999.

[48] A. D. Dinsmore, Eric R. Weeks, Vikram Prasad, andrew C. Levitt, and D. A. Weitz. Three-dimensional confocal microscopy of colloids. *Applied Optics*, 40(24):4152–4159, 2001.

[49] Alfons van Blaaderen and Pierre Wiltzius. Real-space structure of colloidal hard-sphere glasses. *Science*, 270(5239):1177–1179, 1995.

[50] Eric R. Weeks, J. C. Crocker, Andrew C. Levitt, Andrew Schofield, and D. A. Weitz. Three-dimensional direct imaging of structural relaxation near the colloidal glass transition. *Science*, 287(5453):627–631, 2000.

[51] John C. Crocker and David G. Grier. Methods of digital video microscopy for colloidal studies. *Journal of Colloid and interface Science*, 179(1):298 – 310, 1996.

[52] Roberto Cerbino and Veronique Trappe. Differential dynamic microscopy: Probing wave vector dependent dynamics with a microscope. *Physical Review Letters*, 100(18):188102, 2008.

[53] Fabio Giavazzi, Doriano Brogioli, Veronique Trappe, Tommaso Bellini, and Roberto Cerbino. Scattering information obtained by optical microscopy: Differential dynamic microscopy and beyond. *Physical Review E*, 80(3):031403, 2009.

[54] *Zeta Sizer Operating Manual*.

[55] Jinyu Zhao, Doris Vollmer, Hans-Jürgen Butt, and Günter K. Auernhammer. Localized instabilities of colloidal motion in ac electric field gradients. *Journal of Physics: Condensed Matter*, 20(40):404212, 2008.

[56] M. D. Haw. Jamming, two-fluid behavior and self-filtration in concentrated particulate suspensions. *Physical Review Letters*, 92(18):185506, 2004.

[57] R. G. Larson. *The Structure and Rheology of Complex Fluids*. Oxford University Press, Oxford, 1999.

[58] Matthias Fuchs and Michael E. Cates. Theory of nonlinear rheology and yielding of dense colloidal suspensions. *Physical Review Letters*, 89(24):248304, 2002.

[59] Peter Sollich, François Lequeux, Pascal, and Michael E. Hébraud Cates. Rheology of soft glassy materials. *Physical Review Letters*, 78(10):2020–2023, 1997.

[60] Matthias Fuchs and Michael E. Cates. Non-newtonian viscosity of interacting brownian particles: Comparison of theory and data. *Journal of Physics: Condensed Matter*, 15(1):S401–S406, 2003.

[61] T. G. Mason and D. A. Weitz. Linear viscoelasticity of colloidal hard sphere suspensions near the glass transition. *Physical Review Letters*, 75(14):2770–2773, 1995.

[62] J.C. van der Werff, C.G. de Kruif, C. Blom, and J. Mellema. Linear viscoelastic behavior of dense hard-sphere dispersions. *Physical Review A: General Physics*, 39(2):795–807, 1989.

[63] Aditya S. Khair and John F. Brady. "microviscoelasticity" of colloidal dispersions. *Journal of Rheology*, 49(6):1449–1481, 2005.

[64] Tai-Hsi Fan, Jan K. G. Dhont, and Remco Tuinier. Motion of a sphere through a polymer solution. *Physical Review E*, 75(1):011803, Jan 2007.

[65] A. Buosciolo, G. Pesce, and A. Sasso. New calibration method for position detector for simultaneous measurements of force constants and local viscosity in optical tweezers. *Optics Communications*, 230(4-6):357 – 368, 2004.

[66] Aditya S. Khair and John F. Brady. Single Particle Motion in Colloidal Dispersions: A Simple Model For Active and Nonlinear Microrheology. *Journal of Fluid Mechanics*, 557:73–117, 2006.

[67] A.S. Khair and J.F. Brady. "Microviscoelasticity" of Colloidal Dispersions. *Journal of Rheology*, 49(6):1449–1481, 2005.

[68] I.C. Carpen and J.F. Brady. Microrheology of Colloidal Dispersions By Brownian Dynamics Simulations. *Journal of Rheology*, 49(6):1483–1502, 2005.

[69] T.M. Squires and J.F Brady. A Simple Paradigm For Active and Nonlinear Microrheology. *Physics of Fluids*, 17(7):073101, 2005.

[70] P. Habdas, D. Schaar, A.C Levitt, and E.R. Weeks. Forced Motion of A Probe Particle Near The Colloidal Glass Transition. *Europhysics Letters*, 67(3):477–483, 2004.

[71] with Piezo instruments Private communication.

[72] William B. Russel and Mae Chen Grant. Distinguishing between dynamic yielding and wall slip in a weakly flocculated colloidal dispersion. *Colloids and Surfaces A: Physicochemical and Engineering Aspects*, 161(2):271 – 282, 2000.

[73] S.P. Meeker, W.C.K. Poon, and P.N. Pusey. Concentration Dependence of The Low-Shear Viscosity of Suspensions of Hard-Sphere Colloids. *Physical Review E*, 55(5, Part B):5718–5722, 1997.

[74] W.C.K. Poon, S.P. Meeker, P.N. Pusey, and P.N. Segrè. Viscosity and Structural Relaxation in Concentrated Hard-Sphere Colloids. *Journal of Non-Newtonian Fluid Mechanics*, 67:179–189, 1996.

[75] J.C. van der Werff and C.G. de Kruif. Hard-Sphere Colloidal Dispersions - The Scaling of Rheological Properties With Particle-Size, Volume Fraction, and Shear Rate. *Journal of Rheology*, 33(3):421–454, 1989.

[76] R. Besseling, Eric R. Weeks, A. B. Schofield, and W. C. K. Poon. Three-dimensional imaging of colloidal glasses under steady shear. *Physical Review Letters*, 99(2):028301, 2007.

[77] John C. Crocker. Measurement of the hydrodynamic corrections to the brownian motion of two colloidal spheres. *The Journal of Chemical Physics*, 106(7):2837–2840, 1997.

[78] A.J. Levine and T.C. Lubensky. One- and Two-Particle Microrheology. *Physical Review Letters*, 85(8):1774–1777, 2000.

[79] J. Happel and H. Brenner. *Low Reynolds Number Hydrodynamics*. Martinus Nijhoff Publishers., 1st edition, 1983.

[80] G. K. Batchelor. Brownian diffusion of particles with hydrodynamic interaction. *Journal of Fluid Mechanics*, 74(01):1–29, 1976.

[81] G. H. Koenderink, M. Atakhorrami, F. C. Mackintosh, and C. F. Schmidt. High-frequency stress relaxation in semiflexible polymer solutions and networks. *Physical Review Letters*, 96(13):138307, 2006.